JOHANNES GUTENBERG UNIVERSITY MAINZ

DOCTORAL THESIS

SKYRMIONS AS QUASI-PARTICLES FROM DYNAMICS TO APPLICATION IN UNCONVENTIONAL COMPUTING

Author:
Klaus RAAB

Supervisors:
Prof. Dr. Mathias KLÄUI
Prof. Dr. Peter VIRNAU

A thesis submitted in fulfillment of the requirements for the degree of Doctor Rerum Naturalium

in the

Kläui Laboratory
Institute for Physics
Johannes Gutenberg University Mainz

22. September 2025

This dissertation is licensed under
Creative Commons - Attribution and Share Alike 4.0
CC BY-SA-4.0

Declaration of Authorship

I, Klaus RAAB, declare that this thesis titled, "SKYRMIONS AS QUASI-PARTICLES FROM DYNAMICS TO APPLICATION IN UNCONVENTIONAL COMPUTING" and the work presented in it are my own. I confirm that:

- This work was done wholly or mainly while in candidature for a research degree at this University.
- Where any part of this thesis has previously been submitted for a degree or any other qualification at this University or any other institution, this has been clearly stated.
- Where I have consulted the published work of others, this is always clearly attributed.
- Where I have quoted from the work of others, the source is always given. With the exception of such quotations, this thesis is entirely my own work.
- I have acknowledged all main sources of help.
- Where the thesis is based on work done by myself jointly with others, I have made clear exactly what was done by others and what I have contributed myself.

Signed:

Date:

“”Du musst nur die Laufrichtung ändern”, sagte die Katze zur Maus und fraß sie auf.”

Franz Kavka

JOHANNES GUTENBERG UNIVERSITY MAINZ

Abstract

Institute for Physics

Doctor Rerum Naturalium

SKYRMIONS AS QUASI-PARTICLES
FROM DYNAMICS TO APPLICATION IN UNCONVENTIONAL COMPUTING

by Klaus RAAB

This dissertation explores the magnetic behavior and manipulation of skyrmions - topologically protected spin textures in metallic thin films - focusing on their dynamics, confinement, and application in low-power unconventional computation. Skyrmion flow in the creep regime was studied in straight and modulated channels, revealing boundary-dependent velocity profiles in qualitative agreement with Thiele-based simulations.
Controlled He^+ and Ga^+ irradiation enabled tuning of magnetic properties and enabled creating artificial barrier for e.g., skyrmion compression. The experimental findings of the latter are compared and supported by adapted theoretical models and simulations.
A key part is the development of a novel reservoir computing (RC) scheme based on the Brownian dynamics of confined skyrmions. Even in a simplistic confining geometry like an equilateral triangle, the system performs Boolean logic operations, even nonlinear logic at ultra-low current densities. Its scalability and potential for increased complexity make skyrmion-based RC a promising platform for energy-efficient, unconventional computing.

Acknowledgements

I would like to express my sincere gratitude to Prof. Dr. Mathias Kläui for his continuous support, patience, and for providing me with numerous academic and professional opportunities throughout my time in his research group. Attending national and international conferences, engaging with like-minded people, and participating in stimulating discussions has been an immensely enriching and motivating experience.
Considering these opportunities, I gratefully acknowledge the financial support received from various funding bodies in Germany and the European Union. In particular, I would like to thank the DFG, DAAD, Spin+X, TopDyn, EU Horizon, NIMFEIA, and 3D-MAGiC programs, whose contributions have made this work possible. My sincere thanks extend to the permanent staff of the AG Kläui group and to all collaborators with whom I had the pleasure of working for their support. I would especially like to acknowledge Prof. Dr. Peter Virnau and many more (*censored names*) for their valuable insights and guidance, from whom I have learned a lot.
I am also deeply thankful to my fellow students and colleagues, whose collaboration, friendship, and encouragement have accompanied me throughout my academic journey. To name a few, in no particular order: Fabian Kammerbauer and many more (*censored names*) I had the pleasure of getting to know. I also want to acknowledge people organizing and leading various sports activities loosely linked to the university e.g., dancing communities like the Sientala community, Tango Argentino and Neo-Tango, ballroom dancing, RnR.
I am immensely grateful to my friends for their patience, understanding, and enduring support, even during periods when I may have unintentionally neglected our friendships.
Above all, I wish to extend my deepest gratitude to my family, especially my parents, for their unwavering belief in me and their continued support through every challenge and dark time. Their encouragement has been a constant source of strength.

Thank you all for helping me reach this milestone.

Contents

List of Figures

List of Tables

List of Abbreviations

2D or **3D**	**T**wo- or **T**hree-**D**imensional
AI	**A**rtificial **I**ntelligence
CMOS	**C**omplementary **M**etal-**O**xide **S**emiconductor
DMI	**D**zyaloshinskii-**M**oriya **I**nteraction
DC and **AC**	**D**irect **C**urrent and **A**lternating **C**urrent
EBL	**E**lectron **B**eam **L**ithography
FM	**F**erromagnetic **M**etal
HM	**H**eavy **M**etal
IP	**I**n-**P**lane
LLB	**L**andau-**L**ifshitz-**B**loch equation
LLG	**L**andau-**L**ifshitz-**G**ilbert equation
MRAM	**M**agnetic **R**andom **A**ccess **M**emory
MSD	**M**ean **S**quare **D**isplacement
MOKE	**M**agneto-**O**ptical **K**err **E**ffect
OOP	**O**ut-**O**f-**P**lane
PMA	**P**erpendicular **M**agnetic **A**nisotropy
PVD	**P**hysical **V**apor **D**eposition
RC	**R**eservoir **C**omputing
REE	**R**ashba-**E**delstein **E**ffect
ROI	**R**egion **O**f **I**nterest
SEM	**S**canning **E**lectron **M**icroscope
SHE	**S**pin **H**all **E**ffect
SkHE	**S**kyrmion **H**all **E**ffect
SkHA	**S**kyrmion **H**all **A**ngle
SNR	**S**ignal to **N**oise **R**atio
SOT	**S**pin-**O**rbit-**T**orque
STT	**S**pin-**T**ransfer **T**orque
TMR	**T**unnel **M**agneto-**R**esistance
MTJ	**M**agnetic **T**unnel **J**unction
NN	**N**eural **N**etwork

Dedicated to overcoming the harshest critic - oneself.

Chapter 1

Introduction

As global electricity consumption in general and specially from data centers accelerates - the latter driven primarily by the rapid adoption of machine learning and artificial intelligence (AI) technologies that rely on high-performance, accelerated computing architectures - concerns over the energy and environmental impact of modern computation are intensifying. Electricity use by data centers is projected to nearly double from 460 TWh in 2024 to over 945 TWh by 2030, with AI-specific workloads playing a dominant role in this increase. High performance servers, tailored for machine learning inference and training tasks, are expected to grow at an annual rate of 30%, contributing to nearly half of the overall growth in data center electricity demand. By 2030, data centers are anticipated to account for nearly 3% of global electricity consumption - up from 1,5% in 2024 - highlighting their rising significance in the global energy landscape. Despite contributing less than 10% to the total projected growth in electricity demand, data centers present distinct integration challenges due to their localized power density and deployment timelines that outpace conventional energy infrastructure development [1].

This trajectory underscores the critical importance of energy-efficient computing paradigms. In this context, spintronics, and particularly skyrmionics - the utilization of magnetic skyrmions in spintronic systems - emerges as a highly promising alternative or addition to conventional CMOS-based logic, sensor or storage technology. Magnetic skyrmions are topologically protected, nano-scale spin textures that can be manipulated using extremely low current densities through spin-transfer (STT) or spin-orbit torques (SOT). Their intrinsic nonlinear dynamics, therlly driven stochastic motion, and pronounced sensitivity to geometric confinement render skyrmions particularly well-suited for unconventional, low-power computing paradigms, such as neuromorphic and reservoir computing, as well as energy-efficient memory and sensing applications. These architectures seek to emulate features of biological neural processing by exploiting the stochastic and nonlinear behavior of skyrmions for efficient information storage and computation. Beyond their utility in energy-efficient applications, skyrmions also serve as a potential model system in statistical physics. Their tunability and two-dimensional (2D) nature make them an ideal platform for studying a variety of collective phenomena, including lattice ordering, phase transitions, rheological flow, and emergent interactions under confinement, such as skyrmion-skyrmion and skyrmion-boundary repulsion. Their Brownian-like thermal motion and size adaptability further enable the experimental investigation of 2D non-equilibrium systems.

This thesis also explores permanent tuning of the magnetic properties of thin films via ion irradiation, enabling controlled modifications of skyrmion phase behavior and confinement through engineered boundary conditions. A central contribution of this work is the demonstration of Boolean logic operations and complex

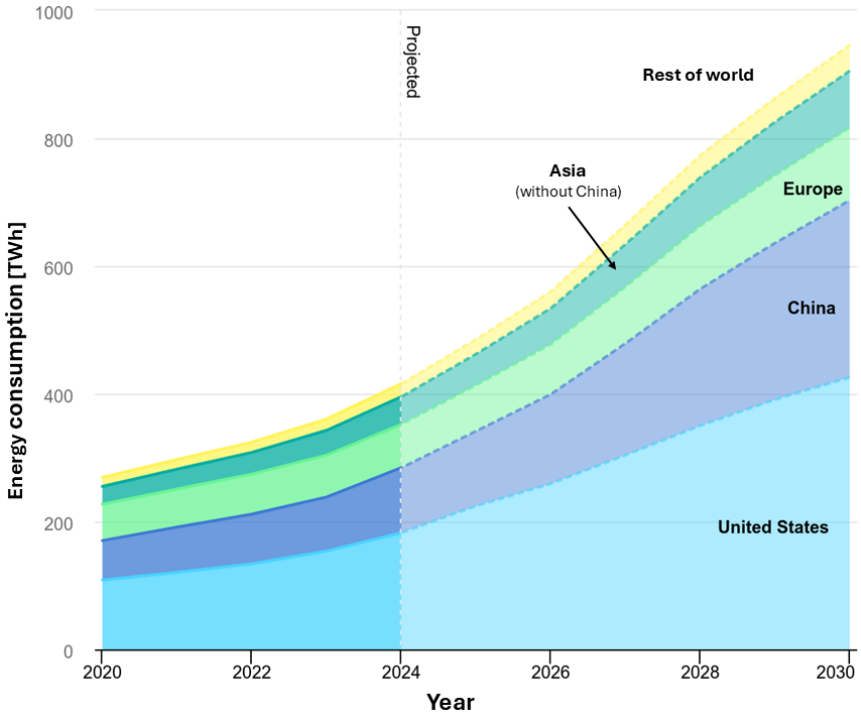

FIGURE 1.1: Regional data center electricity consumption from 2020 to 2030, with projections beyond 2024. the observed and projected increase in energy consumption is primarily driven by the expanding deployment and operational demands of machine learning and artificial intelligence systems. Adapted from [2].

dynamic behavior of skyrmions within minimal geometries at ultra-low power levels. These results reinforce the potential of skyrmion-based logic elements as highly energy-efficient building blocks for next-generation AI hardware.

Given their compatibility with existing thin-film fabrication techniques, scalability in 2D geometries, and sensitivity to external stimuli, skyrmion-based spintronic devices represent a compelling route toward sustainable, unconventional computing. As the computational demands, especially for AI, continue to rise, integrating skyrmionic architectures offers a pathway to reduce power consumption while preserving or enhancing computational complexity. These concepts are of growing importance alongside the integration of renewable and sustainable energy sources, aimed at mitigating the escalating anthropogenic environmental impact of contemporary digital infrastructure and overall energy consumption.

Chapter 2

Theory

This chapter provides an overview of the fundamental origins of magnetism, its governing principles, and its manifestation in solid-state systems. It further discusses methods for the manipulation and measurement of magnetic properties, as well as the connection to spin-related phenomena and structures, including domain walls and spin spirals, known as skyrmions. The study of spins and associated phenomena is of significant interest due to their considerable potential for applications in the emerging field of spintronics - a fusion of spin physics and electronics - which aims to develop novel memory and sensor technologies, and unconventional computing architectures.

2.1 Magnetism

The Standard Model of particle physics is the prevailing theoretical framework describing all currently known fundamental particles and their interactions, with the exception of gravity. It is, from a theoretical standpoint, a quantum field theory that unifies the electromagnetic, weak, and strong nuclear interactions [3–6]. In this model, particles are broadly classified into Fermions - matter constituents with intrinsic half-integer spin - and Bosons, the force carriers, which possess integer spin. The interactions among particles are governed by four fundamental forces: the strong nuclear force, the weak nuclear force, the electromagnetic force, and gravity. The strong force, the most powerful of the four, is mediated by gluons and is responsible for binding quarks together within protons and neutrons, as well as holding atomic nuclei intact. The weak force, mediated by the W and Z Bosons, governs subatomic processes such as beta decay and plays a central role in nuclear fusion and fission. Gravity, although negligible at subatomic scales, dominates at astronomical scales and governs the attraction between massive bodies such as stars, planets, and black holes. Notably, gravity is not currently encompassed within the Standard Model but is instead described by Einstein's general theory of relativity, which interprets gravitational interaction as the curvature of spacetime induced by mass [7]. The fourth fundamental interaction, and the second strongest, is the electromagnetic force. It is responsible for electric and magnetic phenomena and is mediated by the photon. This force plays a central role in the behavior of charged particles and electromagnetic radiation. Since the focus of this thesis lies in the study of magnetism and particle interactions within solid-state systems, the electromagnetic force is of primary relevance. The classical field theory of electromagnetism was formulated by James Clerk Maxwell and published in 1865 in his seminal work "A Dynamical Theory of the Electromagnetic Field" [8]. Maxwell's original equations were later reformulated into the concise and widely known set of four vector equations by Oliver Heaviside, Josiah Willard Gibbs, and Heinrich

Hertz, forming the foundation of classical electrodynamics.

The microscopic Maxwell equations:

Gaussian law of electricity:

$$\nabla \cdot \mathbf{E} = \frac{\rho_e}{\epsilon_0} \tag{2.1}$$

where $\mathbf{E}$ is the electric field and ρ_e is the charge density. Electric field lines diverge if charge is present. Electric charge is source of the electric field.

Gaussian law of magnetism:

$$\nabla \cdot \mathbf{B} = 0 \tag{2.2}$$

where $\mathbf{B}$ is the magnetic field. Magnetic field lines do not diverge; field of magnetic flux is source free; magnetic mono poles do not exist.

Faraday's law of induction:

$$\nabla \times \mathbf{E} = -\frac{\partial \mathbf{B}}{\partial t} \tag{2.3}$$

where $\mathbf{E}$ is the electric field, and $\mathbf{B}$ is the magnetic field. Temporal change in magnetic flux induces an electric cortex field.

Ampere's law (with Maxwell's correction):

$$\nabla \times \mathbf{B} = \mu_0 \mathbf{J} + \mu_0 \epsilon_0 \frac{\partial \mathbf{E}}{\partial t} \tag{2.4}$$

where $\mathbf{J}$ is the current density, μ_0 is the permeability of free space, and ϵ_0 is the permittivity of free space. Electric currents lead to magnetic vortex fields.

These simple-looking equations imply that there are just two origins for magnetism: the motion of electrically charged particles creating a magnetic (vector) field and the intrinsic magnetism of elementary particles based on their spin. A magnetic moment of an electron in an atom is composed of two components. First, the orbital motion of an electron around a nucleus generates a magnetic moment by Ampere's circuital law. Second, the inherent rotation, or spin, of the electron has a spin magnetic moment. The first part is fundamental for the transformation of energy in a process called induction. A time-varying magnetic field forces the motion of electrical charge and can thus be used to transform, e.g. kinetic energy in electrical potentials, which causes electric currents. This process, colloquially known as "electricity production", is fundamental to our society, since electricity is most likely the primary means of energy form used (transformed) day-to-day in the 21st century. The reverse effect, the creation of magnetic fields by time-varying electric currents through a coil, is described by the Biot–Savart law and plays an essential role in the experiments shown later in this thesis. The second part, namely the phenomenon of magnetism in matter, originates from the magnetic moments of elementary particles, particularly electrons. Within atoms, an electron's magnetic moment arises from two primary contributions: its intrinsic spin and its orbital angular momentum. These components combine to form the total angular momentum of the electron. When the magnetic moments of all electrons within a material are summed, the resulting quantity determines the material's net magnetization. Magnetization, in a macroscopic sense, is defined as the magnetic dipole moment per unit volume.

$$\mathbf{M} = \frac{d\mathbf{m}}{dV} \tag{2.5}$$

with M, the magnetization, d**m** the magnetic dipole moment per volume segment dV.

2.1.1 Magnetic moment of an electron

Most elementary particles like, e.g. electrons have intrinsic magnetic moments that are fundamentally linked to their angular momentum based on quantum mechanics [9, 10]. A free electrons magnetic dipole moment $\mathbf{m}_S$ is defined as

$$\mathbf{m}_S = -\frac{g_S \cdot \mu_B \mathbf{S}}{\hbar} \tag{2.6}$$

in which μ_B is the Bohr magneton, **S** is electron spin, and $\hbar$ the Planck constant. The g-factor g_S is a particle-specific constant that characterizes the proportionality between a particle's magnetic moment and its angular momentum. According to Dirac's relativistic quantum theory, the value of g_S for a free electron is exactly 2. However, quantum electrodynamics (QED) predicts a small deviation from this value due to radiative corrections, giving rise to what is known as the anomalous magnetic moment. This deviation has been calculated and experimentally verified with remarkable precision, making it one of the most accurately measured quantities in modern physics [11, 12]. It is important to note that, due to the negative electric charge of the electron, its magnetic moment vector **m** is oriented anti-parallel to its spin **S**. Consequently, the magnetization contributed by electrons is conventionally represented as a negative quantity. When an electron occupies an atomic orbital, it possesses not only an intrinsic magnetic moment from its spin but also an orbital magnetic moment resulting from its orbital angular momentum **L**. Analogous to the spin magnetic moment $\mathbf{m}_S$, the orbital contribution $\mathbf{m}_L$ can be expressed as:

$$\mathbf{m}_L = -\frac{g_L \cdot \mu_B}{\hbar}\mathbf{L} \tag{2.7}$$

With **L** the orbital angular momentum and a differing g-factor g_L of 1. To get the total magnetic moment, the spin magnetic moment and orbital magnetic moment need to be combined by spin-orbit coupling [13, 14].

2.1.2 Magnetization of atoms and matter

The magnetization of a single atom, without the magnetic moment of the nucleus considered, can be calculated by adding the total spins of the electrons and their angular momenta to a total orbital angular momentum. By angular momentum coupling, a total angular momentum can be derived:

$$m_{\mathbf{atomic}} = g_{\mathbf{J}} \cdot \mu_B \cdot \sqrt{j(j+1)} \tag{2.8}$$

where J is the total angular momentum quantum number, g_J is the Landé g-factor, and μ_B is the Bohr magneton.

A complete description based on quantum mechanics for a few atoms is already challenging, since all total magnetic momenta of all particles and their interactions would need to be considered. For macroscopic systems, different models are employed to describe magnetization and interactions on varying length scales, e.g., the

Heisenberg model [15] for below nanometer scale, the Stoner-Wohlfarth model [16] above 100 nanometers for the conduction bands, or the coarse hysteresis model [17] for any length scale. Approximations made in these models are justifiable for their specific purposes, since, e.g., discrete spin orientations vanish on larger scales and can instead be replaced by a continuous classical model like micromagnetics [18, 19].

The energy of such a macroscopic system in this model can be described using thermodynamics by the Gibbs free energy G

$$G = U - TS - V\mathbf{M} \cdot \mathbf{B_{ext}} + pV \tag{2.9}$$

with U being the internal energy of the system, T the temperature, S the entropy, V the volume of the whole system, p the pressure, M the magnetization vector, and B_{ext} the applied external magnetic field. Using the derivative of the Gibbs energy to find a static equilibrium in the system and employing the second law of thermodynamics for closed systems results in minimizing G [20, 21] at equilibrium at a constant temperature. The derivative of the inner energy U in this case is $dU = TdS - pdV + VB_{\mathbf{ext}} \cdot dM$ and putting it into 2.9 leads to

$$\begin{aligned} dG &= dU - TdS - SdT - V\mathbf{M} \cdot d\mathbf{B_{ext}} - V\mathbf{B_{ext}} \cdot d\mathbf{M} + Vdp + pdV \\ &= -SdT + Vdp - V\mathbf{M} \cdot d\mathbf{B_{ext}} \end{aligned} \tag{2.10}$$

Considering an equilibrium state at constant temperature ($dT = 0$) and constant pressure ($dp = 0$) and applied field B_{ext}, we can express the magnetization M of the system as the sum of all magnetic moments m_i divided by the system's volume V at constant pressure and temperature:

$$\mathbf{M} = \frac{1}{V}\sum_i \mathbf{m}_i = -\frac{1}{V}\left(\frac{\partial G}{\partial \mathbf{B}_{ext}}\right)_{p,T} \tag{2.11}$$

Magnetic materials can be classified according to the alignment and interactions of their atomic or total magnetic moments, leading to distinct magnetic ordering phenomena. Common classifications include **ferromagnetic**, **antiferromagnetic**, **ferrimagnetic**, **altermagnetic**, **helimagnetic**, and **non-collinear** systems, among others. In **paramagnetic** materials, the magnetic moments (spins) are disordered in the absence of an external field. Upon application of a magnetic field, these moments tend to align with the field, enhancing the net magnetization. However, this alignment is weak and thermally unstable - thermal agitation at elevated temperatures increases spin disorder, thereby reducing the magnetization. All materials also exhibit **diamagnetism** to some degree, wherein an applied magnetic field induces an opposing magnetic moment due to changes in the orbital motion of electrons. This effect is typically weak and universal but can dominate in materials lacking other forms of magnetic ordering. In **ferromagnetic** materials, the majority of magnetic moments align parallel due to strong exchange interactions, resulting in a spontaneous net magnetization even in the absence of an external field. In contrast, **antiferromagnets** exhibit equal and oppositely aligned spins on neighboring atoms or sublattices, leading to complete cancellation of the net magnetic moment. **Ferrimagnetic** materials feature anti-parallel spin alignment as well, but the magnitudes of the opposing moments are unequal, yielding a residual net magnetization. **Altermagnets** represent a novel class of magnetic materials characterized by a symmetry-protected spin-sublattice configuration that breaks spin-rotational symmetry but preserves global time-reversal symmetry. This unique structure leads

to spin-polarized electronic bands similar to those found in ferromagnets, despite exhibiting zero net magnetization. In **helimagnets**, the magnetic moments rotate gradually from one atomic plane to the next, forming a helical spin structure along a specific crystallographic direction. This arises from competing interactions, such as symmetric exchange and antisymmetric Dzyaloshinskii–Moriya interaction (DMI). **Non-collinear magnets** also exhibit complex spin arrangements, but with magnetic moments oriented at arbitrary angles rather than strictly parallel or antiparallel configurations.

The interactions underlying these diverse magnetic orders significantly influence the magnetization behavior of materials and will be discussed in greater detail in the following sections.

2.1.3 Energy terms of magnetism

Exchange energy

The exchange energy arises from a quantum mechanical effect rooted in the indistinguishability of electrons and is a direct consequence of the Pauli exclusion principle. This principle asserts that no two identical Fermions (particles with half-integer spin, such as electrons) can occupy the same quantum state simultaneously. For electrons in atoms, each must differ in at least one of the four quantum numbers: the principal quantum number n, the azimuthal (orbital angular momentum) quantum number l, the magnetic quantum number m_l, and the spin quantum number m_d [9, 13]. In a two-electron system, the total wave function must be antisymmetric under particle exchange to satisfy Fermi–Dirac statistics. This total wave function is composed of the product of a spatial (orbital) wave function and a spin wave function. To maintain antisymmetry, if the spatial wave function is symmetric, the spin wave function must be antisymmetric, and vice versa. The spin wave function can adopt either a singlet state, in which the total spin is zero (antisymmetric spin configuration), or a triplet state, in which the total spin is one (symmetric spin configuration). The exchange interaction energetically favors one of these spin states depending on the spatial overlap of the electron wave functions. This leads to either ferromagnetic or antiferromagnetic coupling, depending on whether parallel or antiparallel spin alignment minimizes the system's total energy. In position space, considering two electrons with individual spatial wave functions Φ_A and Φ_B, the total wave functions for the two configurations can be written as [9, 13]:

$$\Psi_{S\wedge A} = \frac{1}{\sqrt{2}} \left(\Phi_A(\mathbf{r}_1)\Phi_B(\mathbf{r}_2) \pm \Phi_A(\mathbf{r}_2)\Phi_B(\mathbf{r}_1)\right) \tag{2.12}$$

With the antisymmetric wave function Ψ_A for the triplet state and symmetric wave function Ψ_S for the singlet state, the electrons A and B wave functions θ_i and the according spatial position $\mathbf{r}_i$. Considering a Coulomb potential $U(\mathbf{r}_1, \mathbf{r}_2)$ between the electrons leads to the energies E_A and E_S for the antisymmetric state and symmetric state, respectively. The difference J_{ex} in energy between both states is then given by

$$J_{ex} = \frac{E_S - E_A}{2} = \int d\mathbf{r}_1 d\mathbf{r}_2 \Phi_A^*(\mathbf{r}_1)\Phi_B^*(\mathbf{r}_2)U(\mathbf{r}_1, \mathbf{r}_2)\Phi_B(\mathbf{r}_1)\Phi_A(\mathbf{r}_1) \tag{2.13}$$

The value J_{ex} is called the exchange constant, and its value determines which state is energetically more favorable. For $J_{ex} > 0$, the antisymmetric spatial wave

FIGURE 2.1: Schematically aligned spins from a) ferromagnetic and b) an antiferromagnetic structure. Taken from [22].

function is energetically favorable, which results in a symmetric spin wave function, while for $J_{ex} < 0$, a symmetric spatial and antisymmetric spin wave function is favored. Thus, the value of the exchange constant describes either an antiferromagnetic system with anti-parallel spins with negative J_{ex} or a ferromagnetic state with parallel spins and positive J_{ex}.

The Hamiltonian for two electrons in the discrete spin model can be expressed using the exchange constant and the electrons spin wave functions.

$$\mathbf{H_{orbitals}} = -2J_{ex}\mathbf{S}_1\mathbf{S}_2 \tag{2.14}$$

Up till now we considered only a two-electron system. To expand the system into a state of e.g. solid matter, we consider the Heisenberg exchange energy, which is the generalized Hamiltonian for homogeneous nearest neighbor interactions with J_{ex} of adjacent spin pairs.

$$E_{\mathbf{exchange}} = J_{\mathbf{ex}} \sum_{i,j} \mathbf{S}_i\mathbf{S}_j \tag{2.15}$$

With the exchange constant J_{ex} and the sum over spin wave functions S of neighboring spins i and j. Exchange interaction based on the quantum mechanical indistinguishability of electrons is the main cause of the existence of macroscopic ferro-, ferri, and antiferromagnetic materials.

In the continuum micromagnetic model the energy is the integral over magnetization gradient, using Taylor expansion for small angle $\Phi_{i,j}$ between two adjacent spins [23, 24].

$$E_{\mathbf{exchange}} = \frac{J_{ex}c_s}{aM_S^2} \int dV \left(\left(\frac{\partial \mathbf{M}}{\partial x}\right)^2 + \left(\frac{\partial \mathbf{M}}{\partial y}\right)^2 + \left(\frac{\partial \mathbf{M}}{\partial z}\right)^2 \right) \tag{2.16}$$

with exchange constant J_e, the lattice constant a, lattice-dependent factor c_s, the saturation magnetization M_S and $\mathbf{M}$ the magnetization.

Zeeman energy

A sufficiently strong external field applied to a system causes the magnetic moments of said system to align with the applied field. The resulting potential energy of the magnetized system is called the Zeeman energy and can be expressed as the integral over the system's volume.

$$E_{\mathbf{Zeeman}} = -\int dV \mu_0 \mathbf{H}_{\mathbf{exchange}}\mathbf{M} \tag{2.17}$$

With the system's volume V, the vacuum permeability μ_0, the external field $\mathbf{H}_{\mathbf{external}}$, and the (macroscopic) magnetization. For a discrete spin model, the energy between

a single magnetic moment $\mathbf{m}$ and the external field $\mathbf{H}_{\mathbf{external}}$ is

$$E_{\mathbf{Zeeman}} = -\mu_0 \mathbf{H}_{\mathbf{exchange}} \mathbf{m} \tag{2.18}$$

Stray field energy

While the Zeeman energy describes the influence of an external field on the magnetic body, the magnetic moments of the system itself also create a field. The stray field energy describes this field analogously to the Zeeman energy [24, 25]:

$$E_{\mathbf{strayfield}} = -\frac{1}{2}\mu_0 \int dV \mathbf{H}_{\mathbf{strayfield}} \cdot \mathbf{M} \tag{2.19}$$

Without any external electromagnetic fields or induction by electric currents, the body's magnetic field, consisting of the stray field $\mathbf{H}_{\mathbf{stray}}$ and magnetization M and displayed as $\mathbf{B} = \mu_0\ \mathbf{H}_{\mathbf{stray}}$+$\mathbf{M}$), needs to be conserved as stated by Gauss's law for magnetism (Eq.2.2) and Ampère's circuital law (Eq. 2.4). From the latter, we can use the general solution of a scalar potential U(r): $\mathbf{H} = -\nabla U$. The flux density with $\mathbf{H}_{\mathbf{stray}}$ and the magnetization $\mathbf{M}$ can thus be written as

$$0 = \frac{1}{\mu_0} \nabla \cdot \mathbf{B} = \nabla(\mathbf{H}_{\mathbf{strayfield}} + \mathbf{M}) \tag{2.20}$$

Using the general solution of the Poisson equation we can derive the stray field to be

$$\Phi(\mathbf{r}) = \frac{1}{4\pi} \left(\int_{\partial\Omega} d^2\mathbf{r}' \frac{\sigma(\mathbf{r}')}{|\mathbf{r} - \mathbf{r}'|} + \int_{\Omega} d^3\mathbf{r}' \frac{\rho(\mathbf{r}')}{|\mathbf{r} - \mathbf{r}'|} \right) \tag{2.21}$$

$$\mathcal{H}_{\mathbf{strayfield}}(\mathbf{r}) = -\frac{1}{4\pi} \nabla \left(\int_{\partial\Omega} d^2\mathbf{r}' \frac{\mathbf{M}(\mathbf{r}')n(\mathbf{r}')}{|\mathbf{r} - \mathbf{r}'|} + \int_{\Omega} d^3\mathbf{r}' \frac{-\nabla'\mathbf{M}(\mathbf{r}')}{|\mathbf{r} - \mathbf{r}'|} \right) \tag{2.22}$$

With the integrals over the magnetic system with the volume charges $\rho(\mathbf{r}) = -\nabla\mathbf{M}(\mathbf{r})$ and the system's surface expressed by $\sigma(\mathbf{r})$=$\mathbf{M}(\mathbf{r})\mathbf{n}(\mathbf{r})$ with the surface normal vector $\mathbf{n}(\mathbf{r})$. To minimize the stray field, the magnetic charges need to be minimal in the system's body and surface. This results in the magnetization favoring flux-closure states, so all magnetic field lines need to be closed in the system.

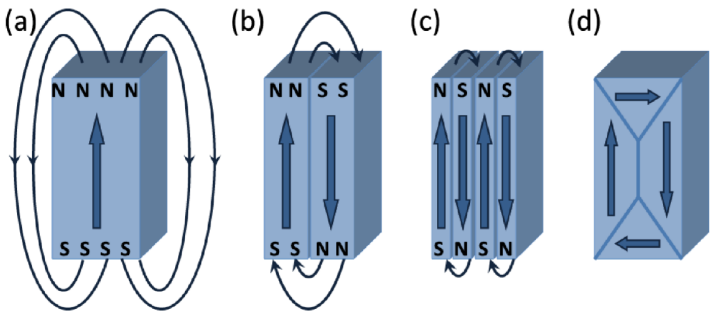

FIGURE 2.2: The stray field energy progressively decreases from a) a monodomain out-of-plane (OOP) configuration to b) and d) domain structures with opposing polarity, ultimately reaching a minimum in d) where a flux-closure configuration is formed. Taken from [22].

Magnetic anisotropy energy

Anisotropy refers to the directional dependence of certain properties of (solid) matter, particularly within crystalline materials. Magnetic anisotropy describes the variation of free magnetic energy as a function of the magnetization direction and is the combination of several effects, if applicable to the system. Magneto-crystalline anisotropy, the structural order of the crystal on the atomic level, causes energetically preferential directions for the magnetization. This phenomenon is intrinsically tied to the symmetry properties of the material. The interactions of the atomic lattice and its orbital moments via spin-orbit coupling can influence the lattice structure by changing the spin-wave functions and overlapping orbitals. This change in electron density also explains the influence of strain and tension on the system's magnetization, called magnetoelastic anisotropy. In an effect called exchange bias or exchange anisotropy, an antiferromagnetic body or layer can interact with a ferromagnetic material, e.g., a hard magnetization antiferromagnetic layer can cause a shift in the (soft) magnetization of the ferromagnetic layer. The directions that correspond to the lowest energy configurations for magnetization are referred to as easy axes. In this thesis, magnetic thin films are used, which show a particular uniaxial anisotropy: perpendicular magnetic anisotropy (PMA).

Uniaxial anisotropy The energy of PMA in thin films refers to the tendency of the magnetization vector in the ferromagnetic layer to align along the surface normal of the film, i.e., perpendicular to the plane of the layer. The associated anisotropy energy for a single spin **S** is typically expressed as being proportional to $\cos^2(\alpha)$, where α denotes the angle between the spin direction and the uniaxial easy axis - here defined by the film's surface normal, and thus out-of-plane (OOP). With the uniaxial easy-axis in z-direction, the anisotropy energy is [24, 25]

$$E_{\text{uniaxial, z}} = -\int dV \left(K_{c_1} \frac{M_z^2}{M_S^2} + K_{u_2} \frac{M_z^4}{M_S^4} + \text{HOTs} \right) \tag{2.23}$$

with the saturation magnetization M, the magnetization along the easy axis M_z, K, a composition and temperature dependent parameter, and HOTs, **h**igher **o**rder **t**erms. The influence of temperature on magnetic anisotropy is particularly critical. Moderate increases on the order of several tens of kelvin can significantly impact the anisotropy energy, as described by Zener's classical theory [26]. At elevated temperatures beyond this moderate regime, annealing effects may occur, which can irreversibly modify the structural composition of thin-film stacks. Such thermal treatment enhances atomic diffusion across interfaces, leading to permanent intermixing and alteration of the magnetic and structural properties of the multilayer system.

Dzyaloshinskii-Moriya Interaction

The antisymmetric exchange interaction, also known as the Dzyaloshinskii-Moriya interaction (DMI) [27, 28], is a spin-spin interaction that arises in systems with broken spatial inversion symmetry and high spin-orbit-coupling (SOC). This contribution to the total magnetic exchange interaction between neighboring spins becomes significant in bulk materials with non-inversion-symmetric unit cells, as well as at interfaces between different materials. The latter is particularly relevant to this thesis, as all used samples consist of thin film metal stacks. In the discrete model. the Hamiltonian term representing the DMI must remain invariant under symmetry operations such as inversion or spatial rotation:

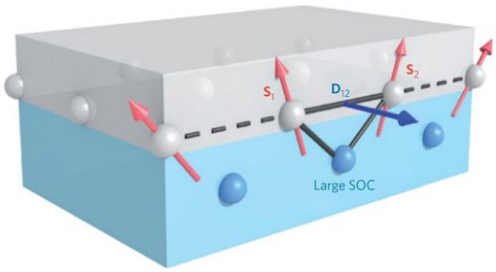

FIGURE 2.3: Schematic representation of interfacial Dzyaloshinskii–Moriya interaction (DMI) at the interface between a ferromagnetic layer (gray) and an adjacent heavy metal layer (blue). The Dzyaloshinskii–Moriya (DM) vector D_{12} is oriented perpendicular to the plane defined by two neighboring spins and an adjacent heavy atom with strong spin–orbit coupling at the interface. Image adapted from [29]

$$H_{\mathbf{DMI}} = \sum_{i,j} \mathbf{D}_{i,j} \left(\mathbf{S}_i \times \mathbf{S}_j \right) \tag{2.24}$$

With $\mathbf{D}_{i,j}$ is the tensor element with the interaction constant between $\mathbf{S}_i$ and $\mathbf{S}_j$, the spins of two neighboring electrons.

In symmetric systems the DMI must vanish, illustrating that the DMI only occurs when inversion symmetry in the system is broken. For bulk systems, the symmetry in each unit cell needs to be broken for DMI to take place, while in thin films DMI exists primarily at the material's interfaces. Important to note is that the materials at the interface need to be of different atoms. In Figure 2.3, the DMI vector lies in the x-y plane due to rotational symmetry. The energy associated with the DMI is minimized when the two spins are oriented in a plane normal to the DMI vector and perpendicular to each other. In contrast, the normal exchange interaction favors parallel or antiparallel spin configurations.

The DMI induces spin canting, which promotes stable spin spirals, and, with additional applied external field causes non-collinear spin textures, such as conical spirals and Bloch skyrmions in bulk materials, as well as spin spirals, chiral magnetic domain walls, and Néel skyrmions in multilayer stacks. Skyrmions are introduced in a later chapter. The strength of the DMI is proportional to the spin-orbit coupling, which scales with the atomic number Z^4. Consequently, the presence of heavy metals with an interface to a ferromagnet in the multilayer stack leads to a significant DMI, enhancing the formation of chiral magnetic spin structures (see Figure 2.4), which are the focus of this thesis. Considering for simplification only DMI and exchange interaction, both lead to a minimization of the total energy for a helical magnetization with periodicity of $l = 4\pi\frac{A}{D}$. Using rotational symmetry conditions, the following equations about the tensor elements of the DMI tensor can be derived [30]:
$D_{xz} = D_{zx} = D_{yz} = D_{zy} = 0$, $D_{xx} = D_{yy}$, $-D_{xy} = D_{yx}$ and for a Néel domain wall $D_{yy} = D_{zz} = 0$ leading to the interfacial Néel DMI tensor:

$$D_{Néel} = \begin{pmatrix} 0 & D & 0 \\ -D & 0 & 0 \\ 0 & 0 & 0 \end{pmatrix} \tag{2.25}$$

For the magnetic thin films examined in this thesis, the z-contributions of the DMI tensor are thus zero. In the continuum micromagnetic model the energy term is as

follows [24]

$$E_{DMI} = \frac{D}{M_S^2} \int dV \left(M_z(\mathbf{r}) \nabla \mathbf{M}(\mathbf{r}) - \mathbf{M}(\mathbf{r}) \nabla \mathbf{M_z}(\mathbf{r}) \right) \tag{2.26}$$

with D the DMI constant, M_S the saturation magnetization and $\mathbf{M}$, the magnetization dependent on $\mathbf{r}$. An overview of the tensor entries and its according symmetries are represented in the following image (Figure 2.4):

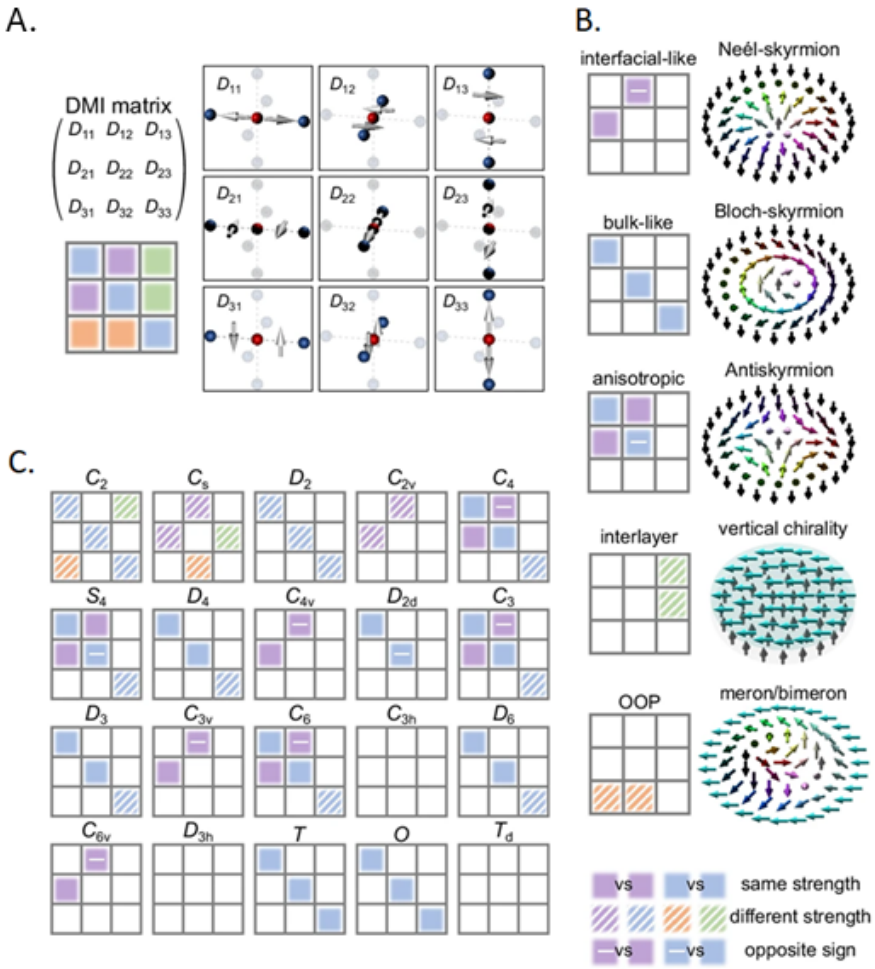

FIGURE 2.4: A.) Matrix and schematic illustration of the DMI, displaying representative DMI vector configurations for all relevant symmetry elements (D_{nm} with n,m $\in [1,3]$). Especially important are the interfacial elements D_{12} and D_{21}, causing the Néel-like skyrmions (see Section 2.4) as seen in B. left upper corner. B.) Classification of major DMI types, visualized through color-coded DMI vectors and their corresponding energetically preferred spin textures. Solid-colored regions indicate uniform DMI strength and orientation, while striped areas represent spatial variations in DMI magnitude or direction. Regions marked with a negative sign denote a reversal in the DMI vector relative to those of identical color. C.) Schematic representations of DMI vector patterns associated with all non-centrosymmetric crystallographic point groups (excluding C_1). Image adapted from [30]

2.2 Magnetic spin structures

Before exploring complex spin textures such as skyrmions, it is essential to first understand the fundamental magnetic configurations - particularly domain walls - and their underlying dynamics. A diverse range of nontrivial spin structures, including antiskyrmions, magnetic bobbers, and Bloch points to name a few, has been identified and continues to be an active area of research. The metallic thin films studied in this thesis support skyrmionic spin textures, with their formation resulting directly from the interplay and total energy minimization of the magnetic interactions previously discussed, within the framework of Gibbs free energy.
The emergence and stabilization of specific complex spin structures are determined by energy minimization, which is the result of the interplay of the relative magnitudes and competing contributions of the individual energy components introduced in prior sections, thereby favoring certain spin textures within the material system.

Anisotropy: Spins align along the easy anisotropy axes. Used thin film samples in this thesis show perpendicular magnetic anisotropy, meaning spins point OOP either parallel or antiparallel to the surface normal.

DMI: Maximum spin canting to adjacent spins, causing spin canting primarily at the interfaces and leading to chiral domain walls.

Exchange interaction: An exchange constant of $A > 0$ is called ferromagnetic exchange and causes all spins to align parallel with each other. Main driver for ferromagnetism.

Stray field: Flux closure at the surface. Magnetic volume and surface charges get minimized. In thin films, spins align with the longest axis of the sample, basically in the x-y plane due to macroscopic size in comparison to film thickness (millimeters vs. nanometers).

Zeeman: Spins align with the applied external field.

2.2.1 Magnetic domain walls

One of the simplest forms of spin structures is the domain wall, which serves as an interfacial transition between two regions with differing magnetization orientations - typically 90° or 180° rotations of magnetization in ferromagnetic materials [25, 31, 32]. Due to the exchange interaction, an abrupt change in spin direction is energetically unfavorable. Consequently, the transition occurs gradually, with spins progressively tilting toward the opposite direction across atomic orbitals. This gradual reorientation is balanced by the magnetocrystalline anisotropy energy, which acts in opposition to the exchange energy [33]. Both energy components seek to minimize their values. The anisotropy energy is minimized when the individual magnetic moments align with the crystal lattice axes, thereby reducing the domain wall width. Conversely, the exchange energy favors parallel alignment of magnetic moments, which results in an increased domain wall width due to the repulsive interaction between anti-parallel spins.
The delicate interplay between magnetocrystalline anisotropy and exchange energy fundamentally determines the domain wall width [25, 34], which typically extends

over 100 to 150 atomic spacings in ferromagnetic materials. In real crystals, structural imperfections - such as vacancies, foreign atoms (from intentional doping or unintentional inclusions), oxides, mechanical strain, and interfaces - modify the local anisotropy and can significantly affect the formation and dynamics of domain walls [35–37]. These defects often require the application of stronger external fields or alternative techniques to initiate or control domain wall motion [38].
Moreover, domain walls can be actively manipulated by external stimuli, including magnetic fields and temperature (gradients) [39–42]. They can also be nucleated [43, 44] and driven [45] by spin currents generated through electric currents or by voltage gating [46], enabling a range of functionalities in spintronic applications [29, 47–61].

Domain walls can be classified into several types based on the spin-tilting mechanism. Here the Bloch-type and Néel-type domain wall is introduced [25]. In a Bloch-type domain wall, the spins rotate within a plane parallel to the domain wall, whereas in a Néel-type domain wall, the spins tilt within a plane perpendicular to the domain wall's direction. Considering the simplification of only anisotropy and exchange energy contributing to domain walls, the profile κ, the width $\nabla_{\mathbf{type}}$, and the domain wall energy $\epsilon_{\mathbf{type}}$ can be displayed as:

$$\begin{aligned}
&\kappa_{\mathbf{Bloch}}(x) = 2\arctan\left(-e^{\left(\frac{\pi x}{\nabla_{\mathbf{Bloch}}}\right)}\right) \qquad \kappa_{\mathbf{Néel}}(x) = 2\arctan\left(e^{\left(-\frac{\pi x}{\nabla_{\mathbf{Néel}}}\right)}\right) - \frac{\pi}{2} \\
&\textbf{with} \qquad\qquad\qquad\qquad \textbf{with} \\
&\nabla_{\mathbf{Bloch}} = \pi\sqrt{\frac{A}{K_u}} \qquad\qquad\qquad \nabla_{\mathbf{Néel}} = \pi\sqrt{\frac{A}{K_N}} \\
&\epsilon_{\mathbf{Bloch}} = 4\sqrt{AK_u} \qquad\qquad\qquad \epsilon_{\mathbf{Néel}} = 4\sqrt{AK_u} \pm \pi D
\end{aligned} \tag{2.27}$$

With x the spatial position, A the exchange constant, and K_u the uniaxial anisotropy. For Néel walls (terms on the right), one must additionally consider the DMI constant D and the shape anisotropy caused by dipolar interaction in the film [33]. The latter depends on the direction of the hard axis saturation field H_K, ultimately, depending on the film thickness and its value ranging between $K_N = \frac{1}{2}\mu_0 H_k M_S$ and $K_N = \frac{1}{2}\mu_0 M_S^2$ [24, 32].

Bloch-type domain walls show low stray fields at out-of-plane anisotropy and are therefore more commonly observed in bulk materials, whilst in thin film (multilayer) stacks, the interfacial DMI favors Néel-type domain walls [33]. In thin films this effect is increased since thinner layers cause smaller stray fields. The energy of a Néel wall also depends on the polarity of the DMI constant, displayed as the $\pm$ sign in the formula, thus breaking the system's symmetry. This also determines the chirality of the wall: A negative DMI contribution to the energy will result in a right-handed rotation, a positive contribution towards left-handed. This chiral rotation of spins can lead to the spin structure called a skyrmion, which will be explored further in a later section.

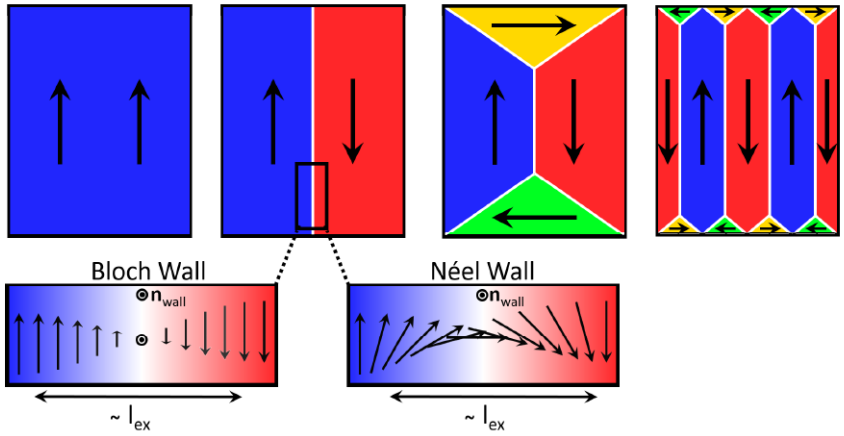

FIGURE 2.5: The formation of magnetic domains is driven by the interplay between exchange interaction, anisotropy, and stray fields, which collectively minimize the system's total energy according to an optimal ratio. To reduce stray fields, flux closure patterns are formed. The strength of the anisotropy influences the size of the edge domains, with higher anisotropy leading to smaller domain boundaries (as illustrated in the top right). The boundaries between adjacent domains are referred to as domain walls, which can adopt two primary spin configurations: Néel and Bloch, depending on the geometry of the system. Image adapted from [62].

2.2.2 Landau Lifshitz Gilbert equation (LLG)

So far, the magnetization and spin structures like domain walls have been investigated in a static fashion. To analyze the dynamic in a system, one needs to calculate the time derivation of the magnetization $\frac{d}{dt}\mathbf{M}(\mathbf{r},t)$. The needed differential equations were derived by L. Landau and E. Lifshitz in 1935 and further modified by T. L. Gilbert in 1955 [18, 63]. Starting with the effective field with all components previously introduced.

$$H_{\mathbf{all}} = H_{\mathbf{ani}} + H_{\mathbf{DMI}} + H_{\mathbf{exch}} + H_{\mathbf{stray}} + H_{\mathbf{Zeeman}} \tag{2.28}$$

$$\mathbf{H_{eff}} = -\frac{\partial H_{\mathbf{all}}}{\partial \mathbf{M}} \tag{2.29}$$

and the exerted torque in the perpendicular direction of $\mathcal{H}_{\mathbf{eff}}$, experienced by the magnetic moments. The magnetic moments start rotating, consequently changing $\mathcal{H}_{\mathbf{eff}}$ until the torque vanishes and the rotation stops. The torque is proportional to the rate of change of angular momentum, which leads to a change of direction of the spin, ultimately leading to the precession. This effect is described by the Landau–Lifshitz equation:

$$\frac{d\mathbf{M}}{dt} = -\gamma \mathbf{M} \times \mathbf{H_{eff}} - \lambda \mathbf{M} \times (\mathbf{M} \times \mathbf{H_{eff}}) \tag{2.30}$$

with γ the gyromagnetic ratio and $\lambda = \alpha \frac{\gamma}{M_S}$ a phenomenological damping parameter with α the damping coefficient. Gilbert improved the equation by introducing the time dependence of the magnetization:

$$\frac{1}{\gamma}\frac{d\mathbf{m}}{dt} = \mathbf{m} \times \mathcal{H}_{\mathbf{eff}} - \frac{\lambda}{\gamma m}\mathbf{m} \times \frac{d\mathbf{m}}{dt} \tag{2.31}$$

Where $\mathbf{m}$ is the magnetic moment, γ is the gyromagnetic ratio, λ' is the damping

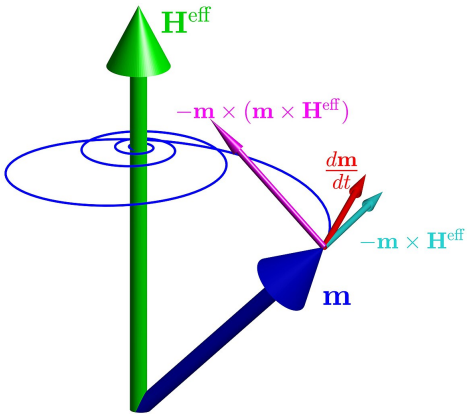

FIGURE 2.6: The precessional motion of a magnetic moment **M** (blue) in the presence of an applied external field $\mathbf{H}_{eff}$ (green) is described by the LLG equation. The terms of the LLG equation include time derivative of magnetic moment **m** (red), precession (cyan) and damping (pink). Due to the damping term, the magnetic moment **m** undergoes a gradual alignment during its rotational motion, ultimately aligning with the effective field $\mathbf{H}_{eff}$ (blue trajectory). Image taken from [64].

coefficient, and $\mathcal{H}_{eff}$ is the effective magnetic field. The first term describes the precession of the spin due to the effective field, while the second term is the damping term, related to the dissipation of energy caused by interaction with the environment. The latter causes the magnetization vector to align with the magnetic field, which leads to precession, circling closer towards the effective field vector (see Figure 2.6).

Influence of finite temperature

So far, we have explored the static and the dynamic case in a continuous model at 0 K, ignoring the influence of temperature. Temperature, as in all physical systems, plays a crucial role in determining the magnetic properties of materials. As heat energy in a closed system increases, thermal agitation affects the electrons in the atomic orbitals, potentially overcoming the exchange interactions. This has a randomizing effect on their alignment to neighboring magnetic moments, leading to significant changes in a material's magnetization order. If the temperature of a ferromagnetic material rises above a critical, material-specific point called the Curie temperature, its magnetic order is destroyed, and the material shows no longer ferromagnetic but paramagnetic behavior [25]. As an example, the Curie temperatures for the three ferromagnetic elements are IronT_C (Fe) = 1041 K, Cobalt T_C (Co) = 1423 K, and Nickel T_C (Ni) = 633 K. Heating a permanent magnet above its corresponding Curie temperature effectively destroys its magnetic order, and it loses permanent magnetization. Above T_C, the material no longer exhibits spontaneous magnetization, and its magnetic susceptibility follows the Curie-Weiss law [65]:

$$\chi(T) = \frac{C}{T - T_C} \tag{2.32}$$

The stochastic Landau-Lifshitz-Gilbert (sLLG) equation extends the conventional LLG equation by incorporating thermal fluctuations as a stochastic magnetic field $\mathbf{H}_{\text{therm}}$ for temperatures below the Curie Temperature. It models the time evolution of a magnetic moment MM under the influence of both an effective magnetic field and random thermal noise. This is crucial for accurately simulating magnetization

dynamics at finite temperatures, where thermal agitation affects stability, switching behavior, and noise in magnetic systems. The stochastic term is typically modeled as a Gaussian white noise field, consistent with the fluctuation-dissipation theorem [39, 66], ensuring that the system reaches thermal equilibrium.

$$\frac{d\mathbf{M}}{dt} = -\gamma \mathbf{M} \times (\mathbf{H_{eff}} + \mathbf{H_{therm}}) + \frac{\alpha}{M_S} \mathbf{M} \times \frac{d\mathbf{M}}{dt} \tag{2.33}$$

Finite temperature: saturation magnetization At absolute zero temperature, the magnetization M(0) represents the maximum saturation magnetization of the system. At such low temperatures, spin structures - such as domain walls - exhibit minimal mobility due to the absence of thermal energy, effectively *freezing* the magnetic configuration. As the temperature T increases, thermal fluctuations enhance spin excitations, promoting domain wall motion and enabling phenomena such as thermally driven diffusion. Upon approaching the Curie temperature T_C, thermal agitation becomes sufficient to overcome magnetic ordering, leading to a phase transition into the paramagnetic state where long-range magnetic order vanishes. The saturation magnetization M_S(T) decreases with rising temperature (2.34) [10], and this reduction accelerates at higher temperatures due to increased spin excitation 2.35.

$$M_S(T) = \mathbf{M}(0) \left(1 - \left(\frac{T}{T_C}\right)^{\frac{3}{2}}\right) \tag{2.34}$$

The temperature dependence of M_S(T) near zero temperature often follows a power-law behavior, consistent with Bloch's law

$$M_S(T) \propto (T - T_C)^{\beta} \tag{2.35}$$

with unit-less β ≈0,4, which depends on the materials composition at temperature T, according to [65] Due to the Curie-Bloch-relation, equations 2.34 and 2.35 can be combined to

$$M_S(T) = M_S(0) \left(1 - \left(\frac{T}{T_C}\right) \alpha\right)^{\beta} \tag{2.36}$$

with α and β, empirically determinable by measuring M_S(T).

Finite temperature: anisotropy The anisotropy in the here investigated materials tends to depend quite strongly on the temperature - If temperature affects the system only like local random fluctuations in the magnetization vectors, a characteristic exponent n can be derived, which depends on the crystal structure at temperature T [26].

$$\frac{K(T)}{K(0)} = \left(\frac{M_S(T)}{M_S(0)}\right)^n \tag{2.37}$$

Finite temperature: DMI Since DMI relevant to this work is of interfacial origin, elevated temperatures that enable atomic diffusion across the interface can result in intermixing of the constituent layers. Such interfacial interdiffusion leads to irreversible modifications of the interfacial symmetry and chemical composition,

thereby significantly altering the DMI. Even in the absence of intermixing, the temperature dependence of DMI remains complex and is not yet fully understood. Only a limited number of theoretical models address this behavior. Some studies suggest that the atomistic DMI constant, along with the atomistic exchange interaction, exhibits minimal variation with temperature. However, the effective DMI used in spin wave-based descriptions is often found to scale linearly with the exchange stiffness parameter [67]. In this context, the temperature dependence of the exchange constant can be described by the relation:

$$\frac{A(T)}{A(0)} = \left(\frac{M_S(T)}{M_S(0)}\right)^{\ni} \tag{2.38}$$

with $\ni$<2 and M_S(T) according to 2.36 [34].

Finite temperature: noise The Stochastic Landau-Lifshitz-Bloch (LLB)) equation is a modification of the traditional LLG equation that incorporates random thermal fluctuations, representing the influence of temperature on the magnetic system. This equation is used to model the dynamics of magnetic moments in the presence of both deterministic and stochastic forces. The deterministic part describes precession and damping of the magnetic moment in an external field, while the stochastic term accounts for random thermal noise that leads to deviations from the deterministic motion. [68]

$$\begin{aligned}\frac{1}{\gamma^-}\frac{d\mathbf{m}}{dt} &= -\mathbf{m}\times\mathbf{H}_{eff} \\ &- \frac{\alpha_\perp}{m^2}\mathbf{m}\times\left(\mathbf{m}\times\left(\mathbf{H}_{eff}+\mathbf{Y}_\perp\right)\right) \\ &+ \frac{\alpha_\parallel}{m^2}\mathbf{m}\cdot\left(\mathbf{m}\cdot\mathbf{H}_{eff}\right)+\mathbf{Y}_\parallel\end{aligned} \tag{2.39}$$

with $\gamma^- = \mu_0\gamma/(1+\lambda^2)$ a reduced gyromagnetic ratio, $\mathbf{m} = \mathbf{M}/M_S(0)$ the reduced magnetization, $M_S(0)$ the saturation magnetization at 0 K, $\alpha_\perp$ and $\alpha_\parallel$ transversal and longitudinal damping parameters [69, 70]. Vector $\mathcal{Y}$ is white noise random numbers as a spatially and temporally stochastic field with zero mean and variance with a diffusion constant Y_n for the parallel and perpendicular case and T the absolute temperature.

$$\mathcal{Y}_\perp = \frac{\left(\alpha_\perp-\alpha_\parallel\right)k_BT}{\mu_0 M_0 V\alpha^2} \qquad \mathcal{Y}_\parallel = \frac{\alpha_\parallel k_BT}{\mu_0 M_0 V} \tag{2.40}$$

Temperature in this thesis also influences the stability of skyrmions, spin textures introduced in a later section. Skyrmions can be thermally activated, leading to Brownian diffusion (see Section 2.4.2), nucleated, or annihilated depending on temperature variations, improving their particle-like behavior. Generally, temperature plays an important role in the magnetic behavior of our ferromagnetic thin films, and temperature stabilization in our open systems is crucial. Temperature in this thesis ranges around ambient (room) temperature, with the lowest temperature measured being 285 K and the highest around 370 K. These are primarily due to experimental limitations, which will further be explored in Chapter 3 methods.

2.2.3 Thiele equation of steady-state motion

The Thiele equation [71] is a reduced, analytical form of the Landau-Lifshitz-Gilbert (LLG) equation that describes the steady-state motion of rigid magnetic textures, such as domain walls or skyrmions, under the influence of external forces. It assumes that the magnetic structure retains its shape during motion and reduces the full magnetization dynamics to a collective coordinate approach, typically describing the center-of-mass motion.The Thiele equation balances three main contributions - the gyroscopic (Magnus) force, arising from the topology of the spin texture, acting in the perpendicular direction of transverse motion. The damping force, which results from energy dissipation due to Gilbert damping, and an external or effective force, such as spin-torques or magnetic field gradients.

$$\mathbf{G} \times \mathbf{v} - \boldsymbol{\mathcal{D}} \cdot \mathbf{v} + \mathbf{F}_{\mathbf{external}} = 0 \tag{2.41}$$

with $\mathbf{G}$ the gyromvector, $\boldsymbol{\mathcal{D}}$ the damping tensor, $\mathbf{v}$ the velocity vector of the magnetic texture, and $\mathbf{F}_{\mathbf{external}}$ is the net external force.

$$\begin{aligned} \mathcal{G}_{i,j} &= \frac{M_S}{\gamma_0} \epsilon_{lmn} \int d^2x n_l (\partial_i n_m)(\partial_j n_n), \\ \mathcal{D}_{i,j} &= -\frac{M_S}{\gamma_0} \int d^2x (\partial_i n_k)(\partial_j n_k), \\ F_{i,j} &= -M_S \int d^2x (\partial_i n_j) H_{eff,j} \end{aligned} \tag{2.42}$$

This Thiele equation of motion is used to model and understand the dynamics of skyrmions, magnetic bubbles, and domain walls, particularly in the presence of spin-transfer or spin-orbit torques, which are introduced in the next section. The influence of skyrmion inertia can be incorporated into the system's description [72–75], although the existence and definition of an effective skyrmion mass remain subjects of ongoing debate [76]. While classical particles exhibit inertial behavior due to well-defined mass, skyrmions - being topologically stabilized spin textures - exhibit inertia as an emergent, dynamic response associated with the deformation of the spin structure during motion.

2.3 Current induced spin torques

Thus far, various strategies for manipulating magnetic spin configurations and the resulting magnetization in materials have been introduced, including the application of external magnetic fields, structural and geometrical engineering (e.g., thin films versus bulk systems), mechanical strain (e.g., modulation of orbital overlap) [77], and temperature variation. Among emerging techniques, the control of magnetic domain walls and skyrmions via electric currents has garnered particular attention due to its lower energy requirements and compatibility with existing electronic architectures, offering promising prospects for spintronic applications [78]. This section focuses on fundamental mechanisms underlying current-induced skyrmion manipulation like **spin-transfer torque** (STT) [79], **spin Hall effect** (SHE) [80–82] and the resulting **spin-orbit torque** (SOT) [83–86].

Section 2.3.1 focuses on the well-established STT mechanism. While STT has found widespread implementation in commercial spintronic technologies such as magnetic random access memory (ST-MRAM) [87], its relatively low efficiency imposes limitations on its suitability for skyrmion manipulation. In contrast, Section

2.3.3 addresses the more recently explored SOT, which offer substantially improved efficiency for skyrmion control. However, the effective utilization of SOT requires more complex multilayer heterostructures, as its underlying physical origin [78] - partly attributed to the SHE - is discussed in detail in Section 2.3.2.

2.3.1 Spin-transfer torque (STT)

The manipulation of magnetic domain walls, including skyrmions, can be effectively facilitated through the application of electric currents, with spin-transfer torque (STT) serving as a crucial mechanism. This phenomenon arises from the interaction between spin-polarized electrons and the local magnetization in ferromagnetic materials. In these systems, electrons whose spins are aligned parallel to the local magnetization experience less scattering compared to those with antiparallel spins, resulting in a spin-polarized current. When these spin-polarized electrons encounter regions of varying magnetization, such as domain walls, they attempt to align their spins with the new magnetization direction. Due to the conservation of angular momentum, this change in the electron spin induces a corresponding change in the local magnetization.

This interaction generates a force on the domain wall in the direction of electron flow, which also influences the motion and dynamics of skyrmions. Consequently, skyrmions can be manipulated via spin-transfer torque[79, 88, 89]. However, the effectiveness of this effect is limited by the quantum nature of electron spin. An individual electron, carrying a spin of $\hbar/2e$, can transfer a maximum angular momentum of $\hbar/e$ during a complete spin flip, which imposes a fundamental limit on the efficiency and scale of spin-transfer torque in skyrmion manipulation.

2.3.2 Spin Hall effect (SHE)

The spin Hall effect (SHE) is a cornerstone phenomenon in spintronics, functionally analogous to the classical Hall effect but governed by spin-dependent mechanisms. Whereas the classical Hall effect generates a transverse voltage as a result of charge carriers being deflected by an external magnetic field, the SHE produces a transverse spin current without the necessity of an applied magnetic field [19, 80–82, 90]. In the SHE, the flow of a charge current through a material leads to a transverse spin current due to spin-dependent deflection of electrons, resulting in spin accumulation with opposite polarization at the lateral edges of the conductor (see Figure 2.7 a)). This effect arises from two principal mechanisms first predicted by Dyaknov and Perel in 1971 [91]: The extrinsic SHE, caused by spin-dependent scattering of electrons off impurities or defects (see Figure 2.7 c, d)), and the intrinsic SHE, arising from the band structure of the material and the intrinsic SOC associated with the host atoms. Materials with strong SOC - particularly heavy metals such as, e.g., platinum, tantalum, and tungsten - exhibit pronounced intrinsic SHE and are widely employed in spintronic applications. The spin Hall angle (θ_{sh}) is essential, representing the efficiency of spin-charge interconversion. It is defined as the ratio of the transverse spin current density to the directed charge current density. Complementary to the SHE is the inverse spin Hall effect (ISHE), which enables spin-to-charge current conversion. In the ISHE, a pure spin current flowing through a material generates a transverse charge current via the same SOC mechanisms (see Figure 2.7 b), enabling electrical detection of spin transport phenomena.

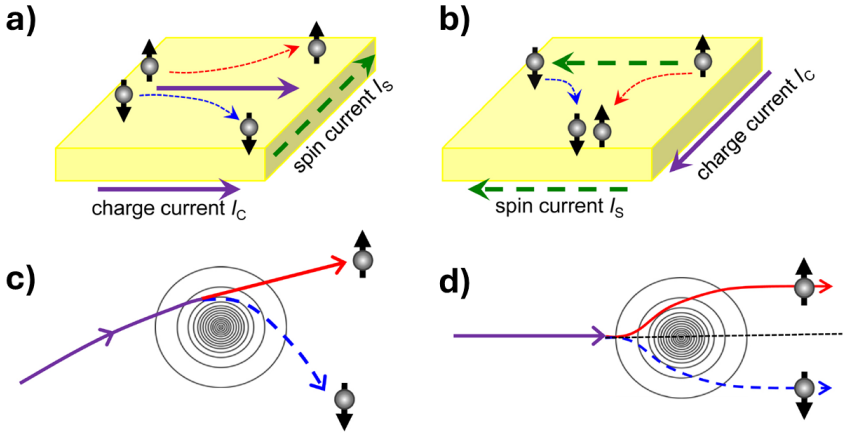

FIGURE 2.7: Schematic representation of the spin Hall effect (SHE) and inverse spin Hall effect (ISHE): a) In the spin Hall effect, a longitudinal charge current induces a transverse spin current through spin-dependent scattering processes, leading to spin accumulation with opposite spin orientations at the lateral edges of the material. b) In the inverse spin Hall effect, an injected spin current is converted into a transverse charge current via spin–orbit coupling, enabling electrical detection of spin transport. c, d) For the extrinsic SHE, two key scattering mechanisms are illustrated: c) skew scattering, where spin-dependent asymmetry in scattering leads to transverse spin flow, and d) side-jump scattering, where electrons experience a lateral displacement upon scattering near a potential atomic center due to spin–orbit interactions. Images adapted from [90].

Rashba-Edelstein effect (REE)

The Rashba–Edelstein effect (REE) occurs in systems exhibiting strong SOC and broken structural inversion symmetry, such as at material interfaces. It describes the generation of a nonequilibrium spin accumulation in response to an applied in-plane electric field, e.g., at interfaces between a ferromagnet and a heavy metal. In such systems, the Rashba spin–orbit interaction gives rise to spin-momentum locking, wherein the electron spin orientation is intrinsically tied to its momentum. When a charge current is applied parallel to the interface, the resulting shift of the Fermi surface leads to an asymmetric occupation of momentum states. Owing to spin–momentum locking, this imbalance produces a net spin accumulation oriented transverse to the current direction. This spin accumulation causes opposite spin orientations at opposite edges of the material and can be interpreted as an interfacial spin current. The REE originates from the coupling between electron spin and the electric field at the interface, causing electrons with momentum to experience an effective magnetic field, leading to spin polarization.

2.3.3 Spin orbit torque (SOT)

Spin-orbit torque (SOT) is caused by the spin accumulation, itself caused by the aforementioned effects like SHE. It can be observed in multilayer systems, in which a ferromagnetic layer is interfaced with a non-magnetic layer that exhibits strong spin-orbit coupling. In these systems, the SHE in the non-magnetic layer generates spin currents when an electric current is applied. These spin currents diffuse across the interface into the adjacent ferromagnetic layer, resulting in spin accumulation and the exertion of torques on the local magnetization. This torque subsequently induces motion of magnetic textures within the ferromagnetic layer.

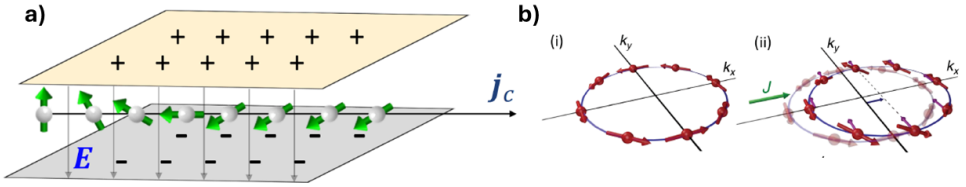

FIGURE 2.8: a) The Rashba spin-orbit torque originates from structural inversion asymmetry, typically caused by an electric field at an interface between two materials. This field induces spin–orbit coupling, resulting in momentum-dependent spin polarization of conduction electrons (with momentum) at the interface. b) Alternatively, the Rashba effect can emerge from a momentum-dependent splitting of the electronic band structure, leading to spin–momentum locking. i) In equilibrium, the electron spins (red) are aligned perpendicular to their momentum, forming a Rashba-split Fermi surface. ii) When an electric current J (green) is applied, the Fermi surface shifts in momentum space. Electrons experience an additional effective spin–orbit field (blue arrow), leading to a current-induced spin polarization. The resulting spin tilt generates a transverse spin accumulation and a net spin current along the y-direction. Adapted from [82].

In addition to SHE, the accumulation of spin-polarized electrons at the interface can also be driven by the spin polarization of REE. While SOT is exclusive to multilayer systems, it offers significantly higher efficiency compared to pure STT, with an enhancement factor of approximately tenfold [85]. This increased efficiency is due to the ability of electrons to diffuse multiple times between layers, repeatedly exerting torque on the magnetic layer, unlike pure STT, where the angular momentum transfer is limited to a single $\hbar$.

Figure 2.9 illustrates the spin-orbit torque mechanism, which can be characterized by two components - an effective field-like component and a damping-like component:

$$\mathbf{B}_{\text{Field-like}} = b(\mathbf{m} \times \sigma) \qquad \mathbf{B}_{\text{Damping-like}} = a\mathbf{m} \times (\mathbf{m} \times \sigma) \tag{2.43}$$

with $\mathbf{m}$ the magnetization, σ the spin polarization, and a and b coefficients. These terms are analogous to the torques in the LLG equation, in which the magnetic fields exhibit similar symmetry. However, this analogy is lacking, as both fields introduce additional precession and damping torques corresponding to the LLG equation, resulting in spin canting. This, in turn, induces a demagnetization field, further introducing precession and damping torques. While a detailed analysis of these effects is highly complex [54] and is not further pursued, it is important to note that most of these torques cancel out.

$$\left[\frac{\partial \mathbf{M}}{\partial t}\right]_{LLG+SOT} = -\gamma \mathbf{M} \times \left(\mathbf{H}_{eff} + a_J \left(\mathbf{M} \times (\mathbf{e}_z \times \mathbf{j})\right) + b_J \left(\mathbf{e}_z \times \mathbf{j}\right)\right) + \frac{\alpha}{M_S} \mathbf{M} \times \frac{\partial \mathbf{M}}{\partial t} \tag{2.44}$$

with $\mathbf{M}$ the magnetization, γ the gyrocoupling, $\mathbf{e}_z \times \mathbf{j}$the interfacial electric current, and SOT parameters a_J and b_J [24].

$$a_J = \frac{\hbar \cdot \Theta_{SH}}{2e\mu_0 M_S d_{mm}} \qquad b_J = \zeta a_J \tag{2.45}$$

with Θ_{SH} the spin Hall angle, M_s the saturation magnetization and d_{mm} the thickness of the magnetic material. Due to this thickness dependence, the effective torque

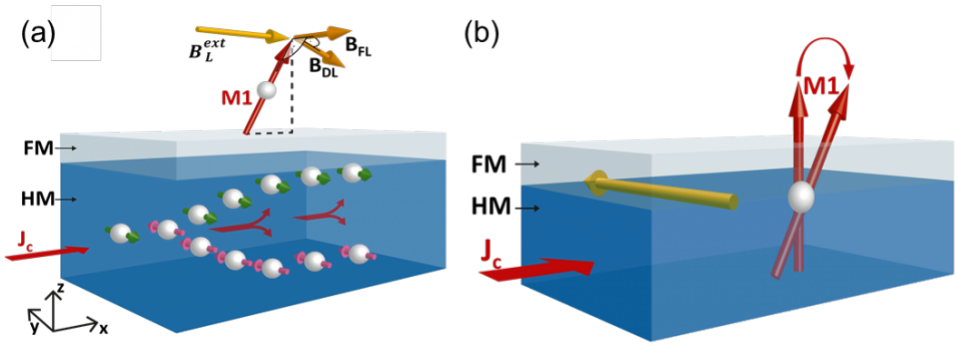

FIGURE 2.9: a) Schematic representation of the SHE. A longitudinal electron current, J_C, flowing through a HM is converted into a transverse spin current via spin-orbit scattering. This spin current causes spin accumulation at the HM/FM interface, which then diffuses into the FM and exerts torque on the local magnetization. b) The effective field induced by the REE at the interface, which can drive the switching of the magnetization. Images adapted from [92].

decreases with increase of thickness, since the same amount of spins have to diffuse through thicker material.

The cumulative effect of all torques resulting from the field-like induced magnetic field tends to cancel out, preventing any significant movement of domain walls. However, it may cause deformation, which could indirectly influence the motion of magnetic structures [93]. In contrast, the damping-like field induces a torque on the magnetization when it has a finite component along the direction of the electric current. Referring to the two types of domain walls discussed in Section 2.2.1, only Néel domain walls possess this component and are therefore affected by spin-orbit torques, assuming the domain boundary is perpendicular to the charge current. When aligned with the charge current, Bloch domain walls move perpendicular to the charge current, while Néel domain walls remain unaffected. The direction of the torque is influenced by two key factors: the spin polarization σ and the orientation of the magnetic component parallel to the electric field, making domain wall chirality a crucial factor. In systems where chirality is not fixed, spin-orbit torques cause domain walls of opposite chirality to move in opposite directions. To establish a preferred chirality of the spin textures, DMI becomes significant. The DMI breaks the symmetry between chiralities, favoring one over the other (see Section 2.1.3). At sufficiently high DMI values, one chirality dominates, ensuring consistent domain wall movement direction [46].

Since skyrmions, introduced in the next section, exhibit a single chirality, the torques on opposite sides of the skyrmion add up rather than cancel, leading to efficient (directed) skyrmion motion. Therefore, the presence of a sufficiently strong DMI that stabilizes chiral skyrmions positions spin-orbit torque as a reliable and highly efficient mechanism for skyrmion manipulation [83, 94–99].

Orbital torques are a subject of ongoing research and promise even higher efficiency, potentially offering another order of magnitude improvement. In this case, the orbital Hall effect generates orbital currents perpendicular to the charge current, while the orbital Rashba-Edelstein effect results in the accumulation of orbital angular momentum at interfaces. This accumulated orbital angular momentum is subsequently converted into spin currents in materials with strong spin-orbit

coupling, often facilitated by an additional heavy metal layer. The resulting spin current then applies torque to the magnetic layer through spin-orbit torques [84, 100–102].

2.4 Magnetic Skyrmion

In 1961, Tony H. R. Skyrme proposed a theoretical framework describing topologically stable soliton-like configurations - referred to as skyrmions - as quasi-particles within field theory to model the strong nuclear force and the structure of atomic nuclei, consistent with the principles of the Standard Model [103]. Although the quark model, developed later in the 1960s, gained greater empirical support - particularly through scattering experiments that validated its predictions - Skyrme's mathematical formalism experienced a resurgence in the 1980s when it was found applicable to condensed matter systems, particularly in the study of topological magnetic structures. In condensed matter physics, magnetic skyrmions - topologically non-trivial spin textures - were theoretically predicted to emerge in magnetic materials lacking inversion symmetry. The first experimental observation of such magnetic whirls occurred in bulk MnSi in 2009 at 28 K [104], followed by their identification in metallic thin films in 2011 [105]. Today, magnetic skyrmions are recognized as topologically protected solitons with exceptional stability, which arises from their non-linear and non-trivial topological configuration [106–109]. Their stability, nano-scale size, and low depinning currents have rendered them promising candidates for applications in information storage, magnetic sensing, and neuromorphic or unconventional computing technologies [58, 110–113]. The ability to stabilize skyrmions at room temperature further accelerates their relevance in spintronic device design [110]. In this thesis, experimental investigations are focused on skyrmions in metallic thin-film systems with interfacial inversion symmetry breaking.

To rigorously describe and classify magnetic skyrmions, the mathematical framework of homotopy theory is employed. This theory categorizes continuous mappings - representing spatial configurations of magnetization - into distinct topological equivalence classes based on their deformability into one another without discontinuities [114, 115]. In this context, the magnetization field is mapped onto a unit sphere [108], where each spin orientation corresponds to a point on the sphere's surface.

The stability of magnetic skyrmions is a fundamental characteristic that underlies their promise for technological applications. A key stabilizing mechanism is the interfacial DMI, which energetically favors chiral, non-collinear spin textures in systems with strong spin-orbit coupling and broken inversion symmetry. Depending on the material properties and system geometry, the DMI can stabilize skyrmions either as metastable configurations - corresponding to local energy minima - or as the true ground state of the magnetic system. In addition to DMI, thin-film systems with strong PMA contribute to skyrmion stabilization through a reduction in stray field (demagnetizing) energy. This reduction minimizes magnetostatic repulsion, allowing for the formation of relatively large, thermodynamically stable skyrmions, particularly in ultrathin films where magnetostatic effects are suppressed (see Section 2.4.1)[116, 117]. The topological stability of skyrmions is further characterized by a quantized invariant known as the winding number or topological charge [109, 118–120]. This integer value quantifies the degree of non-collinearity by counting

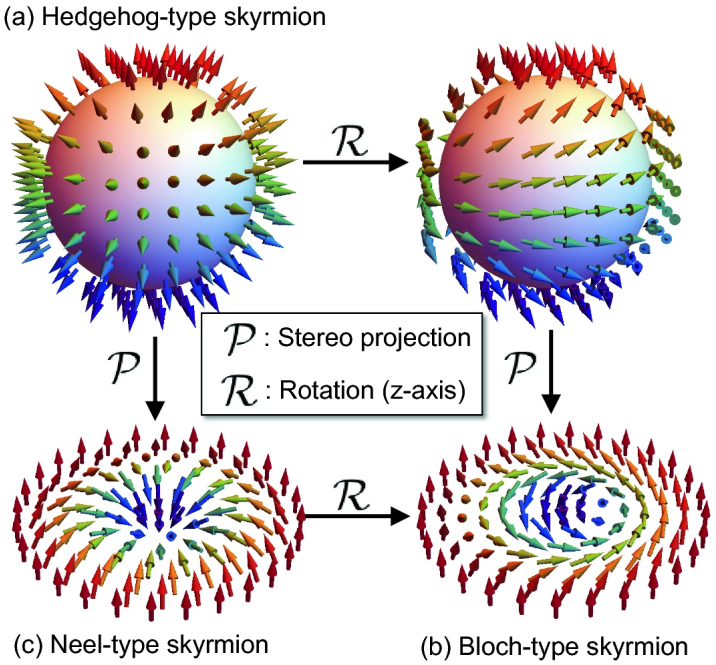

FIGURE 2.10: a) A hedgehog-type skyrmion, initially proposed by Tony Skyrme in the early 1960s, features a radial spin configuration in which the magnetization vectors point outward or inward from the skyrmion core. b) A Bloch-type skyrmion is characterized by a spin texture where the magnetization vectors rotate within a plane perpendicular to the radial direction, resulting in a tangential spin arrangement around the skyrmion core. c) A Néel-type skyrmion exhibits magnetization vectors that rotate within a plane parallel to the radial direction, leading to a cycloidal spin configuration from the core outward. These three skyrmion types are topologically equivalent and can be transformed into one another through stereographic projection and rotational operations about the z-axis. Taken from [121].

how many times the local magnetization vector wraps around the unit sphere across the 2D magnetic texture [108]. As illustrated in Figure 2.10, this mapping provides a geometric interpretation of the skyrmion's topology, where the total number of wrappings determines the structure's classification within topological homotopy classes.

$$Q = \frac{1}{4\pi} \int m \cdot \left(\partial_x \mathbf{m} \times \partial_y \mathbf{m} \right) dxdy \tag{2.46}$$

The typical skyrmion is visualized in the 2D form as a stereographic projection of the three-dimensional (3D) unit sphere with the spins often depicted in color code. In Figure 2.10, the surrounding magnetization with the according spins (*edge*) pointing up is here displayed in red, the chiral domain wall in a color spectrum, rotating towards the single spin pointing down in blue (*center*). Skyrmions can also be characterized by their domain wall type, Bloch and Néel type, basically how the spins are aligned and rotate between the opposite spin configurations of center and edge. In Bloch-type skyrmions, the magnetic moments rotate tangentially, basically a circular, perpendicular rotation around the skyrmion center. They can exist without DMI, which can lead to both chirality in one system but are primarily stabilized by bulk DMI and thus occur commonly in chiral bulk magnets [122]. The 3D unit sphere would be depicted cortex-like, with the spins aligned tangentially to the unit

	Néel-Type	**Bloch-Type**
Spin Rotation	Radial (in-/outward)	Tangential (circ.)
Analogy	Hedgehog-like	Vortex-like
DMI origin	Interfacial DMI	Bulk DMI
Stabilization	Films, interfaces	Bulk chiral magnets
Materials e.g.	Heavy metal/FM	Chiral magnets

TABLE 2.1: Comparison of properties between Néel-type and Bloch-type skyrmions.

sphere's surface. The magnetic moments in Néel-type skyrmions, in comparison, rotate in or outward along the radial direction, which results in a hedgehog-like unit sphere, where spins are parallel with the unit sphere's surface normal. These skyrmions are stabilized by interfacial DMI and are thereby commonly found in thin film heterostructures with strong SOC at the interface (e.g., heavy metal (HM)-ferromagnetic metal (FM)) [107, 116, 123–125].
In Table 2.1, the differences between both types are summarized.[1]

Since only metallic thin film heterostructures have been used, the skyrmions in this thesis are of the Néel-type. Material parameters, in addition to interfacial DMI, such as exchange stiffness (A) and magnetic anisotropy (K) need to be carefully balanced for skyrmions. To achieve this balance, the intrinsic material parameters must be tuned and adjusted, like e.g. the thickness or composition. A material parameter criterion for thermodynamically stable skyrmion is a reduced energy when DWs are present. [119, 126]:

$$\pi D > 4\sqrt{AK} \tag{2.47}$$

With the DMI constant D, exchange stiffness A and anisotropy K.

2.4.1 Observed magnetic skyrmion

Skyrmion size can vary drastically and depends strongly on the stabilizing mechanism [127]. Skyrmions can be stabilized by the dipolar or stray field-dominated mechanism, which occurs at low magnetic fields and results in large skyrmion diameters, exhibiting lower rigidity, and their diameter decreases rapidly with increasing out-of-plane field [128, 129].
In systems dominated by the DMI, typically stabilized under the influence of external magnetic fields, skyrmions exhibit enhanced robustness due to the chiral nature of the DMI, which energetically counteracts their collapse. These DMI-stabilized skyrmions are usually characterized by nanometric dimensions, ranging from several tens of nanometers down to a few nanometers [130], with the ultimate size limit determined by the crystal lattice of the material [127, 131–133].
In contrast, skyrmions stabilized by magnetostatic (stray field) interactions tend to be significantly larger, with typical sizes spanning from tens of nanometers [130] up to tens of micrometers [116]. Magnetic bubbles, which are circular regions of reversed magnetization enclosed by domain walls with trivial topology, can appear on similar or even larger spatial scales [134]. These bubbles are separated from the surrounding magnetization by domain walls that are typically 100 to 300 atomic layers thick.

[1] Note that also Néel skyrmion can be caused by bulk DMI (e.g., in GaV_4S_8)

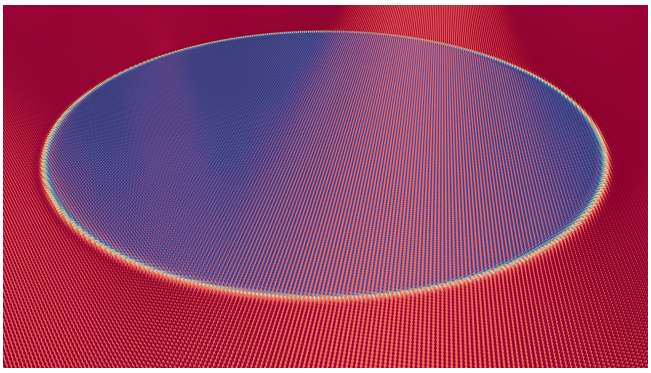

FIGURE 2.11: Simulated skyrmion in micrometer-scale with the inner core (blue), the domain wall (yellow gradient) and the outer magnetization (red). Courtesy of K. Leutner.

The primary distinction between skyrmions and magnetic bubbles lies in the topological character of their domain walls [94]. Skyrmions possess a non-trivial domain wall topology, characterized by a continuous chiral rotation of the magnetization vector and a non-zero topological charge, whereas magnetic bubbles exhibit trivial domain wall configurations and lack such topological protection. Consequently, the classification of a magnetic structure as a skyrmion should be based on its spin texture and topological characteristics rather than its size or morphology.
Importantly, skyrmions with micrometer-scale diameters can still be classified as such if they exhibit chiral domain walls with non-trivial topology, as their spin structure remains equivalent to that of nanometer-scale skyrmions. The manipulation of skyrmion size is investigated in 5 and can be realized by a multitude of internal [127, 135, 136] and external parameters, the latter like electric and magnetic fields [128, 137–139], temperature [67, 110, 139], temperature gradients [140], strain [141], irradiation [142], SOT [143, 144], or occurrence in confined lattices [145].

In this thesis, the investigated skyrmions are of micrometer size and are hosted in metallic thin films composed of sub-nanometer-thick ferromagnetic CoFeB layers [136]. Given their lateral dimensions in the micrometer range and a thickness that is more than three orders of magnitude smaller, these skyrmions can be treated as effectively 2D. Moreover, their particle-like behavior in such confined geometries makes them an attractive platform for studying collective phenomena and statistical physics, drawing parallels to systems such as colloidal particles.

The formation of skyrmions in these samples is governed by a complex energetic balance between the PMA, the DMI, and the dipole-dipole interactions (stray-field effects). This interplay results in skyrmions with diameters in the micrometer range in samples presented in this thesis. Notably, the magnetic properties in these samples are highly sensitive to temperature variations, necessitating strict temperature control to prevent undesired annealing effects during the sample structuring, ion etching, additional material deposition (e.g., contact pads), or detrimental effects to the skyrmion phase in long-term measurements.

2.4.2 Skyrmion diffusion

Diffusion refers to the movement of particles within a medium driven by concentration gradients, first described by Brown [146] and mathematically formulated by Fick's laws [147, 148]. From an energetic perspective, diffusion is driven by gradients

in Gibbs free energy or chemical potentials. Unlike bulk material transport, diffusion occurs without any net movement of the medium itself; particles in the medium move stochastically, while the medium itself remains stationary, distinguishing diffusion from mass flow. To describe the thermally activated diffusive motion of rotationally symmetric skyrmions, Schütte et al. [73] proposed a theoretical framework based on the Thiele approach [71], which was derived from Gilbert's equation [63]. The Thiele equation, as defined earlier in section 2.2.3, for a moving skyrmion with the constituents (2.42):

$$\mathcal{G}_{i,j}\mathbf{v}_j + \alpha\mathcal{D}_{i,j}\mathbf{v}_j + F_i = 0 \tag{2.48}$$

Schütte's approach provides a quantitative description of skyrmion dynamics under thermal fluctuations, accounting for their topological and dissipative properties. The derived diffusion constant D is

$$D = k_B T \frac{\alpha\boldsymbol{\mathcal{D}}}{(\alpha\boldsymbol{\mathcal{D}})^2 + \boldsymbol{\mathcal{G}}^2} \tag{2.49}$$

With $\boldsymbol{\mathcal{D}}$ the dissipative tensor, α the damping, and $\mathbf{G}$ the gyrocoupling tensor. Atomistic spin simulations demonstrate that equation (2.49) is linked with the mean squared displacement (MSD), which can easily be measured experimentally by tracking the location of a magnetic structure over time intervals:

$$\left\langle (\mathbf{R}(t) - \mathbf{R}(0))^2 \right\rangle = 2dDt^{\alpha} \tag{2.50}$$

$\mathbf{R}$ represents the spatial position of the particle at time t = 0 and t = t', d the dimensionality of the system, D the diffusion coefficient, and α the exponent that characterizes the type of diffusion. When $\alpha = 1$, the MSD exhibits a linear dependence on time, corresponding to normal (Brownian) diffusion [39], which is well described by Fick's laws. However, for $\alpha > 1$ (superdiffusive behavior) or $\alpha < 1$ (subdiffusive behavior) (see Figure 2.12), the system deviates from normal diffusion and can no longer be accurately described by Fick's diffusion models.

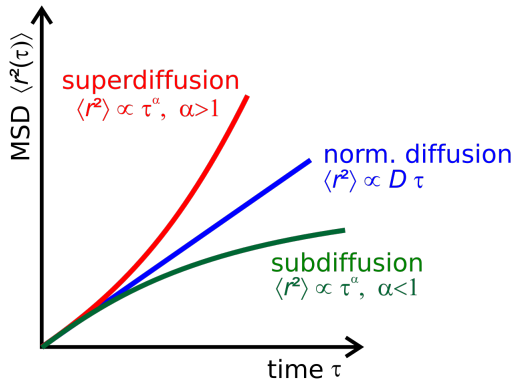

FIGURE 2.12: Mean square displacement for normal (blue), super- (red) and sub- (green) diffusion. Taken from [149]

Thermally activated skyrmion diffusion is inherently a stochastic process, governed by thermal fluctuations and random motion [42, 73]. This intrinsic randomness renders skyrmions promising candidates for applications in stochastic computing architectures, where probabilistic behavior is exploited for data processing [99, 110, 150–152]. To harness and optimize this potential, current research investigates

strategies to enhance skyrmion diffusivity [110, 129, 153], achieve direction manipulated diffusion [154, 155], and mitigate or regulate pinning effects that impede skyrmion mobility [129, 156–158]. These efforts aim to enable reliable and tunable manipulation of stochastic skyrmion dynamics for functional device integration.

2.4.3 Skyrmion pinning and confinement

The energy landscape of magnetic materials like thin films utilized in this thesis is inherently non-homogeneous due to local variations in material parameters caused by e.g., natural or artificial impurities. This heterogeneity leads to energetically favorable regions, known as pinning sites [156, 158, 159], which increase the probability of skyrmion localization at these specific positions. Pinning is intrinsically dependent on the skyrmion size and its chiral domain wall [129, 157], with the pinning effect diminishing as thermal energy increases. At sufficiently high temperatures, thermal fluctuations allow skyrmions to overcome pinning sites, thereby increasing their diffusive motion [110]. Lesser pinning directly correlates with the reduction in the critical current required for skyrmion motion [160, 161], as the applied spin torques no longer need to overcome the energy barriers associated with pinning sites. Pinning sites, natural or artificial, can also be used for applications or potentially for biasing lattice order [162]. Additionally, pinning can be mitigated through oscillation of skyrmion size; skyrmions are pinned primarily at their domain walls rather than at their cores [157]. Consequently, forced size fluctuations by an oscillating magnetic out-of-plane field induce a repulsive interaction between the domain wall and the pinning sites, increasing skyrmion depinning [129]. Skyrmion motion can not only be inhibited by pinning sites, but they can also be confined in 2D structures by a repulsive interaction with the system's boundaries [94, 159, 163–166] or artificial barriers [45, 46, 155, 167–169]. The long-range repulsion from structural edges arises primarily due to dipolar energy effects, which originate from the structure's stray magnetic field [116, 170] or by interlayer exchange coupling [171]. In geometrically constrained systems, such as triangular structures, this effect increases the localization probability of skyrmions in the geometries' center [99, 152, 172]. When a skyrmion is displaced from the central equilibrium position, it experiences a repelling force directed inwards. Higher temperatures improve this depinning and diffusive mechanism. The repulsive interaction exists not only between skyrmion and system boundaries but also between skyrmion themselves [163, 172–174], leading to intricate lattices at higher skyrmion density. Comparative analysis indicates that the repulsive potential between the boundary and skyrmion is of an exponential decay nature [173].

2.4.4 Skyrmion lattice

Skyrmions nucleated under appropriate magnetic bias out-of-plane fields can form a densely packed 2D lattice due to their mutual repulsion [104, 105, 145, 175]. In confining structures, the repulsion of the boundaries can influence skyrmion density and lattice order [170, 172]. To characterize this lattice and its phase transitions, the Kosterlitz-Thouless-Halperin-Nelson-Young (KTHNY) theory of 2D melting can be utilized. According to the KTHNY theory, 2D systems of particles interacting via short-range forces can exhibit a distinct intermediate phase known as the hexatic phase - an ordering phase absent in 3D systems [176, 177]. This phase is characterized by quasi-long-range translational order and true long-range orientational order, distinguishing it from both the crystalline and liquid phases.

The KTHNY framework describes a two-step continuous phase transition in which the system progresses through three distinct phases: crystalline (solid), hexatic, and isotropic liquid, each marked by the unbinding of topological defects such as dislocations and disclinations [176].

Solid phase: Translational correlation functions decay algebraically, and dislocations remain bound in pairs.

Hexatic phase: Features quasi-long-range orientational order but short-range positional order, with free dislocations emerging.

Liquid phase: Both positional and orientational correlations decay exponentially, with free dislocations decomposing into disinclinations, leading to isotropic behavior and semi-free skyrmion diffusion.

To characterize the lattice, the dimensionless relation between one skyrmion and their nearest neighbors is introduced:

$$\Psi_6(\mathbf{r}_i) = \frac{1}{N_{nn}} \sum_{j=1}^{N_{nn}} e^{i6\theta_{ij}} \tag{2.51}$$

Let N_{nn} denote the number of **n**earest **n**eighbors of a skyrmion located at position r_i, and let θ_{ij} represent the angle between the vector connecting the skyrmion center at r_i to its nearest neighbor at r_j, relative to a predefined reference axis. The bond-orientational order parameter Ψ_n is used to quantify the degree of angular order in the lattice, where n corresponds to the symmetry being investigated. A value of $|\Psi_6|$=1 indicates a perfectly ordered hexagonal lattice, characterized by six equidistant nearest neighbors positioned at 60° intervals, reflecting six-fold rotational symmetry (see Figure 2.13 a)). In the context of this thesis, both six-fold (hexagonal) and four-fold (square) lattice symmetries are evaluated. The latter corresponds to $|\Psi_4|$=1, which denotes a square lattice where each skyrmion has four equidistant nearest neighbors arranged at 90° angles (see Figure 2.13 b)). The $|\Psi_4|$ order parameter is defined by:

$$\Psi_4(\mathbf{r}_i) = \frac{1}{N_{nn}} \sum_{j=1}^{N_{nn}} e^{i4\theta_{ij}} \tag{2.52}$$

Skyrmions can be accurately modeled as 2D disk-like particles, allowing for the application of classical statistical mechanics frameworks to describe their phase behavior [104, 175, 178, 179]. Their unique properties, along with the ability to control their size, lattice structure, phase transitions, confinement, and diffusion, make them a compelling subject of research in 2D systems, analogous to colloidal particles.
This section has been adapted from "*Dynamics of topologically non-trivial spin structures*", K. Raab, MSc. Thesis, section 3.2.8. Lattice Formation [180].

2.4.5 Skyrmion Hall effect

Skyrmions subjected to external driving forces - such as SOT generated by spin currents - exhibit a characteristic transverse displacement known as the skyrmion Hall effect (SkHE) [97, 181–186]. This phenomenon is analogous to the classical Hall effect observed in charged particles but originates from the topological nature of

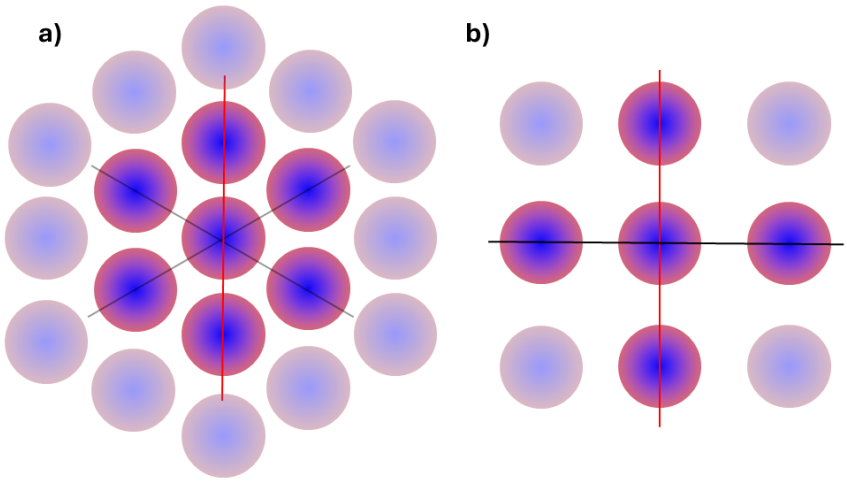

FIGURE 2.13: Schematic of hexagonal and square lattice order, and their respective symmetry axes.

skyrmions rather than electric charge. Specifically, when skyrmions move, they experience a Magnus force, which acts perpendicular to the direction of the applied force. This transverse response arises from the skyrmion's non-trivial topology, characterized by its integer-valued winding number (see eq. 2.46 in section 2.4). The topological structure gives rise to an effective emergent electrodynamic field during motion, which governs the interaction between skyrmions and conduction electrons. As a result, the skyrmion trajectory deviates from the direction of the applied current, leading to a deflection angle. This deflection is influenced by the interaction mechanism - either via STT or SOT - and manifests both in driven [184, 187] and thermally activated diffusive regimes [153, 188]. The equation of motion follows the Thiele equation:

$$\mathbf{G} \times \mathbf{v} - \alpha \mathbf{D} \cdot \mathbf{v} + F_{ext} = 0 \tag{2.53}$$

with $\mathbf{G}$ is the gyrocevtor, which is proportional to the topological charge Q, $\mathbf{v}$ the skyrmion velocity, α the damping coefficient, $\mathbf{D}$ is the dissipative tensor, and $\mathbf{F}_{ext}$ the external forces. The combination of the Magnus force and dissipation results in a skymrion trajectory deviating from the external force direction at a specific angle. This angle is known as the skyrmion Hall angle:

$$\theta_{\mathbf{SkH}} = \arctan\left(\frac{\mathbf{G}}{\alpha}\right) \tag{2.54}$$

Since the gyrocoupling is dependent on the topological charge Q by

$$\mathbf{G} = \pm 2\pi Q \mathbf{z} \tag{2.55}$$

the skyrmion Hall angle also depends on Q. With $\mathbf{z}$ the out-of-plane vector, considering motion in the x-direction. The angle also depends on the skyrmion size, the velocity and thus the driving force, and the underlying material properties, e.g., damping α.

The transverse motion resulting from the Magnus force presents a significant challenge, particularly in confined geometries. As the Magnus force is proportional to the skyrmion velocity ($\mathbf{G} \times \mathbf{v}$), skyrmions driven at high velocities experience an

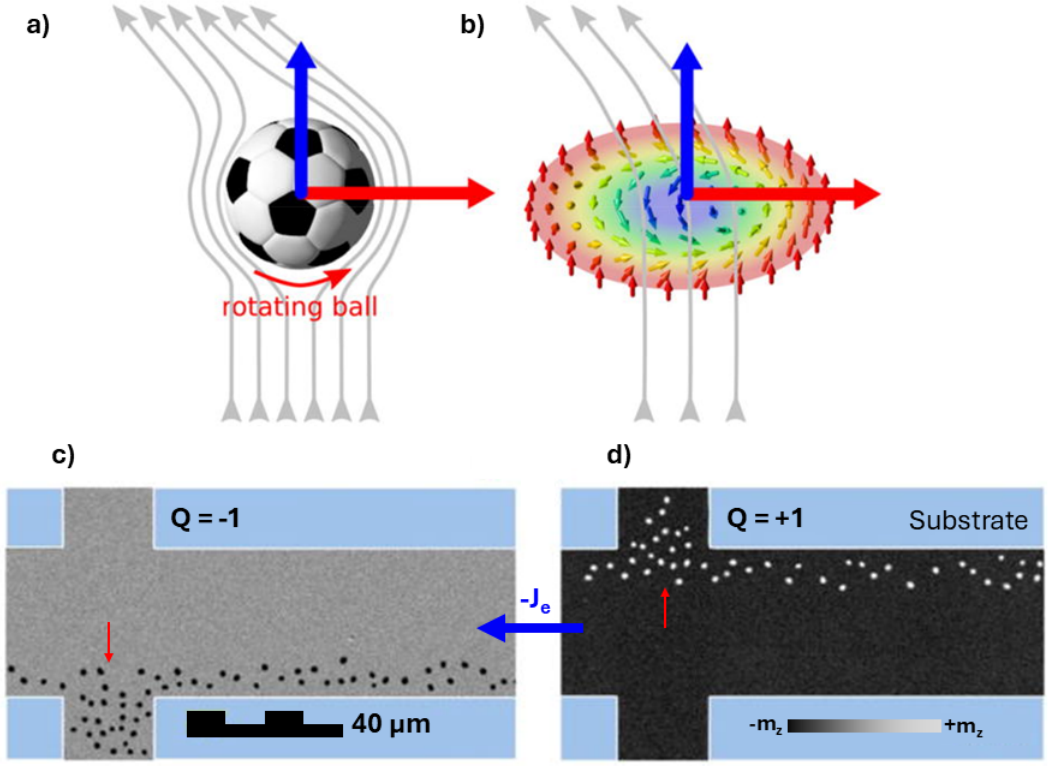

FIGURE 2.14: a) Illustration of the Magnus force acting on a rotating sphere: when the ball is propelled in a certain direction (blue arrow), it experiences a transverse Magnus force (red arrow) due to its rotation, which alters its trajectory relative to the surrounding airflow (gray streamlines). b) Analogously, a magnetic skyrmion experiences a transverse Magnus force (red arrow) when subjected to an external driving force, such as a spin-polarized current (blue arrow). This force results in a lateral deviation of the skyrmion's trajectory (gray path), analogous to the classical Magnus effect. c) and d) Schematic representations of skyrmions with different topological charges Q, highlighting their contrasting responses to the Magnus force. Upon application of a spin current (blue arrow), skyrmions are driven along a central channel but are deflected toward opposite channel edges (red) due to the sign of their respective topological charge. This topologically induced deflection demonstrates the chirality-dependent nature of the Skyrmion Hall Effect. Adapted from [184, 189]

increasingly strong lateral deflection. This deflection can cause skyrmions to drift toward device boundaries, as illustrated in Figure 2.14 c,d), potentially leading to their annihilation. Such behavior imposes a critical limitation on velocity and thus the performance and reliability of skyrmion-based technologies, including racetrack memory [48] and spintronic computing architectures, where controlled and robust skyrmion motion is essential, e.g., token-based computing [190]. One way to mitigate the influence of the skyrmion Hall effect is to employ systems with synthetic skyrmion bilayers or antiferromagnetic skyrmions, due to the cancellation of fields from opposite topological charges [153, 191, 192].

A deliberately induced SkHE presents challenges for practical applications, as one of the primary advantages of skyrmions lies in their controllable and deterministic motion.

In the experimental investigations presented in this thesis, the skyrmion Hall effect is considered negligible. This is attributed to the relatively low current densities employed (10^6 to $10^8 \frac{A}{m^2}$), which result in skyrmion velocities that are insufficient to produce a significant skyrmion Hall angle. Consequently, transverse deflection of

skyrmion trajectories due to the Magnus force remains minimal with skyrmion Hall angles below 1° under the applied conditions.

2.4.6 Skyrmion compression theory

In Chapter 5, the influence of external and internal pressure on skyrmion size is systematically investigated. As previously discussed in Sections 2.4 and 2.4.1, skyrmion size is highly sensitive to various intrinsic and extrinsic parameters [110, 127, 128, 135, 136, 139, 144, 145, 193]. This study extends current understanding by examining skyrmion deformation under two forms of mechanical confinement; the internal lattice pressure and forced compression against artificial barriers. Internal pressure effects have been experimentally explored in cobalt-based bulk materials [194, 195]. Moreover, simulations incorporating the SkHE have demonstrated a reduction in both skyrmion lattice spacing and ordering, and individual skyrmion size when subjected to directional forces that push skyrmions against rigid boundaries, as a consequence of the Magnus force [143].
When a driving force is applied, skyrmions follow the direction of motion. In confined systems where the skyrmion lattice is densely packed, repulsive interactions between skyrmions, as well as between skyrmions and boundaries, generate an effective internal pressure. This pressure leads to local compression of skyrmions near immovable barriers, such as physical sample edges [89, 163, 171] or irradiated regions [155, 158, 169, 196–198].
Analogous to atmospheric pressure, which depends on the number density of gas particles, the local density of skyrmions within the lattice seem to critically influence the degree of compression, with implications for lattice structure, stability, and dynamic behavior under confined geometries as observed in Chapter 5.

The following theoretical Ansatz was derived by K. Leutner[2] based on experimental findings and supported by simulations presented in the second half of chapter 5 and is currently still under development.

The derivation starts with an extended Thiele equation for position **r** and radius R analogous to the normal Thile equation, only for energy minimization. Also the gyroscopic force is neglected and D is set to D = 1.

$$\begin{aligned} D\dot{\mathbf{r}} &= -\nabla_{\mathbf{r}} E + \mathbf{F}_{SOT,\mathbf{r}} \\ D\dot{R} &= -\partial_R E + \mathbf{F}_{SOT,R} \end{aligned} \tag{2.56}$$

Considering the magnetic film height h is significantly smaller than the radius R of the skyrmions (R≫h), while the domain wall width Δ is also significantly smaller than the radius R (R≫ Δ), the energy E consists of the following terms:

$$\begin{aligned} E &= E_{\mathrm{DW}} + E_{\mathrm{Z}} + E_{d,s,s\leftrightarrow f} + E_{d,s\leftrightarrow s} + E_{d,s\leftrightarrow b} \\ \textbf{with} \quad E_{DW} &= 2\pi R h \sigma \\ \textbf{and} \quad E_{\mathrm{Zeeman}} &= 2B_z M_s h \pi R^2 \end{aligned} \tag{2.57}$$

With E_{DW} the domain wall energy, E_{Zeeman} the Zeeman energy, $E_{d,s,s\leftrightarrow f}$ the dipole skyrmion self-energy with magnetic film skyrmion interaction for R≫h term, $E_{d,s\leftrightarrow s}$ the dipole skyrmion-skyrmion interaction with distance l between skyrmions, $E_{d,s\leftrightarrow b}$, the dipole skyrmion-boundary interaction (at x_0). The complete terms

[2] with helpful discussions with Dr. R. Frömter

$E_{d,s,s\leftrightarrow f}$, $E_{d,s\leftrightarrow s}$ and $E_{d,s\leftrightarrow b}$ can be found in Section C.1.

The external force on the skyrmion, the electric current induced SOT, is derived by integration of the skyrmion magnetization ansatz to be:

$$\begin{aligned} \mathbf{F}_{SOT,\mathbf{r}} &= -\frac{\hbar\pi^2}{2e}\theta_{SH}\mathbf{J}R \\ \mathbf{F}_{SOT,R} &= 0 \end{aligned} \tag{2.58}$$

The first term, $\mathbf{F}_{SOT,\mathbf{r}}$, represents the external SOT-induced force acting on a skyrmion of radius R located at spatial position $\mathbf{r}$, and depends on the spin Hall angle θ_{SH} and the applied current density $\mathbf{j}$. The second term corresponds, $\mathbf{F}_{SOT,R}$, to a hypothetical radial SOT-induced force directed toward or away from the skyrmion center, which is set to zero in this context, as there is currently no experimental evidence indicating a change in the skyrmion size due to SOT in free, unconfined conditions.

Macroscopic description

In a macroscopic description K. Leutner derived further modeling of skyrmion compression system. Starting with the analytical skyrmion lattice model with the expression of energy in a unit cell E_{uc}(R,P,σ,B_z). Analogous to the barometric formula, the derivation of $dp \sim \rho dx$ with ρ the particle density is calculated, followed by p(ρ) for skyrmions, mimicking an *ideal gas law for skyrmions* with limited degree of freedom for $\rho = \frac{2\sqrt{3}}{P^2}$. The resulting analytical and simulation results are used to compare with the experimental findings. The detailed derivation can be found in the Section C.1.2.

The **ideal gas law for skyrmions** derived by K. Leutner:

$$\begin{aligned} P(R) &= \kappa\frac{R}{(R_c - R)^{\frac{1}{3}}} \\ \textbf{with} \qquad \kappa &= \frac{4,108}{\left(\frac{4B\pi}{\mu_0 h M_s}\frac{1}{R_c}\right)^{\frac{1}{3}}} \\ R_c &= -\mu_0 h M_s W_{-1}\left(-\frac{\pi B_e^{\frac{\pi\sigma}{\mu_0 h M_s^2}-\frac{1}{2}}}{4\mu_0 M_s}\right)\frac{1}{2\pi B} \end{aligned} \tag{2.59}$$

with W_{-1} the Lambert W function

$$R(P) = \frac{\sqrt[3]{2}\left(\kappa^{\frac{9}{2}}P^3\left(9\kappa^{\frac{3}{2}}R_c + \sqrt{81\kappa^3R_c^2 + 12P^3}\right)\right)^{\frac{2}{3}} - 2\sqrt[3]{3}\kappa^3P^3}{6^{\frac{2}{3}}\kappa^3\sqrt[3]{\kappa^{\frac{9}{2}}P^3\left(9\kappa^{\frac{3}{2}}R_c + \sqrt{81\kappa^3R_c^2 + 12P^3}\right)}} \tag{2.60}$$

Finally leading up to the formula to determine pressure out of the experiment (see 5) and Thiele equation.

$$dp = -\frac{\hbar\pi^2}{2e}\theta_{SH}j_xR(p)\rho(p)dx \rightarrow p(x) \quad = -\frac{\hbar\pi^2}{2e}\theta_{SH}j_x\int_{x_0,p(x_0)=0}^{x} dx'R(x')\rho(x') \tag{2.61}$$

and the formula for unit-cell energy in dependence of R, P, and p.

$$\begin{aligned} E_{uc}(P) &= \int_{P_0}^{P} dPP \int_{x_0}^{x} dx' R(x')\rho(x') \\ &= \frac{p(x_0)}{\rho(x_0)} - \frac{p(x)}{\rho(x)} - \frac{\hbar\pi^2}{2e} j_x \int_{x_0}^{x} dx' R(x') \end{aligned} \tag{2.62}$$

The analytical and simulation results in comparison with the experimental data will be shown in Chapter 5 and the detailed calculation in Section C.1.2.

2.5 Magneto-optical Kerr effect

The experimental key aspect of this thesis is the use of Kerr microscopy, which enables the visualization of the magnetization in thin film samples. By capturing images and videos, the magnetization dynamics can be recorded and analyzed. To understand this technique, the underlying theory of magneto-optical effects is introduced:
These interactions give rise to magneto-optical phenomena, where the optical response depends on the magnetization M of the material. In transmission, the Faraday effect describes the magneto-optical modification of light that is linearly proportional to the magnetization ($\propto$ M), whereas the Voigt effect involves changes that scale quadratically with magnetization ($\propto M^2$) [199]. When light is reflected and modified magneto-optically, the phenomenon is known as the magneto-optical Kerr effect (MOKE). Depending on the power of magnetization contributing to the optical response, MOKE can be categorized into

Linear MOKE (LinMOKE), with an intensity change proportional to M ($\propto$ M),
Quadratic MOKE (QMOKE), scaling with the square of M ($\propto M^2$), and
Cubic MOKE (CMOKE), dependent on the cube of M ($\propto M^3$).

Although higher-order MOKE contributions are theoretically possible, they are challenging to detect experimentally and remain less explored. MOKE can further be classified by the angle of incidence in relation to the direction of magnetization. In polar MOKE, the magnetization points out-of-plane, optimally parallel to the surface normal of the sample. If the incidence and reflection plane is parallel with the in-plane magnetization in the sample, the effect is called longitudinal MOKE and transversal MOKE, if the in-plane magnetization is perpendicular to the incidence and reflection plane. All MOKE effects originate from the off-diagonal elements of the dielectric permittivity tensor, which encapsulate the anisotropic and magneto-optical properties of the material. These tensor elements govern how the material's permittivity responds to the magnetization and the electromagnetic field of the incident light. The difference in refractive indices (n) for left- and right-circularly polarized light - responsible for magneto-optical rotation and ellipticity - originates from the asymmetry in the dielectric tensor. This asymmetry is influenced by the material's permittivity, which itself is dependent on the magnetic induction B. Thus, the magneto-optical Kerr effect reflects both the intrinsic dielectric properties of the material and their modulation by the magnetic field.

A phase shift occurs upon reflection due to the real value of the diffraction index and its dependence on B. This phase shift causes a rotation of the polarization axis, which is characteristic for the magneto-optical Kerr effect. Additionally, due to

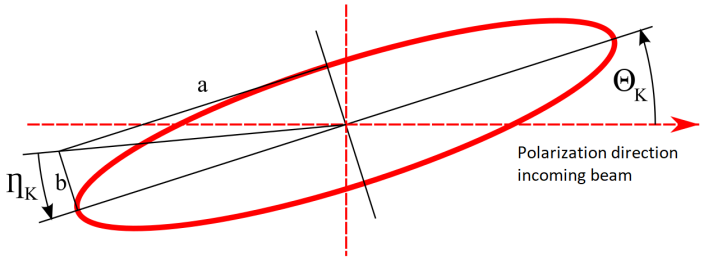

FIGURE 2.15: Transversal amplitudes of elliptically polarized light with the ellipse axes a and b, ellipticity η_K and Kerr rotation angle θ_K. Taken from [200]

different absorption coefficients for left- and right-circularly polarized light, the reflected beam acquires an elliptical polarization, a phenomenon known as magnetic circular dichroism. Φ_K, Kerr rotation and ellipticity, is dependent on the material properties and the relative orientation of the magnetization, applied magnetic field, and plane of incidence of the light, and can be written with the real value of the Kerr angle θ_K and ellipticity η_K:

$$\Phi_K = \theta_K + i\eta_K \tag{2.63}$$

$$\eta_K = \arctan\frac{b}{a} = \arctan\left(\sqrt{\frac{I_r}{I_l}}\right) \tag{2.64}$$

with a and b the amplitudes (see Figure 2.15), and I_r and I_l the intensity of the left-circular and right-circular polarized light, respectively.

In his thesis the focus lies exclusively on the linear MOKE, using a Kerr microscope in which light is reflected from the used magnetic samples. MOKE can be further classified based on the orientation of the magnetization vector relative to the surface and orientation of incident light. The detailed theory is shown later for the polar case, for which the light vector and magnetic field vector are both orthogonal to the materials' surface.

Polar MOKE (PMOKE): The magnetization is perpendicular in respect to the material's surface and parallel to the plane of incident and reflected light. The latter undergoes polarization rotation and transitions from linear to elliptical polarization.

Longitudinal MOKE (LMOKE): The magnetization lies parallel to both the surface and the plane of incidence. The incident light must hit the surface at a finite angle to the normal. Similar to the PMOKE, the polarization of the reflected light becomes elliptical.

Transversal MOKE (TMOKE): The magnetization is parallel to the surface but perpendicular to the plane of incidence. Instead of measuring polarization changes, this mode relies on reflectivity measurements, which depends on the magnetization component perpendicular to the plane of incidence.

2.5.1 Theoretical derivation of PMOKE

The following theoretical derivation of the PMOKE is from reference [201]. The derivation starts with a linear polarized light beam composed of equal amplitudes of left and right circular waves along the $\mathbf{e}_z$ direction.

$$\mathbf{E}_{\pm}(\mathbf{r},t) = \frac{1}{\sqrt{2}} E_0(\mathbf{e}_x \pm i\mathbf{e}_y) e^{i\mathbf{k}_z\cdot\mathbf{z}-i\omega t} \tag{2.65}$$

The related dielectric tensor with nondiagonal elements as a consequence of magnetism and the symmetry of $\varepsilon_{xy} = -\varepsilon_{yx}$

$$\boldsymbol{\epsilon} = \begin{pmatrix} \varepsilon_{xx} & \varepsilon_{xy} & 0 \\ -\varepsilon_{xy} & \varepsilon_{yy} & 0 \\ 0 & 0 & \varepsilon_{zz} \end{pmatrix} \tag{2.66}$$

The normal mode solutions for light parallel to the z-axis ($\mathbf{n}$=n $\cdot\mathbf{e}_z$) are:

$$n_{\pm}^2 = \varepsilon_{xx} \pm i\varepsilon_{xy} \tag{2.67}$$

Leading to the corresponding electric field modes

$$\mathbf{E}_{\pm}(r,t) = \frac{1}{\sqrt{2}} E_0(\mathbf{e}_x \pm i\mathbf{e}_y) e^{\left(i\omega\frac{\mathbf{n}_{\pm}\mathbf{z}}{c}-i\omega t\right)} \tag{2.68}$$

Setting the direction of the reflected light as the positive z-direction, the incident right-/left-circular light mode corresponds to $\mathbf{E}'_r = \mathbf{E}_-$ and $\mathbf{E}'_l = \mathbf{E}_+$. Amplitude and phase of the reflected modes are unequal due to the non-zero diagonal element ε_{xy}. The polarization of the reflected light tilts over a small angle in respect to the incident light's polarization and becomes elliptically polarized. The quotient of the two amplitudes can be expressed using the phase factor α:

$$\frac{E'_r}{E'_l} = \frac{|E'_r|}{|E'_l|} e^{i(\alpha_r-\alpha_l)} = \frac{1+n_l}{1-n_l}\frac{1-n_r}{1+n_r} \tag{2.69}$$

Using the Fresnel equation [202] expression for the reflection coefficient r

$$r_{\pm} = \frac{E'_{\pm}}{E_{\pm}} = \frac{n_{\pm}-1}{n_{\pm}+1} \tag{2.70}$$

The Kerr rotation θ_K is the angle over which the main axis of the polarization ellipse is rotated with respect to that of the incident light. The Kerr angle is then

$$\theta_K = \frac{1}{2}(\alpha_l - \alpha_r) \tag{2.71}$$

The Kerr ellipticity is the quotient of the long and short axes of the ellipse. Together with the complex amplitudes and rewriting, one gets

$$\tan\eta_K = \frac{|E'_r|-|E'_l|}{|E'_r|+|E'_l|} \quad \Rightarrow \quad \frac{|E'_r|}{|E'_l|} = \frac{1+\tan\eta_K}{1-\tan\eta_K} \tag{2.72}$$

In combination with 2.69 one gets the exact expression for PMOKE

$$\frac{1+\tan\eta_K}{1-\tan\eta_K} e^{-2i\theta_K} = \frac{1+n_l}{1-n_l}\frac{1-n_r}{1+n_r} \tag{2.73}$$

Kerr rotation and ellipticity are commonly less than 1° for most materials. The above exact expression can be approximated for small ϵ_K and θ_K by expansion to the leading order of n_r - n_l.

$$\theta_K + i\eta_K \approx i\frac{n_r - n_l}{n_r n_l - 1} \tag{2.74}$$

Substituting $n_{r,l}^2 = \varepsilon_{xx} \pm i\varepsilon_{xy}$ leads to an approximation of the Kerr angle and ellipticity depending on the permittivity and/or conductance of the material. Since the permittivity and conductivity are linked by the Maxwell equations 2.1, one can express equation 2.69 depending om permittivity and conductivity.

$$\theta_K + i\eta_K \approx \frac{-\epsilon_{xy}}{\sqrt{\epsilon_{xx}}(1-\epsilon_{xx})} = \frac{\sigma_{xy}}{\sigma_{xx}\sqrt{\left(1+\frac{4\pi i}{\omega}\sigma_{xx}\right)}} \tag{2.75}$$

On account of the Onsager relationship [203] $\sigma_{xy}(\omega, -\mathbf{B}_z) = -\sigma_{xy}(\omega.\mathbf{B}_z)$, one gets

$$\theta_K + i\eta_K \approx \frac{-\sigma_{xy}(B_z)}{\sigma_{xx}\sqrt{\left(1+\frac{4\pi i}{\omega}\sigma_{xx}\right)}} \tag{2.76}$$

In the case where the incident light impinges on the material surface at a non-normal angle of incidence β, the solution to the Fresnel equations can be expanded to first order in the off-diagonal dielectric tensor element ε_{xy}. This perturbative approach accounts for the magneto-optical effects introduced by the material's anisotropy, allowing a linear approximation of the reflected or transmitted light's polarization state due to the magnetization-induced dielectric asymmetry.

$$n_\pm^2 = \varepsilon_{xx} \pm i\varepsilon_{xy}\cos\beta \tag{2.77}$$

Using the Fresnel equation one can use its solution in first order in ε_{xy}, leading to Kerr rotation and ellipticity for s-polarized light at an angle β to be

$$\theta_K + i\eta_K \approx \frac{-\sigma_{xy}\cos\beta}{\sigma_{xx}\sqrt{\left(1+\frac{4\pi i}{\omega}\sigma_{xx}\right)}} \tag{2.78}$$

From this expression, it becomes evident that polar magneto-optical Kerr effect (PMOKE) measurements conducted at a small incidence angle β deviate from those obtained under strictly normal incidence only by terms of second order in β. Consequently, the influence of a slight angular deviation on the Kerr signal is minimal, rendering small-angle PMOKE experiments effectively equivalent to measurements at perpendicular incidence for practical purposes.

2.6 Tunnel magneto resistance

Tunnel magnetoresistance (TMR) [204, 205] is a quantum mechanical effect observed in magnetic tunnel junctions (MTJs) [206–212], where the electrical resistance of the junction depends on the relative orientation of the magnetizations of ferromagnetic layer(s) separated by an insulating barrier [211], typically made of MgO or Al_2O_3. In an MTJ, when the magnetizations of the two ferromagnetic layers are parallel, electron tunneling is more likely, resulting in low resistance. When the magnetizations are antiparallel, the tunneling probability decreases, leading to higher resistance.

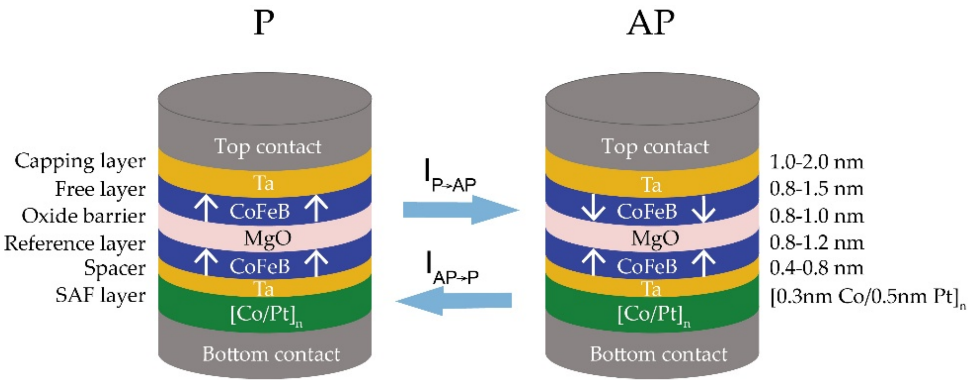

FIGURE 2.16: A magnetic tunnel junction with interfacial perpendicular magnetic anisotropy (PMA-MTJ) is composed of multiple ultrathin layers, including two ferromagnetic layers (CoFeB, blue) separated by a thin insulating barrier (MgO, lavender). Each FM layer is interfaced with a heavy metal layer (Ta, yellow) to enhance spin–orbit effects and promote efficient spin current generation. Additionally, a synthetic antiferromagnetic (SAF $[Co/Pt]_n$, green) structure is often incorporated adjacent to the reference layer to provide magnetic stability and minimize stray fields, positioned near the bottom electrode. The PMA configuration ensures that the magnetization of the ferromagnetic layers is oriented perpendicular to the plane of the layers. Magnetization switching between the parallel and antiparallel states is achieved via the spin-transfer torque (STT) mechanism. When a bidirectional current I exceeds a critical threshold current $I_{c,0}$, spin-polarized electrons transfer angular momentum to the free layer, inducing a torque that drives the magnetization reversal. This enables the PMA-MTJ to switch between high and low resistance states, corresponding to binary logic states in spintronic memory applications. Taken from [209].

The ratio between these resistance states defines the TMR ratio, which is a key performance indicator for reliably differentiating the magnetic states close to the MTJ.

TMR plays a fundamental role in spintronic devices, particularly in applications such as magnetic random-access memory (MRAM) [87], magnetic sensors [60], and read heads in hard disk drives. Its functionality arises from the spin-dependent tunneling of electrons and is strongly influenced by the spin polarization of the ferromagnetic electrodes and the quality of the tunnel barrier. High TMR ratios and thermal stability have made MTJs essential building blocks for non-volatile memory technologies and advanced logic and stochastic architectures [213–215]. Additionally, in chapter 6 hypothetical MTJs would be used for skyrmion detection and skyrmion nucleation [55, 161, 216–218].

2.7 Non-conventional computing

Non-conventional computing [219] refers to a class of computational paradigms that deviate from the traditional von Neumann architecture. Among these, machine learning (ML) plays a central role, utilizing statistical algorithms to identify patterns, extract insights, and generate predictions or novel outputs based on previously acquired data. ML is a foundational component of AI development and finds widespread applications in areas such as natural language processing, pattern recognition, facial and speech recognition, and exploratory data analysis (EDA) [220, 221]. A key subset of non-conventional computing is neuromorphic computing [58], which aims to replicate the functional principles of the human brain. This approach

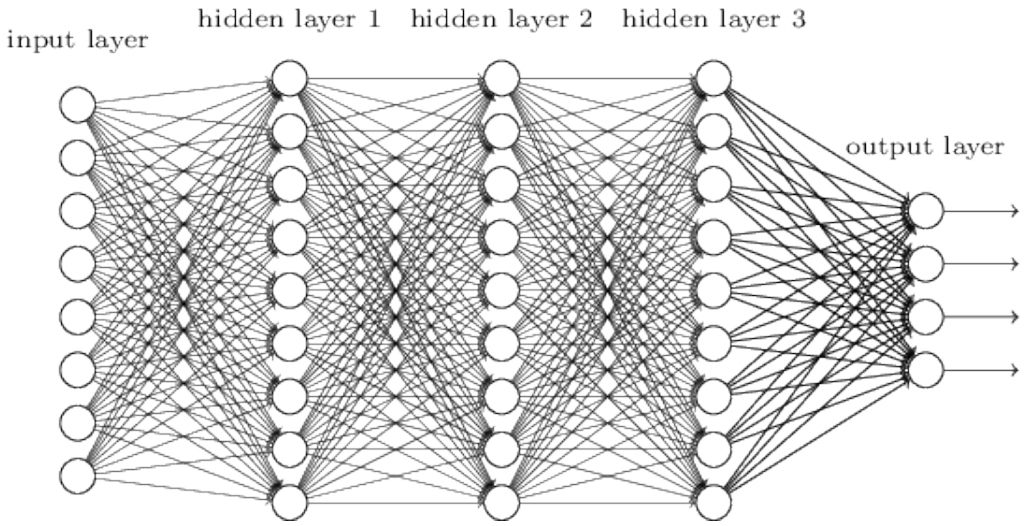

FIGURE 2.17: Neural network with the nodes (circles) of the input layers on the left, nodes of the hidden layers in between and the nodes of the output layer to the right. All nodes of one layer are connected via *synapses* (lines) to all nodes of the next layer. Taken from [223].

seeks to overcome the energy and scalability limitations of conventional computing systems. In the biological brain, neurons are interconnected through vast networks of synapses, enabling highly parallel, adaptive, and energy-efficient information processing. Although the dynamics of biological neural networks (NN) - especially spiking neural networks - remain only partially understood, ongoing research seeks to emulate these processes to develop low-power and high-performance computing systems. In this context, Chapter 6 explores the potential use of skyrmions within a specific non-conventional computing framework known as reservoir computing [222]. Prior to introducing this model, the foundational concepts of artificial neural networks are presented to establish the necessary theoretical background.

2.7.1 Artificial neural networks

Neural networks consist of interconnected nodes, equivalent to neurons in a biological brain, organized in layers that propagate signals to several nodes in the next layer [223]. The network can be tailored by modifying both the number of nodes per layer and the total number of layers. The connections can be compared to synapses in a brain and are assigned a specific weight for signal forwarding.
The layers themselves are organized in the following layers (see Figure 2.17): The input layer receives data or signals (e.g., image pixels, text components, frequency and amplitude information); the hidden layers process data and adjust weights, basically the main processing unit; and the output layer produces the final result, a classification or prediction, using the processed data of the hidden layers (e.g., whether the image shows a cat or not). Training of these networks is achieved through supervised learning with labeled datasets (e.g., image *with* or *without* cat).

Every node n_j assigns a numerical value to each incoming connection from the prior node n_i known as a weight $W_{i,j}$, while the signal itself is just a real number. The resulting value of this node is computed by a non-linear function, called the activation function, and is based on the incoming signals and the weight of the connection over which the signal was received. The non-linearity of the function allows

networks to engage nontrivial problems with a limited number of nodes. If the resulting value of this node is below a certain threshold value, no signal will be sent. If the value is above the threshold, the node will send this value as a signal forward through all connections to the neurons in the next layer. In the beginning of the training of a neural network, all weights $W_{i,j}$ are randomized, while during training, the weights and thresholds are adjusted continually. The data is passed through the layers until the training data delivers the same results, or, in other words, the prediction equals the hypothesis (e.g., the image is properly recognized with cat or not). Note that this explanation is simplified and resembles only the basic functionality.

2.7.2 Back-propagation

In NNs, back-propagation is an essential algorithm for training by minimizing the discrepancy between predicted and actual outputs [220, 224]. It operates by propagating the error from the output layer backward through the network, enabling the adjustment of synaptic weights via gradient descent, an iterative optimization method.
The training process begins with the forward pass, during which input data are propagated through the network to generate an output. This is followed by the backward pass, where the error is quantified using a predefined loss function, and the gradients of the loss with respect to each weight are computed through the application of the chain rule. These gradients guide the adjustment of weights in a direction that reduces the overall loss. Back-propagation facilitates the effective training of deep neural networks by systematically refining the network parameters. However, its iterative nature demands substantial computational resources, including energy, processing time, and specialized hardware, particularly in large-scale or real-time applications.

2.7.3 Reservoir computing

Reservoir computing (RC) is a non-conventional computing concept derived from recurrent neural networks (RNN) [222, 225–227]. A recurrent neural network processes data in multiple time steps using a special hidden layer in the form of a state memory. The state of this layer is updated each time step and is the combination of the time step's current input value and the previous state value of this layer, creating an effective feedback loop. This way the RNN can include previous input signals in the current processing. In reservoir computing, this special layer is the physical reservoir itself.

Reservoir computing uses intrinsic, non-linear dynamics of a reservoir (e.g., a physical system) to process input data and project it into high-dimensional state spaces, effectively reducing complex tasks into linear problems. The fundamental principle of RC is inserting input signals using a dynamic reservoir, a physical medium characterized by intricate internal interactions. The internal state caused by the input is mapped to the output layer and analyzed. Training all synaptic weights in an RNN is computationally and energetically expensive, while in an RC only the weights for the outputs are optimized. The reservoir itself needs to exhibit certain necessities: non-linearity, guaranteeing minor input differences cause distinguishable states; high-reproducibility, identical inputs should lead to the same output state; a reset mechanism for the reservoir state, prioritizing newer inputs over older inputs when analyzing the output state.

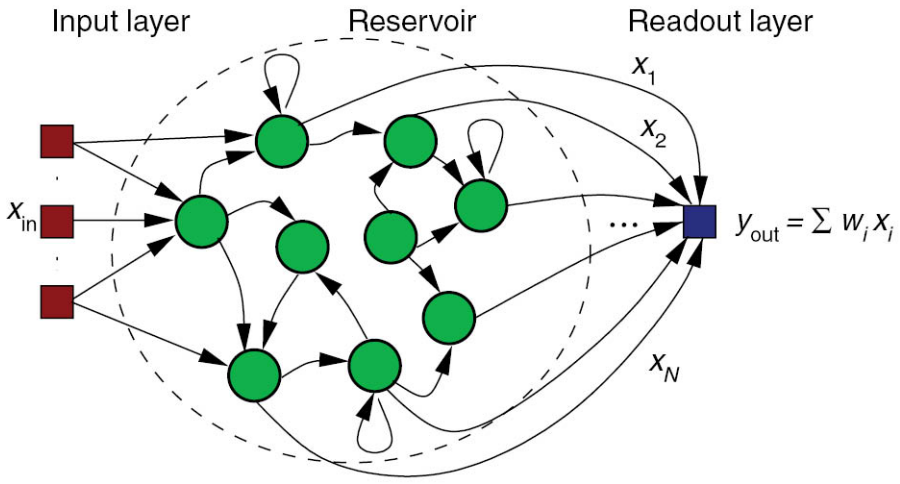

FIGURE 2.18: The concept of reservoir computing consists of an input layer (represented by red squares), a physical reservoir (depicted as a dashed circle containing green circles as nodes, analogous to the hidden layers in deep neural networks), and an output layer (blue square), with connections indicated by black arrows. Owing to the reduction of computational complexity to a linear (single) output, the resulting solution can be efficiently mapped onto the output layer. Taken from [228].

By evading back-propagation, the iterative adjustment of all weights, the main computational function of an RC, executed by the physical reservoir's internal dynamic, leads to inherently energy-efficient computation [225] and high potential for application [226].

2.7.4 Skyrmions in unconventional computing

The integration of magnetic skyrmions into non-conventional computing paradigms represents a compelling and rapidly advancing frontier in the field of information processing. Skyrmions offer a combination of topological stability and dynamic manipulability, making them particularly well-suited for a range of computational applications [113].

In recent years, skyrmions have been extensively explored as nano-scale information carriers across various computing and storage architectures. In particular, their implementation in the racetrack memory concepts has been demonstrated, where they serve as mobile data bits in energy-efficient, high-density memory systems [29, 48, 108, 163]. Additionally, their thermally driven diffusive motion has high potential in the context of Brownian computing, which exploits stochastic dynamics for computation [99, 110, 113, 152, 190, 229]. One of the most promising developments has been the application of skyrmions in reservoir computing schemes utilizing the complex, nonlinear dynamics of physical systems for data processing [56, 99, 141, 152, 230, 231]. Theoretical and computational studies have provided insights into the viability of skyrmion-based reservoirs [57, 151, 229, 231–233], and recent experimental advancements have further validated their potential through direct implementation [99, 141, 152, 227, 234]. This thesis focuses on the investigation and development of skyrmion-based triangular reservoir computing systems performing Boolean logic operations. Moreover, skyrmions have also been proposed

and utilized in a variety of other non-traditional computing approaches, underscoring their versatility and significance in the broader context of next-generation computational technologies [110, 111, 232, 235, 236].

Chapter 3

Methods

This chapter explores the fundamental experimental setups, methodologies, and fabrication processes employed to create structured samples capable of hosting skyrmions. It further details the techniques used for skyrmion measurement and visualization, as well as the additional equipment designed, developed, or utilized to ensure accurate experimental conditions. Additionally, an overview is provided of key processes for measuring critical properties such as surface roughness, temperature control, and general magnetic parameters.

3.1 Physical vapor deposition

Modern microchips are fabricated from thin, multilayered material systems deposited onto substrates, incorporating a wide array of functional materials and nanoscale architectures [237]. This structural configuration facilitates the high-density integration of electronic components—such as integrated circuits—within limited spatial dimensions, thereby supporting a broad spectrum of electronic functionalities and beyond [238]. The formation of these thin-film structures primarily relies on physical vapor deposition (PVD) techniques [239–241], which offer precise control over film thickness, uniformity, and chemical composition, in conjunction with lithographic patterning methods [242] essential for defining nanoscale features and device architectures.

PVD is based on the fundamental process of vaporizing a target material within a vacuum chamber, followed by the transport of the vapor phase species to a substrate, where condensation, nucleation, and film growth occur. This process not only yields coherent thin films but can also lead to significant alterations in the deposited material's morphology, crystallinity, and functional properties. A variety of PVD techniques are employed depending on the target material [243], desired film characteristics, and application-specific requirements. These methods include ablation-based approaches such as pulsed laser deposition (PLD), and thermal-based processes such as pulsed or continuous electron beam evaporation, thermal laser epitaxy, cathodic arc deposition, and conventional thermal evaporation. The films are typically deposited onto planar substrates, referred to as wafers, which serve as the foundational platform for thin-film deposition and subsequent device fabrication.

Wafers are commonly fabricated from materials such as e.g., crystalline silicon (Si), fused silica, silicon carbide (SiC), sapphire (Al_2O_4), Gallium arsenide (GaAs), indium phosphite, or aluminum nitride (AlN) [244]. The choice of substrate material is dictated by considerations including lattice parameter matching, thermal expansion compatibility, optical transparency, electronic properties (e.g., high carrier mobility for high-frequency applications), and economic factors such as cost and availability [244, 245]. Wafer thicknesses are application-dependent, ranging

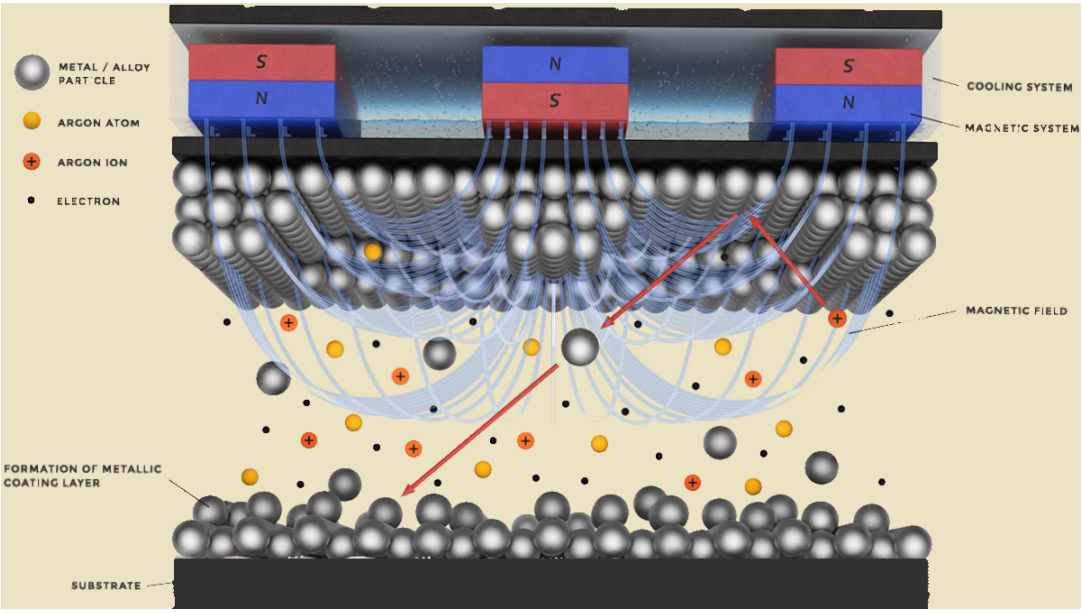

FIGURE 3.1: Scheme of the PVG process of magnetron sputtering. Argon atoms (yellow) get ionized (orange) by the combined effect of electric and magnetic fields, get accelerated and forced onto the target cathode. By elastic and inelastic scattering, the argon ions can punch out single atoms of the target material, which gets vaporized and condensates onto a substrate. Adapted from [248].

from ultra-thin membrane-like structures to several millimeters, with a commonly employed standard of approximately 0.5 mm.

These substrates are integral to the advancement of modern microelectronic and optoelectronic devices, underpinning the fabrication of integrated circuits, sensors, photonic components, and magnetoelectric systems. The thin-film samples used in this study were fabricated via magnetron sputtering deposition, a plasma-based coating and layering technique, within an ultra-high vacuum (UHV) deposition system. Magnetron sputtering employs an inert noble gas, such as argon or xenon, at low pressure, which is ionized into plasma through interactions with applied electric and magnetic fields. After the ionization process, the ions are accelerated towards the cathode, also known as the target electrode, which leads to intense scattering processes between gas atoms and the target material, facilitating material ejection and deposition onto a substrate. During sputtering, an electric field is applied between the substrate (anode) and the target material (cathode), causing ionization of the inert gas and subsequent acceleration of its ions toward the target. A toroidal magnetic field is introduced parallel to the target, increasing plasma density and enhancing the ionization rate at the target surface and gas-target collisions, raising the sputtering efficiency.

When the accelerated gas atoms bombard the target, they penetrate the surface, inducing collision cascades within the material. If sufficient energy is transferred, atoms at the target surface overcome their atomic bonds and are ejected. These ejected atoms then travel toward the substrate, where they condense and form a thin film. The motion of these atoms varies between high-energy ballistic trajectories and lower-energy thermal diffusion, with their behavior influenced by adjustments to inert gas pressure and flow rate [246, 247]. A schematic of the UHV chamber illustrating the magnetron sputtering process is shown in Figure (3.1).

Since the sputtering process generates substantial heat, the target material must

be actively cooled to prevent thermal degradation or dissolution. Magnetron sputtering techniques can be categorized into direct current (DC) sputtering, suitable for conductive target materials, or radio frequency (RF) sputtering, which allows for deposition from non-conductive targets [249, 250]. For optimal momentum transfer and efficient sputtering, the atomic mass of the inert gas should closely match that of the target material - for instance, neon for lighter elements and krypton for heavier elements [239, 241, 251].

3.1.1 Thin film growth

The deposition of material onto the substrate results in the accumulation of atoms, allowing for the controlled growth of thin films to a specific layer thickness. This thickness is primarily determined empirically based on the sputtering rate, the number of atoms reaching the substrate per unit time. However, the way in which material accumulates is a complex process, influenced primarily by inert gas pressure and flow, temperature and sputtering rate [239, 241, 246, 247]. Upon reaching the substrate, each atom seeks the most energetically favorable position to establish a crystallographic bond, which can lead to surface diffusion before its final spot is found. This diffusion process can result in the rather unwanted formation of small atomic islands (e.g., a dusting layer; see below) or the preferential development of a homogeneous, continuous thin film, where vacancies between larger islands are gradually filled by incoming or diffusing atoms. Imperfections in atomic accumulation can lead to structural inhomogeneities, such as crystal polymorphism, in which different crystal orientations form within the same material, allotropic variations, where the same material adopts distinct structural or electronic properties, or impurities or doping effects, introduced by the incorporation of foreign atoms. These variations potentially modify the sample's energy landscape, introducing challenges in achieving consistent thin film properties across multiple depositions.
A specific example relevant to this study is the ultra-thin *dusting layer* of tantalum ($<$100 pm) inserted between the ferromagnetic CoFeB layer and the insulating MgO layer. This dusting layer plays a crucial role in modulating the interface [252–254], especially the magnetic anisotropy, thereby promoting the mobility of skyrmions. However, the term *dusting layer* can be misleading, as the covalent radius of tantalum ($\approx$ 138 pm) exceeds the nominal layer thickness. Given the short sputtering duration required to achieve such a layer, it is more plausible that the tantalum forms semi-homogeneously distributed atomic islands rather than a uniform atomic monolayer. In multilayer thin films, the interfacial growth dynamics play an important role in determining the material properties. Parameters such as surface energy [255], lattice mismatch [256, 257], and deposition conditions [239, 246, 247] influence how layers form atop one another. To further modify or stabilize film properties, a post-deposition heat treatment known as thermal annealing can be applied. During thermal annealing, the sample is heated over a specified period, promoting interfacial diffusion between layers, leading to intermixing, vacancy reduction, improving film uniformity, and stress relaxation, mitigating internal strain introduced during sputtering. For example, in CoFeB-based films, boron diffusion into the thicker tantalum layer during annealing alters the magnetic anisotropy [258], further influencing skyrmion behavior and film stability. Since the effects of annealing cannot directly be controlled, the samples in this thesis have not been thermally annealed, and any extensive heat exposure over extended periods of time has been avoided.

3.1.2 Ferromagnetic thin films

The ferromagnetic thin-film samples analyzed in this study were provided by AG Kläuis group alumni (*censored name*) (sample identifier MVK), PhD candidates F. Kammerbauer (sample identifier FAB) and D. Tran (sample identifier TMD). These samples were fabricated using a Singulus Rotaris deposition system [259] at the Institute of Physics, Johannes Gutenberg University Mainz, Germany, a system capable of processing industrial-scale wafers up to 200 mm in diameter. Prior to the fabrication of FAB629, an extensive optimization process was conducted to achieve the desired magnetic properties, such as thermally diffusive skyrmions and dense skyrmion lattices near ambient temperatures. This optimization involved systematic adjustments and fine-tuning of key deposition parameters, including sputtering conditions (e.g., power, pressure, deposition rate), film thicknesses, and post-deposition thermal annealing treatments [258]. Each iteration was visually analyzed by PMOKE to assess its skyrmionic properties, ensuring that the final sample exhibits the preferred magnetic properties. Table A.3 in appendix A shows the characterization of diffusive skyrmion samples. The three main samples used for this thesis:

MVK763	Ta (5.7) | Pt (3.4) | $Co_{60}Fe_{20}B_{20}$ (0.8) | MgO (1.4) | Ta (5)
FAB629	Ta (5) | $Co_{20}Fe_{60}B_{20}$ (0.95) | Ta (0.09) | MgO (2) | Ta (5)
TMD109	Ta (3) | $Co_{20}Fe_{60}B_{20}$ (0.95) | Ta (0.08) | MgO (2) | Ta (5)

In the provided material stacks, numerical values in parentheses indicate the thickness of material layers in nanometers, while subscripted numbers denote the stoichiometric composition in percentages. For example, the CoFeB layer consists of 60% iron, 20% cobalt, and 20% boron. A review of the relevant energy terms discussed in Chapter 2 may be beneficial for the following sections. The initial tantalum (Ta) layer is deposited onto the thermally oxidized SiO_2 surface of the wafer substrate, where it forms a polycrystalline structure, likely comprising the β phase [260], the α phase, or a mixture of both [261]. This layer serves as a seed layer, providing a smooth surface for the subsequent growth of other layers. Additionally, as a heavy metal, it plays a crucial role in introducing spin-orbit torques (SOTs) into the ferromagnetic CoFeB layer, which facilitates spin current-driven magnetization dynamics. The thickness of the CoFeB layer is a critical parameter influencing the magnetic properties [136, 258], as increased thickness reduces the perpendicular magnetic anisotropy [262], resulting in a preferential alignment of spins within the plane rather than out-of-plane. Furthermore, the interfaces between CoFeB and Ta significantly affect the structural and magnetic characteristics of the stack [263], contributing to modifications in anisotropy and overall magnetic behavior. In the MVK763 sample, platinum (Pt) replaces Ta as the heavy metal layer, enhancing the spin-orbit torque effect. The interface between the heavy metal layer and the ferromagnetic alloy generates DMI, which is essential for stabilizing chiral magnetic textures, such as skyrmions.
At the interface between MgO and CoFeB, PMA is induced [168, 253, 254, 262, 264]. To fine-tune the PMA and optimize the skyrmionic properties, a dusting layer of tantalum is introduced between CoFeB and MgO. It is important to note that the dusting layer thickness is a statistical value derived from the sputtering process rather than a uniform atomic monolayer. Beyond spin-orbit torques, additional interfacial effects influence the system. At the CoFeB/heavy metal interface, REE emerge due to electric fields. Similarly, at the CoFeB/MgO interface, a Rashba-type DMI arises due to charge transfer effects, leading to the formation of an interfacial

electric dipole between the ferromagnetic layer and oxygen atoms.
To prevent oxidation of the underlying layers, a 5 nm tantalum capping layer is added. Intermixing at the layer interfaces significantly modifies magnetic properties and can be influenced by thermal annealing or aging effects such as stress relaxation. For instance, boron from the CoFeB layer can diffuse into the adjacent Ta layer, altering the magnetic anisotropy [258, 262]. To mitigate oxidation at the samples edges and aging effects, the samples are stored in desiccators under vacuum which are flooded with nitrogen during opening.

Table A.3 in Appendix A presents a characterization of samples in the optimization process, including proper skyrmionic phases observed at four different temperatures. Sample FAB629, a wafer regrowth of diffusive skyrmion stacks, and TMD109 were deposited on a 500 µm thick silicon wafer, which can be cut using a diamond cutter and further divided into smaller pieces (typically 10 × 10 mm or 7 × 7 mm) for compatibility with the Kerr microscope sample holders. Lastly, the skyrmions observed in this study exhibit a negligible skyrmion Hall effect at the current densities employed, making them suitable for precise transport and manipulation experiments.

3.2 Lithography and structuring

The observation of skyrmions in confined spaces is essential for the upcoming chapters in this thesis and requires the transformation of uniformly layered thin film samples into structured samples with functional geometries. In this section, lithography, the process of structuring a sample, is introduced, as well as the necessary methods explained [242, 265, 266].

3.2.1 Cleanroom and cleaning procedures

To ensure that during the lithography process the sample surface is not compromised by airborne particles, the whole process is performed in cleanrooms. Cleanrooms are classified in ISO values by the amount of airborne particles above certain sizes. The cleanroom used for lithographic processes in the AG Kläui group is classified as ISO 5 (Class 100 according to the U.S. Federal Standard), with particle concentrations of 0.5 µm-sized particles maintained below 3,500 per cubic meter [267]. To limit the amount of airborne particles, a special high efficiency particulate air (HEPA) filtration system catch airborne particles or microbes, while a constant laminar stream of filtered air pushes potential remaining particles down onto the ground. A slight overpressure inside keeps polluted air out when a door to the sluice is opened. Anti-static suits, gloves, and facial protection must be worn by the operators to prevent pollution or potential electrostatic discharge (ESD). Handling samples and other tools can be transported through a special sluice. The lighting in cleanrooms for microfabrication can be switched to a reduced spectrum of visible light without short wavelengths (e.g., violet, blue, and greenish light), resulting in perceived yellow light. This is necessary since resin-based resists utilized in the lithographic processes can be UV sensitive, and exposure to white light would alter the chemical structure of said resist. More details on the cleanroom environment in appendix A section A.3.

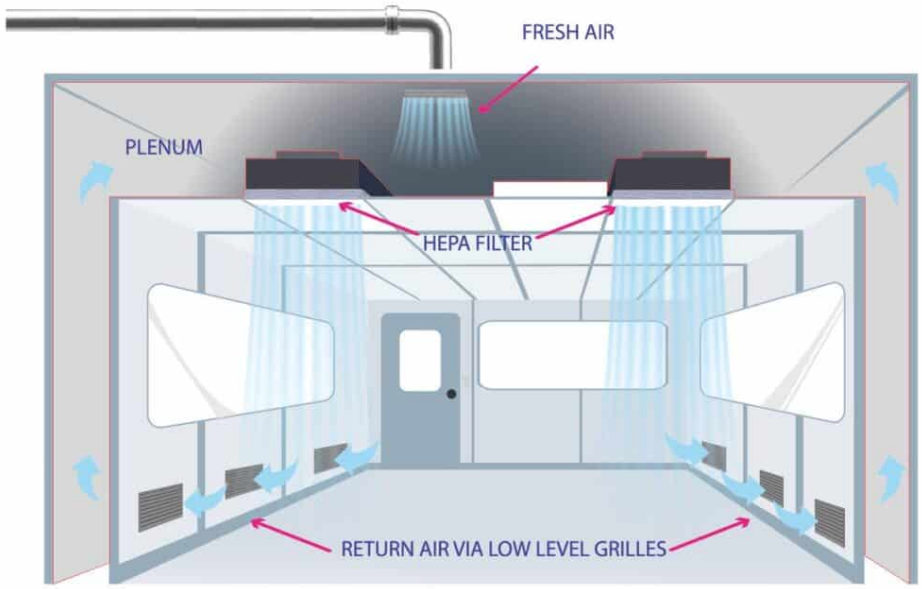

FIGURE 3.2: Scheme of a cleanroom with laminar flow to prevent airborne particle pollution. Filtered air is equally distributed into laminar flows and gets vacuumed at the bottom part. Taken from [268].

Sample cleaning prior lithography

Prior to lithographic processing, samples must be thoroughly cleaned to eliminate surface contaminants such as dust particles, organic residues (e.g., carbohydrates), and remnants from wire bonding or adhesives. The standard cleaning protocol involves sequential solvent exposure, beginning with a puddle rinse followed by immersion of the sample in acetone (2-propanone) and isopropanol (2-propanol), each for a duration of one minute, using clean glassware or compatible beakers. This is followed by a rinse with de-ionized (DI) water to remove residual solvents. If surface contamination persists, the sample-containing beaker can be placed in an ultrasonic bath. The ultrasonic agitation induces alternating high- and low-pressure waves that generate cavitation bubbles. The implosion of these bubbles produces localized mechanical forces that aid in dislodging and removing residual particles and films from the surface. Following the cleaning steps, the sample is briefly heated on a hotplate at a temperature not exceeding 85°C - lower than the standard post-bake temperature of 120°C - for approximately one minute. This step ensures the evaporation of any remaining deionized water, preventing moisture-induced issues in subsequent lithography steps.

3.2.2 Lithography process

Lithography involves the application of a thin resist layer [269, 270], whose chemical properties can be selectively modified by exposure to ultraviolet (UV) light [242, 271–273] or high-energy electrons, as in electron beam lithography (EBL) [265, 266]. The resist is deposited onto the sample through spin coating, a method that ensures uniform thickness. The sample is placed on a vacuum-suction spin-coater holder inside a closed chamber to maintain cleanliness, and a liquid resist is applied onto the sample surface. The holder spins at a controlled rotational speed and acceleration, spreading the resist into a thin layer via centrifugal forces. The thickness of the

resist layer depends on spin parameters (speed, acceleration, duration) and resist viscosity, as specified by the manufacturer. Note that due to surface tension at the sample's edge, the resist can bulge, resulting in a slightly thicker layer. The coated sample undergoes soft baking to evaporate residual solvents and harden the resist. For EBL processing, an additional conductive coating may be required since most resists are insulating and could cause electron accumulation during scanning electron microscopy (SEM) or EBL, leading to image distortions during SEM or diversion of the electron beam. The silicon (Si) substrate wafers [245, 274], functioning as semiconductors, can exhibit electrical conductivity through controlled doping processes. It is important to note that the wafers employed in this study have undergone thermal oxidation, resulting in the formation of an insulating silicon dioxide (SiO_2) layer on their surface [275].
A mask or a focused electron beam is used to selectively expose certain regions of the resist layer, altering its chemical composition. After exposure, the resist is processed with developer solutions, which dissolve either the exposed or unexposed areas, depending on the type of lithography. In positive lithography, the exposed resist is dissolved, leaving open spaces where material can be sputtered or deposited, while in negative lithography, the unexposed resist is dissolved, exposing the underlying material for etching (chemically or physically).

3.2.3 Etching and lift-off technique

In positive lithography, new material is sputtered onto both the exposed substrate and the remaining resist layer. Upon dissolving the resist, the material on top of it lifts off, leaving behind the deposited structures in the developed areas—known as the lift-off process. In negative lithography, the exposed resist acts as a protective layer, allowing material removal (etching) from the developed areas. After etching, the remaining resist is removed (e.g., with acetone), revealing the structured material beneath.

The combination of positive and negative lithography techniques enables the fabrication of samples with structures, such as fine lines, channels, and complex planar geometries, by selectively removing material layers. Beyond 2D structuring, these techniques facilitate the construction of 3D functional architectures through the controlled stacking of additional material layers. Such advancements form the technological foundation of the microchip industry, allowing for the continuous miniaturization of functional components, which has driven the exponential improvement in semiconductor performance. As outlined previously, the reduction in functional structure size not only increases computational efficiency and density per unit area but also introduces challenges, such as higher power densities and associated thermal management issues. The sustained Moore's Law, which predicted an exponential increase in computational performance, has been primarily attributed to advancements in lithography techniques and hardware as well as the adoption of multi-core architectures in processors. The beam width in electron beam lithography (EBL) systems equipped with modern electron optics is fundamentally limited by optical aberrations and space charge accumulation [277–279]. However, the ultimate resolution is predominantly constrained by forward scattering of electrons within the resist and the generation of secondary electrons, both of which define the minimum achievable feature size (see Figure 3.5) [280]. Enhanced resolution can be attained by using thinner resist layers or by increasing the electron beam energy, thereby reducing secondary electron scattering.

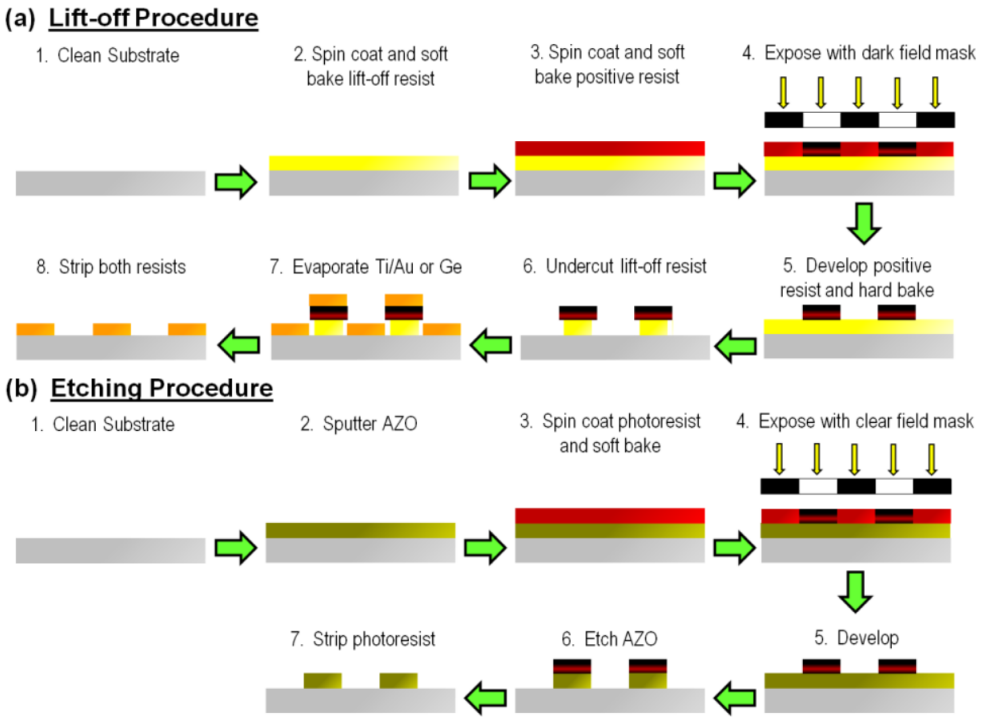

FIGURE 3.3: Sketch of the standard (negative) and lift-off (positive) lithography process with arrows (green) in procedural order. Photoresist (yellow and red) is coated onto the samples and soft-baked. Selective exposure by UV with masking or e-beam for both procedures (Step 5). Development to remove (a) unexposed or (b) exposed resist. a) Material (orange) sputtering and lift-off for structuring. b) Etching and resist removal for structuring in the etching procedure. Taken from [276].

In contrast to optical or ultraviolet lithography, where entire wafers or large write fields are exposed simultaneously, EBL operates via serial exposure of individual features. This results in significantly longer exposure times, making the technique impractical for high-throughput wafer-scale production. Furthermore, precise alignment - referred to as stitching - is critical, particularly when writing features across adjacent write-field boundaries, which was avoided during this thesis Beam current is measured using a Faraday cup, where the electron beam is directed into the conductive enclosure. The measured current is then used to determine the appropriate step size, dwell time, and beam scanning speed required to deliver the resist-specific electron dose (3.1).

$$D \cdot A = T \cdot I \tag{3.1}$$

with D, the dose [C/cm^2], A, the area to be exposed [cm^2], T, the time to expose the area [s] (which can also be expressed as exposure time/step size), and I the beam current [A].

To overcome the time limitations of EBL and resolution limitations of near UV lithography, deep ultraviolet (DUV) and extreme ultraviolet (EUV/xUV) lithography have been implemented in semiconductor fabrication [281], enabling the production of increasingly smaller features [271–273]. The transition to shorter wavelengths (Beyond UV, BUV) necessitated the replacement of lenses with high-precision mirrors, improving beam focusing capabilities. This evolution has culminated in the development of sub-3 nm fabrication processes, where the

smallest functional structures reach single-digit nm in size [281, 282].

3.2.4 Process optimization

For the fabrication of samples FAB629 and TMD109, a modified lithography protocol was employed, building upon the standard procedures established in the AG Kläui group for patterning structures larger than 10 nm. The original processing methods, detailed in appendix A, were observed to induce unintentional annealing effects due to prolonged thermal exposure during structuring. These effects can lead to a reduction in magnetic anisotropy and enhanced interfacial intermixing [253, 258, 262], likely accompanied by increases in grain size and improved crystallographic ordering . As a result, shifts in the skyrmion phase stability window were observed, and in some instances, skyrmion formation was completely suppressed within the typical temperature range of 300 K to 340 K and OOP magnetic field range of –1 mT to 1 mT.
To mitigate these thermally induced alterations, the lithography protocol was refined by optimizing process parameters. These included a reduction in electron beam exposure time, the introduction of cooling intervals during etching and additional sputtering steps, and the adjustment of the soft-bake temperature exposure to minimize cumulative thermal load while ensuring effective solvent removal. Lithography process adjustments:

1. Cleaning and preparation - Nitrogen blow drying followed by a 30-second heat treatment at $85°C$ was found to be sufficient for water desorption during the cleaning step.
2. Negative Lithography with E-Beam Resist - Spin-coating of AR-N-7520.17 (.17 indicates 17% AR-N-7520 in solution) [283] with soft-bake process at $85°C$ for one minute, which remained unchanged from the standard recipe
3. Lift-Off Lithography with MMA and PMMA [284] - An optimized soft-bake at $85°C$ for 150 seconds was determined to be sufficient for solvent evaporation, ensuring a resist viscosity suitable for EBL. The original soft-bake process of $180°C$ for 90 seconds for both MMA (methyl methacrylate) and PMMA (polymethyl methacrylate) was adjusted.

These process modifications minimized thermal exposure on the samples during fabrication, preserving the desired magnetic properties and skyrmion phase stability.

3.2.5 Electron beam lithography (EBL)

Electron beam lithography (EBL) is a high-resolution patterning technique that utilizes a focused beam of accelerated electrons to modify the molecular structure of a resist through inelastic electron scattering. The primary advantage of EBL over conventional optical lithography (e.g., UV exposure) lies in its superior resolution, which is fundamentally limited by electron scattering within the resist rather than diffraction constraints. However, the exposure process of the resist is influenced by secondary electron scattering, leading to an unwanted broadening of the exposed area - an effect known as proximity effect [285, 286].
Unlike photolithography, where an entire wafer is exposed at once using a mask and ultraviolet light, EBL requires serial exposure by scanning the electron beam over the designated regions. This inherently results in significantly longer exposure

times, particularly for large-area patterns, due to the necessity of beam movement across the sample (see 3.1). The exposure dose is typically expressed in terms of energy per unit area (mJ/cm^2) and is substantially different from the power-based process used in UV lithography (mW/cm^2).

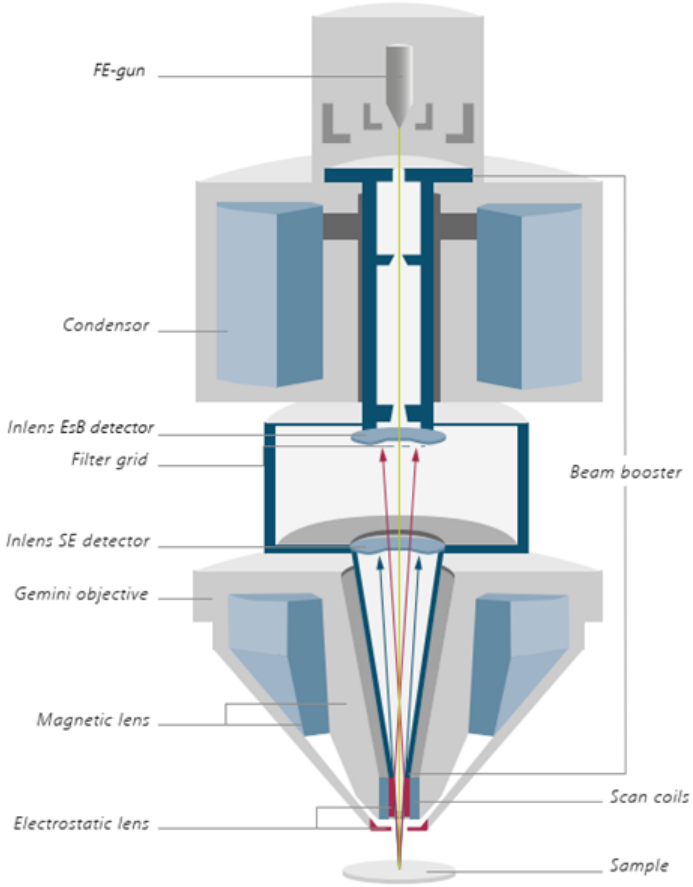

FIGURE 3.4: Schematic of an electron gun with beam booster, allowing to focus the electron beam and detect the reflected electrons from the sample as an scanning electron microscope. Detection can take place with the Inlens SE detector (secondary electron) or the Inlens EsB detector (energy selective backscattering). Taken from [287].

Even though slow, the key advantage of EBL is its maskless operation, which allows for flexible and rapid prototyping of nano-scale designs. In this work, sample layouts were generated using the EBL system's proprietary PIONEER software [287]. The lithography process is conducted in a high-vacuum chamber, where sensitivity to external electric and magnetic fields necessitates environmental shielding. In the laboratory Helmholtz coils spanning the room are employed to nullify residual magnetic fields, ensuring stable beam positioning. The sample, coated with electron-sensitive resist, is mounted within a conductive holder equipped with a grounding clamp to prevent charge accumulation. Prior to exposure, the electron beam system needs to undergo focusing and calibration of the SEM and EBL apertures.

The alignment of the design layout with the sample's reference markers is critical for accurate pattern transfer. Exposure is performed in discrete regions called writing fields, typically measuring 1×1 mm^2. To maintain pattern fidelity, features spanning multiple writing fields require precise alignment to avoid stitching errors

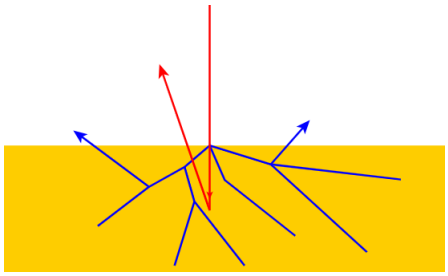

FIGURE 3.5: Primary electron scattering (red) and secondary electron scattering (blue) in resist (yellow). The secondary electrons can also expose out of bounds resist, an effect known as proximity effect. Taken from [288].

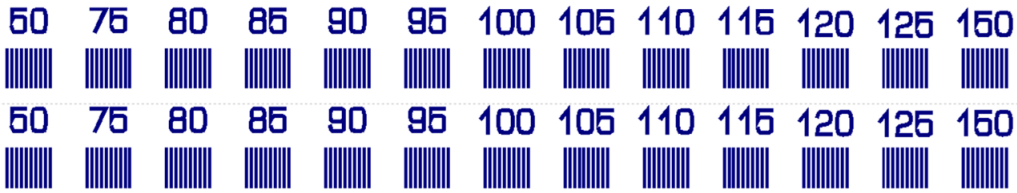

FIGURE 3.6: The PIONEER layout featuring fine lines was employed for electron beam dose testing. Insufficient doses can lead to underexposure of the resist, resulting in partial or complete removal of the exposed resist during development, which in turn can cause unintended etching of the target structure. Conversely, excessive doses increase the proximity effect, leading to overexposure of the resist. This may result in incomplete development, causing excessive masking during ion etching (see [286]). Such effects can manifest as rounded edges in the etched structures or, in the case of narrow nano-scale gaps, residual material bridging adjacent features. The structural labels indicate the applied electron beam dose as a percentage of the nominal reference dose (28 $\mu C/cm^2$).

at field boundaries. In this study, all structures were confined within single writing fields to eliminate such complications. Following the first EBL step, development, etching and cleaning, the second spin coating and EBL exposure, a lift-off process, was employed to establish the spaces for added material sputtering for electrical connections between the patterned structures and then larger contact pads. Proper alignment during exposure is crucial to ensure connectivity between these elements. Specialized alignment markers, positioned at strategic locations on each corner of write fields, aiding in proper structural overlap, and on the outer corners of the sample for calibration, alignment, and prevention of unintended exposure of the resist. Additionally, these markers can help account for resist bulging at sample edges. To optimize exposure parameters, dose tests were conducted, allowing for qualitative evaluation of dosage needs desired for sharp edge and corner quality. A representative dose test is presented in Figure 3.6.
This methodology ensures high-resolution, reproducible nano-structures with precise alignment, demonstrating the efficacy of EBL for advanced micro- and nano-scale fabrication. As an example, in Figure 3.7 typical EBL layouts are presented. More layouts can be found in Section A.10.

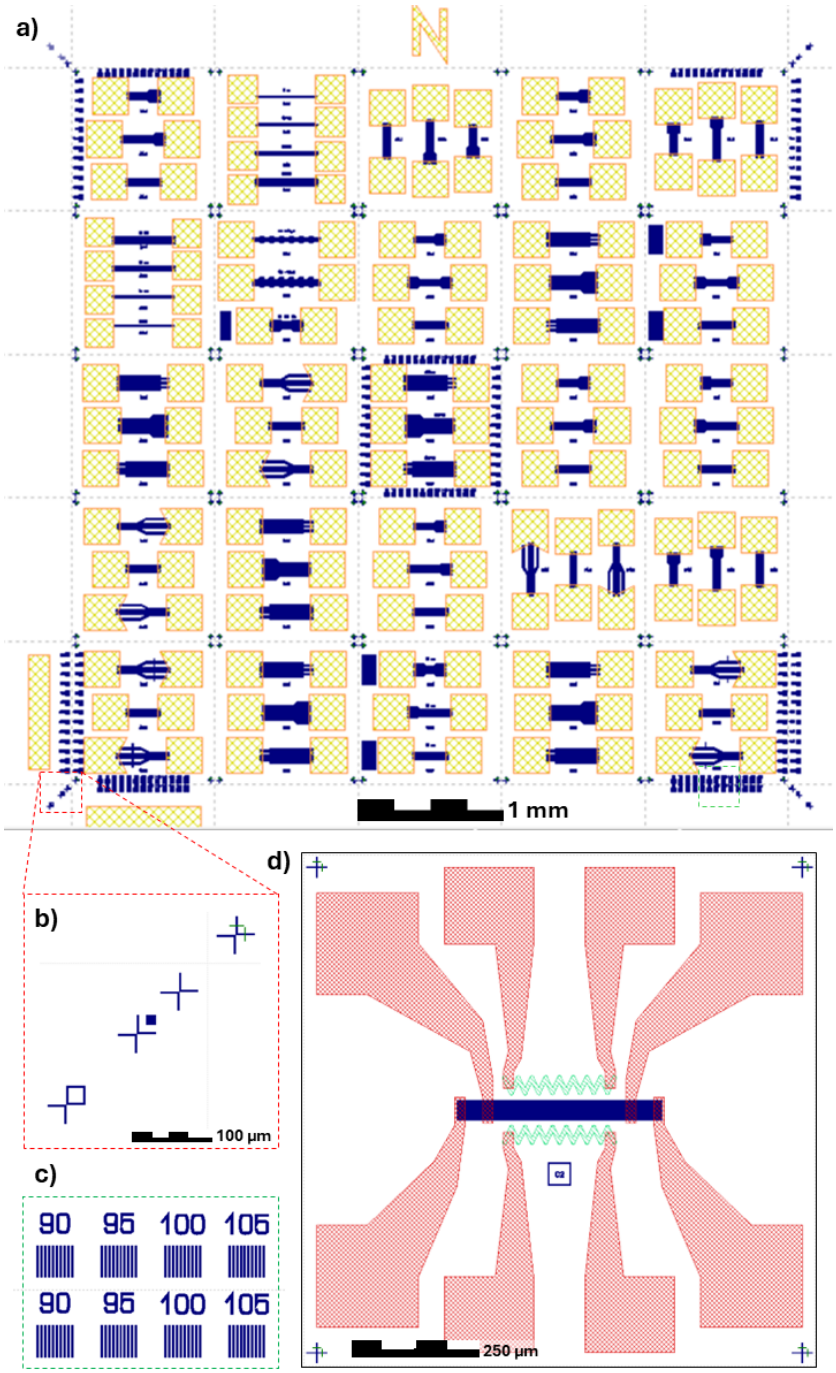

FIGURE 3.7: PIONEER layout examples. a) Full sample layout designed for skyrmion compression studies on a 7×7 mm^2 work field, incorporating a 5×5 array of write fields. Blue regions indicate thin film stack after etching, while hatched yellow areas are Cr/Au pads. Gold markers - bars in the lower-left corner and an *N* in the upper region - serve as visual aids for sample orientation. b) Individual alignment markers are positioned in the corners outside the write fields (dashed red box) to facilitate coarse alignment without accidental exposure. c) Magnified view of a dose test region corresponding to Figure 3.6. The dashed green box highlights the selected area, which includes additional dose test structures located in both the corners and central write field of panel a). d) Single 1×1 mm^2 write field used for skyrmion-based temperature gradient measurements. Red-shaded areas represent gold pads, blue to the stack, and turquoise a resistive heating structure. Some alignment marker feature automatic alignment recognition (green).

3.2.6 Ion etching

Between the negative lithography step, during which structures are defined within the resist, and the subsequent positive lithography step used to define contact pad areas, it is necessary to remove both the excess resist and any unwanted surrounding material. In negative (positive) lithography, non-exposed (exposed) resist is selectively dissolved during the development process using a chemical developer that specifically targets and removes non-exposed (exposed) resist.
Metallic material removal is achieved via ion beam etching, which employs an argon plasma to bombard the sample within a vacuum chamber, enabling controlled, layer-by-layer material ablation. For uniform etching, the sample is mounted on a cooled, rotating stage. While the incidence angle of the plasma can be adjusted by tilting the stage, a standard perpendicular (normal incidence) configuration was used in this work. Following development, the remaining resist acts as a hard mask, protecting underlying regions from ion bombardment. The fidelity of this masking layer is highly dependent on the quality of EBL exposure and development. Underexposure increases the risk of overdevelopment, which dissolves the underexposed resist too much during development and may lead to unintended etching of the protected features. Conversely, overexposure coupled with insufficient development can leave excessive resist on the sample, hindering complete material removal. These effects may result in irregular feature edges or even the persistence of unetched regions, thereby degrading the pattern transfer fidelity [285, 286].
The precision of development and etching was especially critical in this study for fine structures and edge definition (see Figures 3.6 and 3.7). This was particularly relevant for geometries such as triangular confinements and their extensions, which were designed to enable efficient electrical contact (see Chapter 6). Furthermore, the comb-like structure played a dual role: ensuring robust electrical connectivity and serving as an effective skyrmion barrier, as discussed in Chapter 5.
Based on manufacturer-supplied and empirical parameters like etch rates for the constituent materials, the etching duration for sample FAB629 was estimated at 93 seconds. To ensure complete removal of residual conductive layers, the etch time was extended to 120 seconds, reaching the thermally oxidized substrate layer. To mitigate potential thermal effects, etching was performed in 30-second intervals interspersed with 60-second cooling periods under closed-shutter conditions. For a list of all standard parameters see Section A.5.

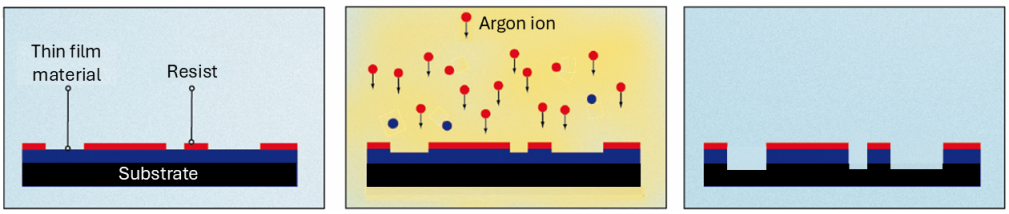

FIGURE 3.8: Ion etching on a sample with resist in red and thin film stack in blue on substrate in black. Noble gas plasma (here argon) is accelerated towards the sample, bombarding and ablating material, which is not protected by resist. This process is essential for negative lithography. Adapted from [289]

For more precise etch control, endpoint detection techniques - capable of real-time monitoring of the plasma composition and etched material - may be employed

to determine the exact moment when the desired layer is fully removed. For additional accuracy of etch rates, the thickness was measurements using x-ray reflectometry (XRR) by AG Kläui alumni. Following ion etching, the residual resist is often thermally degraded, making its removal more challenging. Complete removal typically requires multiple cleaning steps, including acetone rinses and ultrasonic bath treatment, to ensure the surface is fully cleared and ready for subsequent lithography.

3.2.7 Electric contact sputtering

To establish electrical connectivity to the fabricated structures, conductive contact pads were deposited following the second EBL step. During development, the exposed MMA/PMMA resist [284] was selectively dissolved by the developer, creating defined openings for subsequent metal deposition.

DC magnetron sputtering was then performed in a dedicated vacuum chamber. A 5 nm chromium adhesion layer was first deposited to promote strong adhesion to the substrate [290], followed by the deposition of a gold layer ranging from 30 to 60 nm, depending on the sample. As with the negative lithography and etching steps, the quality of EBL exposure and development critically influenced the definition of the pad edges and corners. During deposition, the Cr/Au layers were deposited both within the patterned pad regions and on top of the unexposed resist. The unwanted metal layers were subsequently removed through a lift-off process. This process involved puddle soaking, the submersion of the sample in a beaker with acetone, and, when necessary, ultrasonic bath treatment. Ultrasonic agitation generates cavitation bubbles that implode, producing localized mechanical forces that aid in dislodging the resist and the metal layer deposited on top of it. This ensures that only the metal within the predefined developed regions remains, thereby preserving the intended geometry of the contact pads.
Effective lift-off requires complete resist removal to avoid residual contamination that may impair electrical contact. In particular, proper overlap and edge contact between the Cr/Au contact pads and the underlying thin film structure is essential to ensure reliable electrical connection across all layers, especially at the edges of the stack. To minimize thermal effects during the sputtering process, deposition was performed in 30-second intervals, interspersed with 90-second cooling breaks. As only the cathodes in the sputtering system were actively cooled, passive cooling was achieved via thermal conduction through the sample holder. Gold, due to its excellent malleability and conductivity, is well suited for wire bonding. In this process, an aluminum wire is ultrasonically bonded to the gold surface, forming a robust and low-resistance electrical connection between the on-chip devices and external leads or contact pads.

3.3 Kerr microscope set-up

The experimental setup utilized in this study for the visualization of skyrmions in magnetic thin-film samples is a wide-field Kerr microscope, specifically a commercially available Zeiss AX10, which has been modified by Evico Magnetics GmbH to enable different MOKE analysis (see Figure **??**). Depending on the selected magnification and objective lens, the system can visualize sample areas ranging from millimeter-scale regions down to structures or objects as small as a few hundred nanometers when using the highest magnification (100× objective).

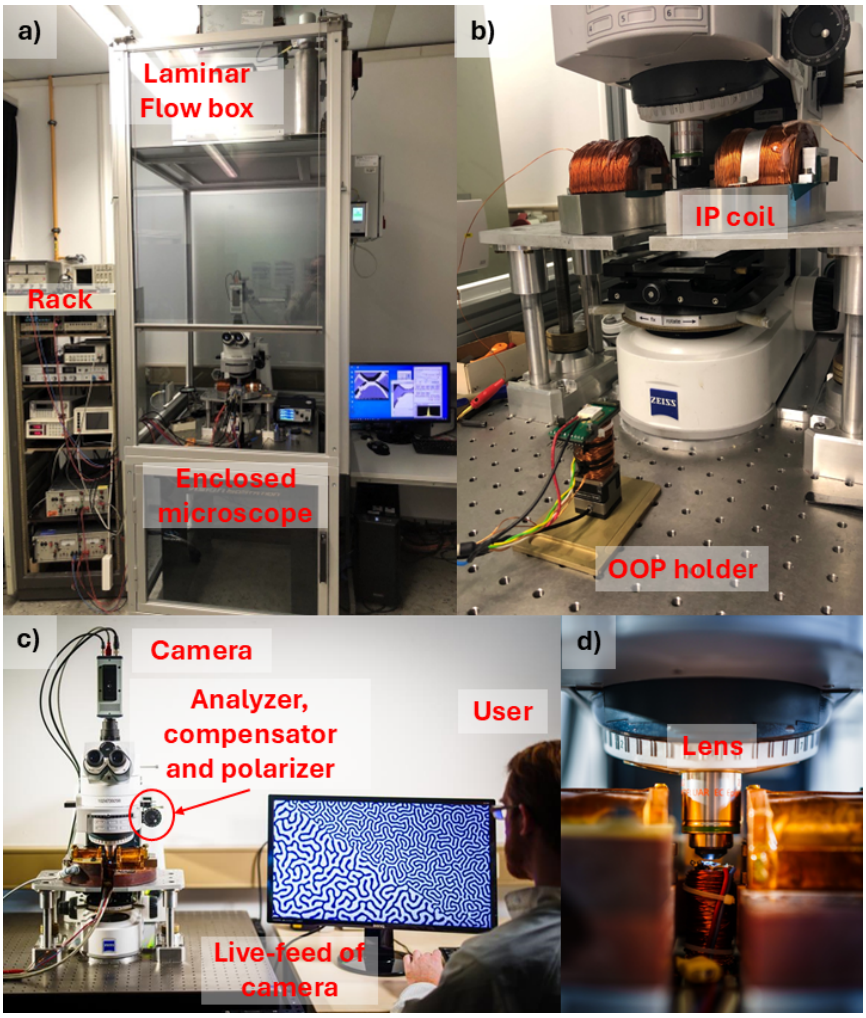

FIGURE 3.9: a) Schematic overview of the Kerr microscope setup. The system is based on a modified Zeiss AX10 wide-field microscope, enclosed within a laminar flow box and mounted on a vibration-isolated optical table. Peripheral components such as power supplies, temperature controllers, and auxiliary instruments are housed in the adjacent equipment rack. b) Close-up view of the optical table in front of the microscope. The OOP coil and its holder are positioned in front of the black x–y-stage, which is mounted on the microscope's focus stage. The IP coil is placed on a separate support, mechanically decoupled from the focus stage. c) Microscope equipped with a camera system mounted above the optical path. The camera delivers a live image feed - typically displayed via differential imaging (see Section 3.3.2) - to the control PC and user. Magnetic contrast is optimized by appropriate adjustment of the analyzer, compensator, and polarizer. d) Detailed view between the IP coil arms. The OOP coil holder, mounted on the focus stage, is located directly beneath the objective lens. Pictures c) and d) were taken professionally for AG Kläui.

For illumination, high-intensity blue light is generated by eight light-emitting diodes (LEDs) and delivered to the microscope via optical fiber cables. The fiber-optic inputs are arranged in a cross configuration, with two light sources oriented in each of the four directions. The internal beam paths of the microscope, illustrated in Figure [3.10], result in light reflection at an incident angle on the sample surface, providing sensitivity to the magnetization components along the three principal axes. This enables multiple MOKE measurement modes (see Section 2.5).
MOKE is classified based on the magnetization orientation relative to the incident

and reflected light. The three primary MOKE configurations include polar MOKE (PMOKE), sensitive to magnetization perpendicular to the sample surface, aligned with the reflection direction. Longitudinal MOKE (LMOKE) with sensitivity to in-plane magnetization aligned parallel to the incidence plane, and transverse MOKE (TMOKE), sensitive to IP magnetization-oriented perpendicular to the incidence plane.

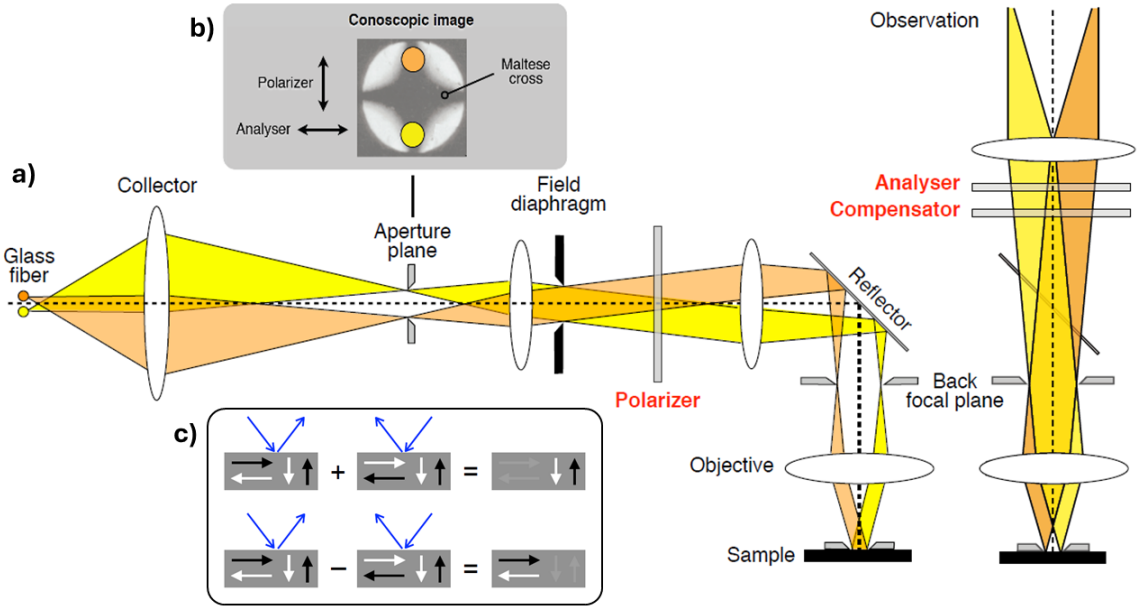

FIGURE 3.10: a) Schematic light beam paths in and out of the microscope. Explanation from left to right: Light enters microscope through glass fibers; gets collected and focused through the aperture plane; becomes linearly polarized by the polarizer and is redirected by the reflector through the objective onto the sample. After reflection the beam enters the microscope through the objective again (right beam path). It is important to note that the aperture plane b) (Maltese cross, also extinction cross) is used to extinct the central light path perpendicular to the sample, as no phase shift happens during reflection. The off-center beams (here yellow and orange) experience a different plane of incidence and thus a phase shift, resulting in an elliptical and rotated polarization state. Due to this polarization state, the reflected beam is not fully extinguished by an analyzer perpendicular to the central plane. After reflection (beam path to the right) the beams pass through the compensator and analyzer, in which the main part of non-rotated component of the reflected light is extinct. The reflected light influenced by magnetization can either be seen or recorded with the camera. c) Schematic of two beams with different incidence angles produce either enhanced polar and reduced in-plane contrast in a sum image or enhanced in-plane and reduced polar contrast in a difference image. Adapted from [291] manual.

Figure [3.10 c)] demonstrates how beam path configurations can be used to enhance contrast selectively. By summing the signals from both beams, the polar MOKE contrast is maximized while in-plane magnetization effects cancel out. Alternatively, for enhanced in-plane sensitivity, a difference image is generated by alternating the activation of each beam in synchronization with the detecting camera, effectively isolating in-plane contrast while subtracting the polar contribution.
For the primary purposes of this thesis, only the polar MOKE configuration is employed, as it is ideal for observing out-of-plane magnetization, e.g. skyrmions. In the polar MOKE configuration, the polarizer converts the incoming light into linearly polarized light. Under ideal conditions, a perfectly aligned beam would pass

through the polarizer and reflect off the sample without undergoing any phase shift. However, in the polar configuration, both light rays are intentionally misaligned from the central axis, as depicted in Figure 3.10. This misalignment, combined with extinction of the main beam path caused by the Maltese cross in the aperture plane, causing Kerr effect upon reflection from the sample surface. As a result, the polarization axis is rotated, and the light is transformed into elliptical polarization (See Section 2.5).
After reflection, the elliptically polarized light first passes through the compensator, a $\lambda/4$ wave plate, which converts the light back into linear polarization. It then passes through an analyzer, which converts the Kerr effect caused polarization rotation into an intensity difference by extinguishing the unrotated component of the light. This modulated light can either be visually observed or captured by the camera's charged coupled device (CCD) sensor. To achieve high contrast, precise adjustments of the polarizer, compensator, and analyzer are required, as well as proper aperture alignment and equalization of LED light intensity.
For recording, the transmitted light is captured by the CCD sensor with a native resolution of 1344x1024 pixels, integrated into a digital camera (Hamamatsu ORCA-03G) mounted atop the microscope. This setup provides a live video feed to the connected computer. Spatial resolution can be reduced through pixel binning, where squares of multiple physical pixels are combined into fewer digital pixels, improving time resolution (frames per second, fps). In this study, 2×2 binning was applied, yielding a spatial resolution of 672×512 pixels and a maximum frame rate of 16 fps, corresponding to an exposure time of 62.5 ms. The highest frame rate of 40 fps is achieved with an 8x8 binning, at the expense of reduced spatial resolution (168×128 pixels). The KerrLab software provided by Evico Magnetics, includes various tools and settings to optimize contrast and control the systems devices.
An advantage of using the Kerr microscope in a laboratory setting is its user-friendly interface and flexibility. The LED lamp house, microscope camera, and power supply devices are all connected through a BNC box, which is connected with the PC. Figure 3.11 shows the organigram of the Kerr microscope setup, which allows the KerrLab software to control the LEDs, the Kepco BOP power supplies connected to the coils, as well as the camera and the acquisition of its captured signals.

3.3.1 Additional equipment

Holders and electromagnets

Several sample holders have been designed, created and adapted for use with the Kerr microscope. These holders are compatible with the microscope's x-y-focus stage and can be positioned between the commonly used IP coil and its holder (see Figure 3.12 a)). The most essential component of the holders is the coiled wire, which generates an out-of-plane magnetic field when a current is applied. The in-plane coil consists of two spatially-separated, hollow coils with the same helicity, formed by a continuous wire, and is used with soft magnetic pole shoes made from stacked sheet metal inside the coils. This configuration enhances the maximum achievable magnetic field strength.
The out-of-plane coils, mounted on brass bases, slide into the x-y holder and generate the OOP field for the samples placed on top beneath the objective lens. Due to the limited space under the microscope and between the IP coils, the size of wire windings is constrained, resulting in magnetic field strengths only ranging from 3 to 8 mT. However, an OOP coil with a cylindrical soft magnetic pole shoe in the

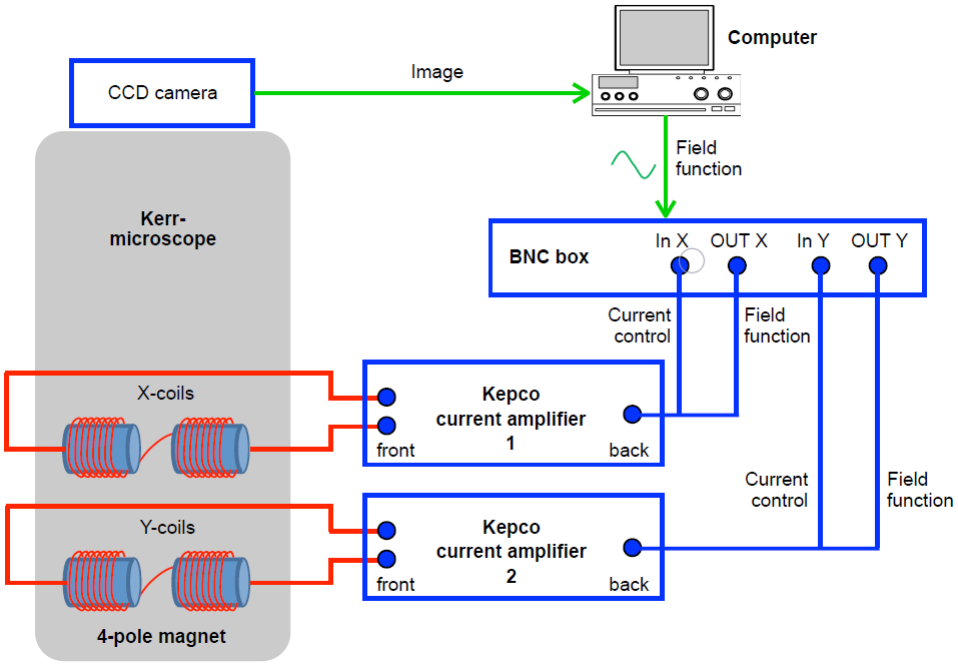

FIGURE 3.11: Organigram of the Kerr microscope setup. PC's data acquisition (DAQ) card controls both Kepco power amplifiers and thus the magnetic fields of the coils through the BNC box and simultaneously controls the camera and receives signals. Taken from [291] manual.

center is capable of producing a field of up to 13 mT. Several parts and whole holders were designed using computer-aided design (CAD) software and manufactured using 3D printing and/or in the in-house workshop. Additionally, custom printed circuit boards (PCBs) were designed and ordered to facilitate the application of electrical currents, which are transferred to the sample via wire bonding of the gold pads on both the sample and the PCB (see Figure 3.12 b)).

Power supplies and coil calibration

Two linear Kepco bipolar operational power supplies (BOP) in current mode are used to provide stable electric currents for the coils in the Kerr microscope system. The primary Kepco BOP, with 100 V and 4 A (L-version, suitable for inductive loads up to 2 mH), is commonly used for the out-of-plane coil, while the secondary Kepco BOP, with an output of 48 V and 12 A, is used for the IP coil. It is important to note that the magnetic field is not directly measured during experiments with the Kerr microscope. Instead, the magnetic field strength is inferred using calibration files specific to each coil. These files convert the applied current into the corresponding magnetic field strength, which is then displayed in the software and added in the image frame legend. To calibrate the electromagnets, a Hall probe is used. The experimental setup is shown in Section A.8.1.
A voltage is applied to the electromagnets, and the resulting magnetic field is manually entered into the KerrLab software while the according current is automatically added. By measuring multiple data points, the relationships between voltage and magnetic field, as well as current and magnetic field, can be interpolated and saved as a calibration file. It is crucial to consider whether the residual Earth's magnetic field should be treated as a constant offset or whether a constant current should be

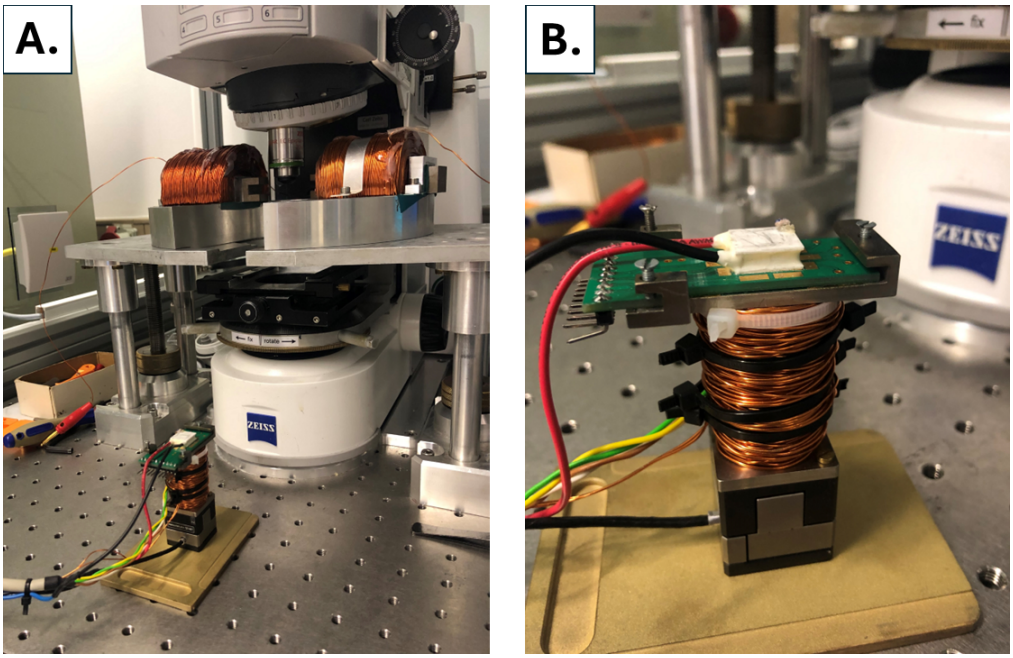

FIGURE 3.12: A.) Close-up of the Kerr microscope with the IP coil on its holder and Piezo stage holder in front. B.) Titanium sample holder with coil on three axis piezo stage with brass base and PCB holder on top, providing 10 pin connected to various gold pads on top for wire bonding. On top of PCB is the Peltier element (connected via black and red wire) and Pt100 heat sensor (top right). Taken from [291] manual.

applied to cancel out the Earth's magnetic field at the sample position when calibration files are created. The current offset can also be accounted for in software by shifting the interpolation curve by the offset value. Accurate calibration relies on proper positioning, alignment, and polarity of the Hall probe during measurements.

Peltier element heating

For temperature control, Peltier elements are installed on top of the sample holder, accompanied by a Pt100 temperature sensor, allowing for both heating and cooling of the sample placed on the holder. Used Peltier elements and their specifications are listed in Section A.6. The Pt100 sensor is adhered to the sample holder using a two-component thermal conductive glue, though the adhesive has limited stability. G. Beneke found that the temperature distribution of the Peltier element is not perfectly homogeneous due to the thermal sink effect of the lead wires, which causes a temperature gradient during heating. In addition to serving as thermal sinks, the lead wires also generate magnetic fields during DC operation. Owing to their close proximity and the opposing direction of current flow (as illustrated schematically in Figure 3.13), the resulting magnetic field near the wires exhibits an OOP component. Since the magnetic field is not measured at the sample location, it may nevertheless interfere with sensitive magnetic measurements. To minimize such artifacts, Peltier elements with low current and high voltage specifications were selected, thereby reducing the magnitude of the current-induced magnetic fields.

Temperature sensing

A Pt100 temperature sensor, in its simplest form, consists of a platinum wire with specific spatial dimensions such that its electric resistance is exactly 100 Ohms at 0°

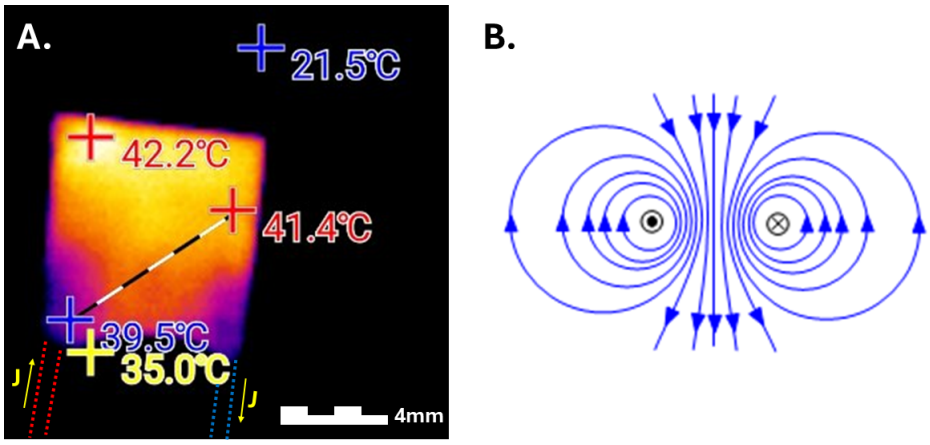

FIGURE 3.13: A.) Infrared thermal imaging of the holder's Peltier element reveals a temperature gradient of approximately 2○C, attributed to the heat dissipation effect of the connected lead wires (indicated by red and blue dashed lines), which act as thermal sinks. Due to their lower surface temperature and the presence of rubber insulation, the wires are not visible within the infrared detection range of the thermal image. The heat sensor located in the upper left corner of the image records the maximum temperature at 42.2○C, while the ambient background temperature is approximately 21.5○C, indicated by the blue regions. Yellow arrows denote the direction of the applied DC. Courtesy of G. Beneke. B.) Schematic illustration of the magnetic field lines induced by two parallel wires carrying current in opposite directions, shown in the x–z cross-sectional plane leading to the Peltier element. At elevated current levels, the resulting magnetic fields may interfere with sensitive magnetic measurements conducted on samples placed atop the Peltier element. Adapted from [292].

C. The resistance of the Pt100 sensor increases linearly with temperature for a large temperature range, and the temperature range used in this thesis is determined by the resistance measured via four-terminal sensing for high accuracy, with the data recorded by a Lakeshore 330 temperature controller. The sensor can be seen on top of the Peltier element in Figure 3.12 B.).

3.3.2 Recording magnetic images

Once the sample is correctly positioned and the microscope manually adjusted for optimal measurement settings (e.g., polarizer, analyzer, compensator, focus), the KerrLab software can be used to enhance contrast and record magnetic contrast videos. To improve magnetic contrast, a differential imaging approach is employed. First a background image is taken in a magnetically saturated state in z-axis, typically at 1 mT for the presented skyrmion stacks, and then the intensity subtracted from the current image. This subtraction enhances the magnetic domain contrast, which can be further optimized using an internal contrast shift mechanism, though this increases noise levels successively. To mitigate this noise, averaging over multiple images (typically powers of two) is applied, at the cost of reduced or smeared dynamics. The intensity values of the resulting images are recorded in 8-bit grayscale, with values ranging from 0 to 255. Single images or video sequences can be recorded, with a legend added on the frame to provide information on the image settings and applied magnetic fields.

In hysteresis loop mode, image averaging is automatically activated to ensure accurate gray-scale evaluations. The KerrLab software controls the electromagnet, stepping through the desired field values, with the option for finer steps, particularly near zero field, to accommodate sensitive samples. To ensure proper field setting and optimal averaging of the gray-scale levels, the step time should not be less than 0.2 seconds.

3.3.3 Skyrmion Nucleation

Skyrmion nucleation is initiated by heating the sample to a specific skyrmion phase temperature range and applying a bias out-of-plane field. This bias field is typically set at the spin-reorientation transition point (see hysteresis figure), where spins aligned along a given axis (e.g., positive z-direction) have a low energy barrier for flipping to align with the bias field (e.g., negative z-direction). An in-plane field burst magnitudes stronger than the bias field is then applied, forcing spins to align approximately in-plane. After the in-plane field is turned off, the spins tend to realign either parallel or anti-parallel to the bias field, aided by the strong PMA of the sample. During this realignment process, skyrmions can form. It should be noted that while the theoretical understanding of this process is still incomplete, it remains a reliable experimental method for nucleating skyrmions.
Experimentally, also other ways of skyrmion nucleation has been realized using, e.g., laser [83, 119, 169], current and electric field pulses at artificial [94, 293–297] or natural inhomogeneties or structures [110, 119, 161], or induced by SOT [298].

3.3.4 Piezo drift correction

During extended measurement times, sample drift occurs due to a combination of mechanical slack and thermal expansion in the mechanical parts of the holders, potentially leading to defocusing and reduced object visibility. Subtraction imaging further amplifies drift-induced artifacts, particularly at structural object boundaries or defects like scratches or dirt, producing artificial high-contrast black-and-white edge lines that degrade image quality and hinder quantitative image analysis. To mitigate these detrimental effects, a self-regulating, three-axes piezoelectric system was implemented [299]. The piezoelectric holder utilizes piezo crystals, which undergo elongation along a specified axis when an electric potential is applied. This system enables precise movement of up to 80 µm along each spatial axis (x, y) for real-time drift correction, while simultaneously compensating for focus drift along the z-axis. A dedicated image plugin within the KerrLab software facilitates automatic spatial correction by continuously analyzing predefined object features in a previously recorded mask to detect and counteract drift in real-time. For focus stabilization, the field diaphragm is adjusted to partially close until an edge feature becomes visible in the image. Due to the principles of Köhler illumination [300, 301] in scientific microscopes, optimal focus on the sample coincides with focus on the field diaphragm. Consequently, defocusing induces measurable changes in contrast sharpness along the diaphragm's edge, intensified by the subtraction imaging, allowing for automated focus correction. This self-regulating process ensures stable focus and well-defined structural edges over prolonged exposure times, thereby enhancing the reliability of the subtraction imaging.

3.3.5 Electric connections

Wire bonding is the process of connecting the contact pads of the sample to off-sample pads electrically using a thin wire. In this process, the wire is pressed into the pads by a needle, creating a connection between two pads, and then cut using a combination of mechanical force and ultrasonic vibration from the needle. Custom-designed and fabricated printed circuit boards (PCBs) with chemical gold (electroless nickel immersion gold, ENIG [302]) contact pads are mounted onto the out-of-plane holders to facilitate wire bonding between the PCB gold pads and the corresponding gold pads on the sample. The PCB features a 10-pin connector, enabling up to 10 simultaneous electrical connections. However, achieving this is technically challenging due to potential wire overlap or crossing, which may lead to short circuits. For all on-sample current applications, a Keithley 2400 SourceMeter was utilized, ensuring stable and precise current delivery.

Device safety from electric burnout

High electrical currents lead to extensive Joule heating causing potentially the burnout of conductive elements, such as wires or micro-structures on chips. In particular, highly sensitive devices, such as the triangular micro-structures discussed in Chapter 6, which exhibit a decreasing cross-sectional area toward the corners, are susceptible to high current density even at relatively low applied currents. When activating power supplies connected to the electromagnets, a transient high-voltage pulse is generated. This pulse induces a magnetic field surge within the coil, which may induce unintended currents within the circuit of the on-chip device. Additionally, the movement of conducting leads in the presence of external magnetic fields can generate destructive currents through electromagnetic induction. To mitigate these risks, a self-built breaker box has been implemented, allowing for the sensitive devices and their conducting leads to be grounded prior to the application of any intended current. By short-circuiting and grounding the electromagnet power supplies, the detrimental effects of the initial power surge can be effectively suppressed, thereby protecting the integrity of the micro-structures.

3.3.6 Laminar flow box temperature stability

To facilitate ongoing highly temperature-sensitive CoFeB-based skyrmion research, a protective laminar-flow box was installed to enhance temperature stability. Functionally, the laminar-flow box operates as a controlled cleanroom environment, utilizing filtered, adjustable laminar airflow. This airflow minimizes contamination within the box and can be thermally regulated via a heat exchanger, which improves temperature stability. The heat exchanger can cool by water from either the internal in-house cooling system or by an external chiller, and heat by an integrated electric heating element. Although the laboratory's ambient temperature is regulated by an air conditioning system, it exhibits fluctuations over extended periods due to external factors such as the day-night cycle, human activity within the lab or heating by absorption of extensive sunshine by the laboratory's laser absorption (safety) curtains.

To assess the temperature stability within the box, a Pt100 temperature sensor was positioned for multiple hours inside the box with 100% airflow and the front panels closed. Temperature measurements were recorded over several days using a custom LabVIEW-based program in conjunction with the Lakeshore 330 temperature controller (see Section A.7.1). It is important to note that the sensor used for

FIGURE 3.14: Full microscope setup with device rack on the left and PC on the right. The microscope is placed on top of a vibration reduction table and inside the laminar flow box. Temperature and flow control on the right upper side of the flow box.

these measurements was independent of the proportional-integral-derivative (PID) control unit of the flow box, which may introduce a systematic offset from the set temperature.

Temperature measurements conducted in spring 2022 using the in-house cooling water system demonstrated a temperature stability of approximately $\pm 0.1°C$ over several days. However, unexpected temperature oscillations were observed, with their origin initially unknown with the PID controller under suspicion to be the cause. Further investigation involved monitoring the temperature of the internal cooling water supply at the laboratory's valve, which also exhibited oscillatory behavior. These findings suggest that the oscillatory temperature fluctuations within the laminar-flow box are correlated to the temperature of the internal cooling water system.

A Fast Fourier Transform (FFT) analysis of the cooling water temperature revealed periodic fluctuation with a cycle of approximately 14 minutes (see Figure 3.16). In contrast, the temperature oscillations within the laminar-flow enclosure exhibited a periodicity of $\sim$28 minutes, corresponding to twice the periodicity of the cooling water fluctuations. This indicates a potential thermal coupling effect between the cooling system and the laminar-flow box.

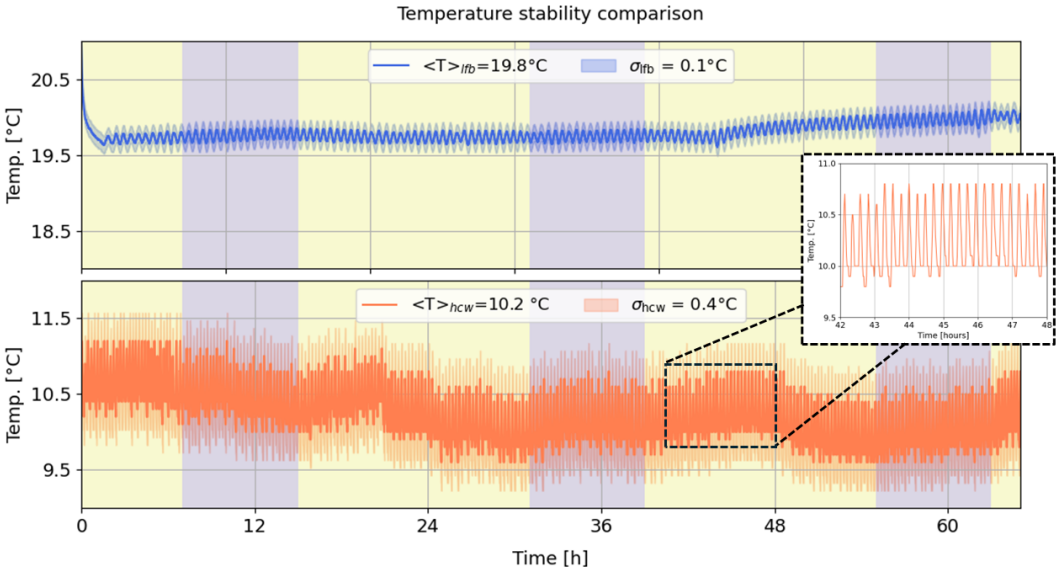

FIGURE 3.15: Temperature measurements on same y-range. Top) Temperature inside laminar flow box using the internal house cooling water system over multiple days in June 2022. Yellow background represents daytime, while dark violet nighttime. Shaded area is the standard deviation, every data point has its own error bar. The temperature shows oscillatory behavior with a periodicity of approximately 15 minutes and the overall increase trend around 45h is most likely attributed to a reduction of ventilation by a laboratory user. Measurement every 15s. Bot) Temperature graph of internal house cooling water system. Inset shows zoomed-in data and its oscillatory behavior. Extract of larger data set (see appendix). Green shading is the standard deviation. Yellow and dark violet resemble day-night cycle. Data was taken by Censored Name with an unknown temperature sensor at the laboratory's water valve in June 2022.

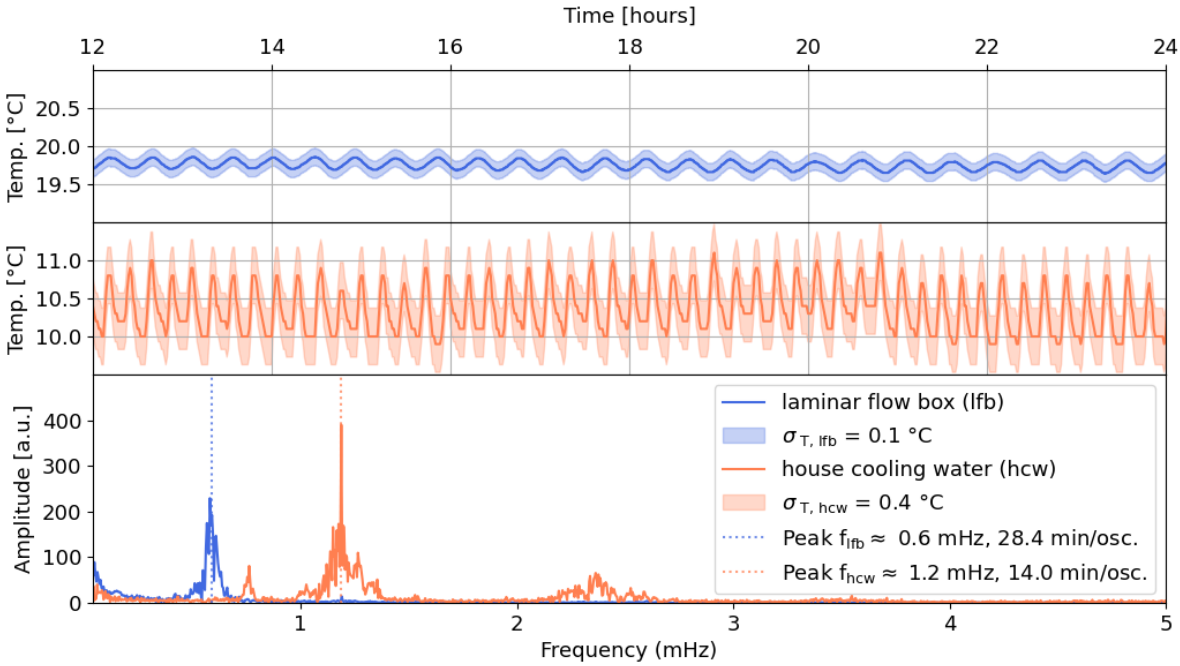

FIGURE 3.16: 12 h extract of >60 h comparative temperature measurement inside flow box (top, blue) and house intern cooling water (middle, orange) in June 2022 (see 3.15). Shaded area presents standard deviation of the data. Both temperatures, of cooling water and laminar flow box, show oscillatory behavior. Bot) Fast Fourier Transforms (FFT) of both data sets reveal main periodicity of the cooling water at ∼14,0 minutes and ∼28,4 minutes for temperature in laminar flow box.

In an email conversation *Censored*, head of cooling department JGU, wrote: "*Temperature fluctuations* [of the cooling water] *are normal; the system has a control mechanism via valves, which reduce the primary water flow when the temperature is reached and reopen when the temperature rises. Furthermore, the cooling system is distributed throughout the entire building, and multiple consumers are connected, which can lead to fluctuations. A precise temperature control cannot be guaranteed.*" [1]

The observed rough doubling of the periodicity within the laminar-flow enclosure lacks a definitive explanation. It is likely influenced by the interaction between the cooling water supply and the delayed response of the PID controller, which regulates temperature based on measurements taken at the height of the microscope. Further investigations, including experiments with alternative PID settings, are recommended to better understand this phenomenon.
Since modifications to the internal cooling system were not feasible, an external chiller set to 18°C was connected to the flow input of the laminar-flow box. This resulted in a stabilized temperature without significant fluctuations after a equilibration period of several hours, as illustrated in Figure 3.17, particularly when compared to the ambient laboratory temperature. For experiments requiring high-precision temperature stability, the use of a chiller in conjunction with closed flow box doors is essential.

[1] „Schwankungen der Temperatur sind normal, das Netz hat eine Regelung über Ventile, welche bei erreichen der Temperatur die Primärwassermenge reduzieren und wieder öffnen bei Temperaturanstieg. Des Weiteren ist das Kühlsystem über das ganze Haus verteilt und mehrere Verbraucher sind angeschlossen, was zu Schwankungen führen kann. Eine Punktgenaue Temperatur ist da nicht zu gewährleisten." – *Censored*, Sachgebietsleiter TLM 1.4, Kälteversorgung

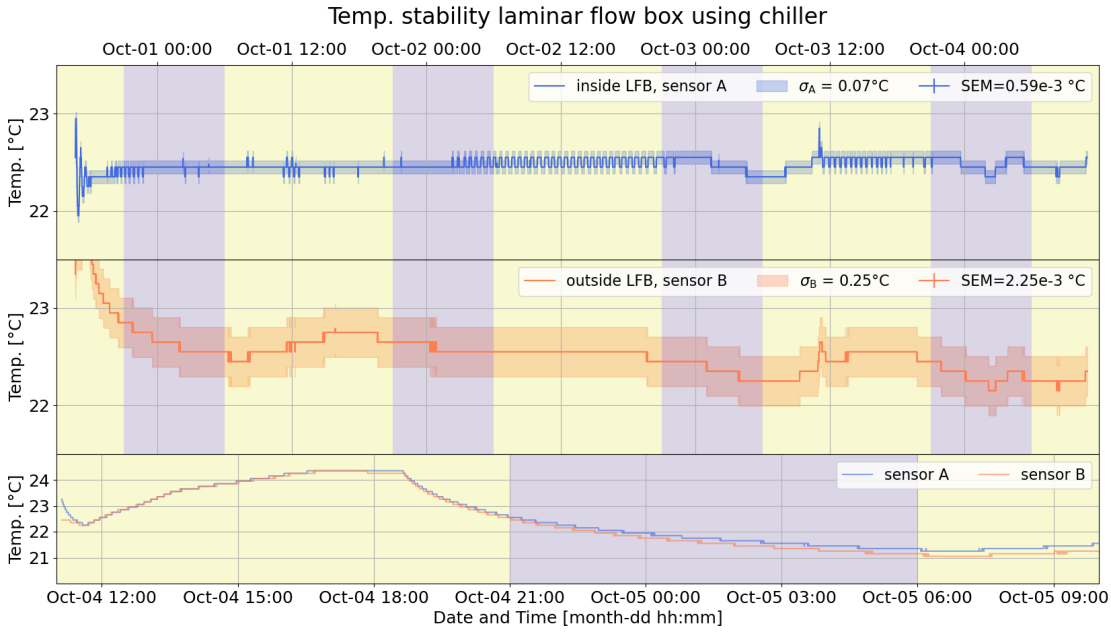

FIGURE 3.17: Top) Temperature stability of the flow box used with an external chiller set at 20°C and measured with sensor A (blue) and Mid) outside the flow box (orange) measured with sensor B. Shaded area is the standard deviation, also displayed in the legend with the standard error. Yellow and dark violet parts represent day-and-night cycle in October 2022. An excerpt of the data for better visibility is displayed in appendix A.3. Bot) Measurement of both sensors located in the laboratory. Difference could be caused by the holders varying heat absorption or dissipation.

Due to the combined effects of the laminar-flow box and the integrated Peltier element, temperature stability can be maintained over several days following an initial equilibration period of a few hours. However, external disturbances such as frequent flow box openings, increased personnel activity within the laboratory, or enhanced sunlight exposure on the laboratory's laser-absorbing curtains may compromise temperature stability.

3.4 Feature analysis and skyrmion tracking

To extract skyrmion features like their trajectories, velocity, and other characteristics such as size, ellipticity, and skyrmion-skyrmion distances, recorded images and videos from the KerrLab software require detailed analysis. In this study, three distinct methods were employed for image processing and skyrmion tracking:

3.4.1 Fiji (ImageJ/ImageJ2)

The first approach utilized Fiji, a distribution of ImageJ/ImageJ2 (Image Processing and Analysis in Java) [303] with various plugins for image processing. The primary tool used was the TrackMate plugin, originally developed for tracking biological cells in dark field microscopy [304, 305]. The Simple Linear Assignment Problem (LAP) tracking algorithm by Jaqaman et al. [306] was primarily employed, enabling efficient skyrmion detection and trajectory analysis.

3.4.2 Python-based analysis with trackpy

The second method involved trackpy [307], a Python-based library for particle tracking, implementing the algorithm developed by Crocker and Grier [308]. Python's extensive ecosystem of libraries for image processing and data analysis provides a flexible and powerful framework for skyrmion research. Once objects are detected and tracked using trackpy, further statistical and quantitative analyses can be efficiently performed. For both Fiji and trackpy approaches, image preprocessing was necessary to enhance skyrmion identification and tracking accuracy. Low contrast, high noise, and high-contrast defects pose significant challenges for skyrmion classification. To improve tracking performance, the image preprocessing consisted of Gaussian blurring to reduce noise, contrast enhancement for improved feature distinction, and binarization of images into black and white features to facilitate skyrmion identification. Since only the center of mass of skyrmions is required for tracking, these preprocessing steps effectively improved detection accuracy.

3.4.3 U-Net - machine learning image segmentation approach

A third approach, developed during this study by I. Labrie-Boulay and T. Winkler, with subsequent improvements by K. Leutner, employed machine learning for skyrmion detection and classification [309]. This method is based on U-Net, a convolutional neural network (CNN) optimized for image segmentation. The model was trained on raw Kerr microscopy data provided by AG Kläui group members [310], incorporating features like skyrmions, defects and background identification. U-Net demonstrated high accuracy in distinguishing manually pre-classified features, such as skyrmions with dark MOKE contrast, bright contrast background, and potential defects that could be misinterpreted as magnetic contrast. A procedure for opposite magnetic contrast, dark background and bright skyrmions, is shown in Section C.2.3. Unlike the previously introduced tracking methods, U-Net does not require direct parameter tuning for detection. However, contrast adjustments and noise reduction can enhance classification accuracy and e.g. size determination [311]. The primary limitations of this approach include the requirement for manually labeled training data, and potential performance issues when processing images with parameters (e.g., contrast, resolution, image size) outside the range of the training data set. Despite these limitations, U-Net offers significant advantages, particularly in consistency, ease of use, and feature classification accuracy. The pre-determined model parameters allow for reliable identification of skyrmion properties, such as size, ellipticity, and positional tracking, facilitating comparative analysis.
The extracted skyrmion trajectories and quantified properties - including size, count, and lattice distances - form the basis for further investigations discussed in the subsequent chapters. An example for classification and identification can be found in Section C.2.3.

3.5 Focused ion beam

A direct method for modifying the magnetic properties of a sample - including those associated with skyrmions - is ion irradiation of the material layers. In this context, irradiation involves exposing the sample surface to a focused, perpendicular flux of energetic ions. The interaction between the incoming ions and the atomic lattice is determined by the ion species and their kinetic energy. These ions can undergo both elastic and inelastic scattering upon impact, leading to atomic displacements and

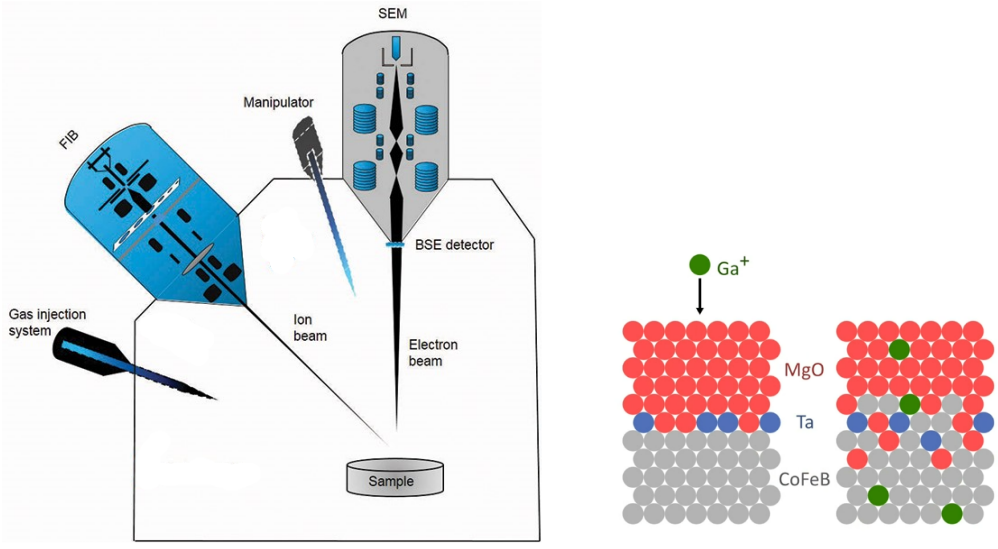

A FIB concept B Irradiation concept

FIGURE 3.18: a) Scheme of focus ion beam (FIB) and scanning electron microscope (SEM) system with focussing apertures. Sample will be rotated towards FIB for perpendicular incidence. No SEM measurements are performed during ion beam exposure. Adapted from [318] b) Gallium irradiation on the MgO(red)/Ta(blue)/CoFeB(grey) interface. Gallium atoms (green) can implement itself and displace the material and thus intermix the interface. Adapted from G. Beneke.

potential implantation within the material. Consequently, the magnetic properties are modified - primarily due to interfacial intermixing and alterations in magnetic anisotropy [44, 253, 312–315] - thereby enabling the precise tuning of skyrmion characteristics [142, 169, 198, 316, 317] and the implementation of artificially engineered pinning sites or boundary conditions [155, 158, 169, 196, 197].

Localized irradiation of devices using high-energy ions was conducted with a Helios NanoLab 600i DualBeam system, which integrates a focused ion beam (FIB) and a SEM for precise irradiation control. Gallium, with its low melting point of $29{,}8^{\circ}C$ [319], was liquefied, ionized in a strong electric field, and accelerated onto the sample for irradiation. With this focused beam of Gallium ions, the sample can be irradiated in fine structures, e.g. artificial skyrmion barriers as presented in Chapter 5. Additionally, wide area helium ion irradiation was performed on MVK763 using an ion beam process provided by Spin-Ion Technologies in Palaiseau, France [320].

3.6 SQUID

SQUID (Superconducting Quantum Interference Device) is a highly sensitive magnetometer that uses superconducting materials to measure very small magnetic fields [321]. It works based on the principles of quantum interference, where a current passing through a superconducting loop can be influenced by external magnetic fields. The extreme sensitive SQUID technique was used to measure the saturation magnetization and anisotropy of samples FAB629 and TMD109 in this thesis at ambient temperature (see Section A.1.2).

3.7 Atomic force microscopy

Atomic force microscopy (AFM) is a type of scanning probe microscopy technique used to study surfaces down to the nanoscale [322]. AFM measures the surface topography by scanning with a sharp tip called a cantilever over the surface and detecting the interaction forces between the tip and the sample by the varying reflection of a laser. It provides high-resolution images of surface features, including roughness, texture, and mechanical properties. A type of AFM called magnetic force microscopy (MFM) uses a magnetically coated cantilever tip, which is specifically used to map the magnetic properties of a surface [323, 324]. It detects the magnetic forces between the MFM tip and the sample's magnetic domains, offering insights into the material's magnetic surface and behavior. AFM was used to scan the surface of several substrates with varying heat conductivity for their specific roughness.

Chapter 4

Modulated Skyrmion Flow

4.1 Introduction

Skyrmions are of significant interest not only for their potential in applications such as unconventional computing [113, 325], data storage [29, 48, 54], and sensing, but also as fundamental objects of study in condensed matter physics. The skyrmions investigated in this work are confined along the out-of-plane (z) direction to the thickness of the hosting ferromagnetic layer - typically less than 1 nm - while extending over micrometers in the in-plane (x–y) direction. This pronounced ratio justifies their classification as effectively 2D objects [115].
Due to their topological stability [109, 118, 326], thermally driven Brownian motion [42, 110, 154], and complex interactions with one another [163, 170, 175] as well as with material or artificial boundaries [155, 157, 159, 163, 171–174, 198], skyrmions exhibit behavior akin to quasi-particles [115, 327, 328]. These emergent characteristics make them compelling model systems for investigating a wide range of physical phenomena, including non-equilibrium dynamics, topological phase transitions [295, 329], and the formation of particle-like lattices [175] in 2D systems.

4.2 Skyrmion Diffusion

Thermally activated diffusion of individual skyrmions has been observed in the in-house-fabricated CoFeB-based multilayer stacks, consistent with previous reports [110]. In this context, skyrmions exhibit random, thermally driven motion across the 2D plane of the sample [73], akin to the Brownian motion of small particles in 3D fluids or gases [147, 148]. However, unlike in ideal systems, this diffusive behavior is strongly modulated by the sample's intrinsic energy landscape [36, 157]. The non-uniformity of the energy landscape—arising from structural inhomogeneities, interface roughness, or compositional variations—leads to frequent pinning events. These localized energy minima act as traps that impede the otherwise random motion of skyrmions, occasionally resulting in extended localization at particularly deep pinning sites. The diffusion coefficient, which quantifies the extent of such thermally driven motion, was extracted via analysis of the mean squared displacement, as defined in Equation 2.50. This was achieved by tracking skyrmion trajectories across sequential frames (see 3, Section 3.4). Multiple factors can influence the diffusion behavior of skyrmions, including the material composition [253, 314] and deposition parameters, out-of-plane magnetic bias fields [110], oscillating fields [129], geometric confinement [99, 133, 330], temperature [110, 139, 331], in-plane magnetic fields [154, 180], externally driven motion, and the use of synthetic antiferromagnetic configurations [153].

Extensive efforts were dedicated to optimizing the multilayer stack fabrication to achieve desirable skyrmion properties, including the formation of dense skyrmion lattices and the realization of thermally activated skyrmion diffusion at room temperature. Owing to the high sensitivity of CoFeB-based skyrmion systems [258], even minor variations in the deposition recipe or sputtering parameters significantly influenced the resulting skyrmion behavior [136, 263] within the targeted temperature range of 290 K to 360 K. Through systematic optimization, skyrmion diffusion was successfully observed across this temperature window, yielding a diffusion coefficient comparable to that reported in Ref. [110]. A detailed overview of the skyrmion phase behavior across multiple growth batches and temperatures is provided in Table A.3.

Gruber et al. demonstrated that pinning of skyrmions occurs primarily at their domain wall rather than their core [157]. This results in thermally activated motion around the pinning site; however, the overall diffusion is reduced due to the extended periods during which the skyrmion remains pinned at these sites [36, 37], which is temperature-dependent and governed by the attempt frequency and non-flat energy landscape. Additionally, it was observed that the pinning strength itself is temperature-dependent [110], with skyrmions being more likely to pin to different sites as the temperature increases [157]. Gruber et al. further showed that the introduction of additional out-of-plane magnetic field oscillations, in conjunction with the skyrmion-stabilizing bias field, can increase the skyrmion diffusion coefficient by over three hundred times [129], despite the limitations imposed by Kerr microscopy and camera resolution.

The structural geometry and skyrmion size itself can also limit diffusion [145]. The stray field and exchange stiffness effects from the edges of the confining structure play a key role in restricting skyrmion motion [163]. Song et al. demonstrated that the number of skyrmions within a given structure can be commensurate with the host's geometry, leading to a significant reduction in diffusion [172]. In contrast, when the number of skyrmions is not commensurate with the structural geometry, skyrmions move towards commensurate sites and interact with each other, which leads to an increase in diffusion compared to the commensurate case.

Kerber et al. demonstrated that applying an in-plane magnetic field parallel to the sample's plane enhances skyrmion diffusion in the direction of the applied field while simultaneously reducing diffusion perpendicular to it, in comparison to the case without an in-plane field [154, 180]. This behavior was attributed to the deformation of the skyrmion caused by the applied field, resulting in the skyrmion elongating into an ellipsoidal shape, which facilitates increased diffusion along the direction of the field. Weißenhofer et al. provided a theoretical explanation for this phenomenon, attributing the differential diffusion to the off-diagonal elements of the dissipation tensor (see Equation 2.49) [326].

While the majority of the skyrmion research presented in this work focuses on single-layer CoFeB as the ferromagnetic material, skyrmions have also been observed in synthetic antiferromagnets (SAF). These systems consist in the simplest form of two magnetic layers with antiparallel magnetization, separated by a spacer layer that induces compensation, thereby reducing the topological charge of the skyrmion bi-system. This reduction leads to an enhancement of the diffusion rate [153, 191, 326]. Zázvorka et al. highlighted the temperature dependence of the skyrmion diffusion coefficient, showing that diffusion increases at higher temperatures [110].

4.3 Skyrmion Lattice

If skyrmions are nucleated under appropriate conditions, which are primarily dependent on sample- and external parameters like e.g., temperature and OOP bias field, as well as an IP field burst (see Section 3.3.3), they can form a dense lattice [175, 332]. In an idealized scenario where the skyrmions are uniformly sized and perfectly spaced, the system would exhibit a hexagonal, even crystal-like lattice structure with long-range orientational and translational order (see Section 2.4.4). However, due to the non-homogeneous energy landscape of the samples, boundary conditions of the host structure, and potential variations in skyrmion size also caused by inhomogeneities, such a perfectly ordered lattice is rarely achieved. Song et al. investigated how the confinement geometry of skyrmion-hosting structures influences both the dynamic behavior and the lattice configuration of skyrmions, with the effects strongly dependent on the exact number of skyrmions present [172].

To enhance the density and ordering of skyrmion lattices, a technique known as lattice shaking was employed, wherein an AC was applied in a single direction at varying frequencies and amplitudes. Figure 4.1 presents a representative measurement of the skyrmion lattice before and after the application of an AC current corresponding to a current density of $5{\cdot}10^8\ \frac{A}{m^2}$ at 10 Hz for a duration of 3 minutes. Following this treatment, the lattice order parameter ψ_6 exhibited an increase of approximately 8,5%, rising from $\psi_{6,\text{begin}} = 0{,}517$ to $\psi_{6,\text{end}} = 0{,}565$.

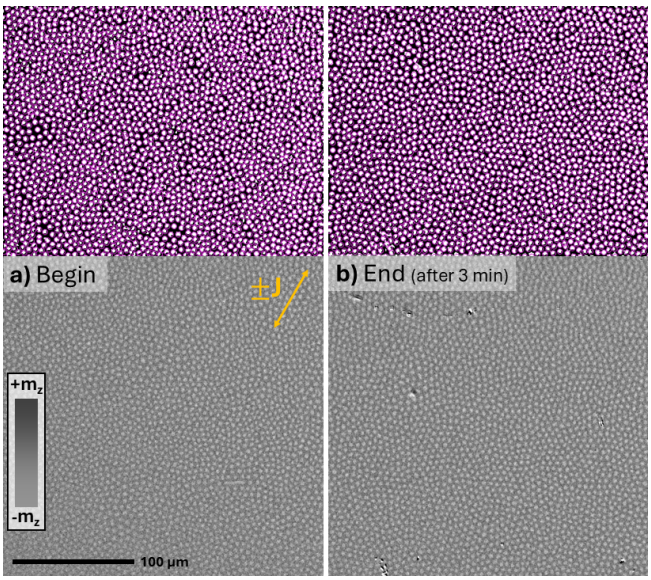

FIGURE 4.1: Two frames of skyrmion lattices, only confined by the samples edges, before and after application of an alternating current of $5{\cdot}10^8\ \frac{A}{m^2}$ at 10 Hz for 3 minutes. Pink circles in top pictures are identified skyrmions by Fiji's Trackmate (see Section 3.4) of their respective bottom picture. It gives a clear visual impression that the lattice is not well ordered and is dependent on the inherent non-flat energy landscape of the sample. Orange double arrow resembles the current direction.

It is important to note that this improvement in lattice ordering may not solely result from enhanced skyrmion mobility. A partial contribution could arise from temperature, relaxation effects or skyrmion annihilation, which would reduce skyrmion density and provide more free space for remaining skyrmions to reorganize into a more ordered configuration.

For these measurements, a fabricated sample was utilized, incorporating structured geometries that allowed current application along specific symmetry axes (see Figure B.1). This was achieved by placing gold contact pads at selected edges or corners of the sample. Applying current along multiple symmetry directions may further enhance lattice ordering, as the experiment shown in Figure 4.1 was limited to a single direction. The capability to direct current along symmetry axes of the geometry is further exploited in Chapter 6, where it is applied for unconventional computing applications.

According to the Kosterlitz-Thouless-Halperin-Nelson-Young (KTHNY) theory, which contributed to the Nobel Prize awarded in 2016 [333], a distinct phase exists between the solid and liquid phases in 2D [176]. As the solid phase begins to melt, it first transitions into a hexatic phase, which is characterized by long-range orientational order but only short-range translational order. This melting process can be triggered by changes in external parameters such as temperature or bias field, influenced by the energy landscape, caused by inhomogeneities or pinning sites, or geometrical confinements.

4.3.1 Skyrmion Pinning and Energy Landscape

Since skyrmion flow refers to the collective motion of skyrmions within a geometrically confined structure, the overall dynamics can be significantly hindered by the immobilization or reduced mobility of a single skyrmion. In the samples studied in this thesis, the energy landscape is considered approximately flat—an essential condition to enable skyrmion diffusion. However, Gruber et al. demonstrated that in comparable samples, local variations in the energy landscape can lead to pinning effects [157]. Their work further revealed that pinning predominantly occurs not at the skyrmion core, but at the surrounding domain wall.
This observation introduces a size dependence to skyrmion pinning and, consequently, to diffusion behavior: larger skyrmions are more likely to interact with multiple pinning sites, increasing the probability of being trapped. In scenarios involving externally driven motion, such as SOT-induced skyrmion flow, pinning can act as a barrier to continuous motion. The magnitude of the applied driving force - typically in the form of an electrical current - must therefore exceed the pinning potential in order to sustain steady skyrmion transport.

In this thesis, the experimentally observed skyrmion flow operates within the creep regime, characterized by a combination of thermally activated diffusion, stochastic pinning, and SOT-driven drift. It is important to note that the simulations presented for skyrmion flow dynamics do not account for the effects of pinning, potentially leading to an idealized representation of the system.

4.4 Skyrmion Flow

Skyrmions as movable quasi-particles [115, 327] bear high potential in spintronic applications like memory [29, 48] or unconventional computing [113, 325] as information carriers. They can also be considered a highly tuneable 2D system for e.g. rheological modeling [88, 185, 334]. One advantage of skyrmions as model systems is that in experiments the trajectory of all particles inside the field of view can be tracked and analyzed. If multiple skyrmions move together or in a lattice/ensemble, their repulsive interaction and the interaction with the harboring

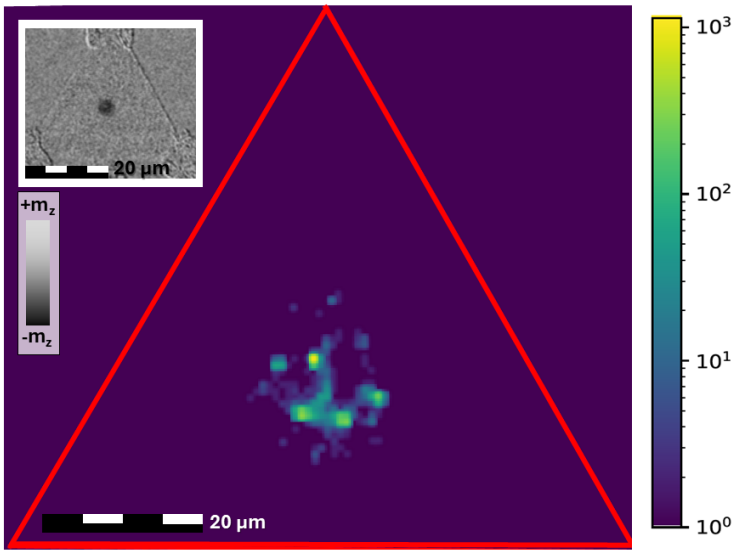

FIGURE 4.2: Probability density of skyrmion occurrence in a triangular confinement. Adapted from [99], supplementary material.

structure's edges [163, 171, 173, 174] cause skyrmion motion in which no skyrmions can overlap or merge due to topology [109, 118, 326] and can only exist inside the structure during the motion. This motion of skyrmions in interacting distances to each other exhibit fluid-like behavior which will be called skyrmion flow.
Skyrmion mostly annihilate rather near inhomogeneities due to a change in the material properties at that location. During flow, skyrmion are moved towards the electrical contact where they most likely annihilate at the edge due to the mentioned material parameter, additional thermal energy due to Joulse heating and being pressed due to current induced SOT. Skyrmions were only observed annihilating in a time-frame of seconds after nucleation and at the end of the channel right at the contact. The interaction between skyrmions and boundary influences the overall skyrmion flow. Due to the experimental limitations, the skyrmion flow has only been observed in the creep regime, in which the pinning plays a crucial role [157, 327, 335]. In this velocity regime the motion is the superposition of the motion by SOT, induced by low electric current densities of the order of $10^7 A/m^2$, and the thermally activated diffusion, resulting in mean velocities not exceeding single-digit micrometers per second, typical for the creep regime. Quasi-particle simulations mimicking the experimental skyrmion flow within the same velocity regime were performed, exploring additional geometrical designs and the influence of artificial skyrmion Hall effect on the flow dynamic.

In classical incompressible Newtonian fluids, as described by Kirby [336], the fluid motion under low Reynolds number conditions typically results in laminar flow[337]. The governing dynamics of such flow are described by the Navier–Stokes equations [338], and in the case of pressure-driven flow through a channel or pipe with straight boundaries, the solution is known as Poiseuille flow [339, 340].
In this regime, the velocity profile across the cross-section of the channel assumes a parabolic shape due to viscous interactions between the fluid and the confining boundaries. These interactions cause the fluid velocity to be zero at the boundary and maximal at the center, resulting from the internal friction of the fluid and the boundary constraints. This scenario is referred to as the no-slip boundary condition,

wherein the fluid at the interface with the boundary is stationary.
If the fluid exhibits a finite but reduced velocity at the boundary compared to the center, the system is described by partial-slip boundary conditions. In contrast, ideal slip boundary conditions - where there is no interaction between the fluid and boundary, allowing the fluid to move unimpeded at the interface - are rarely encountered in practical applications due to unavoidable interfacial friction. For skyrmion flow in context of the LLG equation, the torque term (-$\gamma \cdot \mathbf{M} \times \mathbf{H}_{eff}$, see Eq. 2.30) indicates that a higher gyromagnetic ratio γ results in a faster precession of the magnetic moments, thereby influencing the skyrmion's dynamic response to stimuli such as spin currents. According to the Thiele equation, the gyrotropic force ($\mathbf{G} \times \mathbf{v}$, see Eq. 2.41), where the gyrovector $\mathbf{G} \propto -\gamma$, governs the transverse (Hall-like) motion of skyrmions under current (thus called skyrmion Hall effect, see Section 2.4.5). Consequently, both the magnitude and direction of skyrmion velocity $\mathbf{v}$ are affected by γ. At low current densities, the resulting skyrmion velocity remains small, and thus the gyrotropic force is weak, leading to a minimal transverse component of motion and a correspondingly small skyrmion Hall angle. Under these conditions, skyrmions operate in the creep regime, where thermal activation and pinning dominate their dynamics [88, 188, 327]. This contrasts with the high-current regime, where the skyrmion enters the flow regime, characterized by higher velocities and a more pronounced influence of the skyrmion Hall effect [83, 97, 184, 187].

4.4.1 Skyrmion Flow in periodically modulated Channels

To investigate the influence of boundary conditions on skyrmion flow dynamics along confined geometries, channels with varying widths and engineered boundary modulations were fabricated. Complementary micromagnetic simulations were performed to explore the effects of geometric modulations and flow parameters beyond the constraints of the experimental setup [341].
Several channels with distinct artificial modulations were patterned on sample FAB629 using standard electron beam lithography techniques, followed by the deposition of chromium/gold contact pads for electrical current injection (see Section 3.2). This approach enables precise control over the boundary conditions experienced by skyrmions propagating within the channels.
Figure 4.3 shows a section of a EBL design layout, displaying channels with different widths. Additional layouts are presented in the appendixes. For the purposes of statistical reliability, only a subset of these geometries was experimentally characterized at a fixed temperature of 315 K.

The primary data set used for comparison with simulations was obtained from measurements on channels with widths of 40 µm and 80 µm, each featuring straight edges and a single type of geometric modulation. This modulation consists of periodically arranged isosceles triangular indentations, each with a base of 20 µm and a height of 10 µm, patterned along the channel boundary. In the case of the 40 µm-wide channel, this modulation results in a maximum channel width of 60 µm at the triangular expansions and a minimum width of 40 µm at the unmodulated sections.

Following standard skyrmion nucleation (see Chapter 3, Section 3.3.3), a semi-dense skyrmion configuration is established, populating both the larger reservoirs at the channel ends and the channel itself, including its modulated regions. This initial density is necessary to ensure a sustained skyrmion flow over an extended period. The field of view in the video recordings used for analysis spans approximately 280 µm at 1.6× magnification and around 200 µm at 2.5× magnification, capturing only the narrow, central section of the channel. Skyrmions from the reservoir flow

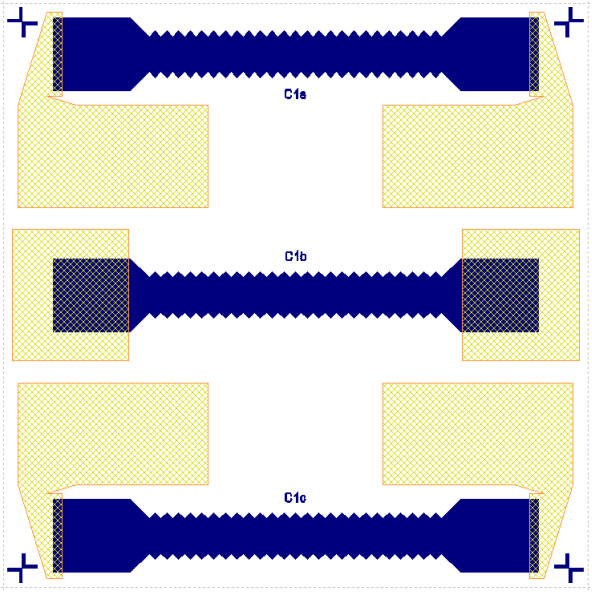

FIGURE 4.3: PIONEER layout of channels with 60 µm inner widths and 10 µm modulation.

through the channel toward the opposite end, where they likely annihilate. Their annihilation cannot be directly observed due to the overlapping electrical contacts at the channel terminations, which - with a thickness of ∼30 nm - obstruct optical skyrmion detection within the thin film stack.
Upon depletion of skyrmions from the channel, worm domains begin to nucleate at the electrical contact and propagate through the channel toward the opposite reservoir and contact. To confirm that the influence of the SkHE on the flow is negligible, the SkHA was measured for free skyrmions under applied current densities, yielding a value of $\theta_{skHA} = (0.58 \pm 0.13)^\circ$.
It should be noted that a small apparent deflection in the skyrmion trajectory may also result from slight misalignment of the camera relative to the channel axis during recording. Such a misalignment can introduce an artificial angle between the skyrmion flow direction and the horizontal axis of the field of view. Nevertheless, COMSOL simulations confirm that the current density distribution within the modulated channel remains homogeneous (see Figure 4.4), indicating that no intrinsic angular deviation of current flow relative to the channel axis is expected.

For analysis of velocity profiles, the average skyrmion displacement between consecutive frames was calculated over the time interval during which the current was applied, yielding the mean skyrmion velocity.
The velocity profile observed in the 80 µm-wide channel with straight edges (Figure 4.5 a, b) reveals a nearly uniform distribution across the entire channel width, indicating no significant velocity reduction near the channel boundaries. Instead, the profile is relatively flat, suggesting slip boundary conditions. Minor deviations from perfect flatness may result from localized pinning effects due to the intrinsic energy landscape or, though less likely, from an inhomogeneous current density - potentially highest at the stack corners pointing inwards. Additional measurements for more statistics would likely further smooth the profile.
In contrast, channels with periodic geometric modulation exhibit markedly different velocity profiles. For both the 40 µm and 80 µm-wide modulated channels, the

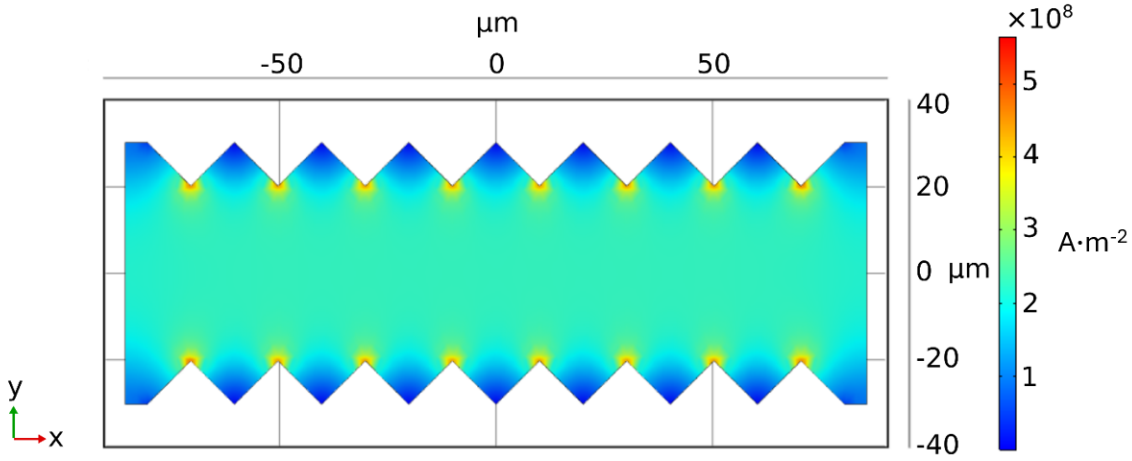

FIGURE 4.4: Qualitative electrical current density distribution simulated in capping Tantalum layer in COMSOL simulation package by M. Brems. The current density is low inside the modulations but high at the narrowest parts of the modulated channel. Taken from [342], supplementary material.

mean skyrmion velocity is significantly reduced compared to the straight-edge case. The velocity profile in the 40 µm-wide modulated channel (Figure 4.5 c, d) approximates a parabolic shape, characteristic of Poiseuille-like flow with partial-slip boundary conditions. Meanwhile, the 80 µm channel with modulation (Figure 4.5 e, f) shows a pronounced velocity drop near the boundaries, yet the profile flattens in the center, indicating partial-slip conditions but lacking the parabolic characteristic expected from classical Poiseuille flow.

In the triangular protrusions of the modulated channels, the local current density decreases due to the wider channel cross-section. Within these regions, current flow is no longer aligned with the channel axis. However, the influence on skyrmion dynamics is negligible, as the skyrmions are repelled from these areas due to stray-field gradients imposed by the modulation geometry, consistent with previous findings [163, 171, 330].
In an idealized, pinning-free environment, skyrmions in straight channels uninfluenced by stray-field and exchange interactions at the boundaries would experience no opposing forces, leading to purely slip boundary conditions.
To assess the impact of the skyrmion Hall effect, the current direction was reversed in the 80 µm modulated channel. The resulting velocity profiles were symmetric and could be mapped onto each other, confirming that observed asymmetries in the original profiles primarily stem from the underlying energy landscape - most likely from pinning - rather than from a non-zero skyrmion Hall angle. For this, skyrmion flow in both channel directions was performed, which, without a SkHA, should lead to mirrored velocity profiles, only influenced by the modulation and non-homogeneous energy landscape.

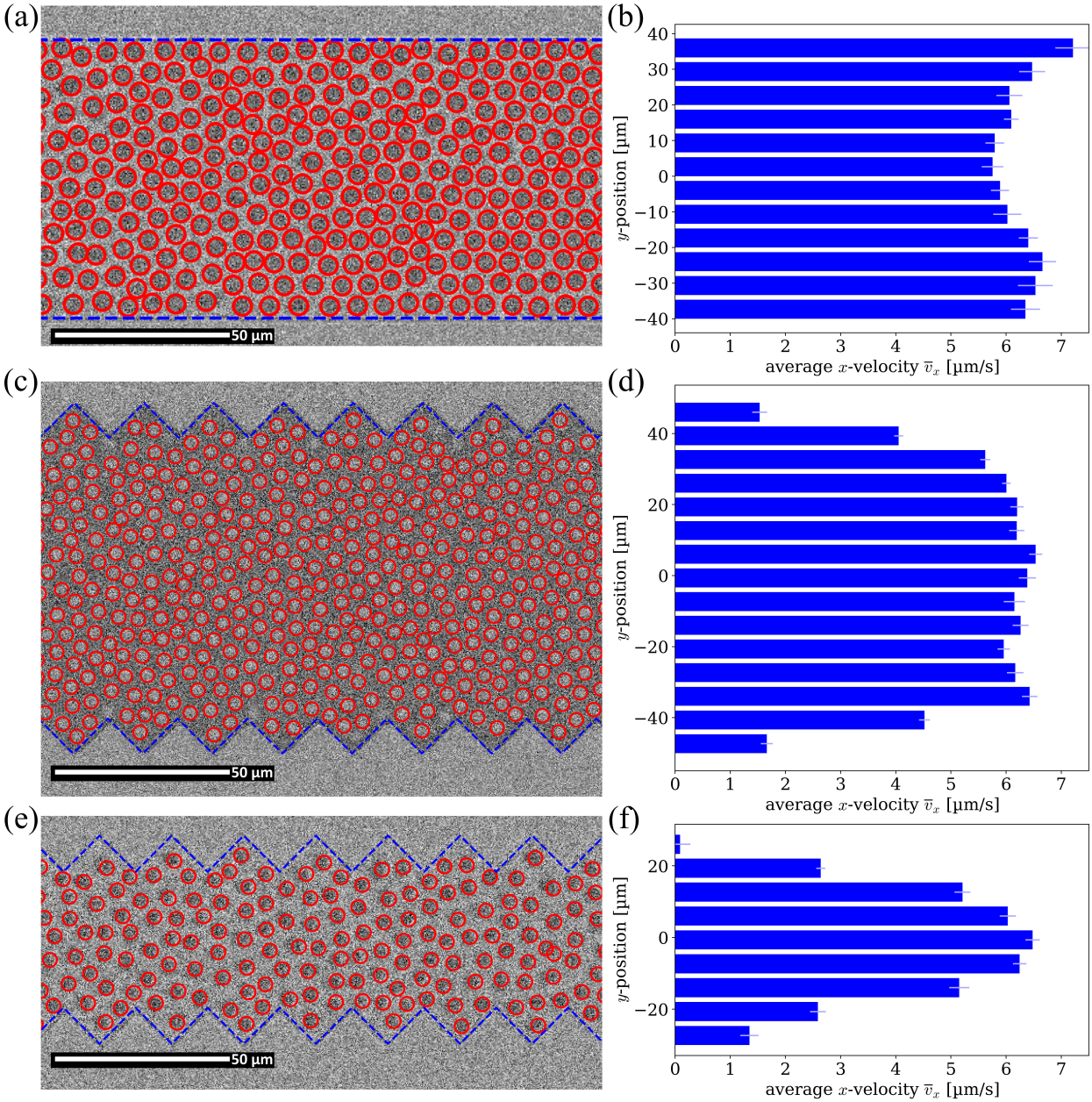

FIGURE 4.5: a), c), e) Single-frame Kerr microscopy images depicting skyrmions (highlighted by red circles) within channels featuring straight boundaries a) and modulated boundaries (c, e). Skyrmions are tracked on a frame-by-frame basis, and their trajectories are analyzed to extract velocity profiles along the x-direction. The blue dashed lines indicate the lateral confinement of the channels, which is not directly visible due to the use of differential imaging (see Section 3.3.2). b), d), f) Corresponding velocity profiles showing the mean skyrmion velocity (in µm/s) as a function of position across the channel width (y-direction), derived from the tracked trajectories. Taken from [342]

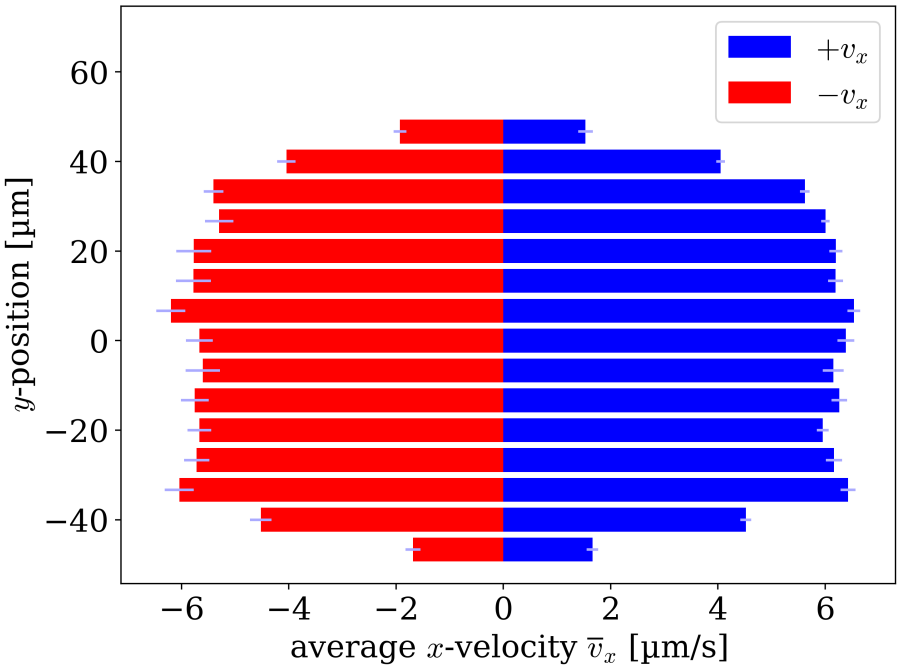

FIGURE 4.6: Velocity profiles of skyrmion flow in a geometrically modulated channel for both current directions. The blue curve corresponds to an applied electric current of +25 µA, while the red curve represents the velocity profile for -25 µA. These values correspond to a current density of approximately $3,1 \cdot 10^7 A/m^2$ in the narrowest part of the modulation of the channel. The near-symmetric shape of the velocity profiles, which can be mapped onto one another by reversing the sign of the current, indicates that the observed asymmetries in flow dynamics are most likely a result of the stochastic non-flat energy landscape rather than the skyrmion Hall effect. If the latter were dominant, a reversal in current direction would lead to distinctly different profiles due to the direction-dependent transverse deflection. Taken from [342].

To further investigate skyrmion flow behavior in the creep regime, quasi-particle simulations were performed using an extended Thiele equation framework (see Section 2.2.3). The experimental velocity profiles were compared qualitatively to simulations in matching channel geometries. Note that the simulations operate in an arbitrary time unit (τ), and hence direct time-scale comparisons are not applicable. Since the experimental skyrmion Hall angle is negligible
($\theta_{\mathrm{skHA}} = (0.58 \pm 0.13)^\circ$), the simulations were carried out with $\theta_{\mathrm{skHA}} = 0^\circ$, effectively removing the Magnus force.
In the simulations, skyrmions are modeled without inertia or mass [74, 76], so upon collisions their velocity is instantaneously reduced to zero but immediately restored to the maximum driving velocity. As a result, the simulated flow mimics that of particle-like systems such as colloids rather than classical viscous fluids [343–345], showing no sharp velocity drop at the boundaries. The Thiele equation used for the quasi-particle simulations:

$$-\gamma \mathbf{v} - \mathbf{G}^z \times \mathbf{v} + \mathbf{F} = 0 \tag{4.1}$$

with the friction coefficient γ, instantaneous velocity $\mathbf{v}$ induced by the total force $\mathbf{F}$, and gyrotropic vector $\mathbf{G}^z = (0, 0, G)$ responsible for the skyrmion Hall effect.

$$|\mathbf{v}| = |\mathbf{v}_{\max}| = |\mathbf{F}_D|\gamma \tag{4.2}$$

The simulations with $\Theta_{\mathrm{SkHA}} = 0^\circ$ is compared with the experimental data for the same modulated channel geometry. As seen in Figure 4.7, the simulated velocity profile is flatter in the middle, while showing slight asymmetry towards the outer modulation. The experimental velocity profile exhibits influence of the non-homogeneous energy landscape in the middle and qualitatively similar characteristic at the boundary.

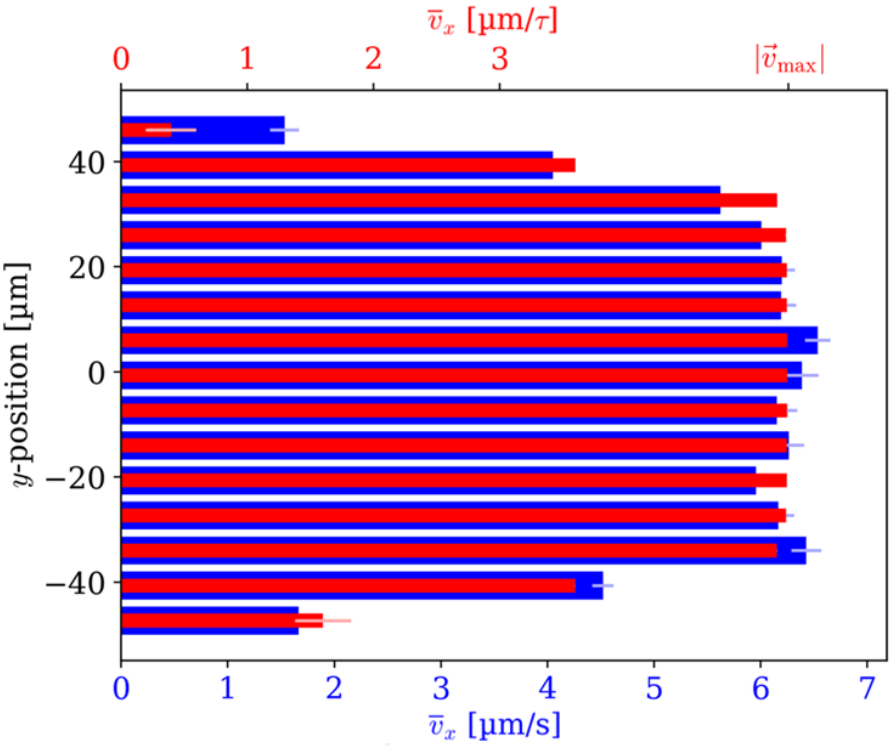

FIGURE 4.7: Skyrmion velocity profiles in a modulated channel of 80 µm width, comparing averaged experimental data (blue, in µm/s) with simulation results (red, in µm/*tau*, where *tau* denotes the simulation time unit). In both cases, the velocity profiles flatten in the central region of the channel. Unexpectedly, the velocities at the modulated boundaries are more symmetric for the experimental data, even though no SkHA was set in the simulation. Taken from [342].

4.4.2 Asymmetric Skyrmion Flow

An important aspect of current-driven skyrmion dynamics not yet addressed is the transverse motion induced by spin-orbit torque, commonly referred to as the Skyrmion Hall effect (see Chapter 2, Section 2.4.5) [97, 183–187]. This phenomenon causes skyrmions to deviate from the direction of the applied electric current, resulting in motion at a finite angle relative to the current axis. This deflection angle is termed the Skyrmion Hall angle. The presence of this effect leads to asymmetric flow behavior, particularly at high skyrmion velocities (on the order of m/s), where skyrmions are driven toward one edge of the confining geometry. This lateral drift increases the likelihood of pinning or annihilation at the boundary, posing a significant limitation for prospective applications such as racetrack memory [29, 48], where reliable and confined skyrmion motion is essential.

To assess the influence of the skyrmion Hall effect on flow dynamics within the experimental channel geometries and additional simulated modulation, the Magnus term was incorporated into the Thiele equation framework. By setting the gyrocoupling constant to G = 0,25 and damping ratio γ = 0, a skyrmion Hall angle of approximately 15° is introduced into the simulated system. This results in a transverse driving force and breaks the mirror symmetry of the skyrmion trajectories along the channel width.

It is worth noting that in the creep regime explored here, lower skyrmion velocities naturally lead to a reduced effective skyrmion Hall angle. In experiments, higher applied currents would increase skyrmion velocity, reduce the influence of pinning, and amplify the observable Hall effect. However, such regimes could not be probed within this study due to experimental constraints such as limited temporal resolution and image contrast.

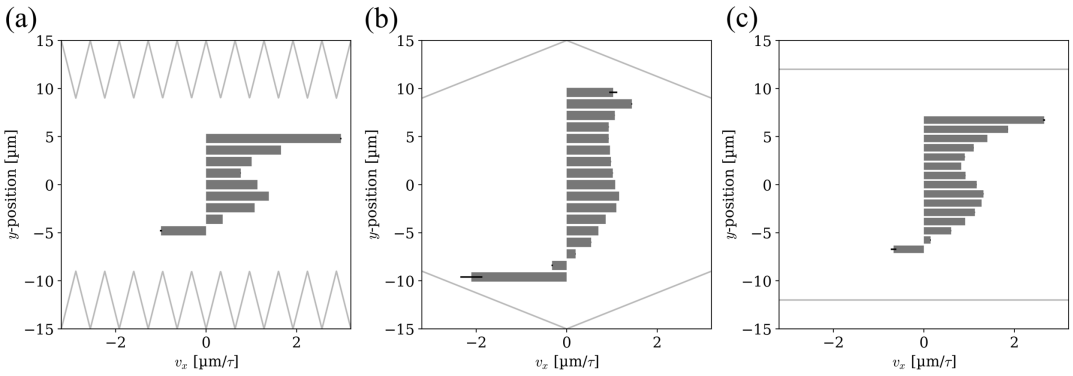

FIGURE 4.8: Flow profiles are shown for modulation lengths of a) 3 µm, b) 30 µm, and c) flat interfaces with equivalent sample area. Backflow is observed in all geometries, but is more pronounced in the modulated configurations where sufficient space allows skyrmions to traverse between adjacent triangular boundaries. The corresponding confinement geometries are illustrated in light gray, with the vertical positions aligned to the y-axis and the horizontal dimensions adjusted to accurately reflect the proportions of the triangular features. Taken from [342], supplementary materials.

4.4.3 Flow phenomenon: Backflow

In the simulations, various novel channel modulations were investigated under the condition of a constant skyrmion Hall angle (see Figure [other channel modifications]). In the absence of pinning and with all other forces symmetric, the inclusion of the skyrmion Hall effect alone causes the skyrmions to be deflected toward one side of the channel. This asymmetric deflection results in a non-uniform distribution of flow: skyrmions accumulate along the upper boundary (in the direction of the Hall deflection), where interactions with both the channel modulation and neighboring skyrmions increase. Conversely, the lower region of the channel experiences a relative reduction in skyrmion density, allowing for more unobstructed flow.
This imbalance leads to an increase in the average velocity near the bottom boundary, while complex dynamical phenomena emerge at the top edge. One particularly notable effect is backflow, wherein a skyrmion—due to repulsive interactions—forces another into the triangular modulation near the upper boundary,

resulting in motion opposite to the applied drive. In regions where the current density is reduced (e.g., inside the wider triangular pockets), such backflow can lead to an overall negative mean velocity locally at the top of the channel. Figure 4.9 illustrates this behavior, showing the interaction-driven reversal of motion within the confining geometry.
Backflow was observed not only for the modulation geometry used in experiments but also for channels with steeper and flatter modulations. The phenomenon is more pronounced in geometries that allow a larger transverse flow path, as shown in Figure [negative velocities]b. Interestingly, backflow was also detected in channels with flat or straight boundaries, highlighting that modulation is not a strict prerequisite. Rather, backflow results from the interplay between the skyrmion Hall effect, the driving force, and skyrmion-skyrmion interactions under confinement.

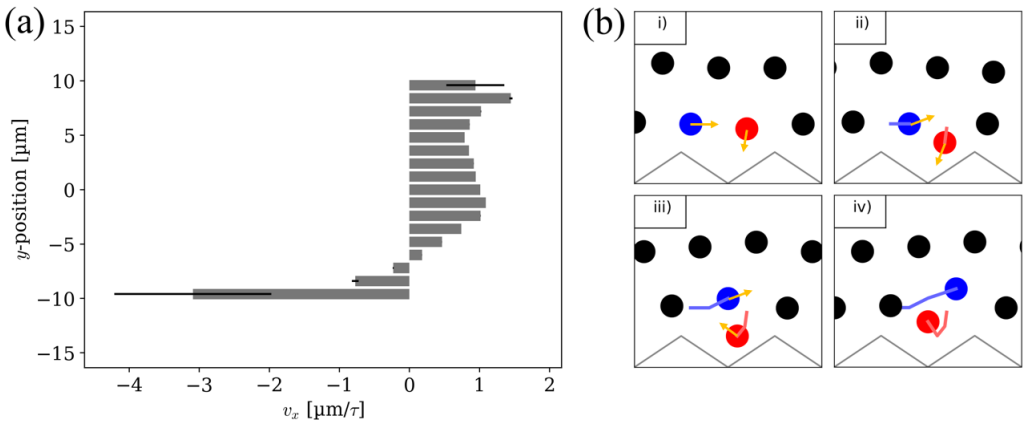

FIGURE 4.9: a) Simulated asymmetric velocity flow profile of a 20 µm channel with oblate modulation as seen in b) and skyrmion Hall angle of $\theta_{\mathrm{skHA}} = 15°$. The mean skyrmion velocity at the upper edge is negative, implying that skyrmions flow opposite to the applied driving force inside the modulation. b) Example of the dynamic process of backflow occurring at the upper edge, leading to negative mean velocities. Skyrmions experience a force from left to right due to SOT but will also be pushed downwards due to the skyrmion Hall effect. This results in the skyrmion marked red to be pushed into the space created between the flowing skyrmions and two triangle tips (i-ii). (iii-iv) The red skyrmion moves against the applied force and moves back in line with the flowing skyrmions, behind the skyrmion it was initially ahead of. Taken from [342].

The emergence of backflow depends critically on the balance between skyrmion Hall angle, driving force, and local skyrmion density near the upper boundary. A sufficiently high skyrmion Hall angle is required to drive skyrmions close to the boundary, where crowding and geometric constraints can induce this counter-intuitive motion.
Experimentally, backflow has not been observed in the current study. As discussed previously, the skyrmion velocities required to achieve a significant skyrmion Hall angle (e.g., $\theta_{\mathrm{skHA}} = 15°$) exceed the limitations of our imaging setup, particularly in terms of temporal resolution and contrast.

4.5 Conclusion

This chapter explored the flow dynamics of skyrmions in the creep regime—characterized by externally driven, low-velocity motion—within both straight and periodically modulated 2D channels. In this regime, skyrmion motion arises from a combination of SOT-driven drift along the current direction, thermally activated diffusion, and the influence of a non-uniform energy landscape. Due to the low velocities involved, the contribution of the Magnus force, as described by the Thiele equation, is negligible and thus can be omitted in first-order approximations.
Experimental observations of skyrmion flow in both geometries showed strong agreement with Thiele-based simulations, revealing a range of flow and velocity profiles modulated by the confining boundary geometry. In wider straight channels, the influence of the boundaries is reduced, leading to a near-uniform velocity profile dominated primarily by the underlying energy landscape. In contrast, in narrow modulated channels, the velocity profile becomes parabolic, indicating strong confinement and partial or no-slip boundary conditions, reminiscent of viscous flow in soft matter systems.
Additional simulations incorporating a fixed $\theta_{\mathrm{skHA}} = 15^{\circ}$ demonstrated that the inclusion of the Magnus term introduces notable asymmetries in the creep flow-deviating from classical quasi-particle behavior. These asymmetries result in novel phenomena such as localized backflow, previously predicted in particle-based models but not observed in conventional systems.
Fundamentally, skyrmions in confined geometries exhibit transport behavior analogous to other overdamped macroscopic particles, such as colloids, but with additional tunable degrees of freedom arising from their topological nature. While research into skyrmion hydrodynamics is still emerging, the ability to control boundary interactions, skyrmion size, and density in real time positions skyrmion systems as promising platforms for investigating fundamental transport processes in non-equilibrium statistical physics.

The next chapter expands on these findings by introducing additional methods for tuning skyrmion size, lattice density, and confinement, enabling more precise control of skyrmion-based transport.

Chapter 5

Skyrmion Compression

Skyrmions exhibit a broad size distribution, ranging from micrometer-scale to nanometer-scale skyrmions, each characterized by distinct physical properties [115, 119]. These topological spin textures are of particular interest for applications in unconventional computing paradigms (see Section 2.7) [113, 325] and next-generation data storage technologies [29, 48], where their size, dynamical behavior and energy efficient driven motion play pivotal roles. Owing to their nanometer-scale dimensions, skyrmion-based devices offer promising prospects for miniaturization, potentially enabling high-density, energy-efficient systems.
To date, the skyrmion size has been extensively studied [119] both theoretically [127, 135, 139, 145, 193, 346, 347] and experimentally [110, 128, 136, 348], with dependencies identified on various factors such as material parameters [130, 136, 144], applied magnetic fields [110, 128, 139], temperature [110, 125, 139, 140, 349], and local energy landscape [157] with inhomogeneities like pinning sites. Among the mechanisms enabling skyrmion manipulation, SOT has emerged as particularly efficient, enabling fast and controlled motion, which is central to most envisioned skyrmion-based applications. However, the impact of SOT on skyrmion morphology - specifically its size and shape - remains largely unexplored.

This chapter demonstrates that skyrmions driven by SOT into structurally confined geometries or artificial barriers exhibit a measurable reduction in size. This size reduction is attributed to increased magnetostatic interactions resulting from compression and the decreased inter-skyrmion (lattice) spacing within the confined region. While this phenomenon has been explored through numerical simulations [143, 350], experimental verification had not yet been achieved.

This behavior bears a conceptual analogy to the vertical distribution of gas particles in an atmosphere, described by the barometric formula [351]. The barometric formula is derived from the condition of hydrostatic equilibrium [352] and the ideal gas law [353–355], expressing the balance between the gravitationally induced compressive force of the overlying atmosphere and the opposing pressure exerted by the lower atmospheric layers. In the isothermal case, increasing compression primarily leads to a reduction in the average interatomic spacing, without significantly altering individual atom sizes.
In the skyrmionic system presented here, current-induced SOT compresses skyrmions against artificial boundaries, reducing not only the average spacing between individual skyrmions but also their intrinsic size. This results in a unique 2D system that emulates internal pressure effects akin to those in gaseous systems - yet within a solid-state context where such behavior is typically difficult to replicate, for instance with colloidal systems [343, 344] that exhibit only fixed sizes. Before examining the implications of confinement-induced modifications in skyrmion size

and inter-skyrmion spacing, this chapter first addresses the qualitative effects of ion irradiation (see 3.5) on the magnetic properties of the employed thin film stack, as well as its role in creating artificial skyrmion boundaries that remain permeable to electrical currents.

5.1 Ion irradiation

Irradiation refers to the deliberate exposure of materials to highly accelerated ions, which may range from light noble gas atoms to heavier elements of the light atoms such as Gallium. As described in Chapter 3, irradiation using ions - specifically Gallium - is commonly carried out using a FIB system. In this process, Gallium, which has a low melting point of 29.8°C [319], is liquefied and subsequently ionized and accelerated toward the target multilayer stack. Ion irradiation significantly modifies the magnetic properties of thin films, most notably the PMA [253, 312–314, 317]. At low ion doses, irradiation can enhance PMA due to an annealing-like effect that promotes crystallization and atomic ordering. However, at higher doses, interfacial intermixing becomes dominant, disrupting the delicate interface structure and thereby reducing PMA. This effect is particularly critical at interfaces responsible for anisotropy induction, such as the CoFeB/MgO interface [44, 253, 314] used in the present samples and in magnetic tunnel junctions.
Miki et al. reported that ion irradiation in a similar sample post exposure can induce gradual, time-dependent modifications in magnetic thin films over the course of several months. This continued aging effect changing material properties is attributed to ongoing atomic diffusion and interfacial intermixing processes triggered by the initial irradiation [155]. Potential annealing could improve the atomic diffusion and intermixing, remove atomic vacancies, and, slowly cooled down, remove strain and stop this time-dependent change in properties.

Beyond a critical irradiation dose, the effective anisotropy constant K_{eff} becomes negative. In this regime, shape anisotropy prevails over weakened interfacial anisotropy, causing a reorientation of the magnetization from OOP to IP. This transition has been observed to occur irrespective of the ion species used, with both heavy and light ions (e.g., He, Ne) producing qualitatively similar effects on magnetic anisotropy [44, 158, 198]. The underlying mechanism appears to depend not solely on atomic mass but rather on the ion momentum - determined by both mass and acceleration - which is sufficient to induce atomic displacements at the interfaces. Light ions such as helium or argon exhibit high mobility and low solubility in metallic systems, allowing them to diffuse out of the thin film stacks, particularly at elevated temperatures or in uncapped structures. In contrast, heavier ions possess greater mass and lower mobility, leading to their implantation and permanent incorporation into the material, which can result in lasting structural and magnetic modifications. Interfacial intermixing also modulates the interface-sensitive DMI, thereby enabling precise tuning of its strength and symmetry [315]. This suggests that irradiation-driven modulation of primarily anisotropy and secondly DMI is a generalizable phenomenon across various ion species and energies.

Ion irradiation can also be employed to engineer artificial pinning sites by locally modifying the magnetic anisotropy of thin film stacks [158, 169]. As domain walls propagate into regions with strong PMA, they encounter a higher associated energy density. In contrast, regions with locally reduced PMA - caused by ion irradiation

- exhibit a lower domain wall energy density. This energy gradient promotes the preferential localization and pinning of domain walls within the irradiated areas, driven by energy minimization principles. Gruber et al. demonstrated that skyrmions are predominantly pinned at their domain walls rather than at their cores [157], suggesting that such irradiation-induced modifications can be strategically utilized to control skyrmion pinning based on skyrmion size or domain wall characteristics.

The exposure also exerts a substantial influence on the saturation magnetization of the FM layer [44, 158, 196]. Typically, the saturation magnetization decreases monotonically with increasing irradiation dose due to ion implantation and interfacial intermixing within the thin film layers [253]. Even though this effect of ion irradiation on saturation magnetization is generally less pronounced than its influence on the magnetic anisotropy, high irradiation doses can induce significant and irreversible changes to the stack. At critically high doses, the irradiated area undergoes a transition from ferromagnetic to paramagnetic behavior [313], marking the loss of long-range magnetic order and the suppression of spontaneous magnetization.

When the irradiation dose exceeds a critical threshold, the induced transition to in-plane magnetization gives rise to a repulsive interaction between magnetic domains or topological structures, such as skyrmions, and the irradiated region. This repulsion is primarily attributed to the mismatch in stray field configurations: non-irradiated regions with strong PMA support alternating up- and down-oriented OOP magnetization, thereby minimizing stray field energy. In contrast, irradiated regions with IP magnetization contribute negligibly to the stray field. As a skyrmion approaches such a boundary, the reduced compensation of stray fields leads to an energetic gradient, raising the local energy density. Due to energy minimization, this generates a repulsive interaction analogous to the skyrmion-edge repulsion observed at physical boundaries or between skyrmions [163, 173, 356], effectively driving the skyrmion away from the irradiated zone (and from each other).

The irradiation-induced repulsion provides a non-structural, tunable method for locally confining skyrmions [198], enabling the creation of artificial magnetic boundaries that are permeable to electric currents. Such boundaries offer a promising approach for spatially controlled skyrmion manipulation, with significant potential for application in skyrmion-based spintronic devices.

5.2 He^+ irradiation

To illustrate the significant potential of ion irradiation for the precise tuning of skyrmion properties and the creation of artificial magnetic boundaries, the promising thin film skyrmion sample MVK763 was partially irradiated by the external company Spin-Ion Technologies[1]. As the irradiation process was conducted externally and without direct involvement in the procedure, specific details regarding the irradiation parameters - such as ion energy and dose - were not disclosed.

Approximately half of the MVK763 sample was subjected to irradiation, resulting in a localized modification of its magnetic anisotropy. The boundary between the irradiated and non-irradiated regions was identified using PMOKE microscopy.

[1] https://www.spin-ion.com/ [320]

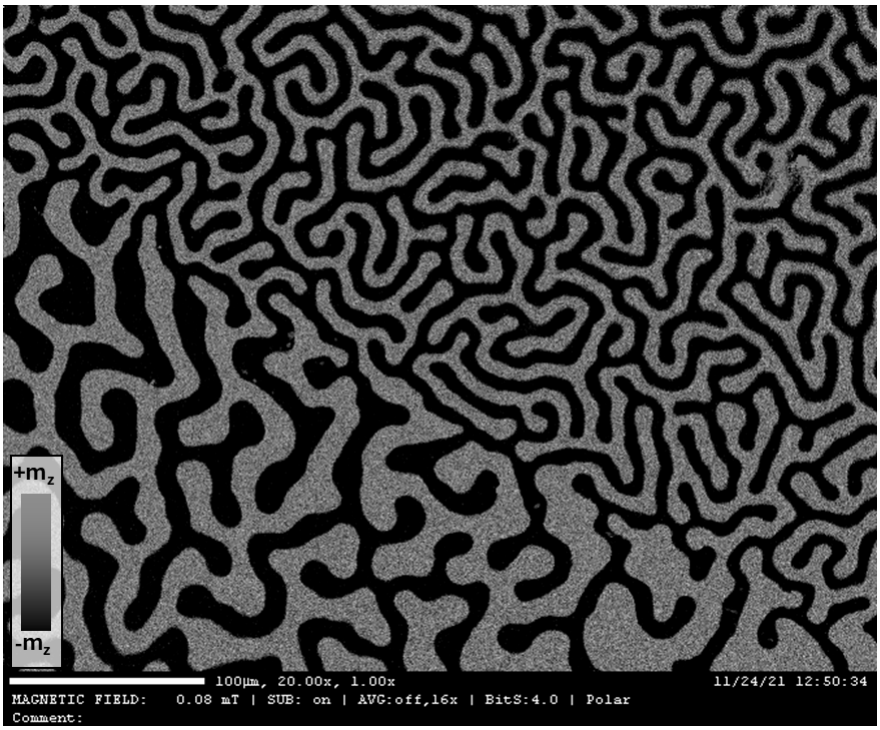

FIGURE 5.1: A PMOKE differential image of the MVK763 sample at room temperature reveals out-of-plane magnetic domain contrast, with alternating light and dark grey regions corresponding to opposing magnetization directions. The image captures the boundary between the irradiated region (left and bottom) and the non-irradiated region (top right), with a distinct transition line clearly delineating the two areas. Near zero applied magnetic field, the non-irradiated region (top right) exhibits smaller but more densely packed domains, indicative of stronger PMA. In contrast, the irradiated region (bottom left) shows larger, more widely spaced domains, consistent with a reduced PMA. Furthermore, the bottom right corner displays an asymmetry in domain distribution, characterized by an apparent bias toward one magnetization polarity - evidenced by a predominance of light grey domains over dark grey - suggesting a locally imbalanced magnetic state, possibly due to a slightly higher irradiation dose in this area.

This boundary provides a clear visual representation of the spatial variation in magnetic properties caused by irradiation, as evidenced by the distinct domain structures observed under the same applied OOP magnetic field, shown in Figure 5.1.
In the top-left portion of the sample, the worm-like domain patterns exhibit a periodicity of λ = 7,3 $\pm$ 1,1 µm, whereas in the lower-left area, the periodicity increases to λ = 11,3 $\pm$ 1,8 µm, indicating a reduction in effective anisotropy. Furthermore, spatial variation is observed between the right and left regions of the sample, with a noticeable increase in positive m_z magnetization bias. Figure 5.2 presents the corresponding local hysteresis loops, further confirming regional differences in anisotropy.
It is hypothesized that the lower-right region of the sample received a slightly higher irradiation dose than the remainder of the irradiated area. This conclusion is supported by the absence of observable temperature or magnetic field gradients during the irradiation process, suggesting that dose variation is the primary factor influencing the observed anisotropy differences.

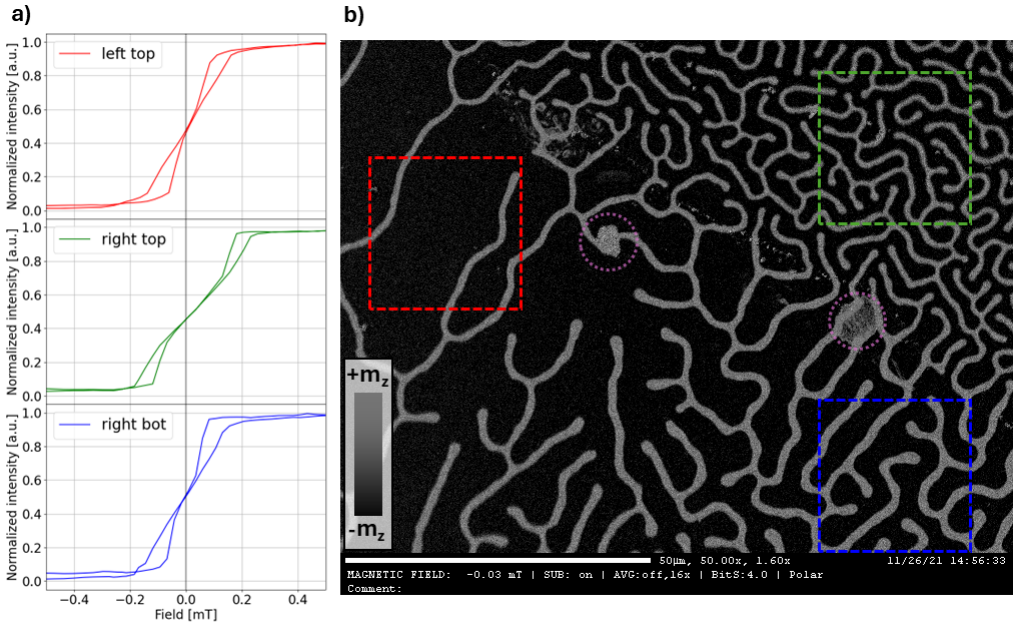

FIGURE 5.2: Colored hysteresis loops corresponding to distinct regions of interest (ROIs) in a differential MOKE image of the irradiated MVK763 sample are presented, highlighting the magnetic response across the boundary between irradiated and non-irradiated areas. Three ROIs exhibiting different magnetic properties are clearly distinguishable, as evidenced by the variation in domain sizes and coercive fields. The region marked in green exhibits a characteristic "butterfly"-shaped hysteresis loop, indicative of skyrmionic behavior and reduced PMA. In contrast, the region highlighted in red corresponds to the lower corner of the previously shown image (Figure 5.1) and displays a further reduction in coercivity, consistent with increased irradiation dosage and a subsequent decrease in PMA. A third ROI, outlined in purple and located along the irradiation boundary, shows signs of image artifacts. These are likely residues from resist or adhesive tape used to mask or protect portions of the sample during the irradiation process. It is important to note that the field of view in this image is not identical to that of Figure 5.1 but is instead positioned further along the irradiation boundary. The magnetic contrast across these regions reinforces the spatially dependent modification of magnetic anisotropy induced by ion irradiation.

5.2.1 Differences between treated and untreated area

Treatment as artificial boundary

As shown in Figures 5.1 and 5.2, a distinct boundary between the untreated and irradiated regions is evident, marked by a change in the distribution and periodicity of worm-like magnetic domains. From the perspective of skyrmion dynamics, this boundary functions as an effective energy barrier. Skyrmions are unable to traverse from the non-irradiated (as-grown) region into the irradiated region, as doing so would require them to overcome a localized change in magnetic anisotropy, which introduces an energy penalty. Figure 5.3 illustrates this barrier effect: despite the fact that both regions support skyrmion formation - as evidenced by the presence of a stable, isolated skyrmion in the irradiated area (bottom left) - skyrmions originating in the non-irradiated domain remain confined and do not cross into the irradiated side. This indicates that the anisotropy gradient at the boundary acts as a selective and robust confinement mechanism for skyrmions, even when the magnetic parameters in both regions permit their existence.

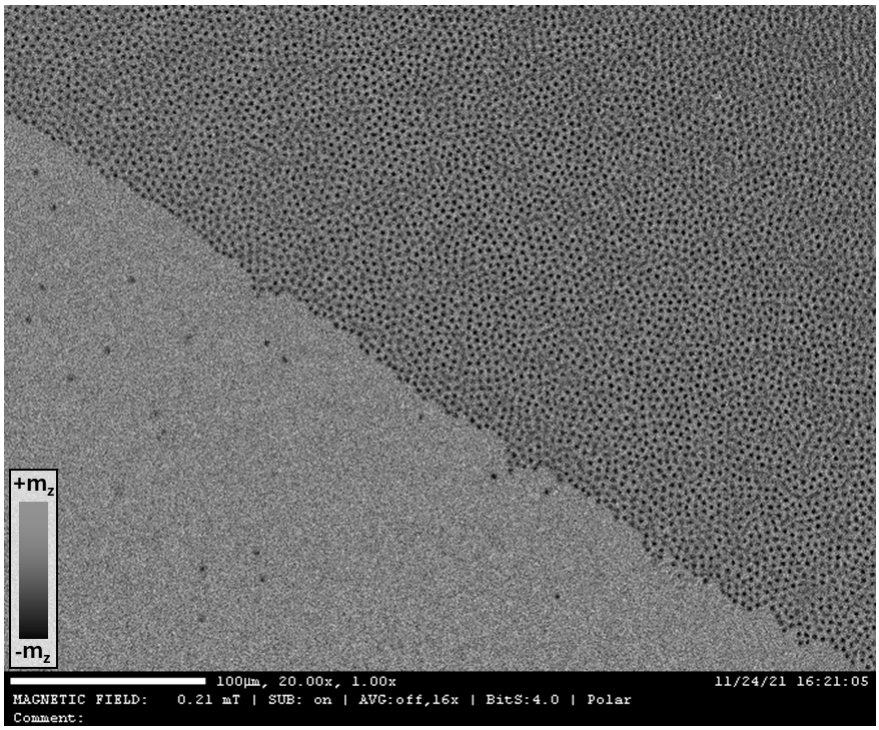

FIGURE 5.3: PMOKE differential image of the MVK763 sample recorded at 322.7 K and 210 µT OOP field reveals a dense skyrmion lattice in the untreated top-right region, with the skyrmions exhibiting alignment along the boundary with the irradiated area. In contrast, the untreated bottom-left region contains individual, slightly larger skyrmions that appear more sparsely distributed and mobile. The irradiation boundary acts as a confining barrier, preventing skyrmion propagation across the interface, thereby spatially restricting their distribution within the untreated area.

This example highlights the potential of ion irradiation as a powerful tool for engineering and precisely tuning boundaries or confinement landscapes for skyrmions and other magnetic textures. In the following sections, the effects of helium ion irradiation on additional skyrmion properties - including skyrmion size, inter-skyrmion spacing, lattice organization, and the emergence of skyrmions with opposite core polarities - are examined in greater detail.

The UNet-based [309] procedure for classifying and identifying skyrmion and their properties (see Section 3.4.3) was applied to a PMOKE differential recording of MVK763 at 311.5 K under an applied magnetic field of $\sim$60 µT, using an inverted gray-scale image (see Section C.2.3 and Figure C.8).

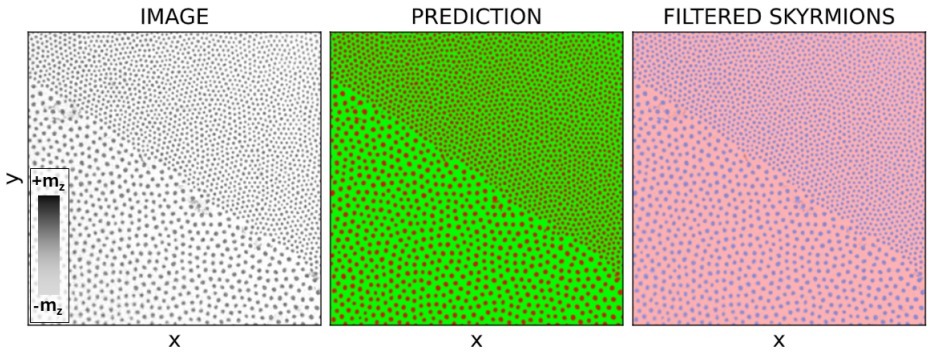

FIGURE 5.4: UNet-based image analysis of a MOKE recording of the MVK763 sample at 311,5 K under an applied nominal magnetic field of 60 µT, illustrating the skyrmion classification workflow. Left: Inverted greyscale image of the raw data. Middle: Pixel-wise classification output of the UNet model, where green represents the non-magnetic background and red corresponds to magnetic structures. Right: Post-processed result showing isolated and filtered skyrmions highlighted in blue against a pink background, corresponding to non-skyrmionic area.

Size: treated vs. untreated regions

As a result of the modified magnetic properties, substantial differences in average skyrmion size, quantity (Figure 5.5), and density (Section 5.2.1) are observed between the irradiated and non-irradiated regions. In the untreated area, the average skyrmion radius is measured to be $r_{untreated} = 1{,}7 \pm 0{,}3$ µm, while in the He^+-treated region, the radius increases to $r_{treated} = 2{,}4 \pm 0{,}3$ µm (Figure 5.6), representing a relative increase of approximately 32.2%.

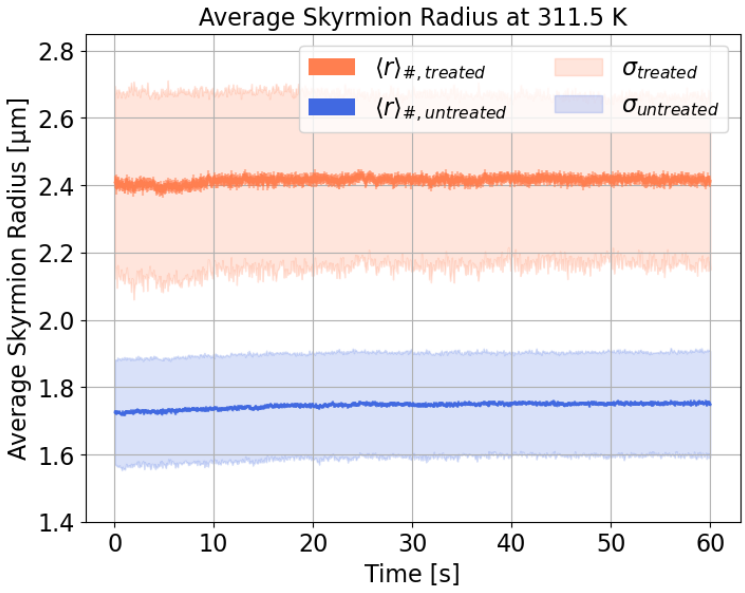

FIGURE 5.5: Average skyrmion radii (in µm) for the treated (orange) and untreated (blue) regions reveal a size difference exceeding 30%. The standard deviation, indicating the distribution of skyrmion sizes within each region, is notably larger on the treated side, likely due to the increased available space allowing for greater skyrmion expansion.

Density: treated vs. untreated regions

The irradiation-induced changes in skyrmion phase and size also affect the skyrmion density. To quantify the skyrmion density for both regions, a square area of 250 × 250 px (equivalent to 166.7 × 166.7 µm^2) was selected for analysis on each side. The skyrmion density was determined to be 3,0 $\frac{\text{skyrmions}}{100\mu m^2}$ in the untreated region and 1,1 $\frac{\text{skyrmions}}{100\mu m^2}$ in the treated region. Considering the average skyrmion sizes previously mentioned, this corresponds to a relative area density of $\frac{A_{\text{skyrmions, top}}}{A_{250\times250\mu m^2}}$ = 29,2% for the untreated side and $\frac{A_{\text{skyrmions, top}}}{A_{250\times250\mu m^2}}$ = 21,1% for the treated side. The relative differences in skyrmion density and skyrmion area density between the untreated (grown-as) and treated regions were calculated to be $\rho_{\text{sky. density}}$ = 92.7% and $\rho_{\text{area density}}$ = 32.2%, respectively.

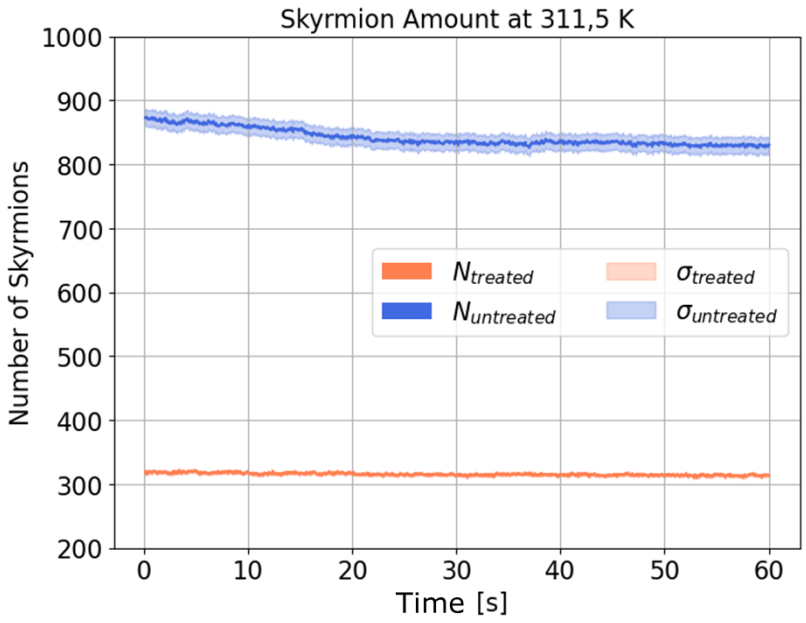

FIGURE 5.6: Number of skyrmions within a 250 × 250 pixel area (corresponding to 167 × 167 µm^2) for each respective region. During the observation period, skyrmions are able to enter and exit the defined area. In the untreated region, the skyrmion lattice is relatively dense and appears to undergo slight relaxation, leading to skyrmions moving out of the region and a corresponding decrease in the skyrmion count (blue). In contrast, skyrmions in the treated region exhibit a lower density and remain largely within the defined area, likely due to a more relaxed state resulting from weaker inter-skyrmion interactions. Consequently, the average skyrmion count remains nearly constant over time (orange)

Distance: treated vs. untreated regions

Under static conditions (311.5 K and 60 µT), the average nearest-neighbor skyrmion distance within the irradiated region remains approximately constant—within the range of measurement noise—indicating a relaxed skyrmion state with minimal spatial constraints. In contrast, the unirradiated region exhibits a denser skyrmion lattice, characterized by significantly reduced inter-skyrmion distances. Over the course of the observation, a slight increase in average distance is observed in the untreated area, which is attributed to gradual lattice relaxation. This relaxation is

likely driven by the annihilation of skyrmions at inhomogeneities, both within and outside the field of view, as e.g. the irradiation boundary itself (see Figure 5.6). As skyrmions annihilate, the remaining skyrmions redistribute to occupy the newly available space, leading to an increase in their average separation (Figure 5.7) and a modest expansion in skyrmion size (Figure 5.5).

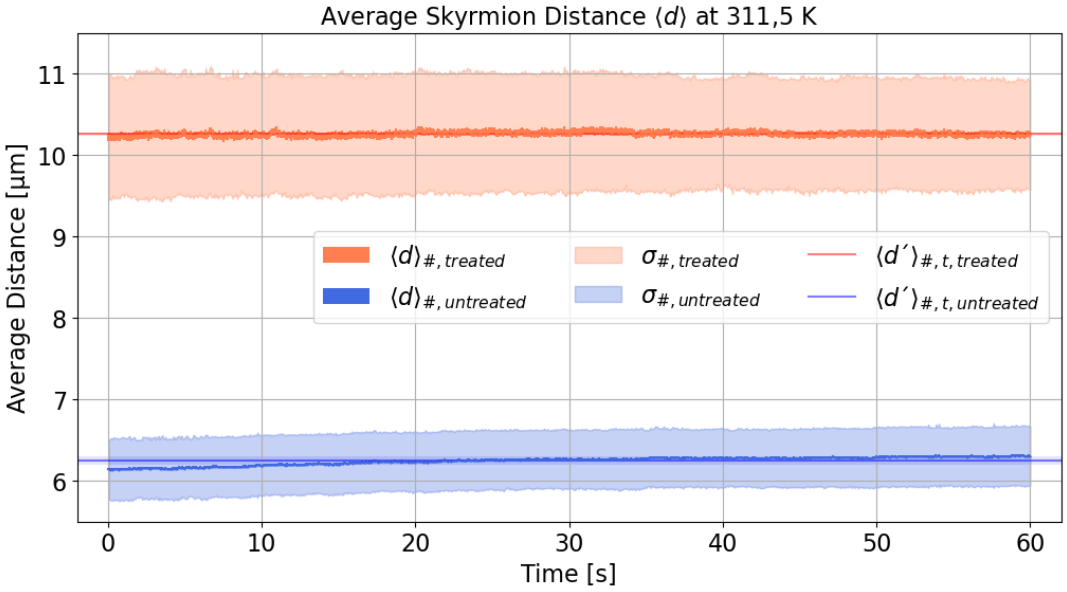

FIGURE 5.7: Average skyrmion distance in the 250×250 px square in the untreated and treated part. The lattice density is visibly different between both sides, with an average distance of . While the averaged (over all skyrmions in the defined area) distance for the treated side stays almost constant, the average distance for the treated side increases slightly, hinting at the slow relaxation process inside the lattice. Also possible is the annihilation of skyrmions outside the field of view, resulting in more space to expand into.

ψ_6 parameter: treated vs. untreated

As discussed in Section 2.4.4, a key parameter for quantifying the local order of the skyrmion lattice is ψ_6, which indicates the degree to which a skyrmion's nearest neighbors align with the sixfold symmetry of the lattice. In the untreated region (top part), the lattice within the selected 250 × 250 pixel area exhibits a ψ_6 value of ψ_6 = 0,63, whereas in the treated region (bottom part), the corresponding value is ψ_6 = 0,52. The lower ψ_6 value in the treated area is expected, as the skyrmions, despite their larger size, exhibit a greater average distance between neighbors, providing more space for diffusion and consequently resulting in poorer local ordering. Furthermore, the treatment boundary impedes the formation of a commensurate, local hexagonal order. The relative difference in local ordering between the untreated and treated regions is calculated as

$$\frac{\psi_{6,\,\text{untreated}} - \psi_{6,\,\text{treated}})}{\frac{1}{2}(\psi_{6,\,\text{untreated}} + \psi_{6,\,\text{treated}})} \approx 19,1\%. \tag{5.1}$$

Overall, the irradiation process significantly impacts the skyrmion properties, with relative differences on the order of tens of percent in the applied parameters (mainly OOP field and temperature), providing a valuable mechanism for tuning

and manipulating magnetic properties, responsible for skyrmion properties and dynamic.

5.2.2 Skyrmions of opposite polarities

Additionally, through the skyrmion nucleation procedure outlined in Section 3.3.3, and under the appropriate bias field and temperature of 319 K, a skyrmion state with opposite polarity was serendipitously achieved. In the treated region, skyrmions exhibit a negative magnetization core (-m_z, appearing bright in the MOKE difference imaging) set against a positive magnetization background (+m_z, appearing dark in the MOKE difference imaging). In contrast, skyrmions in the untreated region exhibit the opposite polarity: a positive magnetization core (bright in dark grey) surrounded by a negative magnetization background (light gray), with both regions separated by the irradiation boundary.

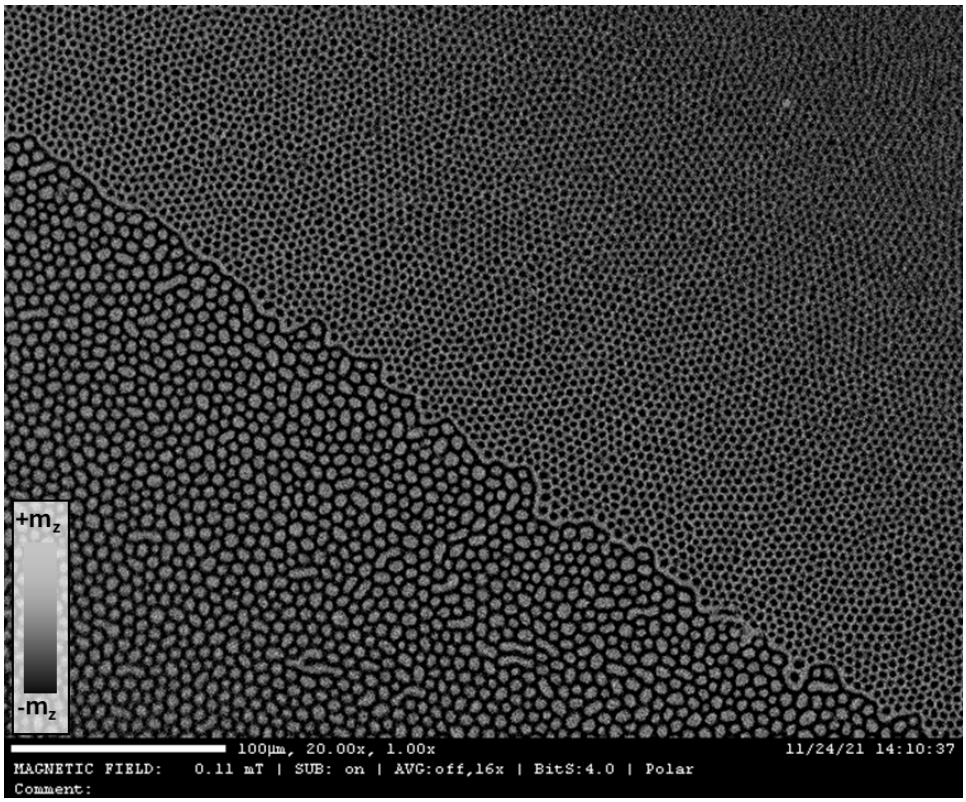

FIGURE 5.8: PMOKE differential image of MVK763 showing the He^+ irradiation treated (bottom left) and untreated (top right) regions. The skyrmion nucleation process at 319 K resulted in a skyrmion state with opposite polarities between the treated and untreated sides. On the treated side, skyrmions exhibit a positive core with a negative background (bright on dark), while on the untreated side, skyrmions display a negative core with a positive background (dark on bright), with both regions separated by the treatment boundary. Notably, the skyrmions differ significantly in terms of size, spacing, and shape uniformity between the two regions, hinting at the irradiation induced altered magnetic properties like PMA and DMI.

This phenomenon is attributable to irradiation-induced interfacial intermixing [253], which modifies both the interfacial PMA and DMI [315], thereby disrupting the delicate energy balance that still persists in the untreated regions. The resulting

altered magnetic properties in that treated region can stabilize skyrmions of opposite polarity, even under a nominally uniform external OOP field that otherwise support a uniform skyrmion polarity in the untreated region.
Moreover, under low OOP bias fields - such as the nominal ∼110 µT applied here, slightly exceeding the double maximum geomagnetic field at Earth's surface - the energy landscape may exhibit degenerate minima. In such cases, skyrmions with opposite core polarity coexist as both configurations are energetically stable in their respective regions. In CoFeB/MgO thin film stacks [253, 314], which inherently support nearly symmetric energy conditions under low-field environments, skyrmion nucleation via IP magnetic field bursts (see Section 3.3.3) can thus generate both core-up and core-down skyrmions, contingent on thermal activation and regional magnetization orientation.

The He^+ irradiation induces a tunable change in magnetic properties in the treated region with a distinct boundary clearly separating the two regions [169, 196]. Significant differences are observed in the size, spacing, and density of skyrmions between the two areas, as well as in the structural uniformity of the treated region. Skyrmions in the treated area exhibit more frequent deformations from a circular structure, while those in the untreated region maintain a more uniform shape. Additionally, skyrmions located near the treatment boundary in the untreated area are slightly larger than those farther from the boundary. These variations are further examined in the following sections. It is important to note that identifying and tracking skyrmions in this particular recording proved challenging due to the opposite gray-scale contrast. Details of the analysis procedure for this recording can be found in Section C.2.3.

Influence on skyrmion properties

Skyrmions on the untreated side, at the given bias field and temperature, exhibit an average radius of $r_{untreated}$ = 1,8 ± 0,3 µm, while on the treated side, the skyrmions have an average radius of $r_{treated}$ = 2,3 ± 0,3 µm, corresponding to a relative increase of approximately 24.4%. It is important to note that due to the dual polarity of the skyrmions, an increase (or decrease) in the bias field causes skyrmions on the untreated side, with their core antiparallel to the applied field, to shrink (or grow), while skyrmions on the treated side, with their core parallel to the applied field, will grow (or shrink) [110, 128]. Additionally, due to the deformation of skyrmions on the treated side, these structures are likely nearing a transition to worm-like domains but remain in the skyrmion state due to confinement within the lattice.

parameter	units	untreated	treated	relative diff.
Radius r	[µm]	1,8 ± 0,3 µm	2,3 ± 0,3 µm	24,4%
Avg. distance $\langle d \rangle$	[µm]	5,4 ± 0,3 µm	7,1 ± 0,3 µm	27,2%
Avg. amount density	$[1/100\mu m^2]$	4,2 ± 0,5	2,3 ± 0,5	58,5%
Avg. area density	[-]	46,8%	39,2%	17,7%
$\langle \psi_6 \rangle$	[-]	0,61	0,56	8,5%

TABLE 5.1: Skyrmion lattice parameters for the treated and untreated side of MVK763 at 319 K and ∼110 µT bias OOP field.

As discussed in the previous section, the quantities for skyrmion size, distance, number density, area density, ψ_6 [175, 176, 332], and their respective relative differences for the recording of opposite polarity skyrmions are summarized in Table 5.1.

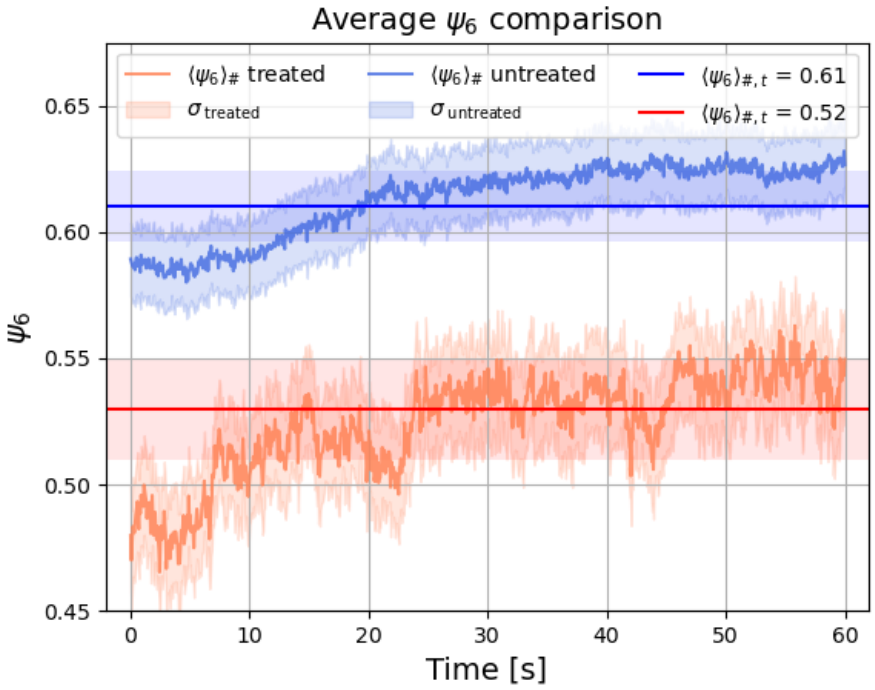

FIGURE 5.9: The development of the overall skyrmion-averaged ψ_6 value per time, representing local ordering, is shown for the untreated (blue) and treated (orange) regions. The blue and orange lines indicate the averaged ψ_6 values across all skyrmions and frames. The shaded areas represent the corresponding standard deviations. As both lattices relax slightly, the ψ_6 value increases for both sides, even though the untreated side has a significantly higher order than the treated side.

If such a state could be reliably realized in systems exhibiting local regions with skyrmions of opposite polarity under identical global conditions, it would introduce novel possibilities for skyrmion-based applications. For instance, in such systems, the skyrmion size could respond oppositely to applied fields, where one skyrmion shrinks while the skyrmion with the opposite polarity expands.

Considering the accumulated relative differences in size, densities, distance, and lattice ordering between the untreated and treated sides in the presented examples, a significant change in skyrmion parameters and phase is observed. This demonstrates the potential for fine-tuning skyrmion properties both locally, for the creation of barrier-like structures, and on a larger scale, for entire regions. Although irradiation is irreversible and permanent, it enhances the available methods for effective and efficient skyrmion manipulation.

5.3 Skyrmion compression

As demonstrated in the previous section, irradiation can be employed to modify skyrmion properties such as lattice density, skyrmion distance, and size due to the change of the magnetic properties [253, 314, 315]. In this section, the concept of compressing skyrmions against an artificial barrier is experimentally explored, along with the resulting effects on skyrmion system size, inter-skyrmion distance, and overall lattice ordering. This concept has been similarly explored numerically in simulation in Ref. [350] and Ref. [143].

5.3.1 Skyrmion nucleation at irradiated barrier

A recurring challenge encountered during the skyrmion flow measurements discussed in Chapter 4 was the control over the number of skyrmions flowing into and through the channel. Since no reliable method for creating additional skyrmions was implemented, other than the system-wide nucleation via IP burst (see Section 3.3.3), only a limited stream of skyrmions, corresponding to the maximum number nucleated, could be moved into and through the MOKE microscope's field of view. The availability of a reliable source for skyrmion generation, or a method to nucleate skyrmions without disrupting pre-existing ones, would significantly enhance the this skyrmion based experiment. In addition to the nucleation process described in 3.3.3, skyrmions can also be created at inhomogeneities such as scratches, holes, or strong pinning sites within the magnetic material, either due to thermal effects, or DC and pulse injection. These sites act as sources for skyrmion formation and subsequent outward movement, akin to an overflowing well, and are thus referred to as skyrmion wells. The irradiation process and its modification of magnetic properties, particularly through local reductions in PMA, can also induce such irregularities, including artificial pinning sites or barriers, which could serve as novel tools for manipulating skyrmion dynamics. Figure 5.10 illustrates the He^+-irradiation boundary at four distinct time points following IP burst nucleation. The images reveal that skyrmions randomly nucleate along the boundary and gradually populate the irradiated region, progressively displacing the pre-existing worm-like domains. This behavior is attributed to the modified magnetic properties at the interface between treated and untreated regions, in combination with thermally activated effects.

Furthermore, by applying current pulses, skyrmions can be nucleated at these sites under the appropriate conditions, including bias OOP field, irradiation-induced reduction in PMA and DMI, temperature, and current (or pulse) strength [96, 142, 294, 329, 357]. The nucleation of skyrmions in the presence of an irradiation-induced barrier, with an increasing dosage gradient towards the center, was tested in a small channel in a FAB629 sample. While skyrmion nucleation was successfully achieved in one of the four channels, its reliability was compromised, as the nucleation process was often interrupted by the formation of worm-like domains. This highlights the sensitivity of skyrmion spin structures to external parameters, as well as the permanent alterations introduced by irradiation. Consequently, reliable skyrmion nucleation without the formation of worm-like domains remains an experimental challenge with the presented thin film samples.

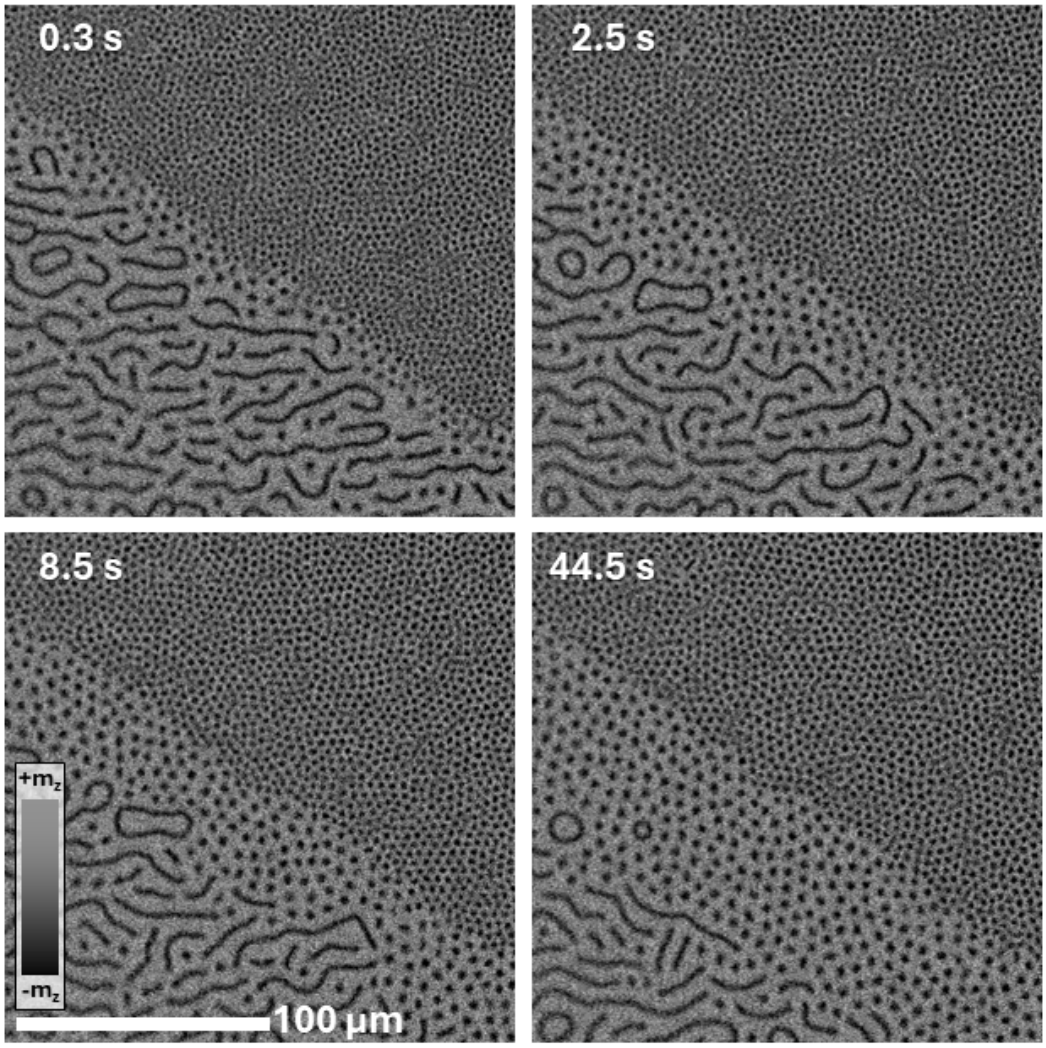

FIGURE 5.10: Differential PMOKE images of He^+-irradiated MVK763 at 322.7 K, captured at identical fields of view, show the system at successive time points following IP burst nucleation. The initial frame corresponds to 0.3 s (5 frames) after nucleation. Skyrmions nucleate stochastically along the irradiation boundary, the effect driven by locally altered magnetic properties and thermally activated processes.

Filling of reservoir

A significant challenge encountered when artificially nucleating skyrmions at irradiated barriers is that the current densities used for skyrmion nucleation and movement into the reservoir are sufficiently high to cause the annihilation of skyrmions at the adjacent electrode structures. This issue complicates the process of filling the reservoir and subsequently increasing skyrmion pressure and potential compression. A dynamic hydrostatic equilibrium, balancing skyrmion nucleation and in-flow with skyrmion annihilation at the electrode, is not achieved. However, skyrmions nucleated via the IP burst in the channel can be directed toward the electrode, where they are annihilated upon the application of sufficient current. Skyrmions moving in the channel outside the field of view flow towards the electrode, with the eventual outcome being either the complete movement of all skyrmions into the field of view, leaving some pressed against the electrode, or the formation of worm-like domains that migrate towards the electrode, entering

the field of view and exerting pressure on the remaining skyrmions. Qualitative observations suggest a size difference between skyrmions near the electrode and those in later stages of movement into the field of view, compared to the original skyrmion size in the lattice post-nucleation. During skyrmion motion induced by SOT, as discussed in the previous section, skyrmions move beneath the gold contact, making them invisible to MOKE imaging. As a result, any changes in skyrmion size or lattice structure beneath the gold contact remain unobservable. To address this, a comb-like structure was designed and fabricated at the ends of the channels using lithography (see Figure 5.11). The protrusions in the structure are 1.5 µm wide, spaced 1.5 µm apart, and are specifically engineered to be too narrow for the skyrmions, at the applied temperature and field conditions, to flow into. However, current can still pass through these protrusions into the chromium/gold contact. Skyrmions are also repelled by the edges of the protrusions, maintaining a specific distance from them due to skyrmion-edge repulsion.

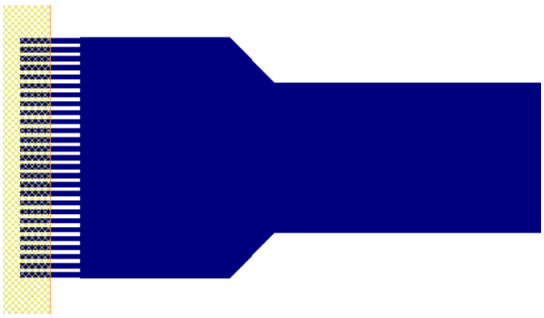

FIGURE 5.11: PIONEER layout with the stack in blue and overlaying Chromium/Gold contact in hatched yellow. Protrusions allow for current to pass through them and the channel while impassable for skyrmions due to the narrow width.

5.3.2 Theoretical ansatz

An appropriate theoretical framework, grounded in experimental observations, has been developed by K. Leutner (see Sections 2.4.6 and C.1). This model suggests that skyrmion ensembles respond to SOT-induced forces exerted on a barrier, effectively generating a pressure analogous to the atmospheric pressure resulting from gravitational forces acting on gas molecules, as described by the barometric formula. The key distinction between this pressure and the inert gas pressure due to gravity is that, in the case of skyrmions, not only do the average distances between individual constituents decrease with increasing pressure, but the size of the constituents at the confining barrier also reduces. The dynamics underlying this behavior are derived from an adapted version of the Thiele equation, as outlined in Section 2.2.3, and are further corroborated through simulation results.

5.3.3 Experimental observations

Field offset

All experimental measurements were conducted at 300 K to minimize the influence of temperature on the skyrmion size. To assess the impact of the OOP bias field and its potential offset, the size of free skyrmions was measured in increments of 5 µT, beginning with the lower field limit where skyrmions begin to transition into

worm-like domains and ending at the upper limit where skyrmions are annihilated. Skyrmions were nucleated using an IP burst, and their numbers were progressively reduced by carefully increasing the OOP field until only a few free skyrmions remained. The field was then decreased, and the skyrmion size was measured at various points. Size data for skyrmions with both positive and negative polarities were linearly extrapolated, and the intersection point was calculated to be B_{offset} = -38.0 µT, which corresponds approximately to the Earth's magnetic field in Mainz at a latitude of 50°.

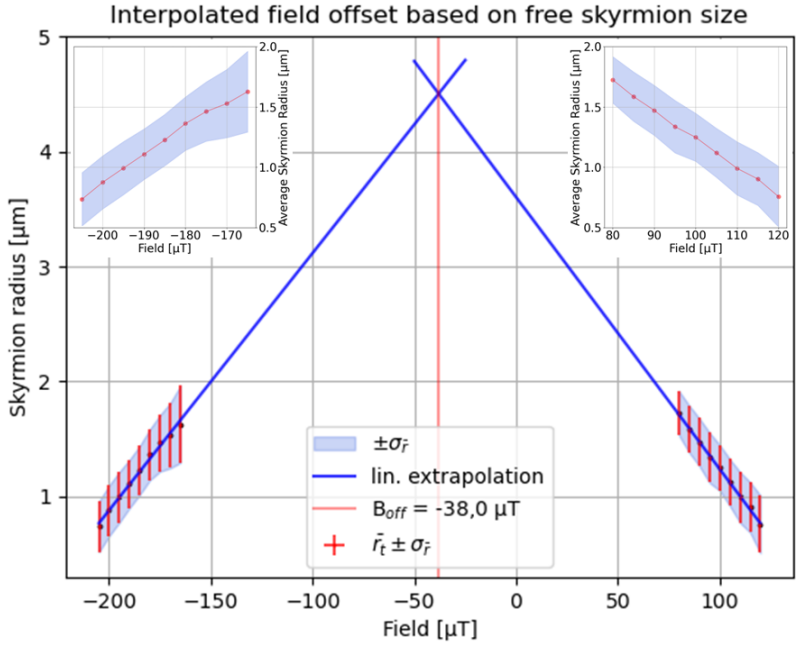

FIGURE 5.12: Skyrmion size measurements for both skyrmion polarities (red) were conducted to determine the field offset (opaque red line) through linear extrapolation (blue), assuming a linear field dependence as described in previous works [110]. At the lower field limit, skyrmions elongate into worm-like domains, while at the higher field limit, skyrmions become too small and begin to annihilate randomly. The shaded region represents the standard deviation of the skyrmion size across all skyrmions and frames within the recorded data. The derived field offset is B_{offset} = -38 µT, which corresponds approximately to the earth's magnetic field at a latitude of 50°.

5.3.4 Artificial skyrmion barriers

Sample TMD109 was structured using the lithography procedure outlined in Section 3.2. A key feature of the structure is the comb-like barrier, composed of protrusions at the ends of the channels, which allows electrical current to flow while preventing skyrmions from passing due to size constraints and skyrmion-edge repulsion. In addition, Ga^+ irradiation was applied in a straight line across the channel (see Figure 5.13 (violet)), with a dose gradient (as detailed in the Section C.3.1) to serve a dual purpose: to nucleate skyrmions and to create an artificial barrier. However, nucleation via current at the irradiated sites was not achieved, and the irradiated region was utilized solely as an artificial barrier. Further research on the used stacks is required to investigate reliable skyrmion nucleation at irradiation sites and its dependence on various parameters, including e.g., stack composition, irradiation

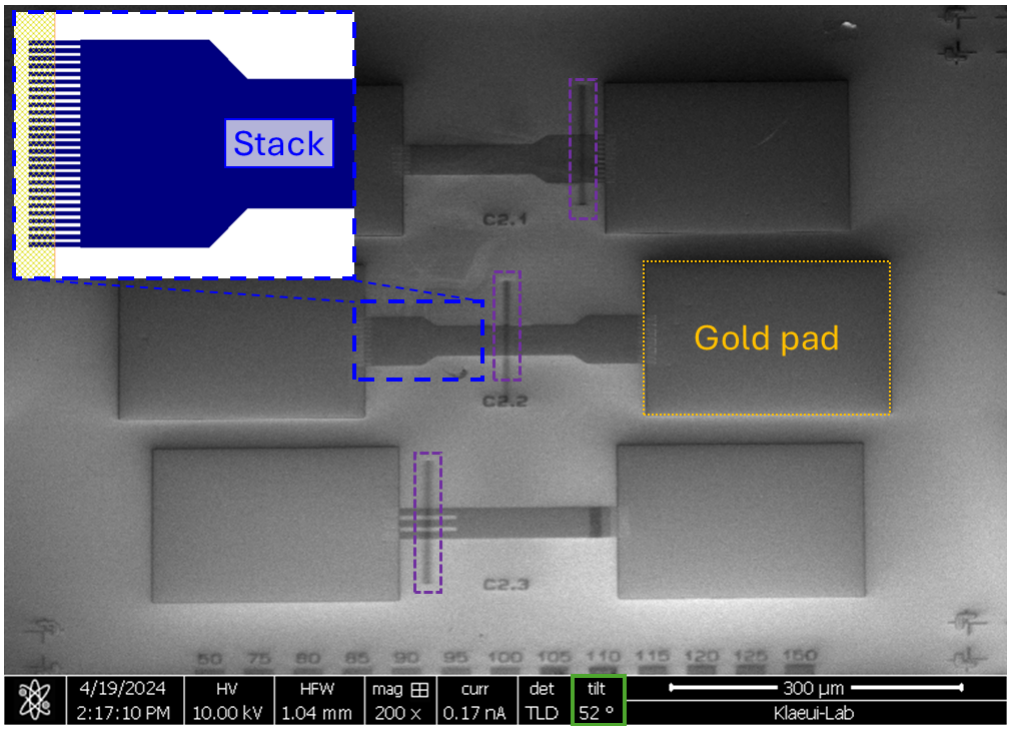

FIGURE 5.13: SEM image showing distorted structures captured at a tilt angle of 52° (green). Three structures treated with Ga^+ irradiation are visible, with the irradiation zone indicated by a dark line (violet). The data presented corresponds to the central structure, C22, with the lithography layout shown in the inset (blue). For reference, the gold pad is outlined by a yellow dashed box.

dose, temperature, current densities, pulse widths, and bias fields. Achieving reliable nucleation at specific sites could significantly enhance the potential applications of skyrmions in storage and non-conventional computing technologies.

Size determination

Given the critical need for a reliable method to determine skyrmion size, the video analysis using UNET offers an efficient and dependable approach, once the recording and UNET [309] filtering parameters are configured. UNET estimates the skyrmion size by fitting two Gaussian curves along the longest axis and its perpendicular short axis, which approximate the skyrmion's edge. These curves form a convex hull, and the number of pixels within the hull is counted to represent the skyrmion's area. It is important to note that during the investigation, the skyrmion size is presented as the radius (in µm) of a theoretical perfect circle corresponding to the area determined by UNET in pixels. The average eccentricity of the skyrmions over time, which reflects the deviation from a perfect circle due to compression or deformation, is discussed in section C.3.3.

5.3.5 Experimental measurements

Significant changes in both size and lattice structure were observed for skyrmions subjected to pressure against the structured comb and the irradiated artificial barrier. In this thesis, only the results from one specific measurement will be examined

in detail. Additional measurements were conducted at the same constant temperature, with skyrmions pressed against both the structural comb barrier and the irradiated barrier. For each setup, two system states were considered: one with a densely packed skyrmion lattice, as nucleated, and another where the lattice density was reduced by increasing the bias field after nucleation.

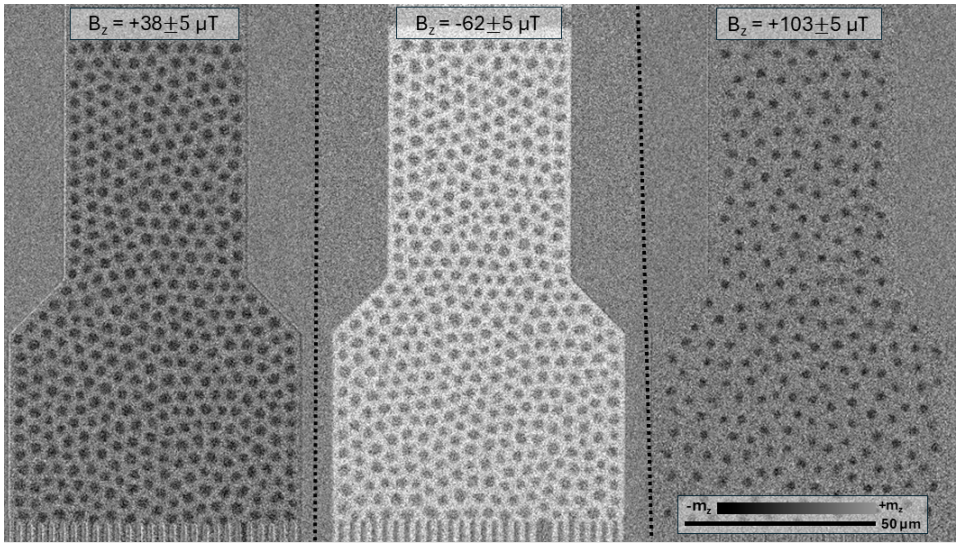

FIGURE 5.14: Structure C22 under varying bias OOP fields and lattice states. The top and middle images correspond to a densely packed lattice as initially nucleated, while the bottom lattice represents a state where the bias field was increased to modify skyrmion size and inter-skyrmion distance. Skyrmions in the high-density lattice, when pressed against the irradiation barrier, exhibit a larger size than the average, attributed to the reduced PMA and DMI.

It is important to note that the skyrmion size for the free skyrmions, as presented earlier in Section 5.3.3, differs significantly from those nucleated into a lattice state. This suggests an internal inert pressure induced by the skyrmions themselves, as they confine their size due to skyrmion-skyrmion and skyrmion-edge repulsion. At the bias OOP fields used for the free skyrmions, the skyrmions would already elongate into a worm-like domain state. Thus, the nucleation of complete skyrmion lattices via the IP field burst method enables the formation of skyrmion lattices with smaller skyrmions compared to individual free skyrmions under the same bias OOP field.
Due to the reduced PMA at the irradiated barrier, skyrmions that are pressed towards the barrier by skyrmion-skyrmion interactions exhibit a significant size increase compared to the average skyrmion size in the channel. This is consistent with the size difference observed in the He^+ irradiated region in previous sections. The size increase due to the reduction in anisotropy may counterbalance the size decrease resulting from the compression of the skyrmions against the barrier. These effects overlap, making it challenging to differentiate them using the current evaluation methods. Additional results using the structural comb boundary are provided in Section C.4.

The applied currents ranged from I = 5 µA to I = 30 µA, resulting in a current density range of $J_{50\mu m}$ = 1,1·$10^7 A/m^2$ to $J_{50\mu m}$ = 6,7·$10^7 A/m^2$ in the narrow 50 µm wide channel. For the 80 µm reservoir, the current density range was $J_{80\mu m}$ = 0,69 · $10^7 A/m^2$ to $J_{80\mu m}$ = 4,17 · $10^7 A/m^2$. It is important to note that widening the channel results in a decrease in current density, and consequently, a reduction in the force

applied to the skyrmions in the reservoir section of the channel.

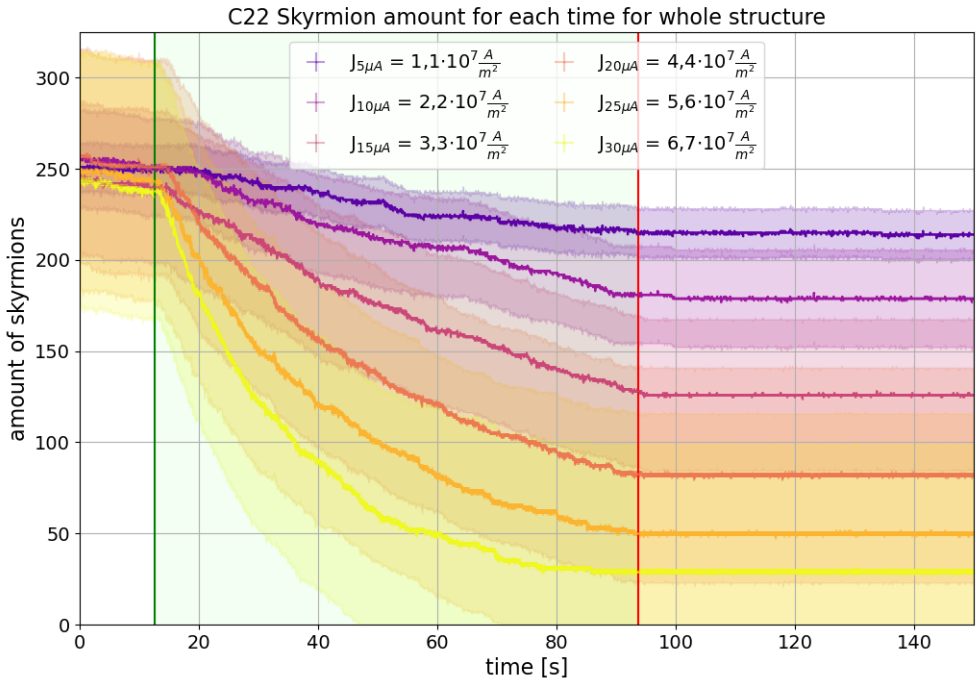

FIGURE 5.15: The variation in skyrmion count over the duration of the recorded video is shown for the applied current densities. The red line indicates the start of current application (green shaded area), while the green line marks the cessation of current application. During the first 12 seconds, the skyrmion number decreases only slightly, likely due to thermal effects at pinning sites. However, during the period of current application (until second 94), the skyrmion count decreases significantly, with a more pronounced reduction at higher current densities. Once the current is stopped, the number of skyrmions stabilizes, with any fluctuations attributed to noise caused by UNET's difficulty in correctly identifying a few remaining skyrmions.

During the measurements, depending on the applied current density, the number of skyrmions decreases due to annihilation at the barrier, particularly near the structural edges of the channel. To confirm that the decrease in skyrmion number is solely attributed to the applied current, no current was applied during the first 200 frames (12.5 s), allowing the system to equilibrate. After 200 frames, the current was applied until frame 1500 (93.8 s), after which the system was allowed to equilibrate again until frame 2400 (150 s). It should be noted that the current was applied by manually switching on a current source, and thus the exact time points of current application and cessation are known.
The annihilation of over 80% of nucleated skyrmions at the highest current density poses a significant challenge for compressing skyrmions against barriers at elevated current densities. This factor must be considered when analyzing phenomena such as lattice effects. Lowering the temperature could potentially enhance the stability of skyrmions pressed against the barrier, mitigating some of the effects associated with high current densities.

The average skyrmion size shows as a function of time in Figure 5.16 increases during the current application, with the rate of increase being steeper at higher current densities. This behavior can be attributed to the fact that, during current

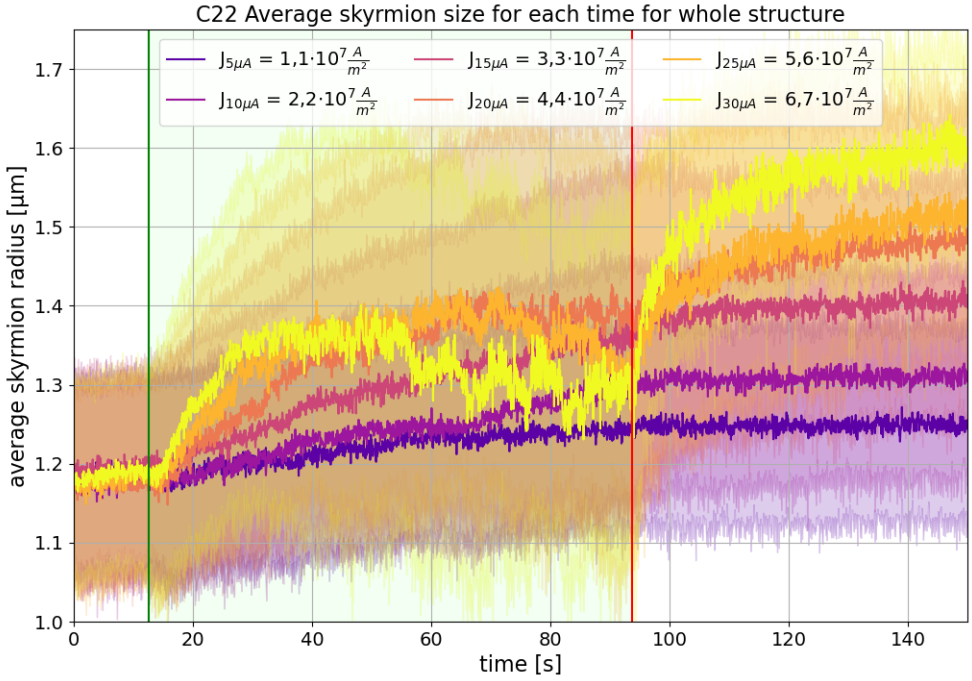

FIGURE 5.16: The average skyrmion size over time for the applied current densities is shown, with the green and red lines indicating the start and end of current application, respectively. During the current application, the average skyrmion size increases as skyrmions move towards the barrier, thereby creating additional space for their expansion. However, as the number of skyrmions decreases with higher current densities, this effect becomes less pronounced. After the current is stopped, a relaxation process occurs, during which the inert pressure drives the skyrmions back into the channel, providing further space for their expansion.

application, skyrmions move towards the barrier and some annihilate (particularly at higher current densities), leaving more space available for the skyrmions furthest from the barrier. Due to the reduced skyrmion-edge and skyrmion-skyrmion repulsion, the skyrmions positioned farther from the barrier are able to expand more freely, leading to a significant increase in their size. As the overall number of skyrmions decreases, the number of skyrmions being compressed, and thus experiencing a reduction in size, also diminishes. This explains the noise observed in the graph for $J_{25\mu A} = 5{,}6 \cdot 10^7 A/m^2$ and $J_{30\mu A} = 6{,}7 \cdot 10^7 A/m^2$ in Figure 5.16. For high current densities, the skyrmions are forced against the barrier, resulting in an overall size reduction, even smaller than at half the current density.

This behavior changes significantly once the current is stopped. The pressure built up in the compressed system state of the artificially denser lattice and the decreased size of the remaining skyrmions is released. The lattice undergoes relaxation, and the skyrmions move towards the left, opposite to the previous current direction, resulting in a drastic increase in their size. This provides additional evidence for the existence of an inert pressure in skyrmion lattice systems, even though the lattice had been artificially compressed prior to the measurements. This expansion effect occurs as the skyrmions move into the newly available space in the channel, thereby creating more room for the previously compressed skyrmions to expand, resulting in an increase in the average skyrmion size. For lower current densities, where fewer skyrmions undergo annihilation, the lattice remains relatively full, and

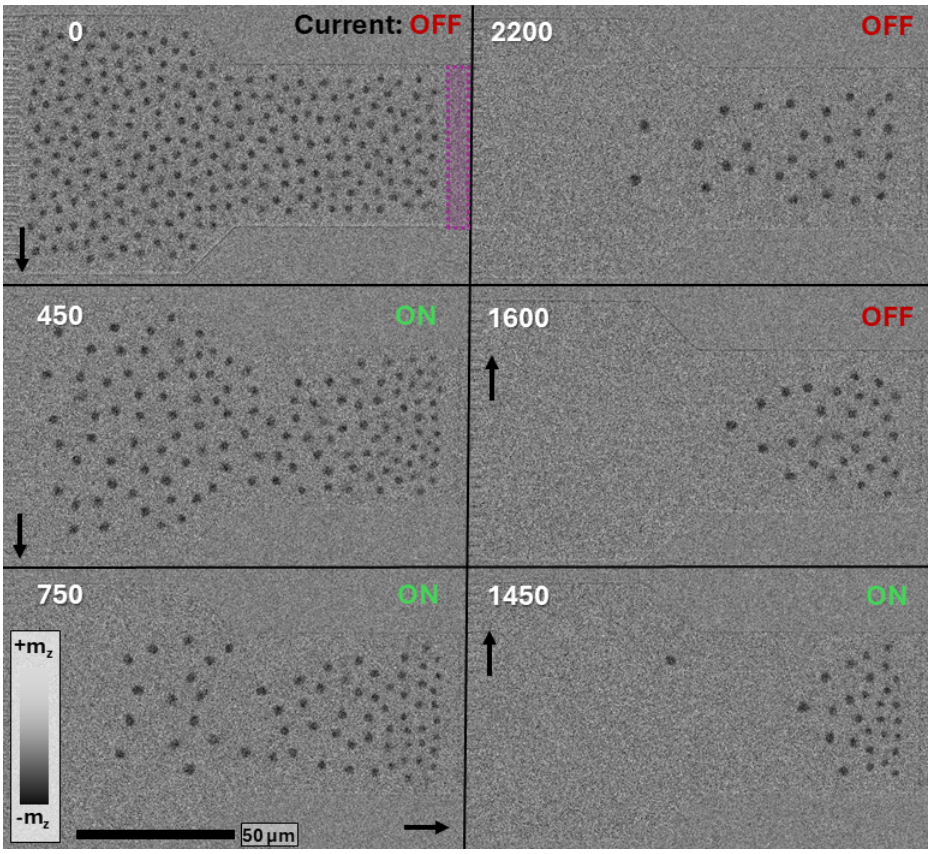

FIGURE 5.17: Single frames from MOKE microscopy recordings at different time points are shown, with arrows indicating the order of the time series. The labels "ON" or "OFF" in the right corner denote whether current was applied during the respective frame. The violet area highlights the irradiated region, which remains consistent across all frames for clarity. The increase in skyrmion size is evident once more space becomes available for individual skyrmions (e.g., at frames 450 and 750) and reaches its maximum during the relaxation period (e.g., at frames 1600 and 2200). The majority of skyrmions undergo annihilation during current application, and the compression of the skyrmion lattice, both in terms of ordering and size, is observed in frame 1450.

no significant free space is created during the current application. As a result, the relaxation process is less pronounced compared to higher current densities.
Comparing the different current densities in this specific measurement run, the compression of skyrmions at the barrier and their subsequent expansion into the newly created space are evident. The skyrmion size increase and their re-migration into the channel upon cessation of the current are also observed.

In Figure 5.19, the focus is placed on the start and end of current application at the barrier. In the [red] and [green] regions, the lattice structure of the skyrmions becomes particularly evident during the current application. In [red], after the current is applied (to the right of the red dashed line), the skyrmions shift approximately 2 µm closer to the barrier compared to the as-nucleated, equilibrated lattice state (to the left of the line), while their size decreases by roughly 20%. This effect reverses once the current-induced SOT is turned off (to the right of the green dashed line): the skyrmions move away from the barrier back into the channel and increase in size by approximately 25%. As the lattice melts, the skyrmions move apart and diffuse into free space, causing the lattice alignment to disappear. It is important to note that

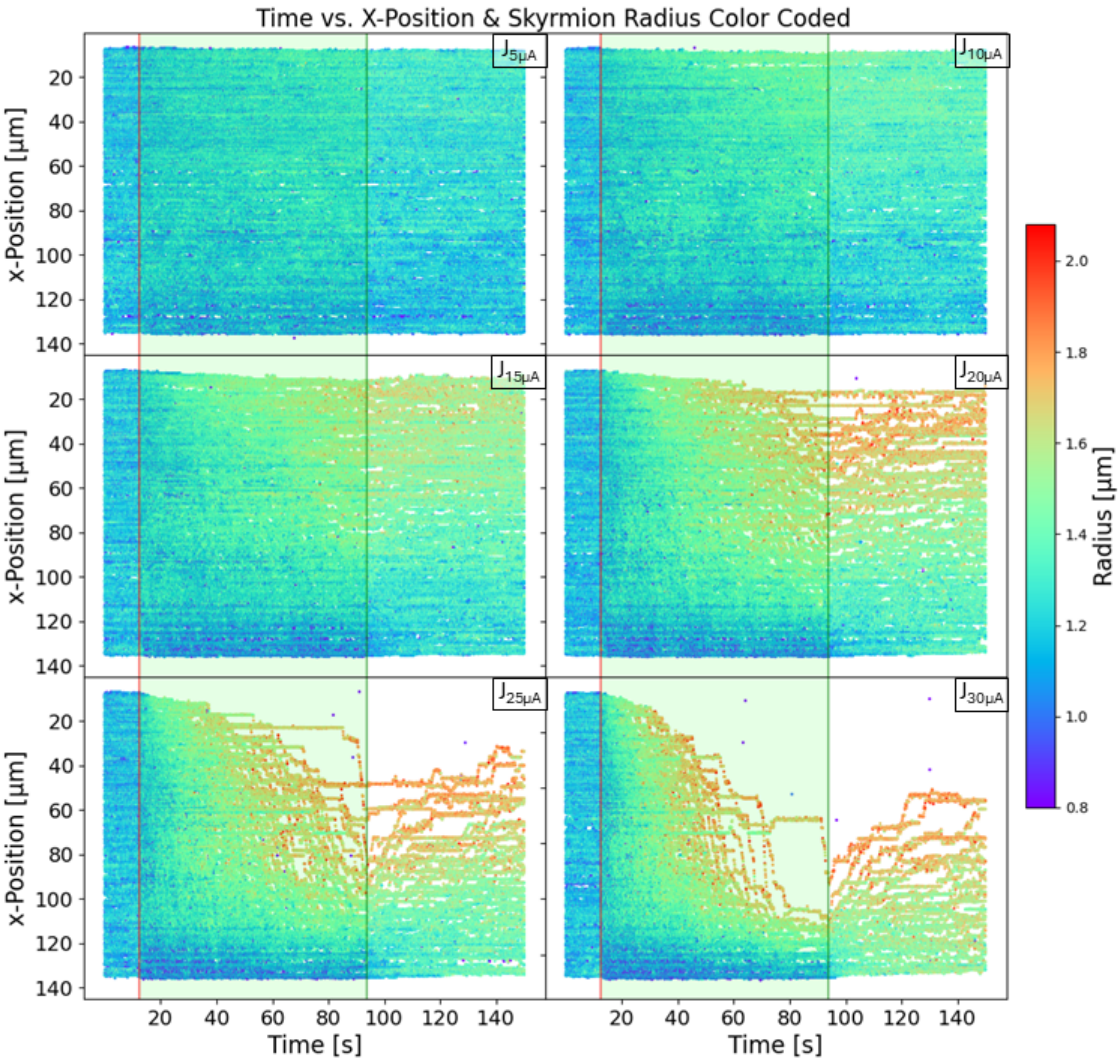

FIGURE 5.18: A spatial projection of the skyrmion positions along the x-axis as a function of time, with skyrmion radius color-coded, is presented. Each point represents the x-position of an individual skyrmion over time. Skyrmions move towards the bottom of the graph, toward the barrier (starting around 135 μm). As the skyrmions approach the barrier, they increase in size when not confined by other skyrmions or the edges, reaching a maximum size determined by the magnetic parameters, temperature, and applied bias field.

only the center of mass of the skyrmions is represented in the x-coordinate, and due to the size change, the outer domain walls of the skyrmions may not move as far into the barrier as the plot suggests.

A key difference from the analogy with the barometric formula and gravity-based atmospheric pressure is that, for the latter, only the average distance between gas atoms or molecules decreases as pressure increases (ignoring internal molecular deformations in larger molecules). In contrast, the skyrmion compression discussed in this thesis involves not only a reduction in the average distance between skyrmions but also a decrease in the size of the individual skyrmions, as demonstrated in the previous sections.

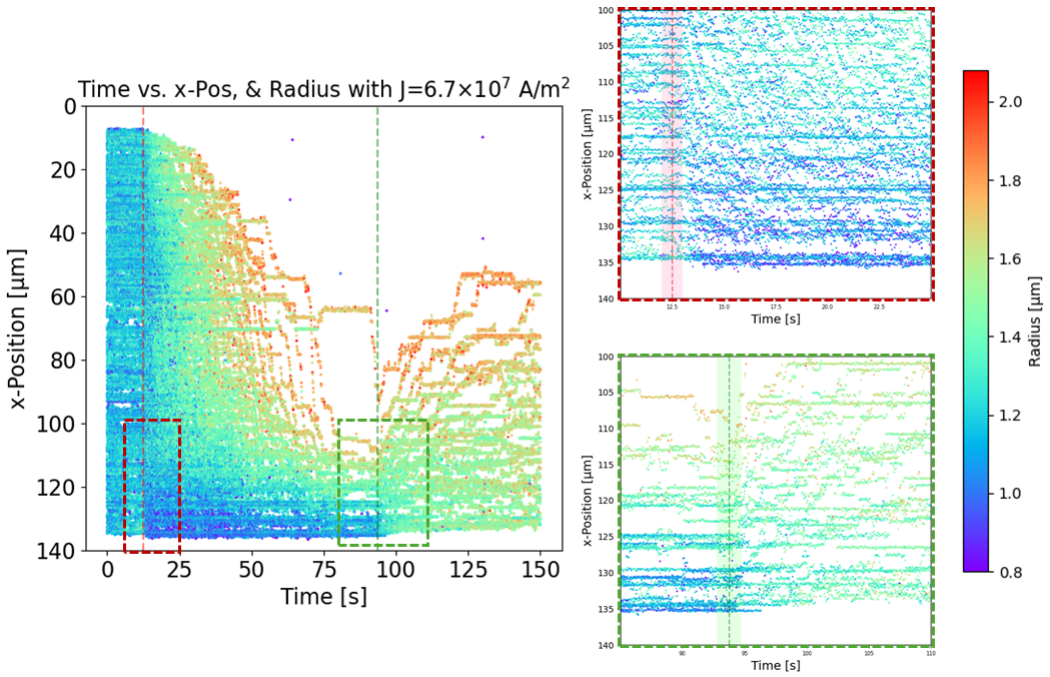

FIGURE 5.19: A detailed version of Figure 5.18 is shown, with insets displaying small time intervals marking the start and end of current application. The red region indicates that, due to the SOT, the skyrmions move closer to the barrier while simultaneously shrinking in size. Once the current-induced SOT ends (green region), the skyrmions slightly move away from the barrier and experience an increase in size.

5.3.6 Distance

In an ideal gas, an increase in pressure under isochoric (constant volume) and isothermal (constant temperature) conditions leads to a reduction in the average distance between atoms, as the number of particles per unit volume increases. In contrast, within a skyrmionic system, compression not only reduces the inter-skyrmion distance but also decreases the individual skyrmion size. This behavior arises from skyrmion–skyrmion and skyrmion–edge interactions under the influence of SOT driving the skyrmions against a confining barrier. Near this barrier, the skyrmions are forced into closer proximity.
At elevated current densities (i.e., higher effective pressure), enhanced skyrmion annihilation occurs, which reduces the overall skyrmion population (see Figure 5.15). As a result, more space becomes available for the remaining skyrmions, allowing for expansion. This expansion manifests as both an increase in skyrmion size and a greater average separation between skyrmions.

Figure 5.20 illustrates the temporal evolution of the mean inter-skyrmion distance for various applied current densities. In general, the average distance increases over time, which correlates with the decreasing number of skyrmions due to annihilation. This indicates that internal pressure within confined skyrmion lattices dominates over the externally induced compression.
For the highest applied current densities ($J_{25\mu A}$ = 5,6 $\cdot 10^7 A/m^2$ and $J_{30\mu A}$ = 6,7 $\cdot 10^7 A/m^2$), the averaged distance data exhibit increased fluctuation, likely reflecting the stochastic nature of annihilation events and the resultant expansion in skyrmion spacing and size (see Figure 5.16). When only a few skyrmions remain under high current, they continue to be compressed near the barrier, leading to a transient

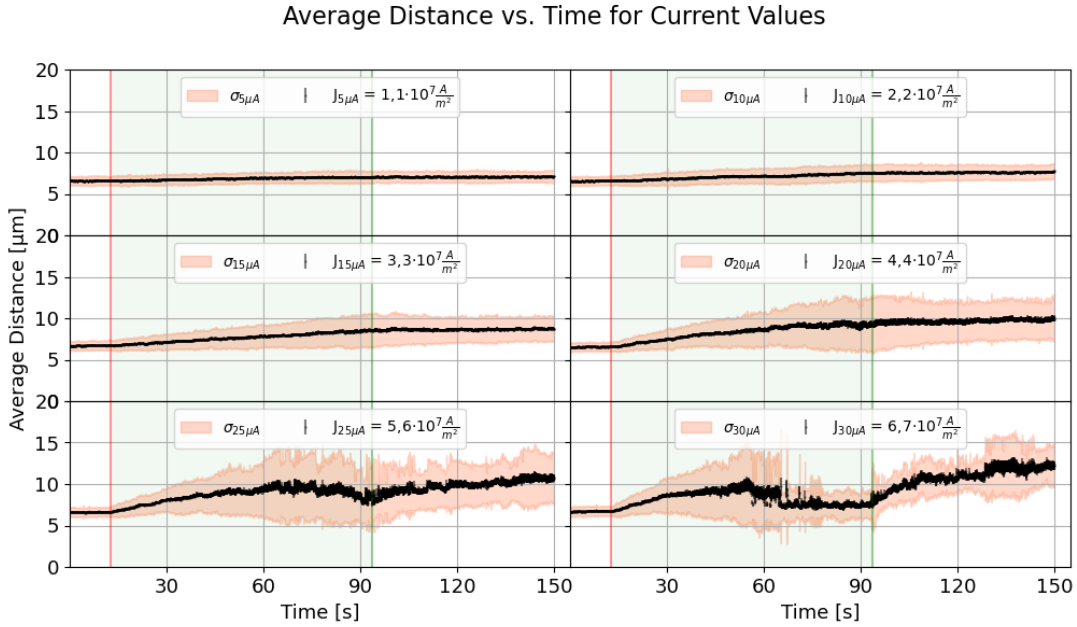

FIGURE 5.20: Averaged skyrmion nearest neighbor distance for all measured current densities. The influence of skyrmion annihilation at higher currents on the average distance is visible, as more space for skyrmion expansion (in size and distance) is available.

decrease in average distance and size. This is evident in the time window between 75 s and 94 s, after which the current is turned off.
Upon cessation of the current, the skyrmions undergo relaxation, diffusing away from the barrier and reoccupying the channel. This free space leads to an increase in both skyrmion size (Figure 5.16) and average inter-skyrmion distance. This relaxation effect is most pronounced in the high-current cases, where only a few skyrmions remain at the end of the current application.
It is important to note that the reported inter-skyrmion distances refer exclusively to the nearest-neighbor separations, calculated based on the centroid coordinates identified by UNet [309]. This process does not account for the physical size of the skyrmions themselves. Consequently, larger skyrmions in a lattice inherently yield greater centroid-to-centroid distances, even if the edge-to-edge spacing between their domain walls remains hypothetically roughly the same.
Qualitative observations confirm that skyrmions in proximity to the barrier are not only smaller in size but are also positioned closer to each other (see Figure 5.17). When restricting the analysis to a 20 µm region in front of the barrier, as shown in Figure 5.21, the average distance behavior differs. In this confined region, the number of skyrmions remains approximately constant, implying that any observed compression must result from either a reduction in skyrmion size, inter-skyrmion spacing, or both. Following the onset of current application, a slight decrease in inter-skyrmion distance is observed, particularly under high current densities. After the current is switched off, the skyrmions undergo relaxation, evident in the increasing mean distance—indicative of skyrmion expansion and diffusion into the available free space.

A more detailed examination of the highest current density case in Figure 5.22

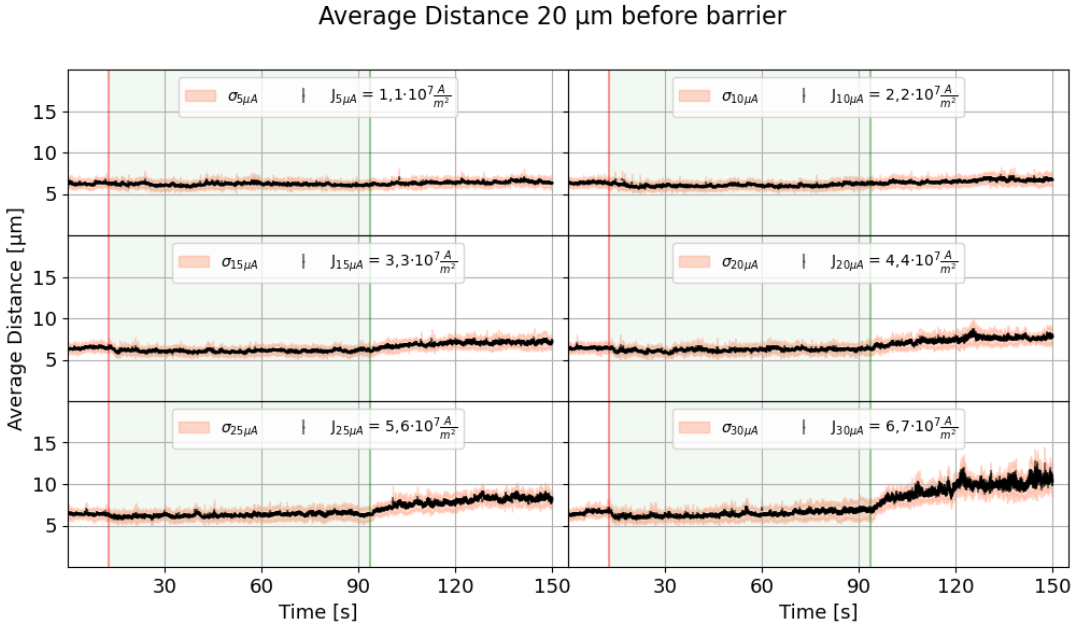

FIGURE 5.21: Analogous to Figure 5.20, the average inter-skyrmion distance is shown in this case specifically for the 20 µm region directly in front of the barrier. This localized analysis highlights the compression effects near the barrier, driven by the combined influence of external forces, skyrmion-skyrmion interactions, and skyrmion-boundary interactions. Given that the number of skyrmions within this region remains approximately constant during current application, the observed compression manifests as a reduction in both skyrmion size and inter-skyrmion spacing. Notably, in the high current density cases, the onset of the relaxation process - marked by a rapid increase in inter-skyrmion distance upon cessation of the current - occurs swiftly. This rapid response suggests a substantial internal pressure buildup within the skyrmion lattice, even when composed of only a few remaining skyrmions.

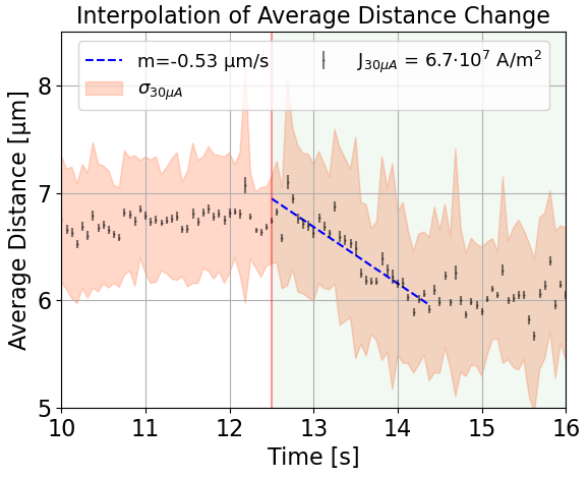

FIGURE 5.22: Close-up view of the average inter-skyrmion distance at the onset of current application. A near-linear decrease in distance is observed over the initial 2 seconds of current application, after which the repulsive skyrmion-skyrmion and skyrmion-boundary interactions counteract further compression, leading to a stabilization of the average spacing.

reveals an approximately linear decrease in the average inter-skyrmion distance immediately following current application. This reduction continues until a quasi-hydrostatic equilibrium is reached after approximately 2 seconds. It is important to note that, due to the elevated probability of skyrmion annihilation at the barrier - where skyrmions accumulate under the influence of spin-orbit torque - the average distance does not converge toward a definitive lower limit. To robustly characterize the lower bound of inter-skyrmion spacing under compression, longer-duration measurements with minimized annihilation effects and a broader barrier region (i.e., a wider channel geometry) would be necessary.

5.3.7 Density

This section examines the density of the compressed skyrmion system. Given the significant loss of skyrmions at higher current densities, the skyrmion density per spatial interval will be analyzed. The channel is divided into approximately 4.5 µm (15 pixels) wide stripes (as shown in Figure 5.23), and the number of skyrmions within each stripe is counted individually and presented as relative density histogram in Figure 5.24. During current application, the skyrmion density increases at the barrier, particularly at higher current amplitudes. Note that the relative density is evaluated for the whole channel and does not account for the widening of the channel into the reservoir. This is clearly visible in Figure 5.24 in the dark violet to turquoise histogram bars. After the current is removed, the skyrmions undergo relaxation, diffuse back along the channel, and expand spatially, consistent with diffusion-driven dynamics.

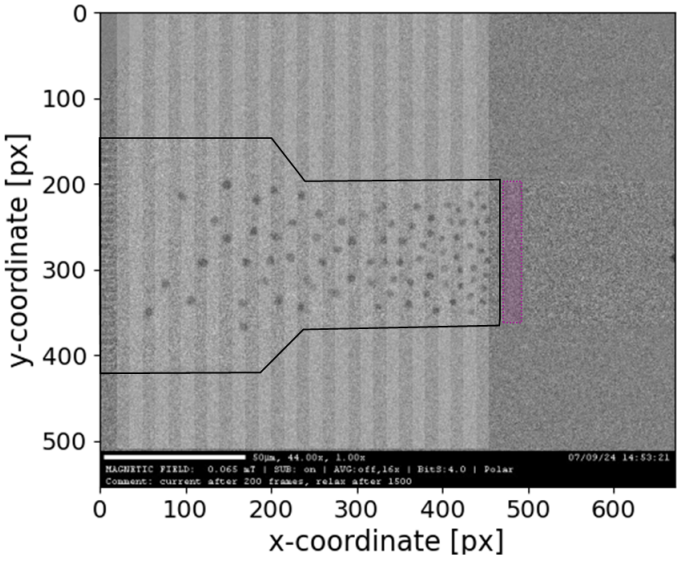

FIGURE 5.23: Channel division in stripes of ∼4.5 µm (15 pixels) width. Alternating grayscale for visual clarification, while violet represents the irradiated barrier.

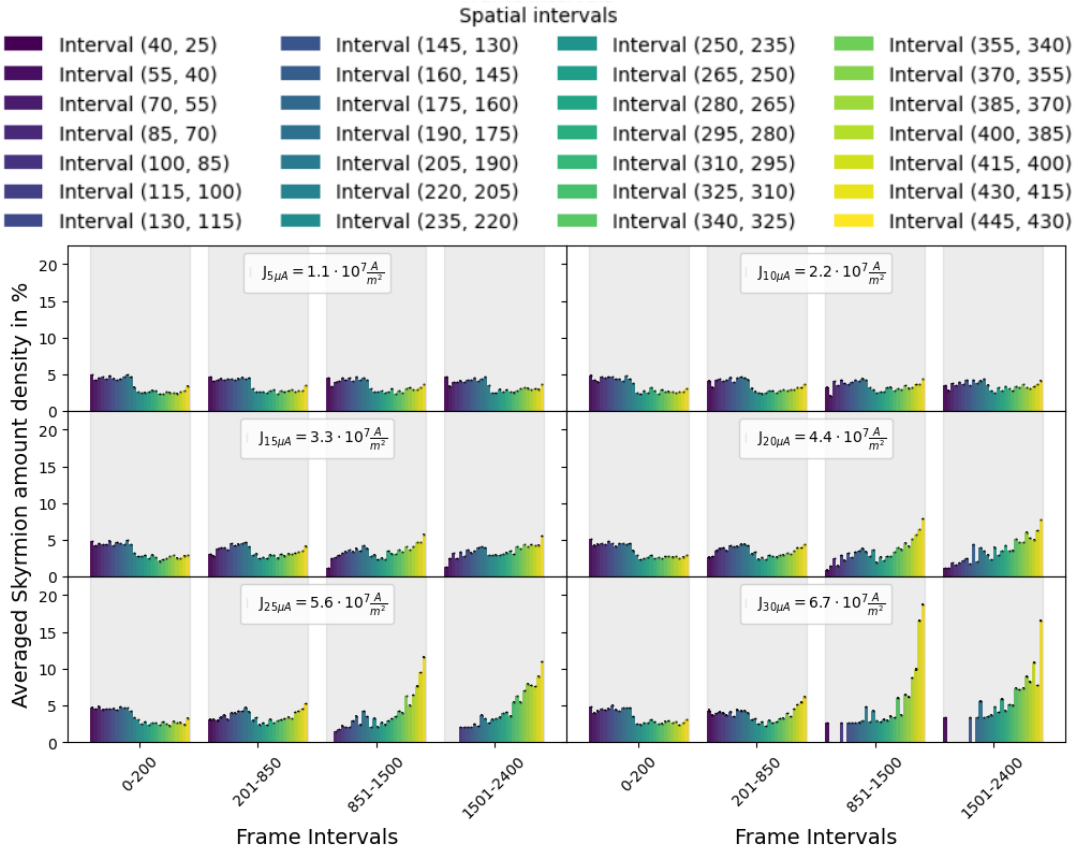

FIGURE 5.24: The normalized, averaged skyrmion amount per 4.5 µm stripe, as shown in Figure 5.23. Skyrmion density is highest in front of the barrier (yellow) and decreases with distance from the barrier (towards violet) during current application. Note that due to the higher amount of skyrmions in the wider reservoir, thus the relative density is higher (x<∼220 px). The data is segmented temporally in four intervals: initial lattice equilibration phase (0–12.5 s), two intervals during current application (12.5–50 s and 50–94 s), and the final relaxation phase without current (94–125 s). Grey background for visual aid when striped are not populated.

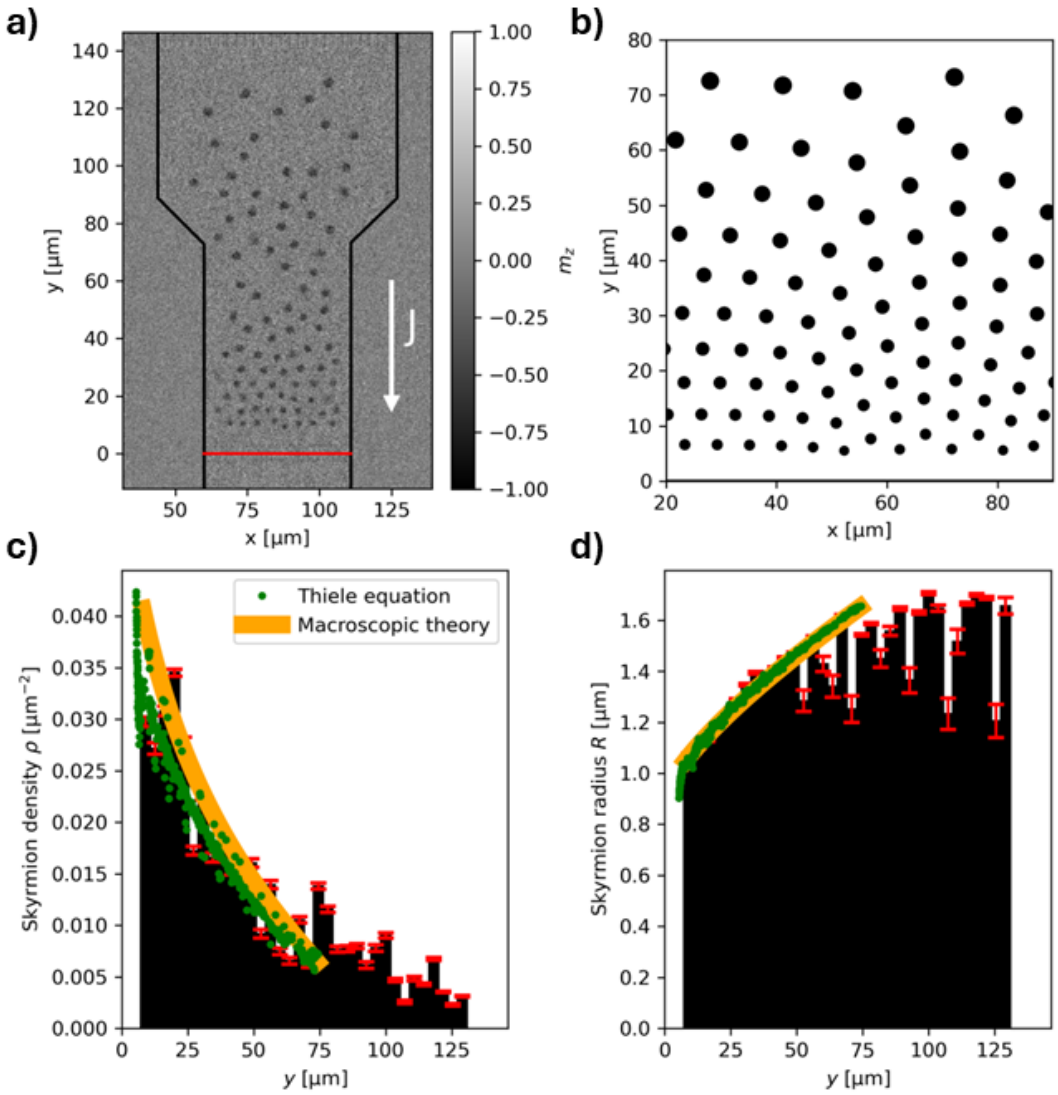

FIGURE 5.25: a) MOKE microscopy image of the presented structure (rotated by 90° to align with the simulations), showing skyrmions being pushed towards the irradiated barrier (red line) by a current density of J = 4,4 $\times$ $10^7 \frac{A}{m^2}$ (indicated by the white arrow). b) Simulated skyrmion compression, based on the adapted Thiele equation, demonstrates qualitatively similar behavior to the experimental observations, with the skyrmion radius and periodicity increasing as the distance from the barrier increases. c) The density histogram (black bars) shows the number of skyrmions per unit area (see Figure 5.23) between 85 and 90 seconds. The error is represented in red. Green dots and the interpolation represent data derived by K. Leutner using his adapted Thiele equation, while orange reflects the qualitative predictions from macroscopic theory. d) Black bars depict the decrease in skyrmion size towards the barrier, with green representing the qualitative data derived from K. Leutner's Thiele-based simulation, and orange indicating the qualitative predictions from macroscopic theory. Graphs partly created by K. Leutner.

5.3.8 Comparison to similar simulations

As discussed at the beginning of the second part of this chapter, two research groups have investigated skyrmion compression in confined geometries through numerical simulations: Zhang et al. - Ref.[350] and Bellizotti Souza et al. - Ref.[143].

In Ref.[350], the authors simulate the temporal compression of a skyrmion lattice by applying an external force at the entrance of a confining channel. As skyrmions are driven toward a barrier, compression arises from mutual skyrmion-skyrmion and skyrmion-edge repulsion, resulting in a reduced average inter-skyrmion distance and a rearrangement of the lattice order. While the skyrmion size itself remains constant in their simulation, the authors note occurrences of skyrmion annihilation, likely due to skyrmion collisions during compression. The simulations involve nanometer-scale skyrmions with dynamics on the nanosecond timescale, enabling the analysis of a transient, compressive skyrmion wave. Given the temporal and spatial resolution limitations in our micrometer-scale experimental system, comparable dynamic behavior is unlikely to be directly observable. Due to lack of skyrmion size compression, only the qualitative lattice change is comparable.
In Ref.[143], skyrmions are also subjected to simulated compression by direct and alternating current forces toward a confining barrier. The authors incorporate the effect of the Magnus force, which causes the skyrmions to deviate from the direction of the applied current, resulting in an asymmetric accumulation of skyrmions in the lower left corner of the confinement. This leads to a gradient in skyrmion size and spacing - denser and smaller skyrmions near the boundary and larger, more sparsely spaced skyrmions farther from the wall - qualitatively resembling the experimental results presented in this thesis, not taking the skyrmion Hall effect into account. The authors describe this arrangement as a conformal crystal. Skyrmion annihilation is observed at increasing current densities, culminating in complete annihilation at a critical current density $J_0^{crit} = 1{,}76 \cdot 10^{11} \frac{A}{m^2}$.
In our experiments, a similar behavior is observed at the maximum current density of $J_{30\mu A}^{max} = 6{,}7 \cdot 10^7 \frac{A}{m^2}$, where the highest rate of skyrmion annihilation occurs. However, since some skyrmions persist at this current level, it is likely that the critical current density has not yet been reached. At higher current values, experimental limitations such as insufficient temporal resolution and the onset of worm domain nucleation hindered further analysis. In contrast, Bellizotti Souza et al. demonstrated that applying AC rather than DC allowed for an increase in the critical current threshold, a method not experimentally explored in this work.

Overall, the findings of Ref.[143] exhibit qualitative agreement with the experimental results presented here. The primary differences lie in the spatial and temporal scales - nanometer-sized skyrmions under high-current conditions with pronounced skyrmion Hall effects in their work versus micrometer-sized skyrmions operating in the creep regime with negligible SkHA in this thesis.

5.4 Conclusion

This chapter explored the impact of wide-area and locally confined irradiation on skyrmion stacks, examining how irradiation can alter magnetic properties and thereby the resulting skyrmion properties. By modifying anisotropy, irradiation plays a crucial role in fine-tuning skyrmion parameters, such as size and ordering, and can also serve to confine skyrmions by introducing barriers, non-structural confinements, or artificial pinning sites.

Skyrmion properties, such as size, can be directly influenced by current-induced SOT when a skyrmion ensemble, subjected to inter-skyrmion and skyrmion-edge interactions, is compressed against a structural or, as in the present case, an irradiation induced artificial barrier. This compression not only reduces the size of skyrmions near the barrier, which are confined by neighboring skyrmions, but also decreases the inter-skyrmion distance, resulting in denser lattices. Building upon these experimental findings, K. Leutner derived a theoretical model of skyrmion compression, based on an adapted Thiele equation.
A comparison between the experimental results and the simulations presented in Ref.[143] reveals qualitative agreement. However, further investigations are necessary to fully understand the underlying mechanisms and detailed dynamics of skyrmion annihilation and the inherent lattice pressure. Notably, the simulations performed by K. Leutner, based on the extended Thiele equation - which has been demonstrated to accurately describe the behavior of micrometer-scale skyrmions[71, 110, 153, 174, 326] - exhibit also qualitative agreement with the experimental observations presented in this work.
Comparative systems in 2D or 3D that exhibit complex dynamics under compression - such as gases - typically consist of an extremely large number of particles, enabling macroscopic descriptions through thermodynamic variables like pressure. In contrast, the skyrmion compression experiments presented here involved an initial amount of approximately 250 skyrmions, which continuously decreased due to annihilation under externally applied forces. While the dynamics of colloidal particles in liquids are influenced by interactions with the suspending medium, the behavior of skyrmions is shaped by their interactions with a non-uniform energy landscape, mutual interactions, and boundary effects. Despite the relatively small particle number, skyrmions as 2D model systems offer unique advantages over colloidal analogues, particularly due to their controllable nucleation and easy manipulation. Expanding the system to include a larger number of skyrmions within a denser lattice and over a broader spatial geometry may reduce the impact of structural or artificial boundaries, thereby facilitating more accurate experimental investigations of intrinsic lattice dynamics under compression. Compression of skyrmions against an artificial barrier, such as voltage-controlled magnetic anisotropy, could pave the way for new applications, such as token control in an hourglass-shaped valve. Moreover, irradiation can be utilized to guide skyrmions through confinements that are permeable to currents, offering new possibilities for skyrmion-based circuitry.

Chapter 6

Brownian Reservoir Computing

This chapter introduces an application of skyrmions in the realm of unconventional computing [113, 219, 325, 358, 359]: exploiting energy efficient displacement of skyrmions in combination with Brownian thermal diffusive motion, a demonstration device is introduced, able to perform Boolean logic operations, including non-linear separable operations, by Brownian reservoir computing. A proof-of-concept device is presented together with the prospect of a scaled down, nanometer scale version and according readout process. An energy estimation for a single skyrmionic operation shows the energy efficiency of such a concept. Optimizations of the concept in general and for this device in particular are discussed.

6.1 Skyrmions in application

As discussed in previous chapters, skyrmions, exhibiting quasi-particle behavior [115, 360, 361], can be displaced deterministically with high energy efficiency via STT [79] and SOT [94, 95, 97, 98, 362], necessitating only low current densities. To date, several potential applications for skyrmions have been proposed [110, 111, 190, 229, 235, 325, 363], with particular attention to their utilization as tokens in novel memory devices [118] like, e.g., racetrack memory [29], taking advantage of skyrmions' potential nanometer size, stability [130] and achievable velocities [192]. However, many of these proposed applications have largely overlooked a fundamental characteristic of skyrmions: the stochastic nature of their thermally driven Brownian motion. Deterministic approaches, which rely exclusively on current-induced torques for skyrmion manipulation in memory and computational devices, have not been systematically integrated with the inherently nonlinear and thermally activated diffusion of skyrmions [110]. Specifically, the high current densities required to induce deterministic motion and meet necessary skyrmion velocity constraints pose a challenge to energy efficiency when compared to existing spintronic reservoir computing architectures [51, 56].
Conversely, unconventional computing paradigms, such as RC (as introduced in Section 2.7), leverage the probabilistic and nonlinear dynamics of skyrmions, potentially reducing the required current densities for their overall displacement. The stochastic and nonlinear behavior is also characteristic of a biological brain, which processes information through networks of neurons connected by synapses. These elements communicate via electrochemical signals (neurotransmitter), enabling highly efficient signal transmission and processing with exceptional energy efficiency [49] and inspire new neural networks based on biological systems [364–366]. Another critical factor in skyrmion dynamics is the ability to modulate their stochastic behavior through geometrical confinement. Due to stray-field and exchange interaction, skyrmions experience repulsion from structural or artificial edges [155,

169, 172, 198, 367], enabling control over their otherwise semi-isotropic diffusion and equilibrium arrangements within confined geometries. In this context, *semi-isotropic* refers to diffusive skyrmion motion influenced by the relatively flat energy landscape of the sample. The interplay between driven motion, confinement effects and stochastic diffusion presents opportunities for tailored skyrmion behavior, which can be exploited in computational [99, 152] and memory frameworks.

6.2 RC using skyrmions

Reservoir computing (RC) [222, 226], as outlined in section 2.7.3, harnesses the intrinsic nonlinear dynamics of a physical system, referred to as the reservoir, to project input signals into a higher-dimensional space. This transformation resembles an efficient readout of the computational output. The input signal modulates the reservoir state, which is subsequently read out and its output interpreted using a perceptron that maps the reservoir output onto a desired result. Crucially, the intrinsic properties of the reservoir perform the computation inherently, eliminating the need for direct training within the reservoir itself. Instead, training is confined to the output stage, simplifying the process to solving a linear optimization problem and thereby reducing computational cost [368].
A fundamental requirement of RC is the implementation of an external reset mechanism that restores the reservoir to its initial state after each computational cycle. This necessity poses significant challenges in many experimental realizations. Later in this chapter, an energy efficient method for resetting the reservoir is introduced.
In previous skyrmion-based RC approaches [234], local pinning sites have been employed [229, 232], which can hinder the effectiveness of skyrmion diffusion. Furthermore, these nonlinear dynamics typically result in small displacements, making the experimental readout in practical devices challenging.
This chapter presents an alternative RC concept that leverages the intrinsic properties of a single thermally activated skyrmion confined within a triangular geometry [99, 152]. By incorporating low-power current-induced motion, the skyrmion is directed toward the corners of the confinement. The geometric constraints and repelling interactions at the edges establish a potential well, naturally driving the skyrmion back to its initial state - centrally positioned within the triangular structure - after each induced displacement. This automatic reset mechanism enhances the reliability and reproducibility of the system, enabling the realization of Boolean logic operations, including nonlinearly separable functions, within this proof-of-concept framework.

6.2.1 The demonstrator device

The demonstrator device, fabricated from stack FAB629 (see details in Sections A.1, A.1.2 and Ref. [99, 110, 152]), consists of equilateral triangles - one of the simplest and symmetric shapes in 2D Euclidean geometry - with electrical leads extending from its corners to enhance electric connectivity. The triangular structures were patterned as described in chapter 3, with side lengths varying between 22 µm and 40 µm. The contacts measure 15 µm in length and have widths ranging from 2 µm to 5 µm.

A well-balanced corner protrusion width is crucial: it must be sufficiently large to ensure reliable electrical connectivity while remaining narrow enough to prevent

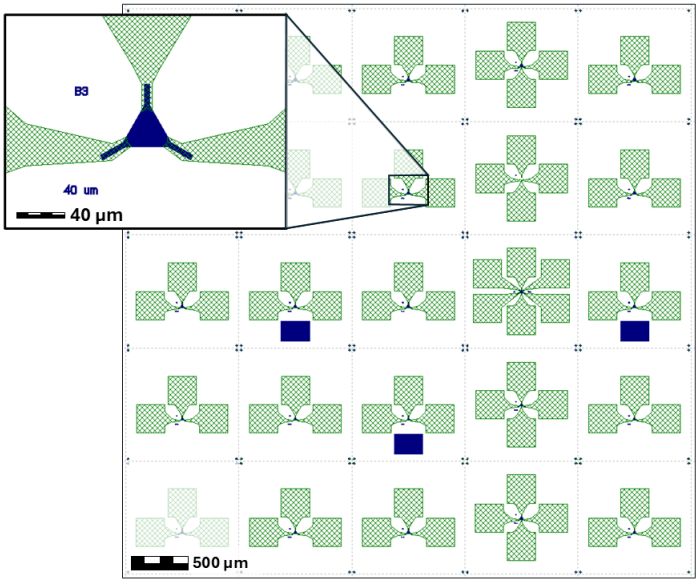

FIGURE 6.1: PIONEER layout for EBL design. Dark blue represents the remaining material stack on the substrate (white) after first lithography step including etching. Chromium/gold layer for second lithography step in diagonally-checkered green. One device per writefield (1×1 mm^2), with each device individually labeled (Horizontal in numbers, vertical in letters), connected to 250×250 µm^2. Inlet represents the zoomed in device B3 with 40 µm side length and visible protrusions from corners overlapped by the gold layer for better contacting.

skyrmions from entering. As shown in Figure 6.1, the gold contact pads are connected via overlapping leads extending over the protrusions, ensuring efficient electrical connectivity, particularly along the sides of the stack. Since the CoFeB- and tantalum seed layer are separated by a non-conductive MgO layer, a gold contact positioned solely on top of the stack would result in current flow primarily through the 5 nm tantalum capping layer. The inhomogeneous current distribution within the stack will be considered later in this chapter when estimating energy consumption. The applied potentials required to induce skyrmion motion range between 2 mV and 5.5 mV, corresponding to electrical currents on the order of a few µA. Given the device geometry, the estimated current densities at the half-height width of the triangular structure (see Figure 6.16, green dashed line) range from $\sim 2\cdot10^7 A/m^2$ to $\sim 3\cdot10^8 A/m^2$.

The presented experimental results were obtained from a triangular device with a 40 µm side length and a 4 µm wide protrusion, hosting skyrmions of approximately 5-8 µm in diameter at temperatures ranging from 315 K to 330 K.

6.3 Functionality of the device

6.3.1 Skyrmions in the reservoir

Devices with varying size were systematically tested and measurement parameters optimized to accommodate a single skyrmion of sufficient size, exhibiting thermal diffusion within the structure at ambient temperature and under a low out-of-plane

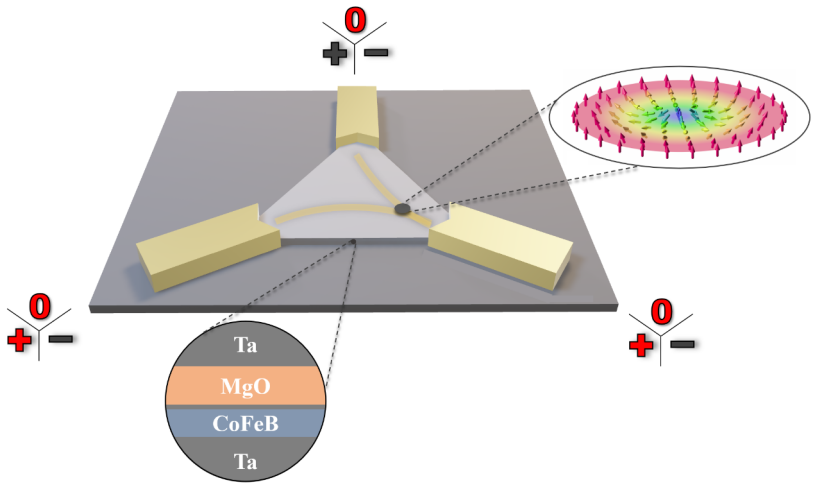

FIGURE 6.2: The figure schematically illustrates the RC device, which consists of an equilateral triangular geometry fabricated from stack FAB629, with gold electrical contacts positioned at its corners. A single skyrmion is confined within this structure and can be displaced through the application of electrical potentials at the corners. In the absence of an applied potential, the skyrmion naturally returns to the central position due to the geometric confinement, thereby resetting the reservoir. The red annotations indicate the applied potentials used to demonstrate Boolean logic operations. The insets provide a schematic representation of the skyrmion spin structure and the stack layer composition. Figure adapted from [99].

bias magnetic field. During this optimization process, devices were initially inspected for contaminants such as resist residues or dust, which could restrict visibility in MOKE microscopy. Additionally, electrical connectivity was verified, resistances determined, and the presence of strong pinning sites assessed, as excessive pinning could displace the skyrmion from the central equilibrium position [156]. The occasional destructive burnout of devices during resistance measurements, experimental setup, and operation necessitated the implementation of extended safety measures, as detailed in section 3.3.5. Skyrmions within the device were nucleated using the procedure described in section 3.3.3 and Ref. [110]. Depending on the applied out-of-plane bias field and the confinement size, multiple skyrmions were typically generated, exhibiting spatial ordering commensurate with the geometry, as reported in prior studies [172]. For this proof-of-concept, the number of skyrmions was controlled by increasing the bias field, which reduced skyrmion size until stochastic annihilation occurred. The bias field was subsequently lowered to achieve a favorable skyrmion size, ensuring that sufficient space remained for thermal diffusion. This is particularly relevant for potential application involving multiple skyrmions. In a scaled-down device, a single skyrmion could be nucleated via spin-transfer torque exerted by a MTJ [297, 298]. For this demonstrator, skyrmion displacement was visualized using MOKE microscopy, as described in chapter 3 section 3.3. However, for a practical spintronic device, optical readout combined with image analysis for skyrmion tracking is not a viable solution due to its low speed and high energy consumption. The use of MOKE image analysis in this study serves as an experimental analog to MTJ-based detection via TMR changes (see Section 2.6) [369]. In a device incorporating MTJs, skyrmions positioned beneath the junctions can be detected via changes in TMR [216–218], provided a significant portion of the skyrmion overlaps with the active area of the MTJ. Accurate detection requires an

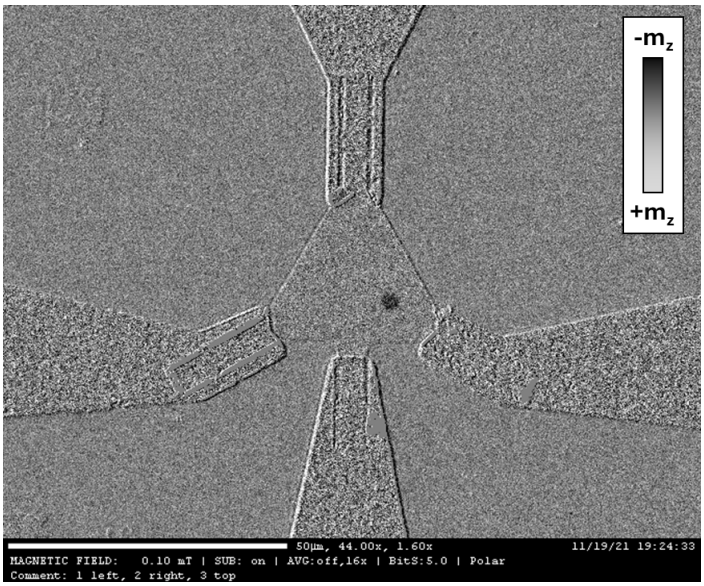

FIGURE 6.3: A representative MOKE microscopy image displays a field of view measuring 125×95 μm. The triangular device, containing a single skyrmion (visible as a dark grey spot), is electrically connected to four contact leads. The contact protrusions are faintly discernible beneath the gold leads due to sample drift and differential imaging. Notably, the bottom contact was not utilized in this experiment.

optimized measurement frequency that is sufficiently high to resolve magnetoresistive variations during the transient overlap, which must be matched to the velocity of the skyrmions. Additionally, the presence of the MTJ must not perturb the skyrmion dynamics, ensuring that the measurement process remains non-invasive. An industrial spintronic implementation would require additional CMOS-based circuitry for MTJ readout and signal processing. The potential dual functionality of MTJs, both as skyrmion nucleation sites and as readout elements in a miniaturized version of this demonstrator, is explored further in subsequent sections.

6.3.2 Forced skyrmion dynamics

This RC concept operates by measuring the probability distribution of the skyrmion's position, which arises from the interplay between current-induced motion driven by STTs and SOTs [79, 94, 95, 97, 98, 362], skyrmion-edge repulsion [172, 367], and thermal diffusive dynamics [110]. By applying an electric potential between the corners of the triangular confinement, the skyrmion is displaced from its initial position at the center of the triangle toward one of the corners. Upon removal of the potential, the skyrmion returns to the central position due to edge repulsion, effectively resetting the reservoir. A key advantage of this system is its energy-efficient operation, leveraging the combined effects of thermal dynamics and edge repulsion. Once a single skyrmion is nucleated, these mechanisms enable automatic initialization and self-resetting upon cessation of the applied potential. The system achieves its initial state without requiring additional input or adjustments to local pinning effects [229, 232], as a single skyrmion predominantly remains near the center of the triangular confinement. Figure 6.4 schematically illustrates the forces acting on the skyrmion within the confinement.

The skyrmion states, including the initial state and corresponding displacements under varying applied potentials, are presented in Figure 6.5. The applied potentials

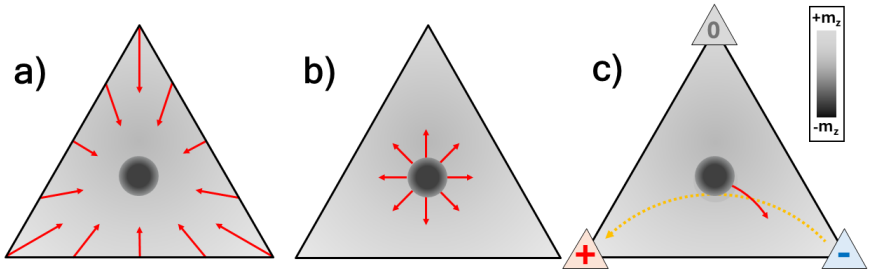

FIGURE 6.4: Schematic of the device with forces acting on the skyrmion (dark gray circle) within the triangular confinement, illustrated by red arrows: a) Skyrmion-edge repulsion: Due to stray-field interactions, the skyrmion experiences a repulsive force from the boundaries, resulting in its preferential localization near the center of the triangular confinement. b) Semi-isotropic, thermally activated diffusion: The skyrmion undergoes stochastic motion driven by thermal energy, with its diffusion behavior significantly influenced by the intrinsic energy landscape of the system. c) Current-induced displacement via SOTs: When an electric current (indicated by the yellow arrow) is applied, the skyrmion is driven toward the bottom corner due to the effect of SOTs. The applied potential configuration consists of a positive potential at the bottom-left contact (red), a negative potential at the bottom-right contact (blue), and a grounded contact (0 V) at the top (gray).

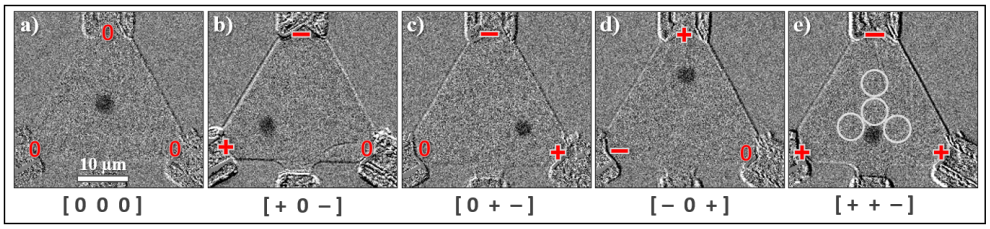

FIGURE 6.5: MOKE images of the same triangular device, each containing a single skyrmion, are presented. The applied electrical potentials - ground (0), positive (+), or negative (-) - are indicated in red characters at the respective contacts and are also summarized in brackets below each image in the order [left, right, top]. In subfigure (e), the locations of potential MTJ placements for readout are additionally marked by circles (not to scale). Adapted from [99].

were controlled using two individual Keithley 2400 SourceMeters. In subfigure (e), white circles indicate potential locations for MTJ placements, representing the positions for the mimicked TMR readout [369]. While numerous input configurations are possible, the Boolean functions presented later utilize only two voltage states - ground (0) and positive voltage (1) - applied to two contacts, while the third contact remains always at ground.

6.3.3 Current density distribution

To quantify the current density within this geometry, the half-height width of the triangular confinement is used, as the cross-sectional area narrows toward the corner contacts. This results in an increased current density near these contacts, where skyrmion annihilation was experimentally observed at higher applied currents. To analyze the underlying mechanisms and precise locations of skyrmion annihilation as current increases, a minimal model simulation was conducted by Censored Name using COMSOL Multiphysics® [370]. As previously mentioned regarding the necessity of gold coating along the edges, the current primarily flows through the

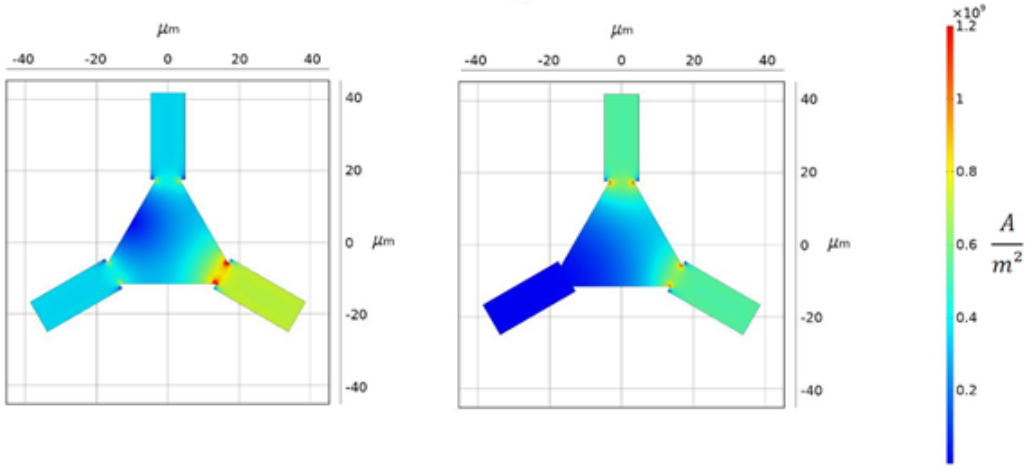

FIGURE 6.6: A simplified COMSOL Multiphysics® simulation was performed to analyze the current density distribution within the device. The left panel displays the current density distribution for a configuration in which a positive potential is applied at the bottom right contact, while the remaining two contacts are grounded. The right panel shows the current density distribution for an alternative configuration, where a positive potential is applied at the bottom right contact, the top contact is grounded, and the bottom left contact remains floating. The highest current density regions, highlighted in red, correspond to the bends where the gold contact terminates on the material stack. At these locations, the elevated current densities may result in localized heating, potentially leading to the annihilation of skyrmions. Simulation performed by Censored Name. Adapted from [99], supplementary material.

top tantalum layer and the bottom CoFeB-tantalum layers. Assuming a comparable current distribution in both layers, the simulation was performed solely for the 5 nm-thick top tantalum layer. In the model, the electrical contact was represented as a chromium pad surrounding the sides of the rectangular protrusion, excluding the top. The resulting simulated current density distribution is shown in Figure 6.6, where the highest current density (indicated in red) occurs at the initial interface between the material stack and the 5 nm chromium contact. Although the actual demonstrator device features a gold contact fully encapsulating the protrusion, empirical observations of skyrmion annihilation at these exact bends align with the predictions of the simplified simulation. Given the high thermal conductivity of the gold pads, which serve as efficient heat sinks, significant thermal effects contributing to skyrmion annihilation are considered unlikely and the higher likelihood of annihilation is assumed to arise due to interfacial effects between the material stack and chromium/gold.

Since only the 0.95 nm CoFeB layer, along with the tantalum seed layer interface, constitutes the *active* layer of the device, a reduction in layer thickness would lower overall power consumption while maintaining a constant current density. In an industrial application, the device would not include a conductive capping layer directly connected to the contact leads and pads; instead, alternative passivation methods, such as silicon nitride (Si-N) or silicon oxide (Si-O) [243], could be employed. Additionally, functional layers like a magnetic tunnel junction overhead or CMOS-based systems could be incorporated above the active region, acting as potential readout and analysis while other layers could further optimize device performance and reduce the required current for achieving the same current density.
Distinctive current-induced skyrmion motion was first observed empirically at a

current density of $J \approx 5 \cdot 10^7 A/m^2$ moving opposite to the direction of the technical current flow. Notably, this current density is approximately four orders of magnitude lower than that reported in previous studies on similar thin-film stacks [95, 110]. This pronounced reduction underscores the low-energy landscape of the fabricated FAB629 sample series and confirms the feasibility of skyrmion motion under ultra-low power conditions. To achieve reliable skyrmion displacement toward the corners of the triangular confinement geometry, a current density of approximately $J \approx 10^8 A/m^2$ was applied. A systematic analysis of the skyrmion Hall angle was not conducted, as the dynamics within the triangular geometry were already highly complex and dominated by geometric confinement effects.

6.4 Boolean Logic operations

The proof-of-concept was demonstrated using MOKE microscopy to visualize skyrmion displacement. For a scaled-down nanometer-scale device, MTJs would be employed, as TMR is sensitive to the local magnetization in the relevant region [369]. To simulate readout via MTJs in the image analysis, four circular readout regions with a radius of 2,2 µm were selected within the reservoir.

6.4.1 Training linear readout

A fundamental advantage of reservoir computing is that training is required only at the reservoir's output stage, where the system's response is mapped to the desired result [58, 222, 225]. In the presented demonstrator, the reservoir's intrinsic dynamics are not trained; rather, only the skyrmion's position in response to specific input conditions is considered. To simulate a potential device array system, multiple images with the same input configuration are analyzed, where each image represents an individual device subjected to the given input. This approach mimics a form of spatially multiplexed reservoir computing, which, unlike time-multiplexed systems relying on temporal input variations, does not require time-dependent evolution of the device state. However, achieving high stochastic accuracy necessitates sufficient sampling, e.g., large number of devices operating simultaneously.
From a technical perspective, training must be performed on each individual device to associate its output with a specific result. In this presented work, training was conducted on a single device, with measurements recorded over time across multiple images to effectively replicate the spatial reservoir computing behavior of multiple devices. The accuracy of this concept is dependent on the sampling, i.e. number of devices utilized, which correlates with the total chip area and the number of samples employed per operation. Given the simplicity and scalability of the triangular confinement geometry, a minimal area is required, making this system particularly advantageous for large-scale chip integration.
Due to the inherent stochastic nature of the system, skyrmion positions vary across different images, each representing a separate instance of the mimicked device. This variability is accounted for during training by assigning a weight, a factor, to each readout location, which corresponds to the probability of skyrmion occurrence at that position. The skyrmion occurrence probabilities are processed externally using a linear readout mechanism, where the final output is computed as a weighted sum of these probabilities plus an offset.
The output Q, which represents the mapped result, is mathematically expressed as the weighted sum of the skyrmion occurrence probabilities P_x at a specific circular

regions x, each multiplied by its corresponding weight W_x, along with an offset term $W_{\text{intercept}}$. Region x refers here to the mimicked MTJ positions as seen in color coded Figure 6.7 e) with **left**, **right**, **middle** and **top**.

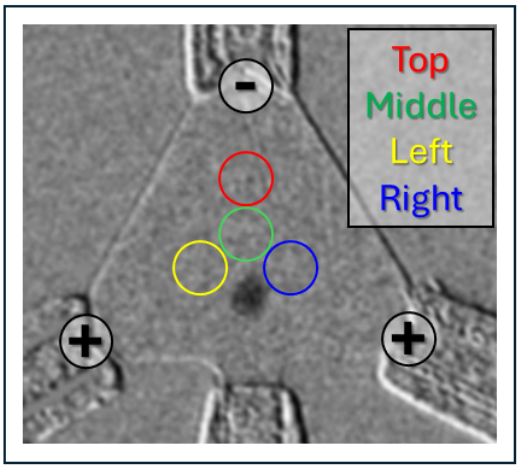

FIGURE 6.7: Potential MTJ positions color coded for visual aid - Reuse of Figure 6.5 e) for better positional clarification with same current applied.

This relationship can be formulated as:

$$\begin{aligned} Q &= \sum_x (P_x \cdot W_x) + W_{\text{intercept}} \\ &= W_{\text{left}}P_{\text{left}} + W_{\text{top}}P_{\text{top}} + W_{\text{middle}}P_{\text{middle}} + W_{\text{right}}P_{\text{right}} + W_{\text{intercept}} \end{aligned} \tag{6.1}$$

The skyrmion occurrence probability P_{region} is dependent on the input patterns applied to the device, specifically the four configurations: [00], [01], [10], and [11] (see Figure 6.8). Through weight optimization, the vector of skyrmion occurrence probabilities across the four designated regions—arising as a result of the applied input voltages—is mapped to either **0** or **1**. This mapping is determined by the specific Boolean operation being implemented for each input configuration.

This method enables the system to perform a variety of computational tasks depending on the assigned weights for each individual device. In this study, weights for multiple operations were trained using a single device, with Kerr microscopy measurements comprising 13,000 frames captured at 16 frames per second. The average skyrmion occurrence at four designated locations was determined over 1,000-frame intervals (corresponding to 62.5 s). These occurrence data were grouped into sets, with the first four of all 13 sets used to optimize (train) the weights for linear readout using the Scikit-learn software package [371], as presented in Table 6.1.[1]
The weight values (provided in Table 6.1) are determined based on the global skyrmion occurrence distribution shown in Figure 6.8 and effectively adjust the probability values to yield the desired output.

By setting the top contact to ground, logic operations were implemented using only the left and right bottom contacts as inputs, where logical states **[0]** and **[1]** correspond to ground (0 mV) and an applied potential (2 mV), as illustrated in Figures 6.9 or 6.10. For the **OR** logic operation, a logical output of **[1]** is expected for the input voltage combinations [2 mV, 0 mV], [0 mV, 2 mV], and [2 mV, 2 mV], applied

[1] Contributions to this work have been lined out in the Section D.6.

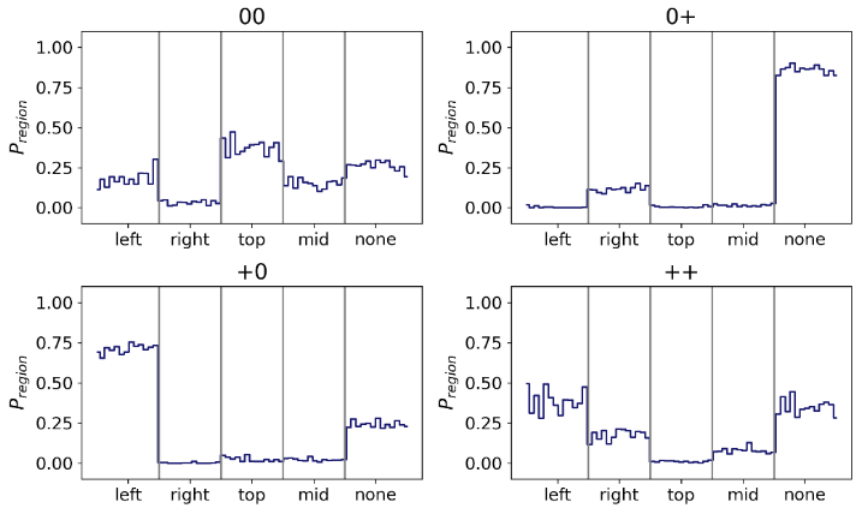

FIGURE 6.8: Skyrmion occurrence probabilities were analyzed for the four designated readout locations (see Figure 6.7), as well as for the region outside these areas (denoted as *none*), based on the two-contact input configurations across 13 sets of 1000 frames each. Taken from [99].

TABLE 6.1: Weights of the linear regression training process for Boolean logic operations using 4 sets of 1000 images each for point-like skyrmion (center readout). Taken from [99].

Operator	$\mathbf{W}_{\text{left}}$	$\mathbf{W}_{\text{right}}$	$\mathbf{W}_{\text{top}}$	$\mathbf{W}_{\text{middle}}$	$\mathbf{W}_{\text{intercept}}$
AND	1.124	7.497	0.623	1.022	-0.797
NAND	-1.124	-7.497	-0.623	-1.022	1.797
OR	0.272	1.09	-1.403	-2.908	0.942
NOR	-0.272	-1.09	1.403	2.908	0.058
XOR	-0.852	-6.407	-2.027	-3.93	1.739
XNOR	0.852	6.407	2.027	3.93	-0.739

to the left and right corners ([**left**, **right**]) of the triangular confinement geometry. In these cases, skyrmions are most likely detected either in the **left** region (for [2mV, 0mV]), the **right** region (for [0mV, 2mV]), or in both regions[2] (for [2mV, 2mV]), with the exact distribution influenced by pinning sites and thermally activated stochastic motion. In the latter case, the grounded top contact allows current to flow symmetrically toward both bottom corners, promoting skyrmion motion toward either confinement regions[3]. In contrast, for the input configuration [0mV, 0mV], corresponding to a logical output of **[0]**, the skyrmion remains predominantly localized in the **middle** region due to the absence of a directional current drive. As illustrated in Figure 6.8, the skyrmion occurrence probability is consistently high in the left and/or right readout regions for the logical **[1]** cases, resulting in the assignment of positive weight values to these regions. The product of the skyrmion occurrence probability P_x and its associated weight W_x determines the weighted output response Q, which either exceeds or remains below a defined threshold, thereby enabling differentiation between output states **[1]** and **[0]**. Conversely, skyrmion presence in the top

[2]It is important to note that the skyrmion cannot simultaneously occupy both regions; however, the probability of its presence in either individual region is high.

[3]The likelihood of skyrmion occurrence is asymmetric, primarily due to the inhomogeneous energy landscape and the (minor) influence of the skyrmion Hall effect (see Section 2.4.5).

readout region is predominantly associated with the input condition [0mV, 0mV], which corresponds to a logical **[0]**. As a result, a negative weight is attributed to the top region to suppress contributions to the output signal in this configuration.
This approach necessitates that each device undergo individual characterization and task-specific training.
The linear readout was trained to implement the Boolean logic operations **AND**, **NAND**, **OR**, **NOR**, as well as the non-linearly separable **XOR** and **XNOR**. In the respective graphs, the light blue sections of the curves represent the four-part training set used for weight optimization, while the black sections correspond to the nine-part test set. The dashed lines indicate possible threshold values for perceptron-based readout, effectively mapping the results onto the output: values of Q above the threshold are assigned to output **[1]**, whereas values below the threshold correspond to output **[0]**. Training and test set outputs demonstrates reliable performance across all presented Boolean logic operations.

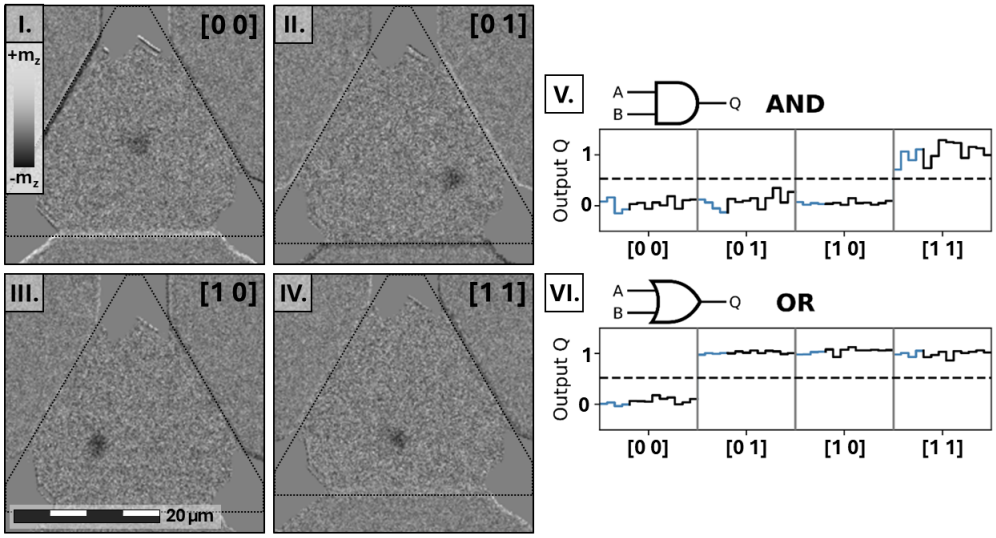

FIGURE 6.9: I.–IV.) Differential MOKE images illustrating skyrmion occurrence states as a function of the applied input (top-right corner). Skyrmions, appearing as dark spots representing -m_z, are displaced towards the corner or, for the input state [1,1], towards the bottom edge. The fine dashed line outlines the triangular confinement region. V.) and VI.) depict the output of Boolean logic operations: V) AND and VI) OR. In each case, for a given input state [left, right], the blue region of the graph represents four sets of 1000 images used for training, while the remaining nine sets, also consisting of 1000 images each, serve as test sets. The dashed line indicates the classification threshold, distinguishing between output states [0] and [1]. Partially adapted from [99].

Boolean operations remain invariant under the input transformation

$$[A, B] \iff [B, A] \tag{6.2}$$

and should yield identical skyrmion occurrence probabilities. Since the readout regions in this system are symmetrically positioned around the vertical mirror axis of the triangular confinement, the trained weights for the left and right regions are expected to be equal, ensuring consistent outputs. For Boolean logic negation (**NOT**) operations, the trained weights (excluding the offset) are simply the negative counterparts of the corresponding positive logic operations, as **NOT** inverts the output

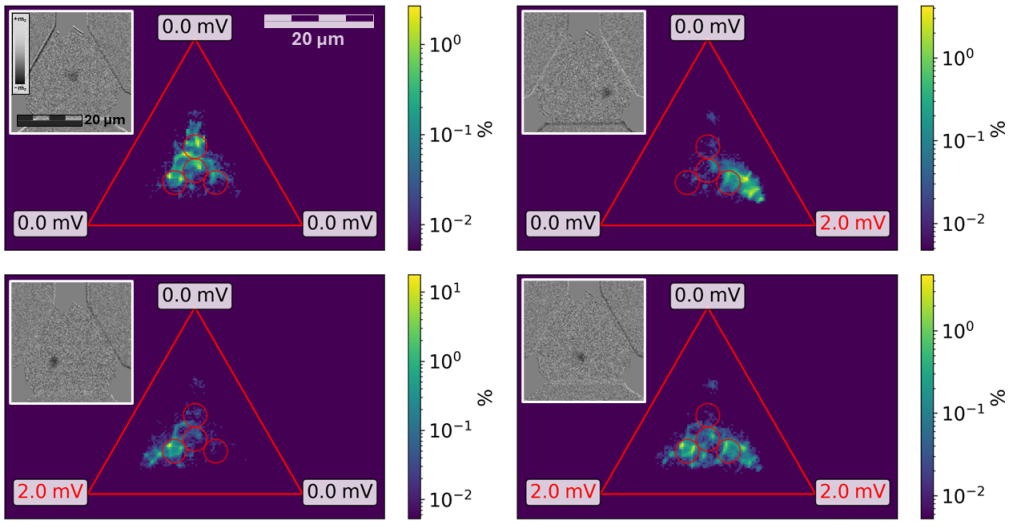

FIGURE 6.10: Skyrmion occurrence probability maps are presented, where yellow pixels indicate the highest likelihood of skyrmion presence and violet represents the lowest probability. The applied electrical potentials at the device corners are color-coded: black denotes ground (0.0 mV), while red indicates a +2.0 mV potential. a) Skyrmion undergoing free thermal diffusion, b) skyrmion displaced towards the bottom-right corner, c) skyrmion displaced towards the bottom-left corner, and d) skyrmion simultaneously influenced towards both bottom-left and bottom-right corners due to stochastic effects. The red circles mark the designated readout regions used for the linear readout analysis. Insets display corresponding MOKE images capturing the skyrmion position for each condition. Adapted from [99], supplementary material.

mapping between 0 and 1. Despite the geometric symmetry of the device, variations in electrical resistance between corner contacts result in different current density distributions at identical applied voltage potentials. Consequently, skyrmion occurrence probabilities deviate strongly due to current density differences, in combination with pinning effects arising from the thermally diffusive interaction with the local energy landscape. Although these irregularities could be minimized through enhancing fabrication techniques, a more uniform energy landscape, or thermal activation to overcome pinning effects, the linear readout training compensates for sample imperfections and experimental variations, including temperature fluctuations, as long as the skyrmion remains within the reservoir. Notably, the [0 mV, 0 mV] input configuration exhibits a high skyrmion occurrence probability in the top region (see Figure 6.10), which reduces noise in logic operations that primarily distinguish this input from others (e.g., **OR** and **NOR**), as shown in Figure 6.11. As discussed in Section 6.3.1, multiple devices were tested, all exhibiting qualitatively similar behavior. This consistency highlights the robustness and reliability of the system, despite its simplicity.

6.4.2 Role of non-flat energy landscape

Although the material stacks have been thoroughly optimized, the energy landscape remains relatively flat, leading to skyrmion pinning, as observed in Figure 6.10 and reported in [36, 37, 157, 172]. As previously discussed, under trivial input conditions, the skyrmion is rarely located in the bottom right of the geometry. However,

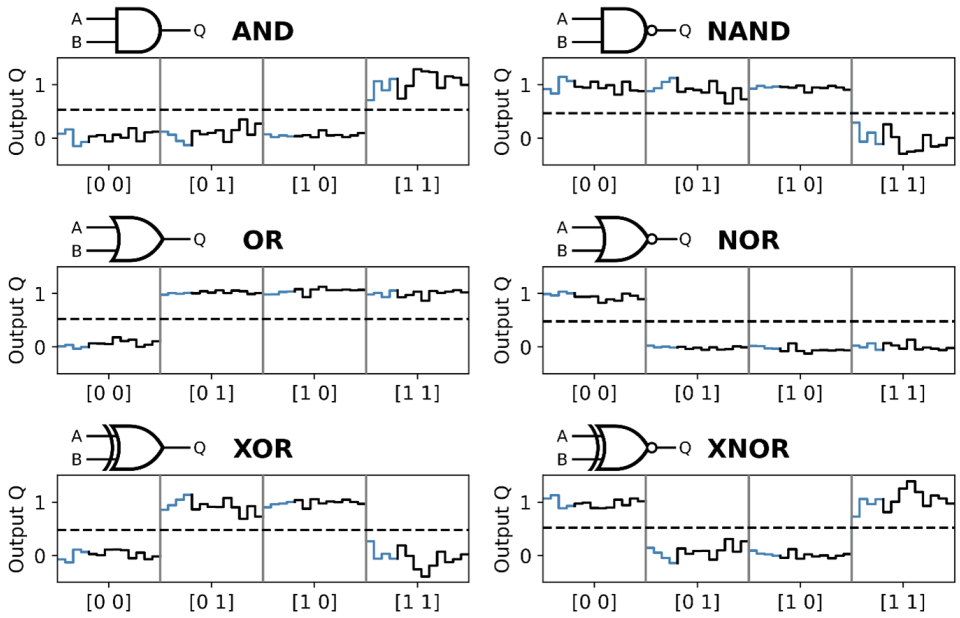

FIGURE 6.11: The outputs of the linear read-out, optimized for various Boolean operations, are presented based on local skyrmion occurrence probabilities. For each input combination ([0 0], [0 1], [1 0], [1 1]), the corresponding linear read-out output Q is shown for 13 distinct sets of local skyrmion occurrence probabilities. The blue and black segments of the curves indicate the data sets used for training and testing, respectively. A dashed horizontal line represents a potential threshold for perceptron-based read-out. Adapted from [99].

for certain input values, skyrmions can reach pinning sites that would be otherwise inaccessible through diffusion alone. For instance, with an input of [0mV, 2mV], the skyrmion is displaced so far to the right that its probability of occurring outside the designated readout region increases. This suggests that the energy landscape in this region is more favorable for skyrmion stabilization outside the readout location.
An increase in temperature - within the non-annealing regime[4] - modifies the nonlinear interplay between exchange interaction, DMI, PMA, and, when magnetic fields are applied, Zeeman energy, thereby directly affecting skyrmion size and thermally activated motion [98, 110, 372] near pinning sites [157]. Specifically, elevated temperatures lead to a reduction in both PMA and exchange stiffness, which in turn results in a shrinking of the large (micrometer-sized) skyrmions observed in this study. At sufficiently high temperatures, thermal excitation may further destabilize the delicate energy balance, leading to a reduction of skyrmion size below the resolution limit of the Kerr microscope used or, above certain temperature limits, to complete annihilation [110, 139, 166, 296, 349, 373]. Additionally, skyrmion size plays a critical role in the interaction with the non-flat energy landscape. As demonstrated by R. Gruber et al., the pinning of micrometer-sized skyrmions is primarily determined by the surrounding domain wall rather than the skyrmion core [157]. Overall, the impact of the non-flat energy landscape on this RC concept is minimal, as device-specific training inherently compensates for pinning effects, provided the skyrmion is not permanently immobilized. A potential challenge arises if temperature variations cause the skyrmion to become pinned at different locations, as temperature

[4] In this context, non-annealing refers to the application of temperatures that do not induce intentional modifications to the sample's structural or magnetic properties, although elevated thermal exposure may still enhance interdiffusion at material interfaces.

influences pinning behavior. Given that a key advantage of this RC approach lies in its energy-efficient training - where training is performed only once for a specific task - such temperature-induced variations could partially undermine this efficiency.

6.4.3 Signal-to-noise

To quantitatively assess the distinction between the chosen two output states derived from the linear read-out Q, the signal-to-noise ratio (SNR) is employed, defined as:

$$\mathrm{SNR} := \frac{\langle \mathbf{T} \rangle - \langle \mathbf{F} \rangle}{\sigma_{\mathbf{T}} + \sigma_{\mathbf{F}}} \tag{6.3}$$

where **T** and **F** represent the subsets of linear read-out outputs Q corresponding to cases where the Boolean operation applied to the device input yields True or False, respectively. The angled brackets indicate the mean values, while $\sigma_{\mathbf{T}}$ and $\sigma_{\mathbf{F}}$ denote the standard deviations of the **T** and **F** subsets. For the presented system, where a single skyrmion is used with two input contacts, the averaged SNR across six different Boolean logic operations exceeds 5. This value is obtained from the full data set of 13000 frames, effectively mimicking 13000 independent (trained) devices operating simultaneously. The SNR decreases as the time interval used to determine local skyrmion occurrence probabilities is reduced, which is equivalent to decreasing the number of devices in this spatially multiplexed RC system. This trade-off leads to increased energy efficiency at the cost of reduced SNR. If the time interval is halved - while maintaining the ratio between training and testing sets - the SNR decreases to approximately 4. The Boolean logic operation results obtained with only half the number of frames (devices) are shown in Figure 6.12. To enable robust discrimination between output states, it is essential to sufficiently sample the skyrmion occurrence probabilities, thereby ensuring a comprehensive representation of the reservoir dynamics. Adequate sampling captures the spatial (or potential temporal) variability required for the system to generalize effectively and perform the intended computational task with high reliability.

6.4.4 Skyrmion size effect impact

The size of free skyrmions in the studied samples exhibits a temperature dependence [110], which constrains skyrmion tracking and recognition via Kerr microscopy at elevated temperatures. However, within the temperature range used for these measurements, skyrmions remained sufficiently large for reliable identification and tracking by Kerr microscopy. Skyrmion size can also be influenced by geometric confinement and interactions with neighboring skyrmions, which compete for available space, as described in Chapters 4 and 5. A critical factor related to skyrmion size is that the analysis has been limited to determining the probability of the skyrmion center - defined by tracking algorithms - located within one of four predefined circular regions, emulating MTJ read-out. The effects of skyrmion size, particularly the partial overlap between a skyrmion and one or even multiple MTJ read-out regions, have not been fully characterized. Since the TMR signal is influenced by the degree of overlap between the skyrmion and the read-out region, the diameter of the circular read-out regions was selected to be approximately equal to the skyrmion diameter. To account for the influence of skyrmion size, the calculation of P_{Region} was refined by weighting occupation counts in each frame based on the relative areal overlap between the skyrmion and the read-out region

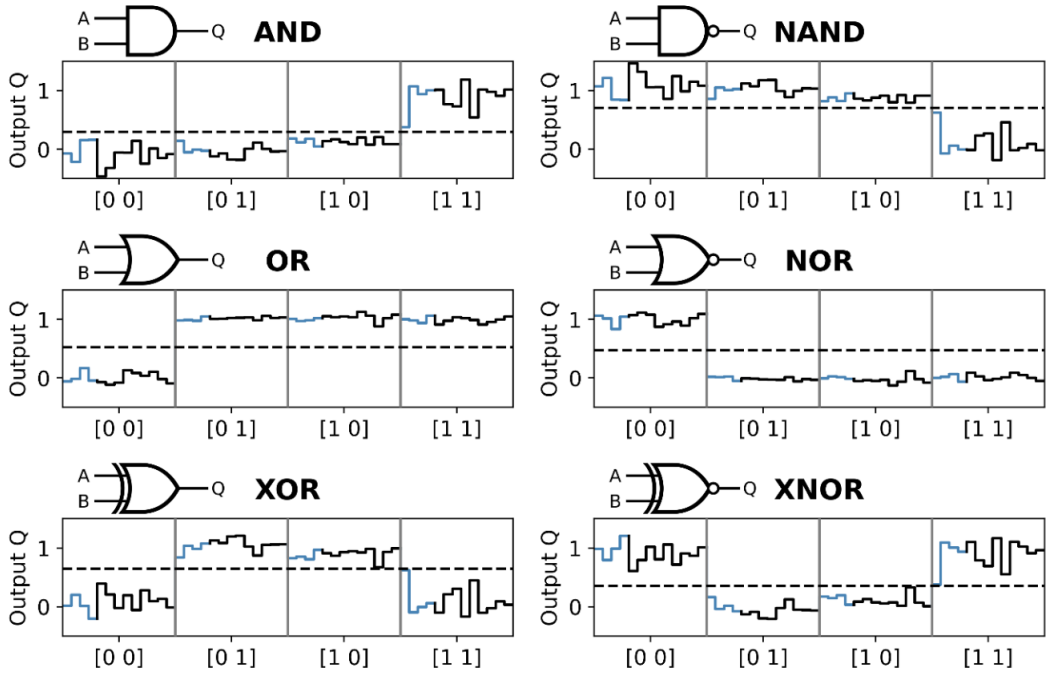

FIGURE 6.12: The linear read-out output Q corresponding to the input combinations [0,0], [0,1], [1,0], and [1,1] for various Boolean logic operations is presented for 13 sets of local skyrmion occurrence probabilities. In contrast to Figure 6.11, the time interval used to average the local skyrmion position probabilities has been halved, effectively reducing the number of sampled devices. This reduction leads to a decreased SNR. The blue and black segments of the curves represent training and testing data, respectively, while the dashed lines indicate potential threshold values for perceptron-based read-out. Compared to Figure 6.11, the signal distances from the threshold are reduced, reflecting the lower SNR resulting from the decreased sampling interval. Adapted from [99], supplementary material.

(assuming similar diameters for both). These weighted counts are then normalized by the total number of frames to obtain P_{Region}. Additionally, given the proximity of the read-out regions, a single skyrmion within a single frame (device) can contribute weighted occupation counts to multiple read-out regions. This methodology alters the calculated occupation probabilities, as illustrated in Figure 6.13.

These modifications can be comprehensively understood by analyzing the spatially resolved skyrmion occurrence probability. For example, a prominent pinning site is observed near the boundary of the right read-out region, resulting in a decrease in P_{Right} when using the revised calculation method. However, the overall distribution of occupation probabilities for each Boolean input remains well-defined, indicating that the influence of skyrmion size is negligible after optimizing the linear read-out (see Figure D.1 in Appendix D). As the relative overlap between the skyrmion and the TMR readout affects the measured skyrmion probability in this example, a real device would require the implementation of a threshold for the TMR readout. This threshold should be defined to reliably identify a skyrmion even with minimal overlap while ensuring a clear and significant distinction from noise. The signal-to-noise ratio, however, remains largely unchanged, highlighting the robustness of the investigated system. Notably, the observed reduction in P_{Right} corresponds to an increase in the optimized weight W_{Right} (see comparison in Appendix D, Tables D.1).

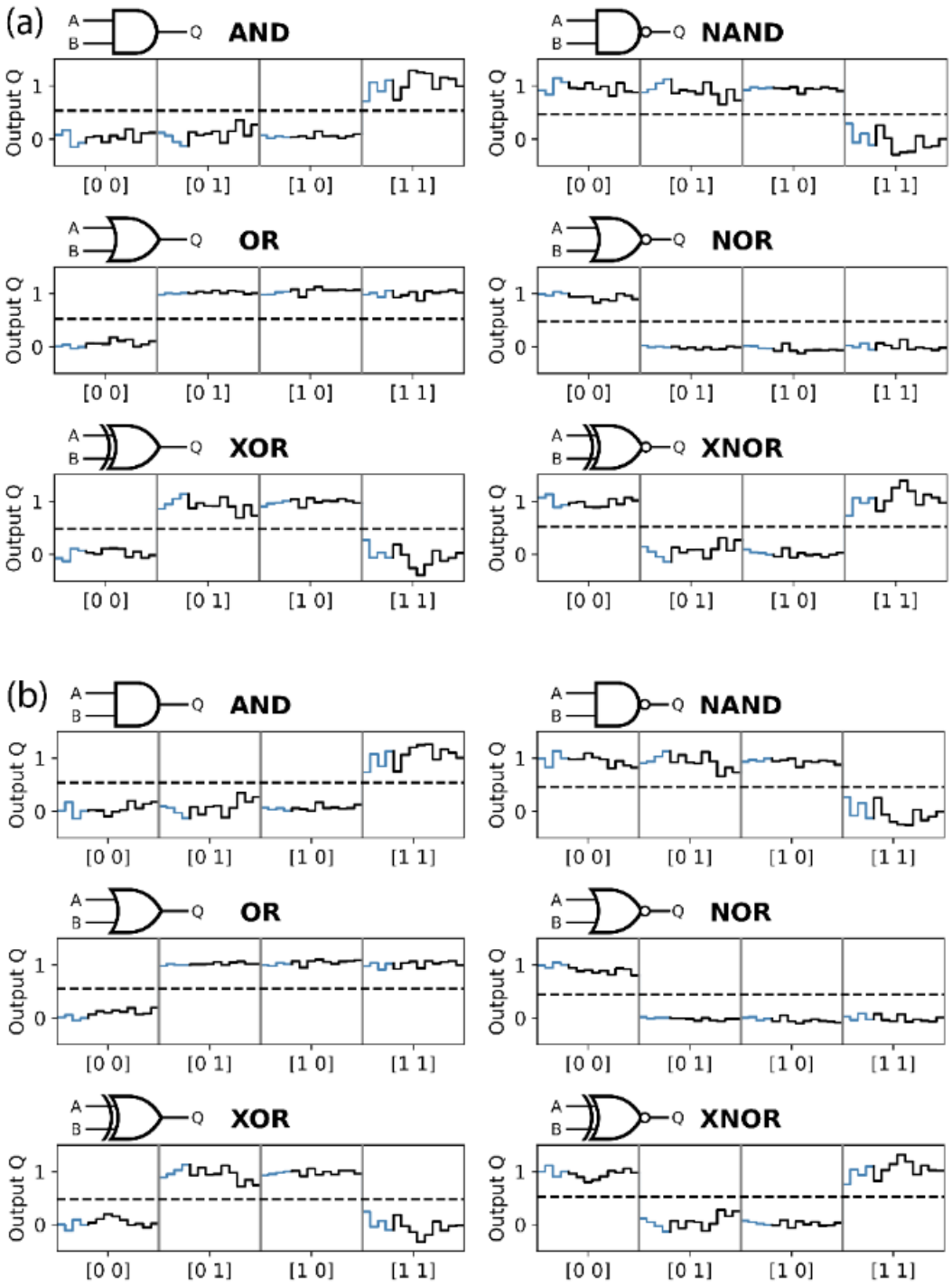

FIGURE 6.13: The outputs of the linear read-out, optimized for various Boolean operations, are presented based on local skyrmion occurrence probabilities determined using two different methods: a) skyrmion center positions and b) the relative areal overlap between the skyrmion and the read-out regions. For each input combination ([0 0], [0 1], [1 0], [1 1]), the corresponding linear read-out output Q is shown for 13 distinct sets of local skyrmion occurrence probabilities. The blue and black segments of the curves indicate the data sets used for training and testing, respectively. A dashed horizontal line represents a potential threshold for perceptron-based read-out. Adapted from [99], supplementary material.

6.4.5 Three input operation

Thus far, only two input terminals have been utilized in the device, enabling the realization of Boolean logic operations while maintaining the third contact at a constant ground potential. To enhance computational complexity, the third input can also be utilized, facilitating three-input composite logic operations, as exemplary illustrated in Figure 6.14. This configuration allows for 27 possible input combinations, although some of states are either redundant or inherit no function. Redundant states arise due to gauge invariance, exemplified by input configurations a) [- - 0] and b) [0 0 +], both of which lead to skyrmion displacement toward the same corner, with a) corresponding [0] and b) to [+]. States without function, such as [- - -], occur in cases where electrical resistance remains uniform across the system. For the three-input demonstration, the same data set comprising 13 sets of 1000 images each was employed, with four sets used for training and nine for testing. The resulting average SNR for the three-input operations was SNR > 3, which is lower than that observed for the two-input operations. This reduction is evident from the decreased separation between output states and the decision threshold. The corresponding truth tables for these operations are provided in the appendix D.2.

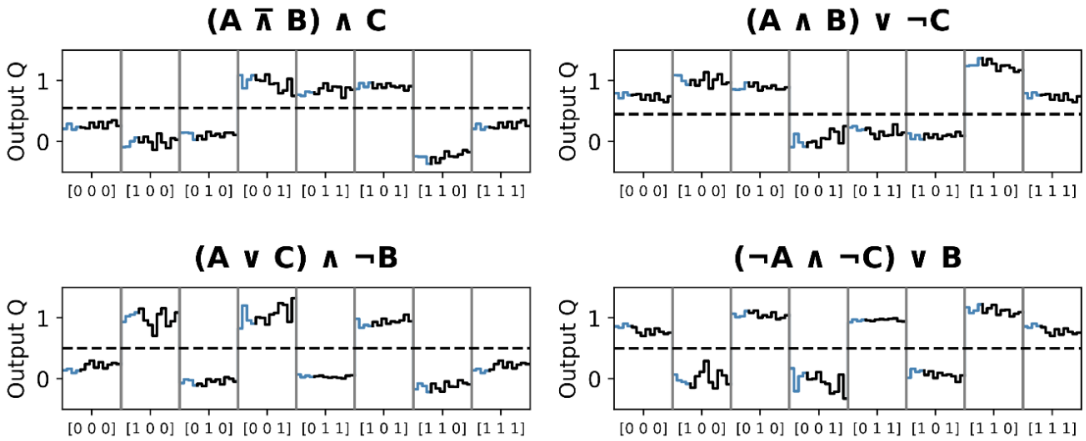

FIGURE 6.14: The outputs of the linear read-out, optimized for various three-input logic operations, are presented. For each input combination [A,B,C], the corresponding output Q of the linear read-out is displayed across 13 sets of local skyrmion occurrence probabilities. The light blue segments of the curves represent the training data set, while the black segments correspond to the testing data set. A dashed horizontal line indicates a potential threshold for perceptron-based read-out. Adapted from [99], supplementary material.

6.4.6 Influence of temperature

As previously discussed, a flat energy landscape and maintaining a sufficient temperature to enable thermally activated skyrmion diffusion are essential for the functionality of this RC concept, given that skyrmion diffusion exhibits an exponential dependence on temperature [110]. For the present measurements, the device temperature was selected to ensure diffusion dynamics compatible with the sampling rate limitations of the Kerr microscope. The integration of MTJs would mitigate this constraint [167, 208], as sampling occurs faster with MTJs in small-scale devices. This is also due to the timescale of directed diffusive motion scaling with the square of the characteristic length scale [148]. Consequently, a nanometer-scale device would enable faster measurement cycles, as nanometer-scale skyrmions exhibit reduced

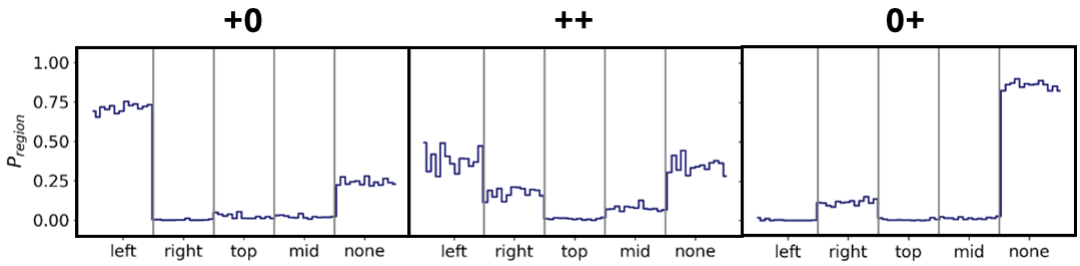

FIGURE 6.15: Skyrmion occurrence probabilities across the four readout locations and the surrounding region (none) are shown for the three-input combinations [0+], [++], and [+0]. In the absence of thermal diffusion, the input [++] in this device would result in the skyrmion occupying the same locations as for [0+], while the locations characteristic of input [+0] would remain inaccessible. Consequently, the input state [++] would become indistinguishable from [+0], highlighting the necessity of thermal diffusion for maintaining the functional integrity of this RC concept. Adapted from [99], supplementary material.

sensitivity to pinning effects [37, 127, 129, 157, 327]. This diminished pinning susceptibility enhances their mobility, allowing for more efficient dynamical response, as further elaborated in the subsequent section on energy consumption (see Section 6.6).

6.5 Necessity of thermal diffusion

In a practical device, thermal fluctuations can be harnessed to mitigate imperfections such as pinning effects and resistance asymmetries, thereby significantly enhancing the robustness and reliability of operations. To demonstrate that thermal diffusion is essential for this demonstrator, the hypothetical behavior of the device with three inputs in the absence of Brownian motion is considered:
Since the top contact in this demonstration is always grounded, applying left and right inputs, [0+] and [+0], drives the skyrmion into the right and left corners, respectively. In an idealized device - characterized by the absence of pinning, perfectly symmetric resistances and current distributions, uniform edge repulsion, and no SkHE - the input [++] would consistently direct the skyrmion to the central bottom region, as illustrated in a single representative frame in Figure 6.5 e). However, in realistic devices, including the presented demonstrator, fabrication-induced inhomogeneities and asymmetries in resistance result in deviations from this ideal behavior. In the absence of thermal fluctuations, the skyrmion is predominantly pushed into one specific corner - left, in this case - even for input [++]. Consequently, input [++] would be indistinguishable from input [+0], as both would lead to high skyrmion occupancy in the left corner. With thermal dynamics, however, the skyrmion, while still preferentially moving toward the left corner due to inherent asymmetries, retains the ability to overcome these energy barriers and diffuse toward the less favorable right corner. As a result, the probability distribution of skyrmion occurrence becomes distinct from that of input [+0], where the likelihood of occupying the left corner remains significantly higher (see Figure 6.15). This demonstrates that thermal diffusion not only counteracts fabrication-related imperfections but also plays a crucial role in preserving the distinguishability of different input states, thereby improving the overall robustness of the system.

A similar consideration applies to skyrmion pinning effects. In a system without Brownian motion, where resistance asymmetries are either absent or compensated by adjusting input voltages, skyrmion pinning is the result of strongly inhomogeneous effective energy landscapes, as demonstrated in Figure 6.10 and previously reported in [298]. As a result, instead of settling into a central downward position, the skyrmion follows the path of lowest energy (i.e., regions of highest pinning), typically migrating toward one of the two sides where the current density is relatively higher compared to the central region (see Figure 6.6). In this scenario, Brownian motion can once again mitigate this effect by facilitating transitions between pinning sites, thereby restoring distinguishable configurations for all three input states ([++], [0+], and [+0]).

Since the applied current densities - and consequently the induced velocities - are relatively low in this system (creep regime, see Chapter 4 and in Section 6.4.2), the influence of the skyrmion Hall effect is negligible [183, 188, 327] and remains superimposed with thermal diffusion, energy landscape variations, and fabrication-induced imperfections. However, in a miniaturized device with potentially higher current densities, the skyrmion Hall effect could become more prominent [97], leading to asymmetric skyrmion trajectories depending on the skyrmion's topology. For instance, considering the input combinations [+0], [++], and [0+] again, due to a fixed topology the skyrmion Hall effect would cause skyrmions to preferentially drift toward one side. In the case of [0+], the perpendicular force induced by the skyrmion Hall effect could shift skyrmion occurrences closer to the bottom center compared to the idealized scenario without a Hall angle. Similarly, under the [++] input, skyrmions would be deflected rightward due to their motion but could ultimately accumulate on the left, leading to a signal similar to that of [+0].
Thus, a balance must be maintained between induced motion, velocity, and thermally activated diffusion in a scaled-down device to ensure reliable operation. If the skyrmion Hall effect remains moderate, the system's training process can compensate for these asymmetries by adjusting the weights accordingly. To completely circumvent the Hall effect, a (synthetic) antiferromagnetic stack - such as a compensated ferromagnetic bilayer - could be implemented, which has been shown to suppress or even eliminate skyrmion Hall motion. Moreover, diffusion in such compensated bilayers is known to be enhanced [153], potentially leading to improved system performance.

6.6 Energy consumption estimation

One of the key advantages of RC concepts is their intrinsic energy efficiency, as the primary computational processes emerge from the system's inherent dynamics. This particular proof-of-concept device demonstrates significant potential for energy-efficient operation due to several factors: i) training is required only once for a given task, ii) the reservoir reset mechanism occurs passively, incurring no additional energy cost, and iii) skyrmion displacement via SOTs requires minimal power. Furthermore, since the device exhibits a stable skyrmion phase at ambient and slightly elevated temperatures, no additional energy consumption for thermal heating (or cooling) is assumed. Consequently, the primary energy cost in this system arises from the current-induced skyrmion motion toward the designated readout regions.

6.6.1 Scaled down device

To estimate the lower bound of energy consumption, a hypothetical down scaled device is considered with an edge length of 400 nm and a skyrmion diameter of 40 nm (r_{sky} = 20 nm), maintaining a similar ratio between device and skyrmion size as in the present study. Readout in such a nano-scale system would entirely rely on MTJs, as discussed in previous sections. Although it is technically feasible to assume further reduction of the system size - down to single-digit nanometer skyrmions and MTJ pillars, with an overall device size in the tens of nanometer range - the conservative assumption of a 400 nm device is based on an upper limit for energy consumption and the currently achievable and reliable fabrication of MTJs, despite reports of single-digit nanometer MTJs being realized [374, 375].

6.6.2 Electric resistance measurement and estimation

Experimental measurements of resistance between device contacts have shown variability across different contact combinations, devices, and samples. For estimation purposes, an average resistance of $R \approx 1$ kΩ between two contacts is assumed. The resistance measurements were conducted using a Keithley 2400 Sourcemeter in combination with a specialized circuit (referred to as the *blue box*) designed to prevent excessive loading on the device circuit (see Section 3.3.5) and were largely distributed around $R \approx 1$ kΩ. To extrapolate resistance and current requirements for a scaled-down device, the geometry between two contacts is approximated as a rectangular wire with a width equal to the inner radius of the triangular device (11.5 µm) and a length of approximately 5/6 of the triangle's edge length (33.3 µm). This setup assumes one contact at a positive potential, one at ground, and the third contact floating. Notably, when recalculating resistance using these spatial parameters (see Section D.4), the scaling factor cancels out, meaning that the nano-scale device would exhibit a resistance comparable to that of the current micrometer-scale proof-of-concept, not assuming potential increased resistivity surface- or interface-effects.

6.6.3 Electric current density and current flow

For current density calculations, the 5 nm tantalum capping layer and full seed layer is included. In a scaled-down spintronic device, the capping layer would be replaced by TMR readout overhead, and only the functional bottom HM/FM layers would remain connected in the circuit. Additionally, samples such as TMD109 (see Section A.1) have demonstrated empirically that the tantalum seed layer thickness can be reduced without significantly compromising skyrmion properties or dynamics. Since a thinner layer reduces the overall current required for a given current density, energy consumption decreases correspondingly. Given a lower threshold current density of J = 5 $\times 10^7 A/m^2$ for distinct skyrmion motion in the present stack, the estimated current required to move a skyrmion in the scaled-down device would be $I = 110$ nA.

6.6.4 Time estimation of skyrmion motion

In the absence of an applied current, the skyrmion experiences a repelling force that drives it toward the center of the device, where thermally activated diffusion dominates its dynamics. Estimating the time required for this reset process is challenging, as the repelling mechanism does not directly scale from the presented micrometer-sized demonstrator to nanometer-scale devices. A study conducted by K. Leutner

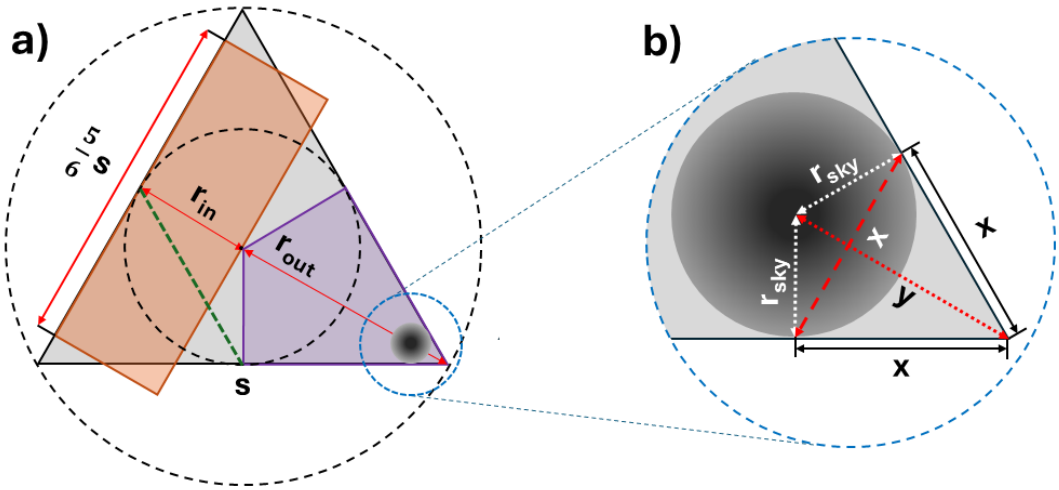

FIGURE 6.16: a) Schematic representation of the device. The black dashed inner and outer circles indicate the inner and outer radii. The orange box represents a simplified approximation of the channel used for estimating current flow between two contacts, while the third contact remains floating. The green dashed line marks the half-height width of the triangular geometry, which is used for current density calculations in previous sections. A dark gray sphere illustrates an in-scale skyrmion positioned at its maximum displacement. The violet region highlights the area that a skyrmion must traverse back to the center region (used in energy consumption estimation) b) Close-up of the device corner with the maximum possible skyrmion displacement (considering no skyrmion size change or deformation), indicated by the blue dashed line. Trigonometric calculations reveal that the skyrmion remains at a distance of $y = 2 \cdot r_{\text{sky}}$ from the triangular tip, while the corresponding chord touching the device edges is given by $x = \sqrt{3} \cdot r_{\text{sky}}$ (not considering protrusions with finite width for electric leads).

et al. presents simulated results based on experimental parameters, demonstrating the extrication of a skyrmion from a similar triangular geometry despite a sharper opening angle. This phenomenon, termed *automotion*, exhibits relatively fast dynamics [330]. If only diffusion is considered, the skyrmion would require additional time to sufficiently explore the device to ensure proper functionality. The time required for a skyrmion to diffusively explore an equivalent portion of the sample [148] in 2D at a different scale can be approximated as:

$$t_{\text{diff}} = \frac{A_{\text{triangle}}}{4 \cdot D} \tag{6.4}$$

where t_{diff} represents the reset time, A_{triangle} is the surface area of the device, and D is the skyrmion diffusion constant. This calculation provides an upper bound, as it does not account for the edge-induced repelling force, which would accelerate the skyrmion's return to the center, thereby reducing reset time. Using a diffusion constant of $D = 1.5 \times 10^{-10} \frac{m^2}{s}$, as determined in a previous study [110], the estimated exploration time for a micrometer-scale demonstrator (corresponding to one-fourth of the device area, highlighted in violet in Figure D.2) is $t_{\text{diff, µm}} = 289$ ms. For a scaled-down nanometer-sized device - assuming the same diffusion constant - the corresponding time is $t_{\text{diff, µm}} = 29$ µs. These values represent conservative estimates, as they do not account for repelling forces, the expected increase in diffusion constant for nanometer-sized skyrmions [42], or the fact that the skyrmion only

needs to return to the central readout region through the readout area of its respective corner and does not need to be pushed towards the maximum possible position in the corner (as displayed D.2 b)). MTJ readout times have been reported in the nano- to picosecond range [167, 208, 375], making them negligible compared to the skyrmion diffusion time. This fast readout speed allows for more than 1000 measurements during a single operation. Since the presented concept employs spatially multiplexed RC, a single readout per device should ideally occur at a predetermined time to ensure sufficient skyrmion exploration. However, given the long exploration time, multiple readouts per skyrmion displacement could further enhance sampling accuracy or could reduce the necessary amount of devices.

6.6.5 Electric energy consumption

The electrical energy required for skyrmion displacement can be estimated using the power equation $P = U \cdot I = R \cdot I^2$, where $I = 110$ nA is the current and $R = 1$ k Ω is the resistance, yielding $P = 12.1$ pW. Considering the previously calculated skyrmion displacement time and the diffusion-based exploration time required for a single readout, the energy per skyrmion displacement is $E = P \cdot t = 349 \cdot 10^{-18}$ J = 349 aJ. The Landauer limit (Ll) [376], the minimum heat energy wasted at the deletion of one Bit of information - at the functional temperature of the device at 315 K would be $E_{Ll} = k_B\ T_{func.} \cdot \ln(2) = 3 \cdot 10^{-21}$J = 3 zJ. The presented estimation therefore remains approximately five orders of magnitude above the theoretical Landauer limit. The total time for a Boolean logic operation, including multiple readouts for enhanced sampling, is estimated to be below $t = 28.87$ µs, excluding any additional CMOS-based overhead.
Considering only the dimensions of a potential miniaturized device and assuming similar current densities and dynamic behavior as the demonstrator, a simplified derivation demonstrates that the required electrical energy is proportional to the square of the scaling factor ($E \propto x^2$). For instance, if the device dimensions are reduced by a factor of 2, the corresponding energy consumption decreases to one-fourth of the original value. With a scaling factor of 100, as employed in the energy estimation, the energy consumption would be reduced by a factor of 10000. The detailed derivation of the proportionality of electrical energy can be found in Section D.4.2.

6.6.6 Dependence on temperature

The skyrmion phase in the demonstrator is stable at and slightly above ambient temperature, exhibiting thermally diffusive behavior. While it is technically feasible to actively cool or heat the device to achieve specific skyrmion properties, such an approach is impractical, as it would primarily serve to counteract environmental overheating or undercooling rather than enhance performance. Moreover, active temperature control could compromise skyrmion stability and overall device functionality. Although localized heating has been shown to improve performance [331, 349], it would come at the cost of reduced energy efficiency - one of the key advantages of reservoir computing for complex computational and machine learning tasks. For instance, a simplified energy estimation for a 10 K temperature increase indicates an energy cost of E = 210 pJ for a micrometer-scale device and E = 21 fJ for a nanometer-scale device, excluding thermal losses due to dissipation or interactions with electric leads, the substrate, or additional layers (see Section D.5).

6.6.7 Discussion of energy estimation

Since conservative upper-limit assumptions were used, the actual energy and time requirements could be further reduced. Additionally, even lower sampling rates have been shown to yield satisfactory results, as demonstrated with half the sampling rate in Section 6.4.3. While the presented proof-of-concept device demonstrates competitive performance relative to other reservoir computing architectures [51, 368], a comprehensive assessment of overall power consumption would also account for the associated MTJ readout and CMOS peripheral circuitry. Notably, the device operates in a DC regime, which significantly lowers the requirements for CMOS peripheral components compared to oscillator-based AC magnetic devices [377–379]. Consequently, a reduction in CMOS overhead relative to previously analyzed peripheral circuit configurations is anticipated. MTJs and any CMOS overhead were thus not included in this estimate. However, compared to the energy consumption of the down-scaled spin-torque nano-oscillator ($\sim$ hundreds of attojoules per oscillation) reported by Romera et al. [377], the estimated energy requirements for this skyrmion-based RC system appear highly promising despite the approximations used in this analysis.

6.7 Concept and device optimization

6.7.1 Complexity enhancement

When multiple skyrmions are confined within the system, the response to input signals exhibits increased complexity. This effect is especially pronounced when the number of skyrmions is incommensurate with the device geometry [172], as long as their presence does not substantially hinder stochastic motion and spatial exploration. As an illustrative example, two distinct four-skyrmion configurations are presented in Figure 6.17. Moreover, the integration of multiple coupled devices would introduce additional distinguishable states, further augmenting the system's computational capacity [174, 378].

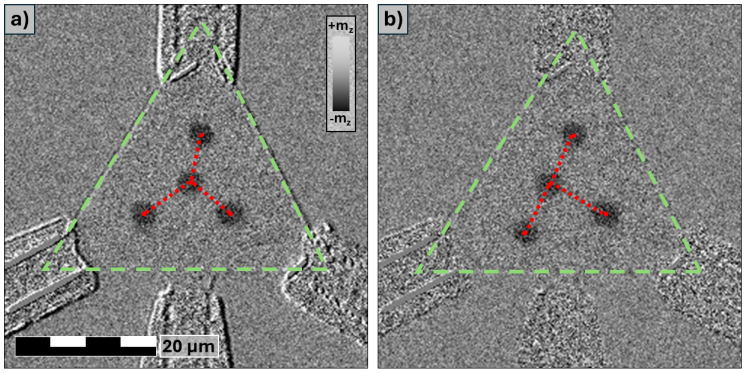

FIGURE 6.17: Devices hosting four skyrmions demonstrate distinct internal states governed by geometric commensurability and skyrmion-skyrmion interactions. The inclusion of multiple skyrmions expands the device's computational capacity. However, ensuring optimal performance requires a balance between the number of skyrmions and the degree of stochastic motion within the confined geometry [174]. Adapted from [99], supplementary material.

6.7.2 Potential enhancements and developments

To enhance the RC device conceptually, as well as its micrometer-scale demonstrator and potential nanometer-scale [130] implementation, several key parameters can be optimized to improve skyrmion stability [349, 380], dynamics [42], computational complexity, and processing speed. Given that this RC concept relies fundamentally on skyrmion properties and dynamics, optimizing the material stack that hosts skyrmions is crucial.

Temperature

Currently, the skyrmion phase in the presented system is stable only within a limited temperature range, restricting its potential commercial applicability. Expanding the operational temperature range [349] while maintaining skyrmion properties necessary for functionality would enhance its viability for commercial applications. Additionally, since skyrmions exhibit improved thermal dynamics at elevated temperatures [110], potentially leading to higher processing speeds, a balance must be struck between maximizing performance and minimizing energy consumption.

Velocity trade-offs

Skyrmion motion driven by spin currents must be carefully optimized to balance computational speed, energy efficiency and skyrmion stability. Enormous velocities up to 900 m/s have been reported at high current densities [98, 192]. Raising the applied current density would increase the skyrmion velocity and thus improve processing speed; however, it would also increase power consumption and by applying too much current, potentially deform, force and annihilate the skyrmion [94, 143, 166, 297]. Improving the spin current injection at the heavy metal/ferromagnet (HM/FM) interface could allow for more efficient skyrmion manipulation at lower currents, improving this trade-off. Importantly, the primary limiting factor for computation time in this device is the exploration time required for skyrmions to diffuse sufficiently during non-active periods.

Skyrmion Hall effect

Although the RC approach inherently compensates for dynamic asymmetries, at higher velocities the SkHE [97] may disrupt controlled skyrmion displacement and impair readout differentiation. This effect can be mitigated using synthetic antiferromagnetic (SAF) stacks, where two highly or fully compensated ferromagnetic layers host antiferromagnetically coupled skyrmions, effectively canceling out the skyrmion Hall effect. Since diffusion also depends on skyrmion topology, employing antiferromagnetically coupled skyrmions with a net topological charge of zero could enhance thermal diffusion dynamics [153], thereby improving overall computation speed. An additional avenue of exploration could involve the deliberate integration of the skyrmion Hall effect into the RC framework by employing higher skyrmion velocities, achieved through increased current densities and potentially optimized confinement geometries.

Device fabrication

A critical aspect of the proposed RC concept is its automatic reset mechanism, which relies on the repulsive force generated by the stray field and exchange stiffness at

the device edges. Further research into the influence of geometry and edge effects on skyrmion behavior, along with precise control over the fabrication of skyrmion-hosting geometries, would enable better tuning of skyrmion dynamics. This is particularly important for scaled-down devices, where edge effects are expected to be more pronounced due to size scaling [330].

Artificial vs. inherent detrimental pinning

While the presented material stack exhibits a relatively flat energy landscape, residual skyrmion pinning still occurs. Reducing this pinning further would lower the computational overhead required to compensate for pinned skyrmions during training while also minimizing the risk of skyrmions becoming trapped, which could degrade computational performance. Although uncontrolled pinning is undesirable, artificially tuning the energy landscape, such as ion irradiation [262, 313] or VCMA [137, 381, 382] to alter magnetic anisotropy, could be used to increase skyrmion mobility [198, 253, 317], bias skyrmion positioning [158, 169, 196], cause skyrmion nucleation [44, 142, 169] or introduce barriers within the geometry [155, 315]. This approach could confine skyrmions to specific regions, reducing their exploration area and thus increasing computational speed without interfering with electric current flow.

Other magnetic structure

Although this thesis focuses exclusively on skyrmions, other magnetic structures with comparable properties, such as merons [383], could also be utilized within this RC framework. Merons exhibit a reduced topological protection (Q = 0.5) compared with skyrmions and thus need less energy for nucleation and manipulation, as well as their asymmetry would allow for interesting directional bias.

Varying geometries

In principle, more complex geometries could be employed in skyrmion-based reservoir computing to enhance computational capabilities. However, increased structural complexity necessitates extended optimization like, e.g., MTJ positioning based on more complex skyrmion dynamic for specific tasks, potentially reducing overall efficiency. Given that even a simple geometry, such as an equilateral triangle, has been demonstrated to function effectively as a reservoir in this study [99, 152], prioritizing the optimization of dynamical complexity (e.g., multiple skyrmions, controllable biasing by artificial pinning, increased thermal diffusion) - rather than structural complexity - may yield greater improvements in performance. Nevertheless, achieving an optimal balance between computational complexity, skyrmion stability and dynamics, and energy efficiency remains a critical consideration.

6.8 Continuation of RC concept device: Gesture recognition

Demonstrating the execution of Boolean logic operations [99] is sufficient to validate the presented device as a demonstrator. However, Boolean logic is not the primary computational task for which RC is favorable. As a machine learning paradigm, RC excels in pattern recognition [222] - an area that is inherently challenging for conventional computational architectures, which rely on predefined algorithms and heuristic methods for pattern identification. Building on the concept of skyrmion-based

Brownian reservoir computing implemented in the presented device, G. Beneke et al., in collaboration with Infineon, demonstrated a time-multiplexed approach for recognizing human hand gestures recorded by two radar sensors [152][5]. This follow-up study showcases the potential of the RC device in solving more complex computational tasks, for which reservoir computing is particularly well suited.

6.8.1 Time-multiplexed RC

In this approach, raw range-Doppler and range-angle data from two radar sensors are digitally pre-processed via a FFT generating two-channel maps that represent either the angle or the amplitude as a function of relative velocity and distance to the radar sensors. A voxel of this map with the most distinguishable change between two gestures is selected and converted into an amplitude time signal, which serves as input to the RC device. The fundamental principle of this demonstration is similar to the Boolean logic operation tests presented in this work; however, by processing time-dependent signals, the system operates as a time-multiplexed RC. Utilizing the reservoir in combination with a linear support vector machine (LIN-SVM) achieves high accuracy in distinguishing between two hand gestures and outperforms the LIN-SVM. This study highlights the significant potential of the proposed RC device - not only in executing Boolean logic operations but also in successfully solving real-world pattern recognition problems through a slightly modified implementation.

6.9 Discussion of concept

6.9.1 Solving Boolean logic

The RC framework, a simple geometry with a single confined skyrmion, has already demonstrated sufficient performance for selected Boolean logic operations. **NAND** and **NOR** operations each represent a functionally complete set of logical connectives. Furthermore, the realization of the non-separable **XOR** function highlights the capability of a single confined skyrmion to perform non-linearly separable tasks, which are otherwise impossible for a conventional single-layer perceptron readout. The demonstrator has been introduced as a spatially multiplexed RC concept, and in a follow-up study, it achieved solving complex pattern recognition tasks in a time-multiplexed configuration.

6.9.2 Enhancement potential

This concept can be readily extended by incorporating more complex inputs and increasing the number of skyrmions. More complex inputs could involve a broader range of input combinations, including time- and amplitude-varying signals. With a higher number of skyrmions, the system exhibits richer dynamical behavior, such as (in-)commensurable ground states, thereby expanding the overall number of accessible states in the reservoir. The computational complexity could be further improved by linking multiple confined geometries, potentially providing an ultra-low-energy alternative to neuromorphic computing architectures based on arrays of nano-scale spintronic oscillators [377–379].

[5] Contribution to this work is listed in Section D.6.

6.9.3 Scalability

Additionally, the scalability of this concept to nano-scale dimensions significantly reduces skyrmion displacement distances, leading to latency in the micro- to nanosecond regime, primarily limited by the skyrmion exploration time. This latency can be further decreased by reducing the required sampling rate, though at the cost of a lower SNR, which could affect accuracy or even overall computational performance.

6.9.4 Conclusion

This novel RC paradigm, which leverages the stochastic Brownian dynamics of magnetic skyrmions in confined geometries, overcomes several challenges faced by existing theoretical proposals for skyrmion-based reservoir computing. By exploiting the stochastic motion of skyrmions, this approach enables operation at current densities several orders of magnitude lower than those required for conventional spintronic RC architectures. The presented concept, based on a single confined skyrmion within a simple and easily manufacturable geometry, has already demonstrated the capability to perform non-separable operations, implement a universal set of Boolean functions, and, in a time-multiplexed configuration, achieve complex gesture recognition. Several concepts for improving this concept, including modifications to the material stack and optimization of skyrmion properties, have been outlined. The ultra-low energy consumption of the system has been estimated for a single skyrmion displacement in a scaled-down version. Generalizing this concept to multiple confined skyrmions and scaling it to nanometer dimensions presents a highly promising path toward ultra-low-energy non-conventional computing.

Chapter 7

Synthesis

General conclusion

This thesis has provided a brief investigation into the magnetic properties, fabrication techniques, and characterization methods of metallic thin films hosting skyrmions - topologically non-trivial spin textures that exhibit quasi-particle behavior. These structures exhibit unique dynamics such as Brownian diffusion and can be efficiently manipulated via spin-orbit torques (SOTs), showing complex interactions with structural boundaries and artificial confinements.

Skyrmion flow The dynamics of 2D skyrmion flow in the creep regime - where motion is governed by low current densities - were studied in both straight and periodically modulated channels. In this regime, skyrmion transport results from a combination of SOT-driven drift, thermally activated diffusion, and interactions with a non-uniform energy landscape. Experiments demonstrated characteristic velocity profiles shaped by boundary conditions: straight channels showed near-uniform flow, while modulated edges imposed partial or no-slip constraints, producing parabolic-like profiles. These results were in strong agreement with Thiele-based simulations. Due to the low velocities, the contribution of the Magnus force was initially neglected; however, additional simulations incorporating a fixed skyrmion Hall angle revealed asymmetric flow behaviors, including localized backflow – deviations not observed in classical particle systems.
Skyrmions in confined geometries were shown to mimic the transport properties of overdamped particles like colloids, while offering unique tunable properties. Their manipulability - via edge design, density control, or size modulation, even in real-time - positions skyrmion systems as compelling experimental platforms for exploring non-equilibrium statistical physics.

Skyrmion compression The thesis further explored the role of He^+ and Ga^+ irradiation in tailoring magnetic properties. Both large-area and localized irradiation were employed to modify anisotropy, influencing skyrmion size, density, and stability. Artificial barriers created by irradiation enabled confinement and structural modulation, affecting skyrmion behavior under compression by SOTs. As skyrmion ensembles are forced against these barriers, they exhibit reduced size and spacing, forming dense, confined lattices. These experimental findings were supported by simulations based on a modified Thiele model developed by K. Leutner, showing qualitative agreement.
This ability to compress skyrmions opens up potential applications, such as

current-controllable valves based on anisotropy modulation or guided skyrmion transport through irradiated channels - laying groundwork for skyrmion-based circuit components.

Brownian reservoir computing A key part of this work is the development of a novel RC approach that exploits the stochastic Brownian dynamics of confined skyrmions. This represents a new class of magnetic RC systems that overcome several limitations of earlier theoretical models. Even in its simplest form - using a single skyrmion in a equilateral triangular as scalable geometry - the system is capable of performing nonlinearly separable operations, implementing universal Boolean logic, and, in a later work, achieved gesture recognition through time-multiplexing.
The required current densities are several orders of magnitude lower than those in conventional spintronic RC architectures, potentially offering exceptional energy efficiency. The system's scalability to nanometer-scale enables displacement events on nanosecond timescales, significantly reducing latency.
Proposed enhancements, such as increasing the number of confined skyrmions, enable access to more complex dynamical regimes - including (in)commensurate states – thereby potentially broadening the computational capacity of the system. Furthermore, coupling multiple confined geometries could significantly increase system complexity, drawing analogies to neuromorphic architectures based on neural networks. These capabilities position skyrmion-based reservoir computing as a highly promising platform for ultra-low-power, unconventional computation, particularly adaptive learning tasks.

Overall, this thesis underscores the utility of skyrmions as highly tunable model systems for transport and lattice studies and as a foundation for energy-efficient, next-generation computing technologies, battling the anthropogenic environmental impact of contemporary digital infrastructure.

Magnetism as Art showcase

Magnetism, beyond its scientific and technological significance, can also possess aesthetic appeal. To highlight this aspect, major conferences such as **Magnetism and Magnetic Materials** (MMM) and **INTERMAG** host "*Magnetism as Art*" showcases, inviting submissions of magnetism-related artistic imagery. Throughout the course of this thesis, numerous images were captured, some of which were considered to exhibit notable artistic qualities. One image was submitted to each of the aforementioned conferences. It is a pleasure to report that both submissions were recognized by the respective judging panels for their artistic merit and visual impact, with each being selected as one of the four finalists in their respective competitions.

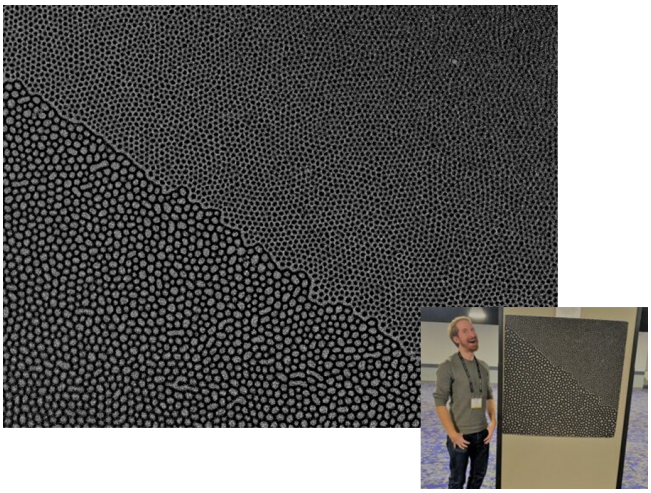

FIGURE 7.1: **Magnetism as Art** submission to Magnetism and Magnetic Materials (MMM) conference in Minneapolis, USA (2022). Best of four.

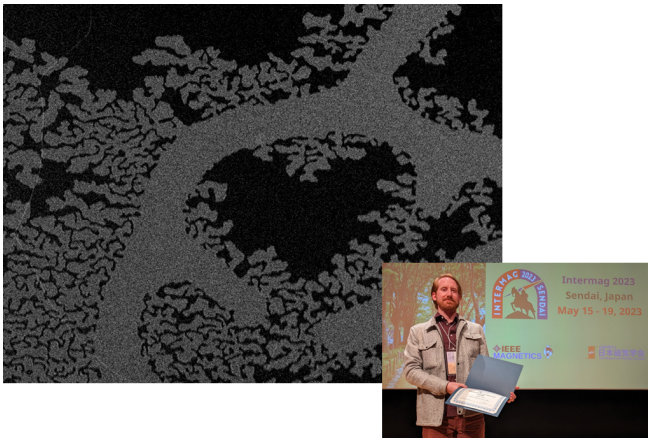

FIGURE 7.2: **Magnetism as Art** submission to Intermag conference in Sendai, Japan (2023). Best of four.

Appendix A

Appendix: Methods

The appendices are organized thematically and separated to the respective chapters of this thesis. Supplementary information, detailed explanations, the individual contributions, and a declaration regarding the use of artificial intelligence are provided in the final appendix.

A.1 FAB629 and TMD109

The primary samples utilized in this thesis were FAB629 and TMD109, with their respective sputtering recipes presented in the table below. No sputtering recipe could be located in the logs of the Singulur Rotaris sputtering machine for sample MVK763.

A.1.1 Sputtering recipes

FAB629				
Step	Material	Thickness [nm]	Power [W]	Gas [sccm]
1	Ta	5	200	60
2	CoFeB	0.95	400	40
3	Ta	0.09	200	60
4	MgO	2	500	55
5	Ta	5	200	60
TMD109				
Step	Material	Thickness [nm]	Power [W]	Gas [sccm]
1	Ta	3	200	60
2	CoFeB	0.95	400	45
3	Ta	0.08	200	60
4	MgO	2	500	55
5	Ta	5	200	60

TABLE A.1: Sputtering recipes for the samples used in this thesis. FAB and TMD samples were sputtered by F. Kammerbauer and D. Tran using the Singulus Rotaris sputtering machine, respectively.

A.1.2 Magnetic properties of samples

The magnetic properties of samples FAB629 and TMD109 were characterized using SQUID magnetometry. For sample MVK763, SQUID measurements were not performed due to mechanical damage during prior preparation, which resulted in an irregular sample geometry. Additionally, because a large portion of MVK763 had been subjected to ion irradiation, the resulting magnetic response reflected a superposition of properties from both irradiated and non-irradiated regions, preventing a clear attribution to either state.

FAB629	
Saturation Magnetization M_s	391 ± 28 kA/m
Anisotropy Field (Oe)	1170 ± 42 Oe
Anisotropy Field (mT)	117.0 ± 4.2 mT
Anisotropy Constant K_1	229 ± 2 kJ/m^3
TMD109	
Saturation Magnetization M_s	495 ± 19 kA/m
Anisotropy Field (Oe)	355 ± 25 Oe
Anisotropy Field (mT)	35.5 ± 2.5 mT
Anisotropy Constant K_1	47 ± 1 kJ/m^3

TABLE A.2: Magnetic properties of FAB629 and TMD109 at 300 K derived by SQUID measurement.

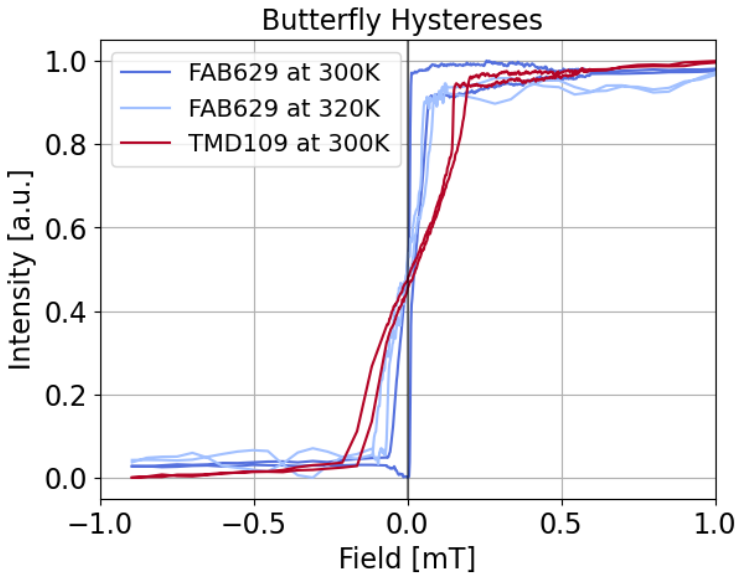

FIGURE A.1: Hysteresis of TMD109 and FAB629 at 300 K and, additionally, FAB629 at 320 K. TMD109 exhibits a typical out-of-plane hysteresis for skyrmionic stacks with the spin reorientation transition right before maximum intensity.

A.2 Stack optimization

An initial optimization of multilayer stacks exhibiting diffusive skyrmion motion and densely packed skyrmion lattices - nucleated via the IP burst method - was conducted. The parameter space explored included variations in CoFeB layer thickness, Ta interfacial (dusting) layer thickness, sputtering power, and argon gas flow during deposition. Following deposition, two samples from each fabrication condition were subjected to post-annealing treatments at either (a) 150 ° or (b) 250 ° for 30 minutes. All samples were subsequently characterized using PMOKE microscopy across four different temperatures, employing the standard skyrmion nucleation protocol. In the resulting phase diagrams, an 'X' symbol denotes the observation of a skyrmion phase characterized by mobile skyrmions and the formation of a dense skyrmion lattice.

Sample	CoFeB [nm]	W / sccm	Ta_{int} [nm]	T [°C]	297K	310K	325K	340K
FAB435	0.9	400/40	0.07			X	X	X
FAB435_a	0.9	400/40	0.07	150				
FAB435_b	0.9	400/40	0.07	250				
FAB438	1.0	400/40	0.07					
FAB438_a	1.0	400/40	0.07	150	X	X	X	X
FAB438_b	1.0	400/40	0.07	250				
FAB441	0.9	1200/60	0.07		X	X	X	
FAB441_a	0.9	1200/60	0.07	150				
FAB436	0.9	400/40	0.08		X			
FAB436_a	0.9	400/40	0.08	150				
FAB436_b	0.9	400/40	0.08	250				
FAB439	1.0	400/40	0.08					
FAB439_a	1.0	400/40	0.08	150	X	X		
FAB439_b	1.0	400/40	0.08	250				
FAB442	0.9	1200/60	0.08		X	X	X	
FAB442_a	0.9	1200/60	0.08	150				
FAB437	0.9	400/40	0.09		X			
FAB437_a	0.9	400/40	0.09	150	X			
FAB437_b	0.9	400/40	0.09	250				
FAB440	1.0	400/40	0.09					
FAB440_a	1.0	400/40	0.09	150	X			
FAB440_b	1.0	400/40	0.09	250				
FAB443	0.9	1200/60	0.09		X			
FAB443_a	0.9	1200/60	0.09	150	X	X	X	

TABLE A.3: Optimization process for samples exhibiting diffusive skyrmions. The temperature dependence of skyrmion occurrence is indicated by X. The material composition is detailed in the first column, specifying layer thicknesses. The third column provides information on sputtering power and gas flow parameters. Annealing with temperature (T) was conducted exclusively for the FABxxx_a and FABxxx_b variants, with a duration of 30 minutes.

A.3 Cleanroom environment

To prevent contamination of the sample surface by airborne particles during the lithography process, all fabrication steps are carried out in a controlled cleanroom environment. Cleanrooms are classified according to ISO standards, which specify the permissible concentration of airborne particles larger than 0.5 µm. To maintain a low-particle environment, cleanrooms employ high-efficiency particulate air (HEPA) filtration systems, which capture airborne particles and microbes. Additionally, a continuous laminar airflow directs any remaining particles downward to the floor, preventing their deposition on working surfaces. The internal air pressure is maintained slightly above atmospheric pressure, ensuring that unfiltered external air does not enter when doors are opened. Operators inside the cleanroom must wear anti-static suits, gloves, hair nets, and facial protection to minimize potential pollution. Tools and samples are transported through a dedicated sluice chamber, preventing the direct introduction of external dirt. Furthermore, the cleanroom lighting system is designed to operate in a restricted visible spectrum, emitting yellow light by filtering out shorter, higher energy wavelengths (violet, blue, and greenish light). This is necessary because resin-based photoresists used in lithographic processes are often sensitive to UV and short-wavelength visible light. Exposure to full-spectrum white light could alter the chemical composition of the resist, compromising the lithographic process.

A.4 Sample processing recipes

A.4.1 Standard negative EBL recipe

The following recipe for negative lithography was taken from the non-public, internal tutorial database. Resist: AR-N7520.17 [283]

Cleaning procedure
Aceton for 60s; Isopropyl alcohol for 60s; high-purity water for 60 s; blow dry with Nitrogen; hotplate at 120°C for 60 s (water-desorption); cool down substrate for 60s

Coating procedure
Adhesion promoter, if necessary; AR-N7520.17 ∼0,1 ml; prespin for 1 s at 500 rounds per minute (rpm); spin for 60 s at 4000 rpm; softbake at T = 85°C for 60 s; cool down substrate for 60s; use e-spacer, if necessary for EBL. E-spacer is a conductive resist that avoids charging of insulating samples during SEM imaging.

EBL - exposure
Set 20 kV high-voltage for beam acceleration with a dose of 28 $\mu C/cm^2$ for structures wider than 1µm

Development
If e-spacer was used, remove with high-purity water first; AR300-47 puddle development for 150 s; development break with high-purity water for 20 s; blow dry with nitrogen.

A.4.2 Standard positive (lift-off) EBL recipe

The following recipe for positive lithography was taken from the non-public, internal tutorial database. Resist: MMA/PMMA (methyl methacrylate / poly methyl methacrylate) [284]

Cleaning procedure
Aceton or Ethanol for 60s; Isopropanol for 60s; High-purity water for 60 s (optional); hotplate at 120°C for 60 s (water-desorption); blow-dry the sample with N_2 gun; cool down substrate for 60 s.

Coating procedure
MMA (8.5) MAA EL6 ∼0,1 ml; prespin for 2 s at 500 rpm and set acceleration of 500; spin for 60s at 3000 rpm and set acceleration of 3000; softbake at 180°C for 90s; cool down substrate for 60 s.
PMMA 950k A4% ∼0,1 ml; prespin for 1s at 500 rpm and set acceleration of 500; spin for 45 s at 3000 rpm and set acceleration of 3000; softbake at 180°C for 90 s; cool down substrate for 60 s; optional: spin coat e-spacer for PMMA if sample is insulating (2000 rpm for 30 s should be fine).

EBL - exposure
Set 10 kV high-voltage for beam acceleration; use aperture of 30 - 60 µm at a working Distance of 9 mm; stepsize: 20 - 100 nm (normally, one cannot use 20 nm stepsize with the 60 µm aperture, because the beam speed must be below 10 mm/s to avoid distortions! Increasing the step size reduces the beam speed); Use a dose of 160 µC/cm^2 and the meander vectormode. Alternatively, one can use EHT 20 kV and a dose of 220 µC/cm^2 (but then the undercut is not good anymore!).

Development
If e-spacer was used, remove with high-purity water first; dive development in MIBK:IPA for 30 s; development break after 30s in pure IPA; blowdry with N_2.

A.5 Ion etching with IonSys 500

A.5.1 Standard ion etching parameters

The following parameters are the standard etch parameters for the IonSys 500 as suggested by the manufacturer (Roth&Rau) and listed in the AG Kläui internal tutorial database. To mitigate potential thermal annealing effects, etching was performed in 30-second intervals interspersed with 60-second cooling periods under closed-shutter conditions.

Parameter	Value
Mass flow control 1 (MFC)	4 sccm
Mass flow control 2 (MFC)	5 sccm
He pressure	2 mbar
MW power	250 W
Beam voltage	300 V
Acceleration voltage	200 V
Plasma bridge neutralizer (PBN) current	100 mA

TABLE A.4: Standard IonSys 500 etch parameters.

A.5.2 Etch rates

The following etch rates were supplied by the manufacturer of the IonSys 500 ion etching machine. All rates are at an etching angle of 90°. Information taken from AG Kläui's non-public, internal tutorial database.

Material	Etch rate (nm/min)
Ta	8.33
MgO	9.00
$Co_{20}Fe_{60}B_{20}$	7.60

TABLE A.5: Etching rates of materials used in the thin film stack.

A.6 Peltier elements

TABLE A.6: Specifications of Peltier Elements

Model	P_{max} [W]	I_{max} [A]	U_{max} [V]	ΔT_{max} [K]	Size [mm^2]
QC-32-0.6-1.2M	3.2	1.5	3.7	72	8×8
QC-17-1.0-2.5MS	3.2	2.8	1.9	72	12×12
QC-31-1.0-2.5CM	5.8	2.8	3.5	72	15×15

Temperature gradient dT is the maximum reachable temperature difference between the hot and cold side of the Peltier element. Peltier elements of 12×12 mm^2 were sealed by silicone.

A.7 Laminar flow box

A.7.1 LabVIEW organigram

In this adapted LabVIEW VI for the Lakeshore temperature controller 330 the temperature of potentially both input channels is saved into a .txt file every 15 s.

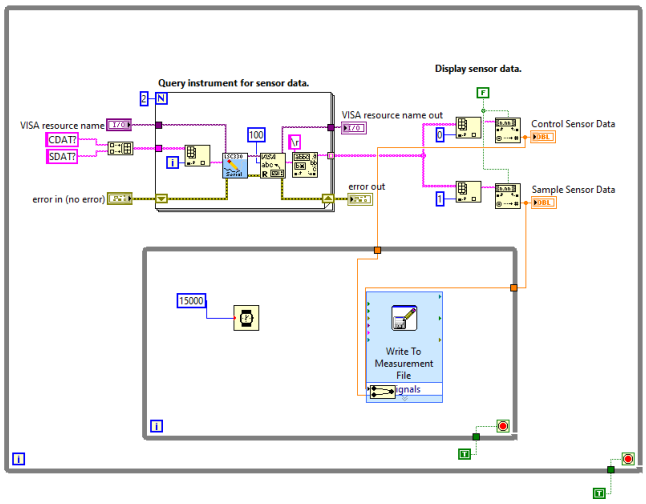

FIGURE A.2: LabVIEW organigram of the adapted LabVIEW VI for controlling the Lakeshore Temperature controller.

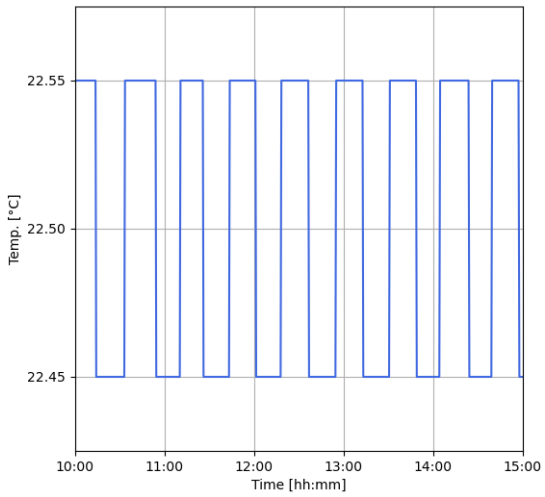

FIGURE A.3: 5h excerpt of temperature stability measurement with chiller. Measurement was recorded in Kelvin, thus by subtracting 273.15 from the value, the second decimal point is used, even though only one decimal point was recorded. Temperature oscillates by 0.1°C, the smallest increment measurable in Kelvin mode.

A.7.2 Temperature stability

A.8 Equipment

A.8.1 Coil calibration

To calibrate the electromagnets, a Hall probe is used. A voltage is applied to the electromagnets, and the resulting magnetic field is manually entered into the KerrLab software while the according current is automatically added. By measuring multiple data points, the relationships between voltage and magnetic field, as well as current and magnetic field, can be interpolated and saved as a calibration file. Figure A.4 shows the calibration setup.

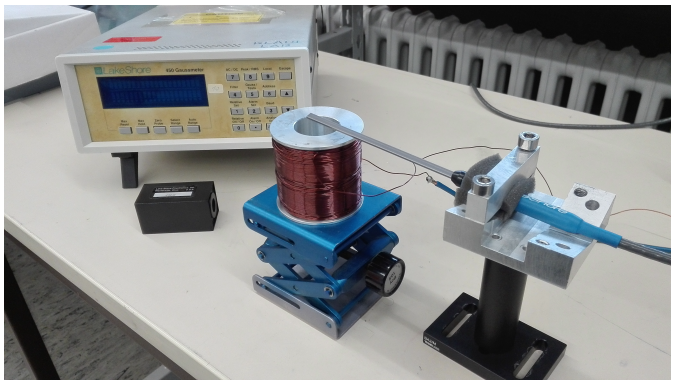

FIGURE A.4: Typical setup to calibrate a coil with a Hall probe. Corresponding magnetometer to the left. Black box in the front is a Faraday cage to null the probe.

A.9 Contribution

As mentioned, raw samples were produced primarily by F. Kammerbauer and D. Tran. All Gallium-based irradiation processes were performed together with G. Beneke, while the Helium irradiation was performed by Spin-Ion Technologies company [320] in a collaborative meeting including Beatrice Bednarz with no further involvement. SQUID measurements for magnetic property determination were helped by F. Kammerbauer. T. Reimer assisted with occurring EBL alignment issues. Wire bonding processes were performed or assisted by helpful colleagues (e.g. in no particular order, D. Schönke, F. Fuhrmann, T. Dohi, S. Krishnia, T. Reimer).

A.10 Sample layout examples

The following selection of layouts are examples for few of the designed sample layouts used for this thesis.

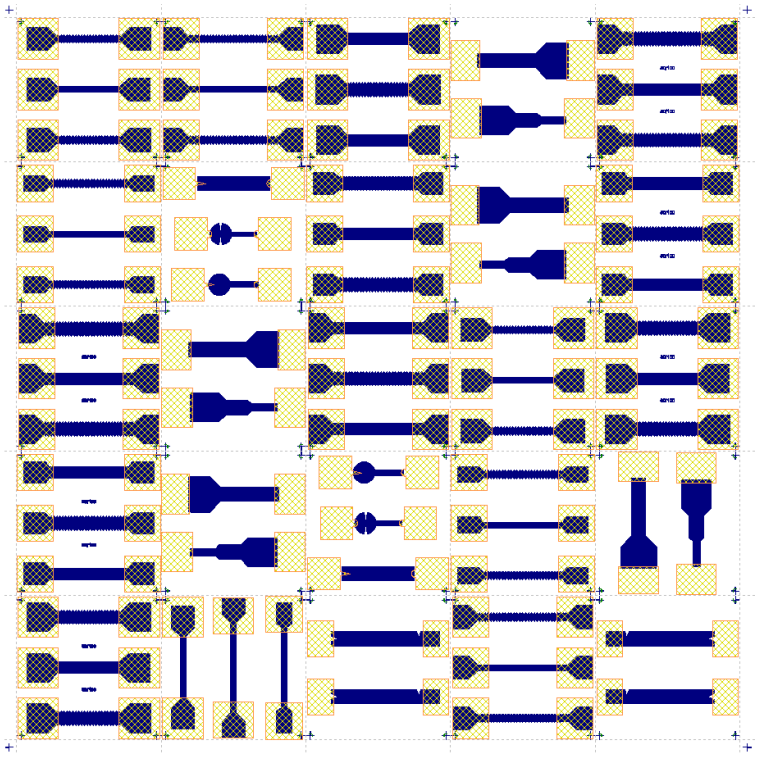

FIGURE A.5: Channel (blue) with contact pads (yellow) for reservoir filling and skyrmion compression.

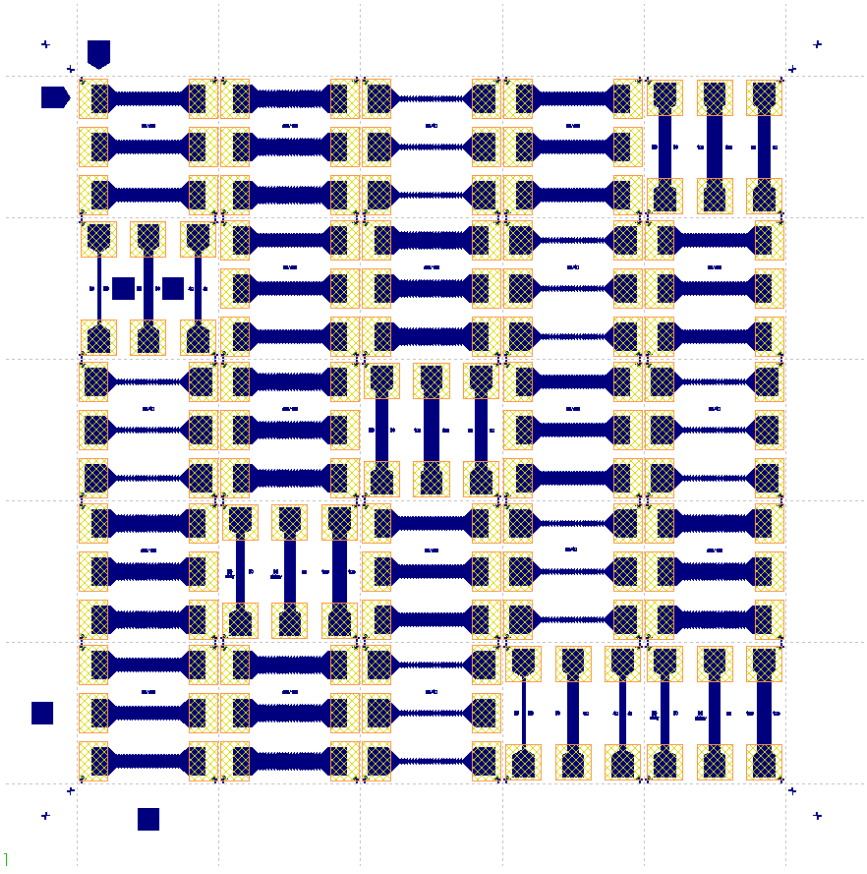

FIGURE A.6: Channel (blue) with varying widths with contact pads (yellow) for skyrmion flow in straight and modulated edges.

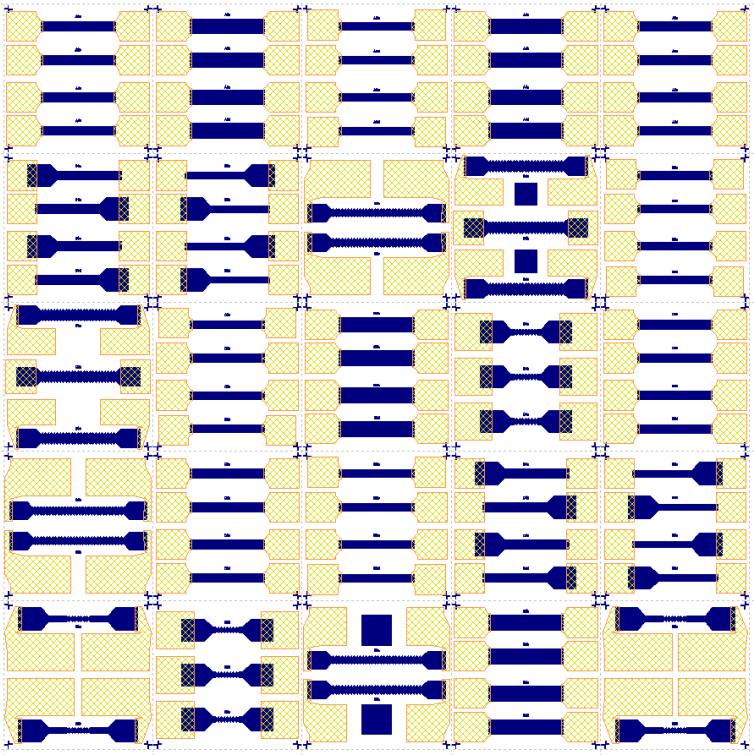

FIGURE A.7: Channel (blue) with varying widths with contact pads (yellow) for skyrmion flow in straight and modulated edges.

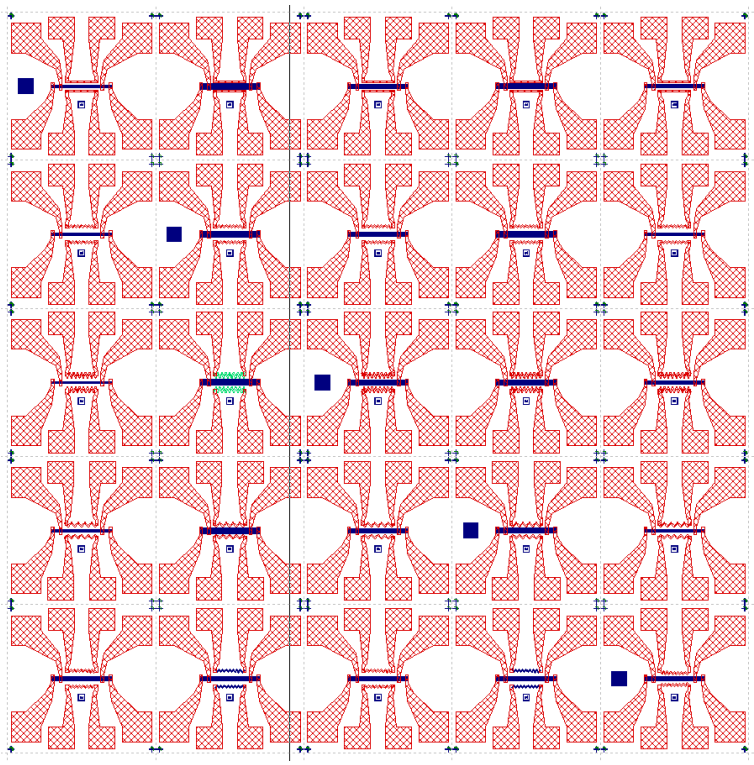

FIGURE A.8: Channel (blue) with varying widths with contact pads (red) for skyrmion motion under temperature gradient. Turquoise and bright red shows heating elements.

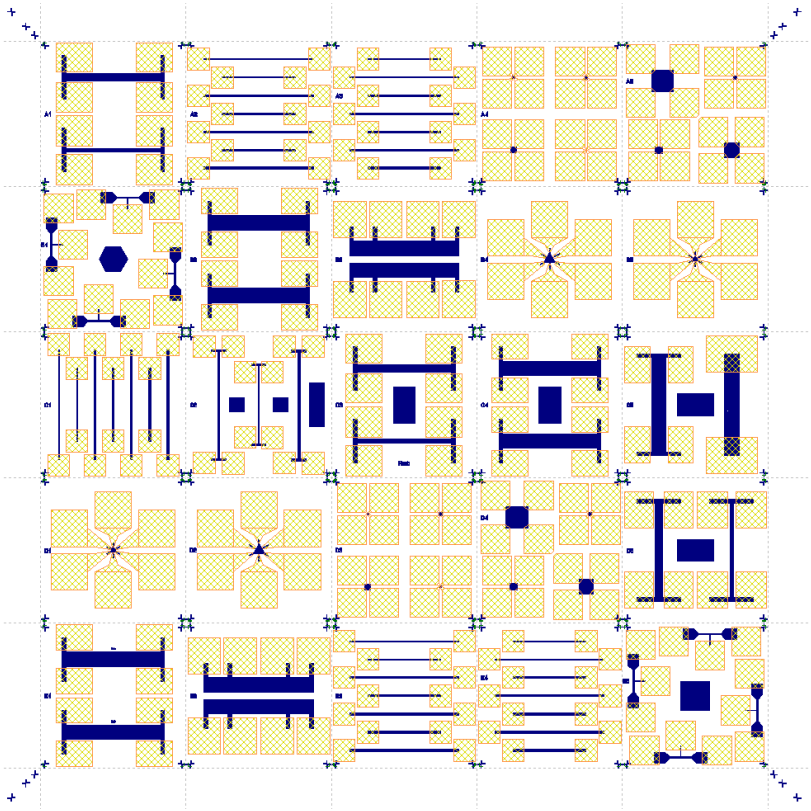

FIGURE A.9: Layout with channel (blue) with varying widths, triangular and square reservoirs and experimental *skyrmion cannon* design with contact pads (yellow) for electric noise measurement.

Appendix B

Appendix: Modulated Skyrmion flow

B.1 Layouts

B.1.1 Lattice shaking layout

Manufactured lattice shaking sample for lattice density and order improvement by application of AC current along geometrical symmetry axes..

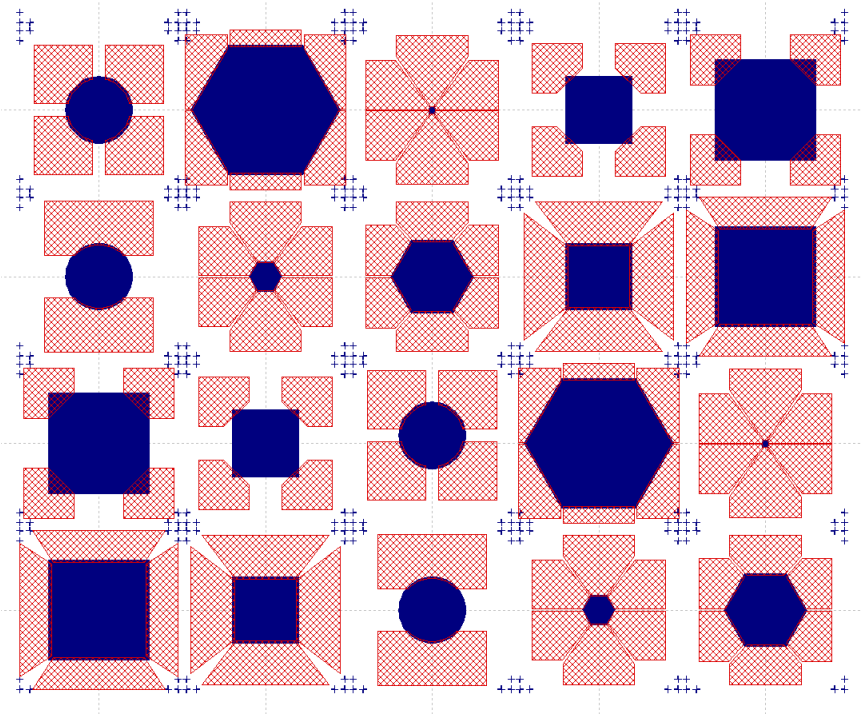

FIGURE B.1: PIONEER layouts designed for lattice shaking by AC or pulses for skyrmion lattices in commensurate (hexagons) and incommensurate geometries (squares and circles) of different sizes for dense, hexagonal lattices.

B.1.2 Modulations layout

Various layouts featuring different channel widths and modulation schemes were developed. However, the primary analysis in Chapter 4 focuses exclusively on the modulation scheme presented therein.

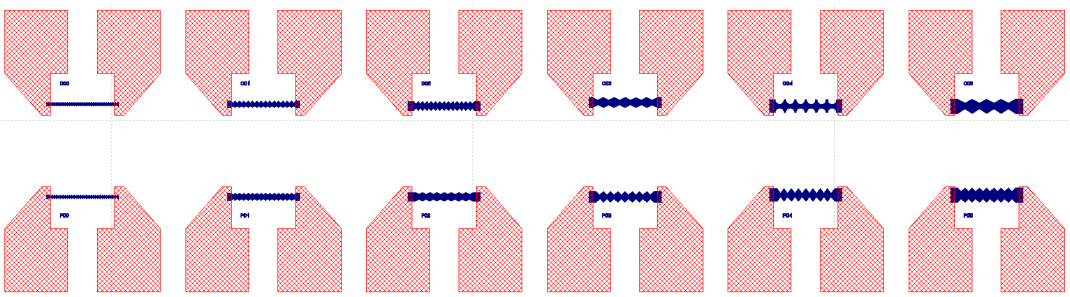

FIGURE B.2: EBL layout with multiple modulated channel designs, which have not been experimentally analyzed. With blue the material and dashed red the gold contact pads.

B.2 Outlook

The concept of confined skyrmion flow [235], including implementations utilizing the SkHE [165], has traditionally relied on structural boundaries to constrain skyrmion motion. By introducing artificial boundaries via irradiation, as detailed in Chapter 5, the skyrmion flow can be further modulated through active manipulation of the energy landscape. Moreover, irradiation techniques allow for localized control of skyrmion trajectories - either by confinement, creation of pinning sites, or local repulsion [155, 169]. When combined with the SkHA, this approach offers significant potential for studying flow dynamics and lattice-phase phenomena that are otherwise difficult to access in systems such as colloidal particle flows.

B.3 Contribution

The concept of periodically modulated skyrmion flow was developed by K. Raab, who also fabricated the structured samples and acquired the video data using PMOKE microscopy. P. Virnau contributed the theoretical framework and conceptual support. M. Schmitt performed part of the video data analysis, generated the flow profiles, and conducted the comparative evaluation with simulation results.

Appendix C

Appendix: Skyrmion Compression

C.1 Extended theory

C.1.1 Extended energy terms

In this appendix section the energy terms for K. Leutners derivation of the skyrmion compression theory are listed. Note that this is still unpublished work in progress.

$E_{d,s,s\leftrightarrow f}$ - the dipole skyrmion self-energy with magnetic film skyrmion interaction for R≫h,
$E_{d,s\leftrightarrow s}$ - the dipole skyrmion-skyrmion interaction with distance "l" between skyrmions,
$E_{d,s\leftrightarrow b}$ - the dipole skyrmion-boundary interaction (at x_0).

The terms $E_{d,s,s\leftrightarrow f}$, $E_{d,s\leftrightarrow s}$ and $E_{d,s\leftrightarrow b}$ were calculated using multipole expansion.

$$E_{d,s,s\leftrightarrow f} = -\mu_0 M_s^2 \frac{h^2\left(4\left(h^2+32R^2\right)\log\left(\frac{R}{h}\right)+h^2(1+\log(4096))+64R^2(\log(64)-1)\right)}{64R} \tag{C.1}$$

$$\begin{aligned} E_{d,s\leftrightarrow s} = {} & \mu_0 M_s^2 \pi R_1^2 R_2^2 \left(\frac{1}{l}-\frac{1}{\sqrt{h^2+l^2}}\right) + \frac{\mu_0 M_s^2}{8}\pi R_1^2 R_2^2 \left(\frac{2h^2-l^2}{\left(h^2+l^2\right)^{\frac{5}{2}}}+\frac{1}{l^3}\right)\left(R_1^2+R_2^2\right) \\ & + \frac{\mu_0 M_s^2}{64}\pi R_1^2 R_2^2 \left(\frac{-8h^4+24h^2l^2-3l^4}{\left(h^2+l^2\right)^{\frac{9}{2}}}+\frac{3}{l^5}\right)\left(R_1^4+3R_1^2R_2^2+R_2^4\right) \\ & + \mu_0 M_s^2 \frac{5\pi R_1^2 R_2^2 \left(\frac{16h^2-120h^4l^2+90h^2l^4-5l^6}{\left(h^2+l^2\right)^{\frac{13}{2}}}+\frac{5}{l^7}\right)\left(R_1^2+R_2^2\right)\left(R_1^2+5R_1^2R_2^2+R_2^4\right)}{1024} \end{aligned} \tag{C.2}$$

$$\begin{aligned} E_{d,s\leftrightarrow s} = {} & \mu_0 M_s^2 R^2 \left((x_0-x)\left(\log\left(h^2+(x_0-x)^2\right)\right)-\log\left((x_0-)^2\right)-2h\tan^{-1}\left(\frac{h}{x_0-x}\right)\right) \\ & - \mu_0 M_s^2 \frac{h^2R^4}{4\left(x_0-x\right)\left(h^2+(x_0-x)^2\right)} \end{aligned} \tag{C.3}$$

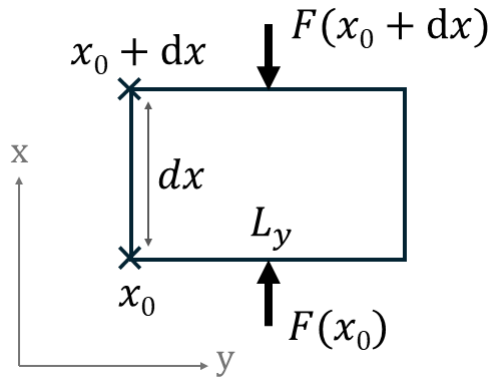

FIGURE C.1: Sketch of a barometric 2D volume element (dx·L_y) with the respective forces F(x_0) and F(x_0+dx). Adapted from original sketch by K. Leutner

C.1.2 Macroscopic derivation

Considering the length L_y in the system in a confined space:

$$\begin{aligned} L_y \Delta p &= F_x\left(x + \frac{\sqrt{3}}{2}P\right) - F_x\left(x - \frac{\sqrt{3}}{2}P\right) = -\frac{\hbar\pi^2}{2e}\theta_{SH}\mathbf{j}R(x) \\ L_y dp &= \sqrt{3}dF_x = -\frac{\hbar\pi^2}{2e}\theta_{SH}\mathbf{j}R(x)\frac{dN_{sky}}{dx}dx \\ dp &= -\frac{\hbar\pi^2}{2e}\theta_{SH}\mathbf{j}R(x)\left(\frac{1}{L_y}\frac{dN_{sky}}{dx}\right)dx \\ \Rightarrow dp &= -\frac{\hbar\pi^2}{2e}\theta_{SH}\mathbf{j}R(p)\rho(p)dx \end{aligned} \tag{C.4}$$

with density ρ for hexagonal lattice:

$$\Rightarrow \rho(p) = \frac{1}{L_y}\frac{dN_{sky}}{dx} = \frac{1}{A_{uc}} = \frac{2}{\sqrt{3}P(p)^2} \tag{C.5}$$

one gets the expression for the pressure difference dp in dependence of dx and the skyrmion number density $\frac{dN_{sky}}{dx}$, which can be used to get the pressure dependent density ρ(p). This leads to the simulated skyrmion lattice with parameters from Table C.1:

Parameter	Value
M_s	$6 \cdot 10^5$ A/m
h	0.95 nm
B_z	200 $^-$T
$\theta_{SH} j$	10^5 A/m^2
σ	2.42 $\mu_0 M_s^2 h$
N_{sky}	2835

TABLE C.1: Simulation parameters and values used in the model.

Further integrating dp using ρ(p) leads to

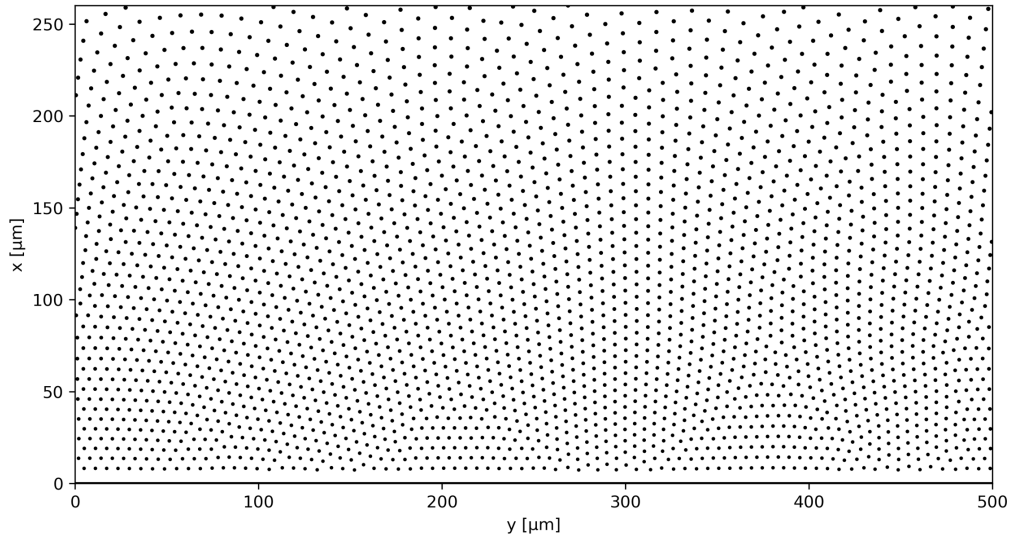

FIGURE C.2: Simulated skyrmion lattice with periodic boundary conditions to the sides with barrier on the bottom. Original from K. Leutner

$$\begin{aligned} \int_p^{p_1} \frac{\mathrm{d}p}{R(p)\rho(p)} &= -\frac{\hbar\pi^2}{2e}\theta_{\mathrm{SH}} j_x \int_x^{x_1} \mathrm{d}x = \frac{\hbar\pi^2}{2e}\theta_{\mathrm{SH}} j_x (x - x_1) \\ &\Rightarrow \quad p(x) \quad \textbf{with} \quad p(x_0) = p(R(x_0)) = p_0 \end{aligned} \tag{C.6}$$

equation p(x) with $p(x_0) = p(R(x_0)) = p_0$.

$$\begin{aligned} A &= \frac{\sqrt{3}}{2}P^2 \Rightarrow \frac{\partial A}{\partial_P} = \sqrt{3}P \\ p &= \frac{\partial E_{uc}}{\partial A} = -\frac{\partial E_{uc}}{\partial P}\frac{\partial P}{\partial A} = -\frac{\partial E_{uc}}{\partial P}\frac{1}{\sqrt{3}P} \end{aligned} \tag{C.7}$$

Now one can express the energy E_{uc}(R,P) in dependence or R, skyrmion radius, and P, the distance of next nearest neighbor skyrmions, and by minimizing R to get the effective model with only P as a degree of freedom one can express R in dependence of P.

$$R(P) = \min_R \frac{E_{uc}(R,P)}{P^2} = \min_R E_{uc}(R,P) \tag{C.8}$$

Reaching the analytical result of minimization with skyrmion lattice model for $P/h \to 0$, and $R/h \to 0$ limit.

$$R(P) = \frac{4,11R(\mu_0 h M_s)^{\frac{1}{3}}}{\left(-4\pi BR - \mu_0 h M_s\left(-1 - 6\log(2) + \frac{2\pi\sigma}{\mu_0 h M_s^2}\right) + 2\mu_0 h M_s \log(\frac{R}{h})\right)^{\frac{1}{3}}} \tag{C.9}$$

Putting equations together leads to:

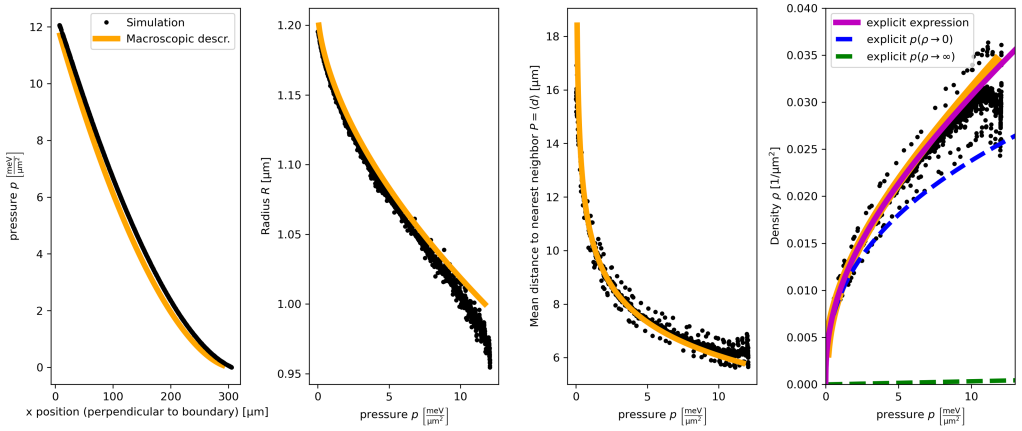

FIGURE C.3: Simulated and analytical results from the macroscopic description for p(x), R(p), P(p), and p(ρ). Used for qualitative comparison with the experimental results from 5, section 5.3.7. Original from K. Leutner

$$
\begin{aligned}
p(R) &= -\frac{1}{\sqrt{3}P\frac{dP}{dR}}\frac{\partial E_{uc}(P(R),R)}{\partial R} \\
\rho &= \frac{2}{\sqrt{3}P^2} \\
\frac{\hbar\pi^2}{2e}\theta_{SH} j_x (x - x_0) &= \int_p^{p_1} \frac{dp}{R(p)\rho(p)} = \int_p^{p_1} dR \frac{dp}{dR}\frac{1}{\rho(P(R))R}
\end{aligned}
\tag{C.10}
$$

This results in:

$$
\begin{aligned}
x(R) - x_0 = \frac{ehM_s\left(8\pi B(R - R_0)\right)}{2\sqrt{3}\pi^2\hbar j_x} + e\mu_0 h^2 M_s^2 \frac{\log\left(\frac{R_0}{R}\right)}{2\sqrt{3}\pi^2\hbar j_x} \\
\cdot\left(6\log(h) - 3log(RR_0) + \frac{6\pi\sigma}{\mu_0 h M_s^2} + 7 - 18\log(2)\right)
\end{aligned}
\tag{C.11}
$$

If x(R) linear: R(x) is given by

$$
R(x) = R_0 - \frac{2\sqrt{3}\pi^2\hbar j_x R_0 (x - x_0)}{ehM_s\left(-8\pi B R_0 + 6\mu_0 h M_s log\left(\frac{h}{R_0}\right) + \mu_0 h M_s\left(\frac{6\pi\sigma}{\mu_0 h M_s^2}\right) + 7 - 18\log(2)\right)}
\tag{C.12}
$$

C.2 He^+ irradiation

C.2.1 He^+ irradiation: Hysteresis

Following the hysteresis curves and the selected slopes at low fields for the untreated and treated regions are displayed. A comparative analysis of the hysteresis curves between the He^+-irradiated (treated) and non-irradiated (untreated) regions reveals distinct magnetic behavior. At lower temperatures, both regions exhibit hysteresis loops characteristic of skyrmionic states, with features such as reduced remanence and smooth magnetization reversal, consistent with the presence of skyrmions. However, at elevated temperatures (e.g., 335 K), the hysteresis shape changes markedly and begins to resemble that of IP magnetization, indicating a

transition away from the skyrmion phase.

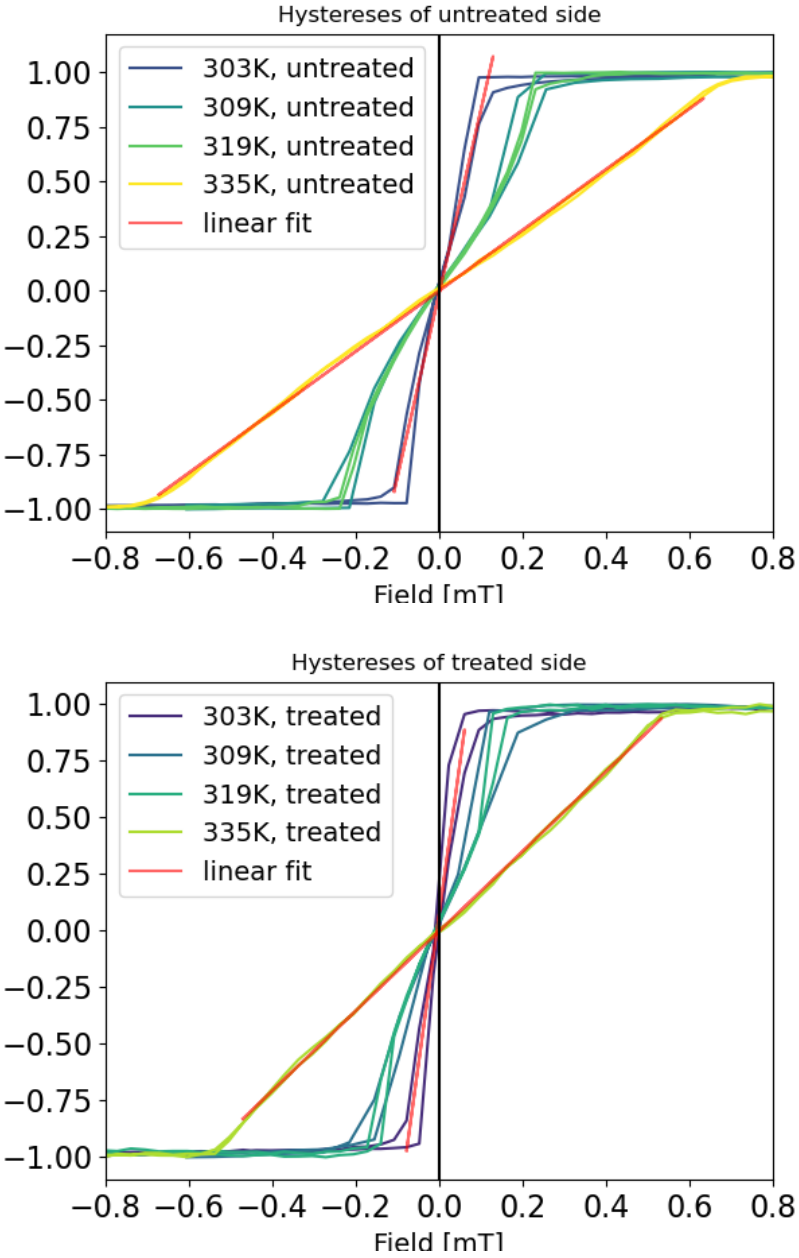

FIGURE C.4: Hysteresis and slopes of hysteresis of untreated (top) and treated (bot) side.

Linear slope V1: 13.4 - treated at 303,1 K
Linear slope V2: 8.4 - untreated at 303,1 K
Linear slope V7: 1.8 - treated at 335,0 K
Linear slope V8: 1.4 - untreated at 335,0 K

Notably, the hysteresis curves in the treated region display steeper slopes compared to those in the untreated region. This suggests a higher effective PMA in the treated area. The relatively lower PMA in the untreated side could be indicative of a

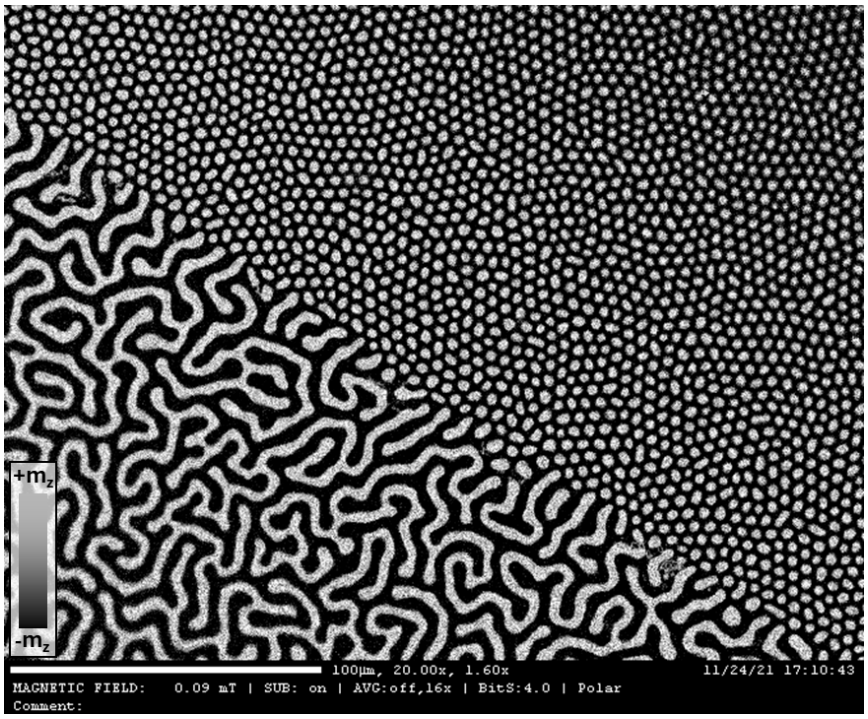

FIGURE C.5: Sample MVK763 exhibits the well-defined boundary separating two distinct magnetic phases within each segment: an equilibrated worm-like domain structure on the treated side and a skyrmion phase on the untreated side.

more relaxed magnetic configuration or increased disorder. The observed PMA enhancement in the treated region may be attributed to a mild annealing effect induced by He^+ irradiation, which promotes crystallinity and thereby increases anisotropy, as suggested by previous studies [314]. However, without complementary measurements - such as SQUID magnetometry - quantitative determination of the anisotropy remains uncertain.
Interestingly, the magnetic property modifications are sufficient to support the coexistence of different magnetic phases under low external magnetic fields (e.g., 90 µT): while skyrmions are stabilized in the untreated region, the treated area maintains a worm-like domain state under the same conditions (see Figure C.5).

C.2.2 He^+ irradiation: parameters of double polarity skyrmions

Figures C.6 and C.7 display additional data for the PMOKE differential recording of the double polarity skyrmion measurement.

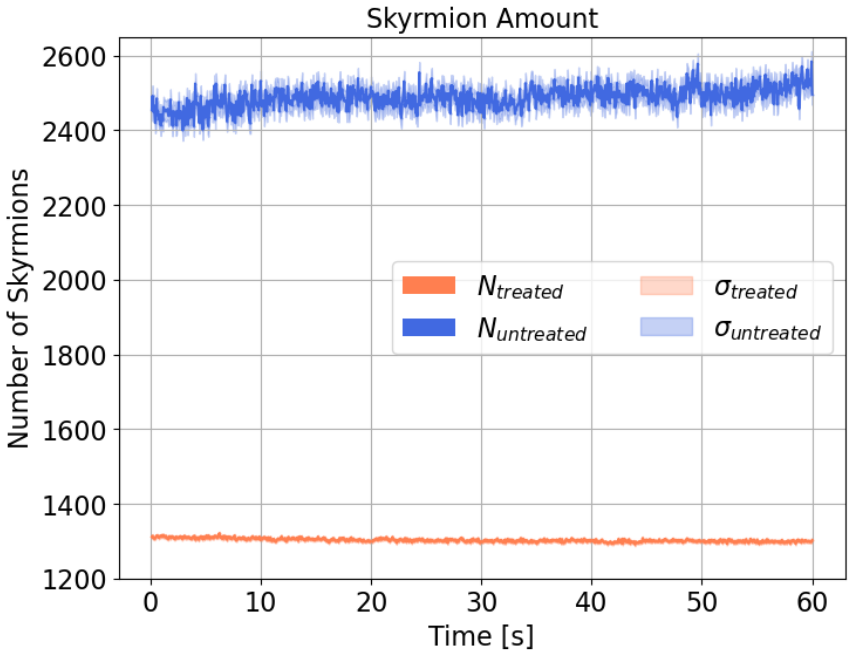

FIGURE C.6: Skyrmion amount over time for the treated and untreated part of the opposite polarity skyrmion PMOKE recording on MVK763 at 322,7 K and 110 µT.

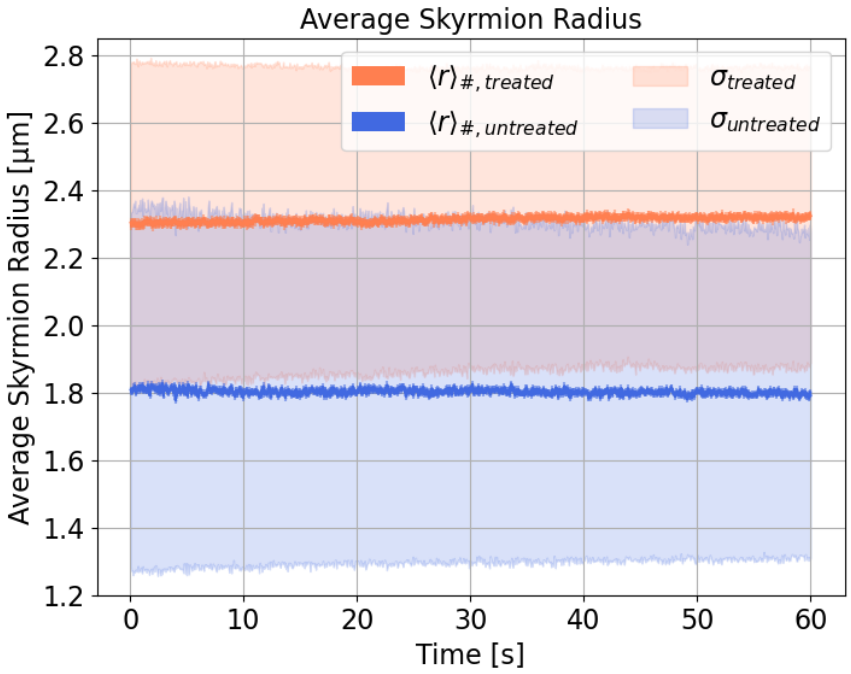

FIGURE C.7: Average skyrmion radius over time for the treated and untreated part of the opposite polarity skyrmion PMOKE recording on MVK763 at 322,7 K and 110 µT.

C.2.3 UNET skyrmion identification

The skyrmions in this study were tracked using the UNET procedure (Section 3.4.3). UNET was primarily trained on MOKE images with a specific polarity for skyrmions: dark skyrmions on a bright background. In cases where the MOKE contrast is reversed, with bright skyrmions on a dark background, a simple solution is to invert the greyscale, allowing UNET to process the image as dark skyrmions on a bright background again. Although a modified version of UNET can classify skyrmions with reversed greyscale, its performance is lower. To maintain consistent performance and comparable classification, the original version of UNET was used. Due to the dual polarity observed in this particular recording, UNET struggled to correctly identify skyrmions on the treated side, as both bright and dark skyrmions were identified simultaneously. To address this issue, the recording and analysis were split into three parts, with UNET applied separately to each:

1. The untreated side in its natural greyscale (dark skyrmions on a bright background), with the treated side masked in black.

2. The treated side in inverted greyscale (dark skyrmions on a bright background), with the untreated side masked in white.

3. The treated side in its natural greyscale, with the untreated side masked in black.

This approach allowed UNET to independently identify skyrmions in each region, as demonstrated in Figure C.8. For each frame, a pre-check is performed to ensure proper parameter fitting, displaying three images: [_1] the raw input image, [_2] the prediction of the trained classes, where the background is marked in green and the potential magnetic structures (e.g., skyrmions) in red, and [_3] the frame with identified and filtered skyrmions highlighted in blue, with the background in pink. Image [a1] shows the untreated side, with the treated side masked in black. In [a2], UNET classifies the treated side as background, with the skyrmions marked in red. [a3] shows the filtered skyrmions in blue, while the background is pink. Due to a slight focus gradient and the small size of the skyrmions, UNET did not identify skyrmions in the pink areas at the top left corner. Image [b1] shows the raw treated side, with the untreated side masked in black. In [b2], UNET classifies the treated area as background (green), with the intervening area classified as magnetic structure. Consequently, in [b3], no skyrmions are identified, except near the treatment line. Images [c1] and [c2] show the treated side in inverted greyscale, with the upper half masked in white. This allows UNET to correctly classify and identify the skyrmions, as shown in [c3].

C.3 Additional material: irradiated barrier

C.3.1 Ga^+ Irradiation

The Ga^+ irradiation was performed using a focused ion beam as described in 3.5 over a line of 100×22 µm^2 using a dose gradient with a dose interval of 1 µm. Dose gradient increases from left to right, starting with factor 1, 1, 2, 4, 8, 16, 32, 64, 128, 256, 512 $\times 10^{-16} \frac{C}{\mu m^2}$ and decreasing in the same manner to the right, resulting in the 22 µm width. The dwell time was set to 25 ns.

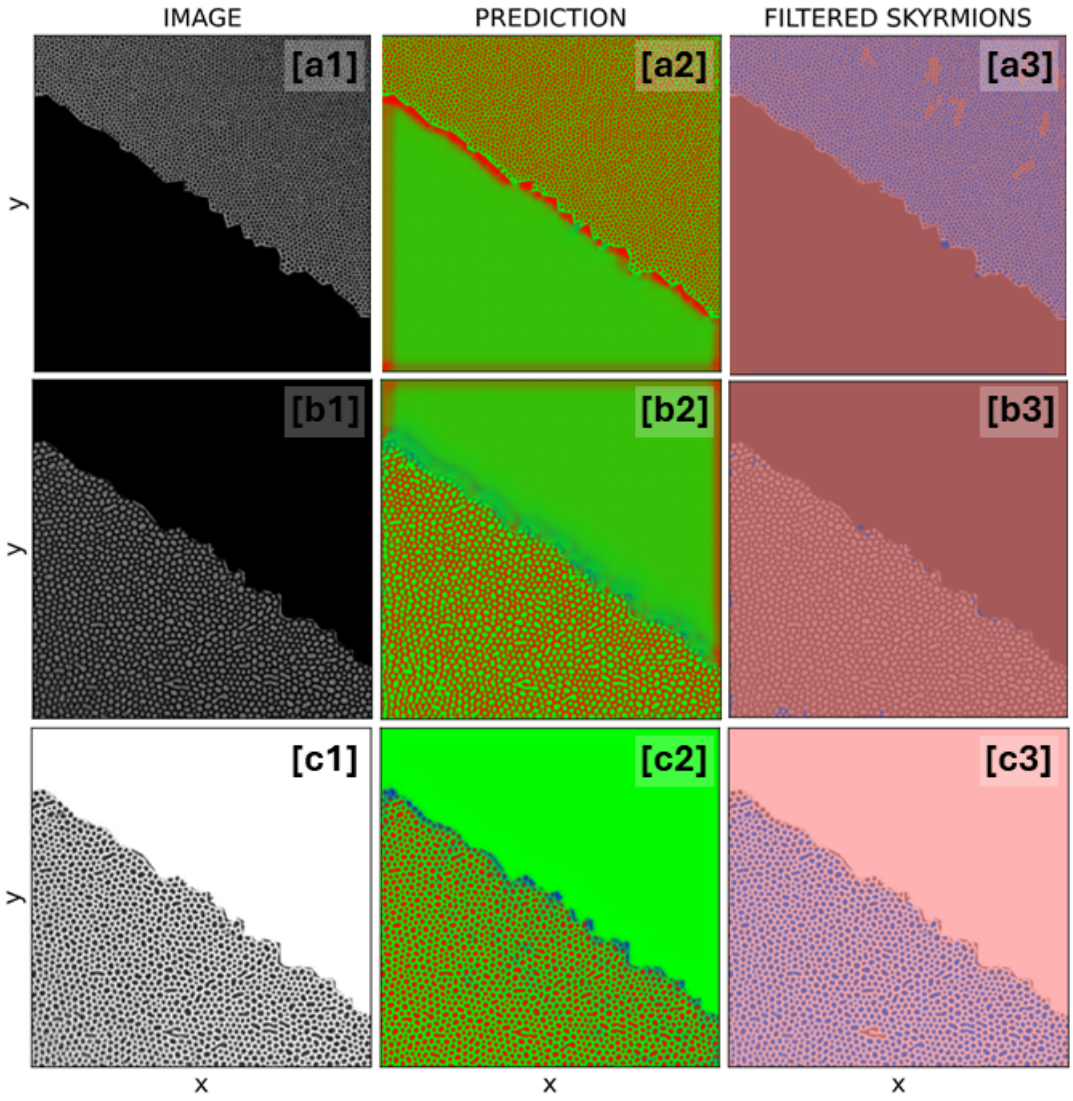

FIGURE C.8: UNET identification for treated and untreated sides. The grey level of the treated side was inverted to analyze the image with UNET.

C.3.2 Summary: irradiation barrier

In summary, Figure C.9 presents the average skyrmion number and average skyrmion radius for each applied current density directed toward the irradiation-induced barrier within the narrow channel. The subsequent section provides a comparative analysis with the structural comb barrier.

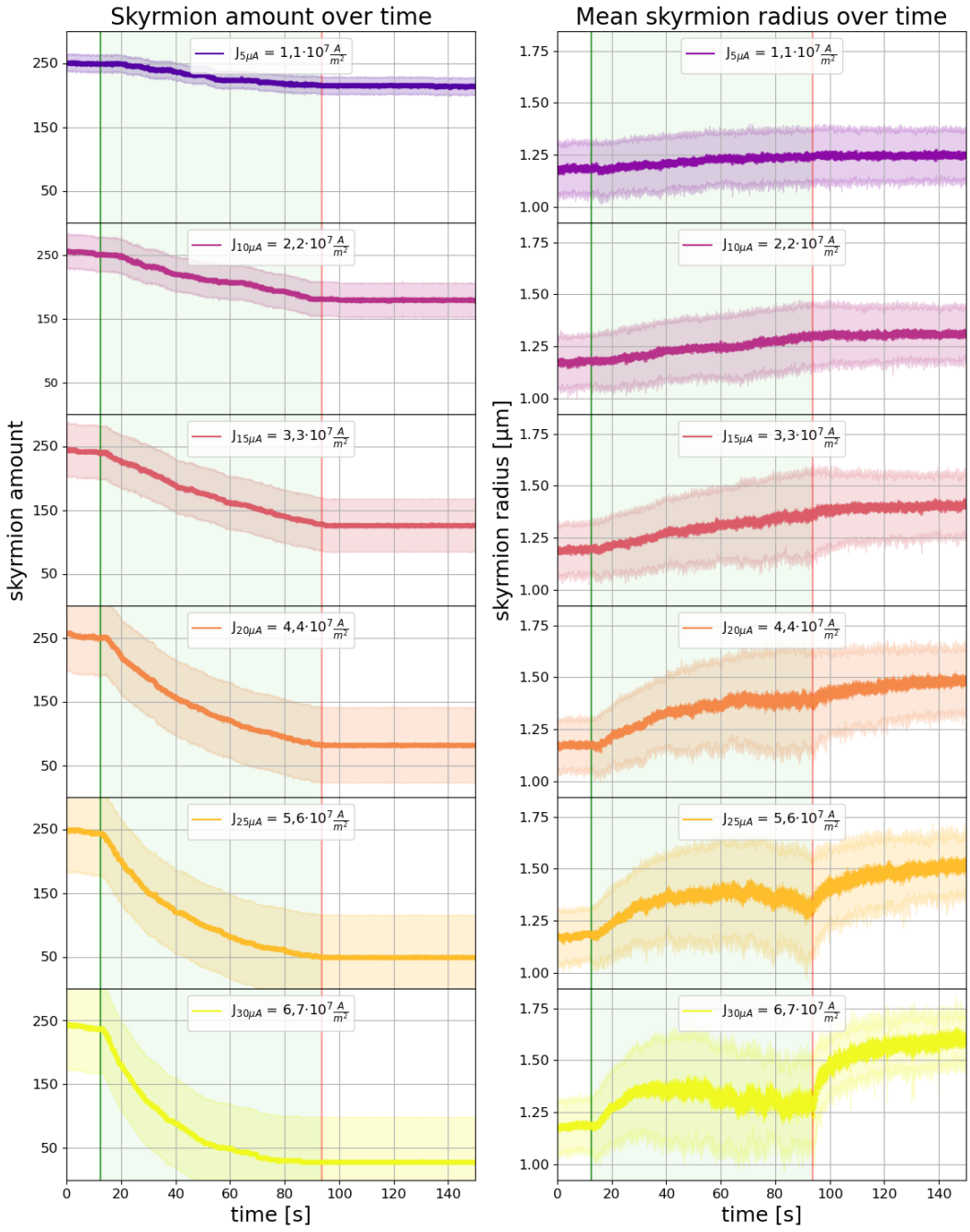

FIGURE C.9: Summary of the average skyrmion amount and average skyrmion radius over time for individual current densities.

C.3.3 Eccentricity TMD109

Eccentricity at 300 K for free skyrmions depending on the applied OOP field. Eccentricity is defined as the ratio of the longest axis in the (elliptic) skyrmion divided by the orthogonal short axis: $a/b = e$.

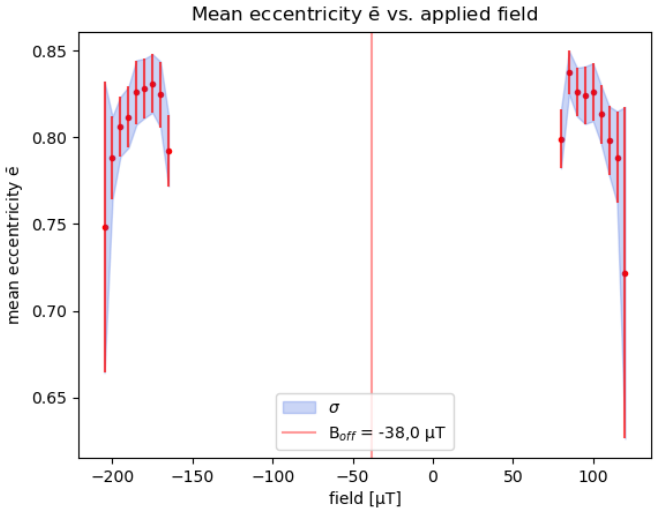

FIGURE C.10: Mean eccentricity for TMD109 sample in structure C22 in dependence of the applied OOP field at 300 K. At low field values the skyrmion elongates thermally into worm-like domains, thus the mean eccentricity becomes lower. With increasing field value, the eccentricity rises to a maximum where skyrmions stay in their circular shape and then drops down again. At the largest field values, the skyrmions become so small and only few are left so that the proper identification and axis-length determination for the eccentricity becomes very noisy, resulting in a large standard deviation.

C.3.4 $\psi_6 - \psi_4$ TMD109

The averaged values of the bond-orientational order parameters ψ_6 and ψ_4 displayed in Figure C.12 for the configuration involving the irradiated barrier indicate the absence of a well-ordered lattice structure - neither hexagonal nor square symmetry is clearly established. Although ψ_6 exceeds ψ_4, suggesting a tendency toward local hexagonal ordering, the overall skyrmion arrangement lacks sufficient density to support long-range crystalline order. Instead, the system exhibits characteristics consistent with the disordered or liquid-like state [175]. Upon relaxation, as skyrmions diffuse away from the barrier and re-expand into the channel, the order parameters display significant fluctuations, reflecting the ongoing melting and destabilization of the skyrmion lattice.

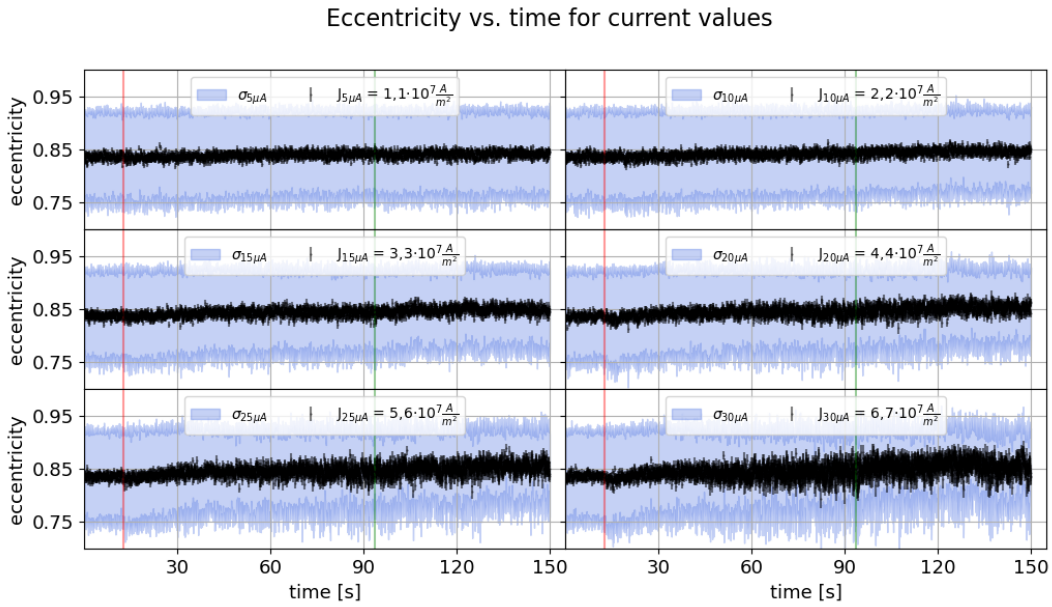

FIGURE C.11: Averaged eccentricity over time for the applied current densities. The skyrmion do not deform significantly during the compression, although at the highest current densities the eccentricity becomes more noisy, due to averaging over fewer skyrmions.

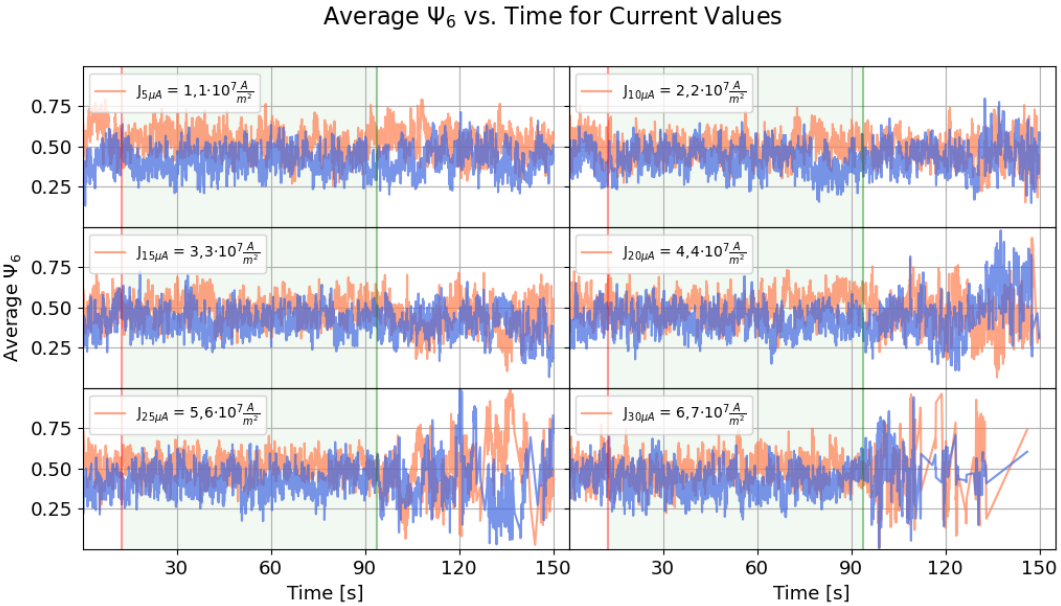

FIGURE C.12: The averaged ψ_6&ψ_4 values over time for the irradiated barrier. The lattice is not dense enough for a hexagonal or square order. During relaxation, when skyrmions diffuse back into the channel away from the barrier and expand, the value becomes very noisy due to the melting and disintegration of skyrmion lattice.

C.4 C22 structural comb barrier

In Section 5.3 the skyrmion compression at an irradiated artificial barrier was investigated. The following comparative plots show the skyrmion compression against the structural comb geometry shown in Figure 5.13 for the same temperature, OOP field and initial lattice state. Note that due to the wider channel (*reservoir*) the current density at the same applied current strengths (5 µA to 30 µA, in steps of 5 µA) is smaller than in the narrow part of the channel with the artificial barrier.

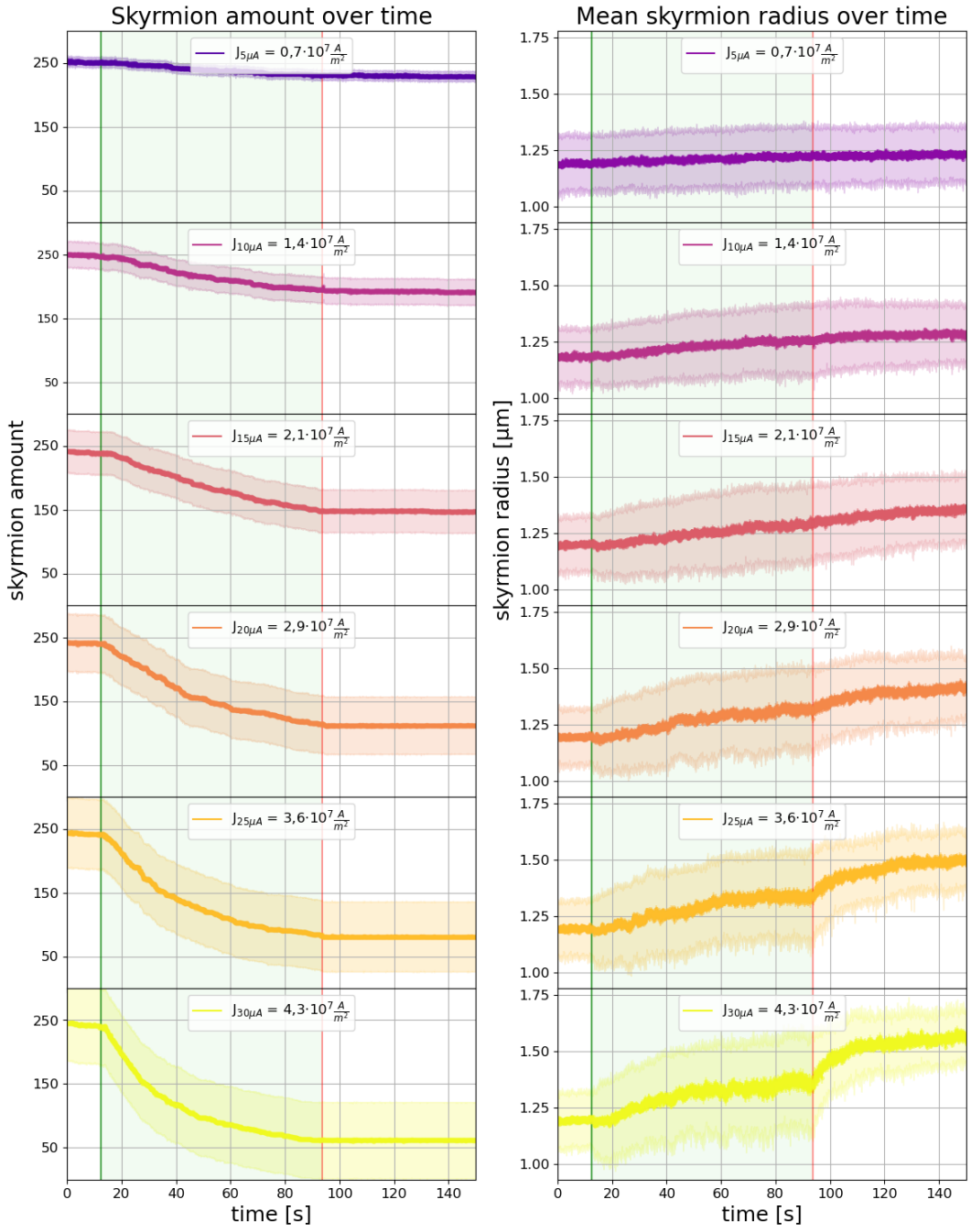

FIGURE C.13: Comparative plot to Section 5.3 for the structural comb barrier. Shown is the average skyrmion radius and average skyrmion amount over time dependent on the applied current density (at the reservoir).

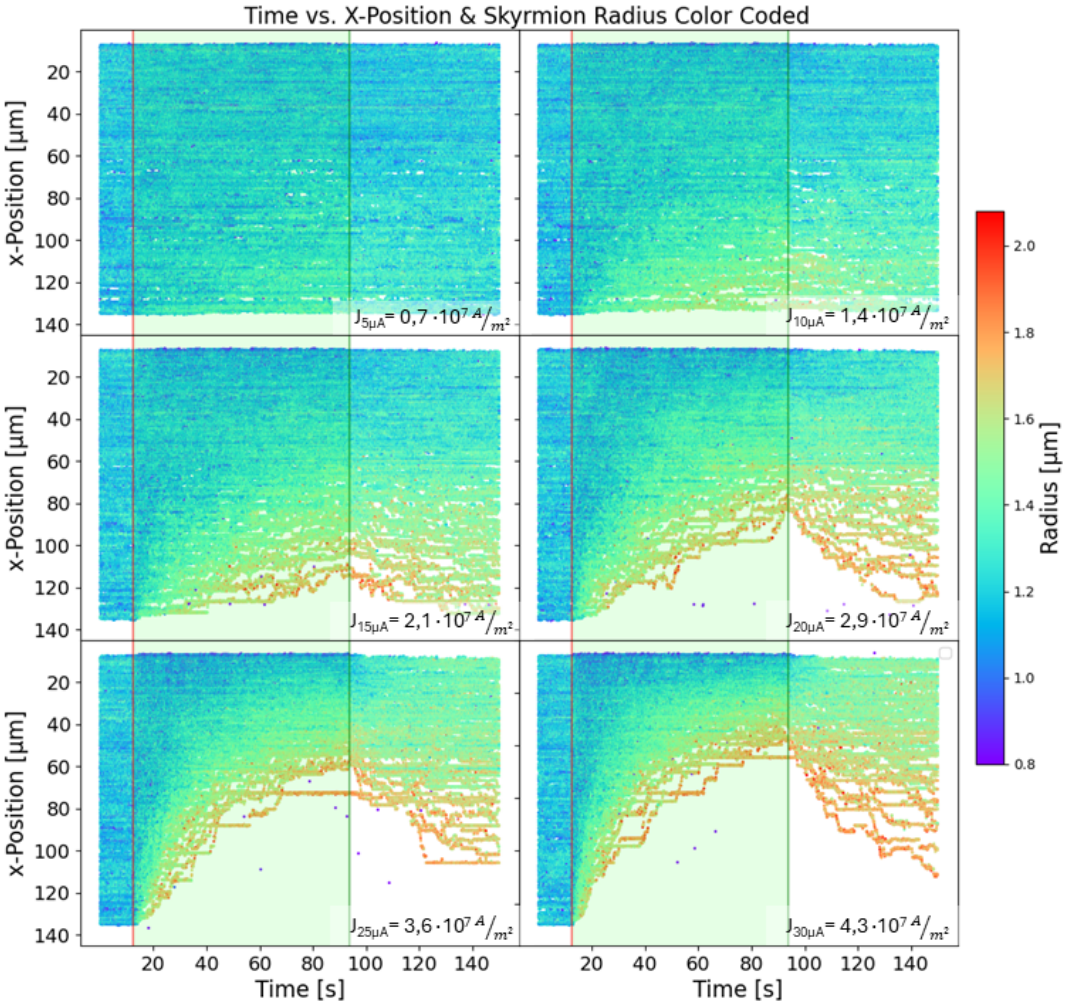

FIGURE C.14: Comparative plot to Section 5.3 for the structural comb barrier. Similarly to Figure 5.18, the skyrmion position is projected onto the x-coordinate over time with the skyrmion size as color code. Here the skyrmion are compressed towards the top, due to the compression against the structural barrier.

Similar to Figure 5.24, Figure C.15 displays the normalized relative skyrmion density per ∼4,5 µm section, which is highest near the barrier region (indicated in yellow) and decreases with increasing distance from the barrier (dark violet). It is important to note that the comb barrier is located at the end of the reservoir - the wider section of the channel - resulting in a higher concentration of skyrmions in this area compared to the narrower portion of the channel. The data are divided into four time intervals: an initial equilibration phase (frames 0–200), two intervals during current application (frames 201–850 and 851–1500), and a final relaxation phase without current (frames 1501–2000). Upon current application, the skyrmion density increases, with a more pronounced effect observed at higher current amplitudes. Once the current is turned off, the skyrmions begin to relax, redistribute within the channel, and expand, indicating diffusion-driven relaxation dynamics.

Interestingly, the average inter-skyrmion distance increases continuously during both the current application and subsequent relaxation phases (see Figure C.16). This behavior is most likely influenced by the widening of the channel geometry. Skyrmion annihilation occurs at comparable rates for both the structural comb barrier and the irradiation-induced barrier, suggesting a balance between the larger

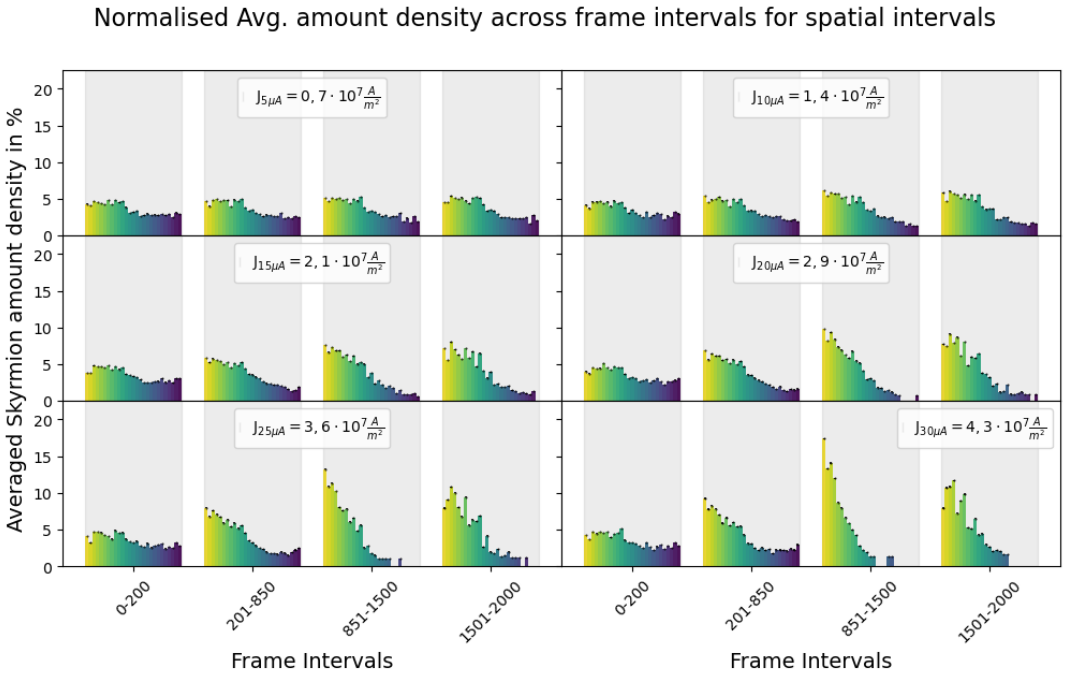

FIGURE C.15: Comparative plot to 5, Section 5.3 for the structural comb barrier.

physical extent and magnetic inhomogeneity of the comb barrier - where annihilation is more likely - and the lower current density present in the wider channel region. The resulting geometry provides additional space for skyrmions to disperse into the reservoir, thereby increasing their spatial separation and contributing to the observed rise in inter-skyrmion distance.

A comparative analysis of the average skyrmion radius over time is presented, corresponding to Figures C.13 (structural comb barrier) and C.9 (irradiation-induced barrier). For the irradiated barrier within the narrow channel, the average skyrmion radius stagnates and even exhibits a slight decrease, indicative of skyrmion compression. In contrast, for the structural comb barrier located in the wider region of the device, the average radius increases steadily—with only minor fluctuations—and continues to grow during the subsequent relaxation phase. Given that the rate of skyrmion annihilation is comparable for both barrier types, the observed differences are likely influenced primarily by geometric factors, particularly the local current density, which is reduced in the wider channel. These findings suggest that geometry plays a critical role in skyrmion behavior, warranting further investigation into annihilation mechanisms at both structural and irradiation-induced boundaries.

Overall, no significant qualitative differences in skyrmion compression were observed between the structural comb boundary and the irradiation-induced artificial barrier. The observed differences in the evolution in time of skyrmion size and distance can be linked to the widening of the geometry and the lesser current density thereof. A notable advantage of the artificial barrier is its negligible impact on the current density distribution, owing to the absence of structural discontinuities. Although the limitations of structural barriers could, in principle, be addressed by introducing non-magnetic yet conductive interlayers adjacent to the skyrmion-hosting

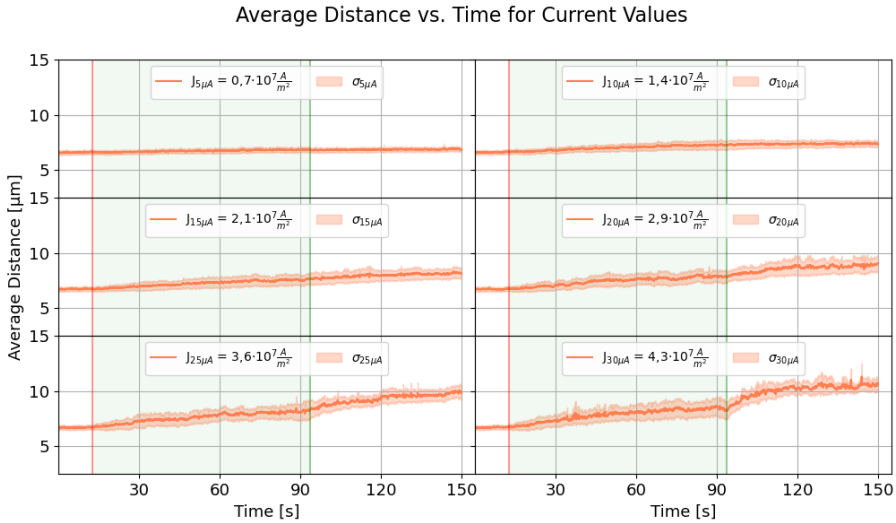

FIGURE C.16: Comparative plot to 5, Section 5.3 for the structural comb barrier.

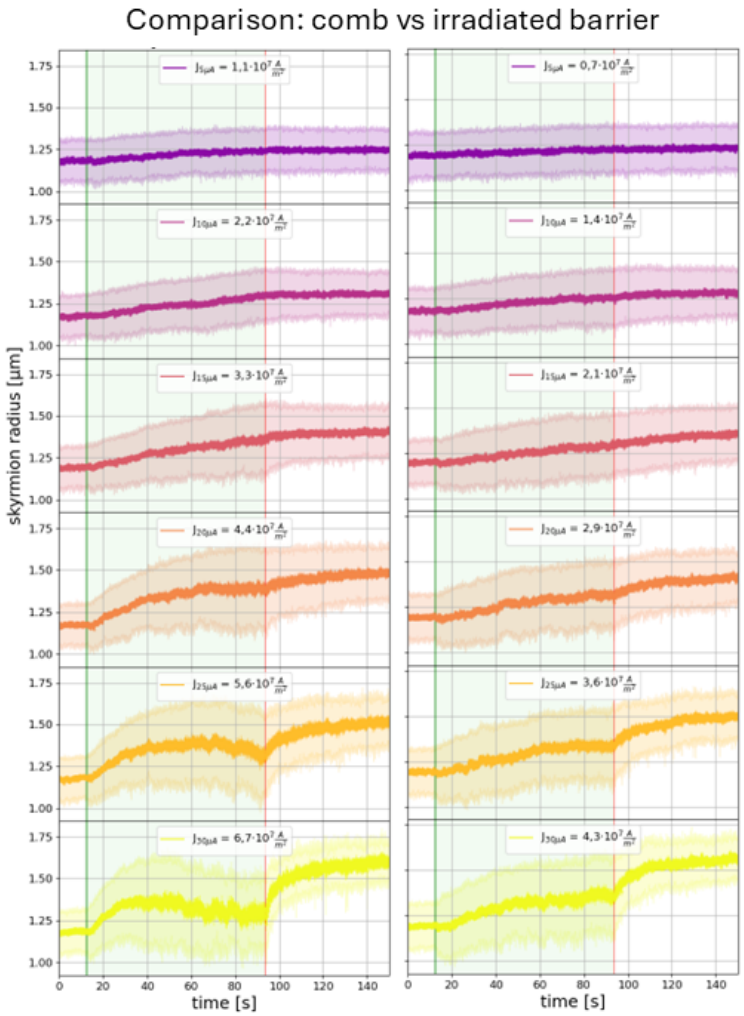

FIGURE C.17: Comparative plot of the average skyrmion radius over time of Figures C.13 (comb barrier) and C.9 (irradiation barrier). The wider geometry, which provides increased space and results in a reduced current density, diminishes the degree of skyrmion compression compared to the narrow channel geometry.

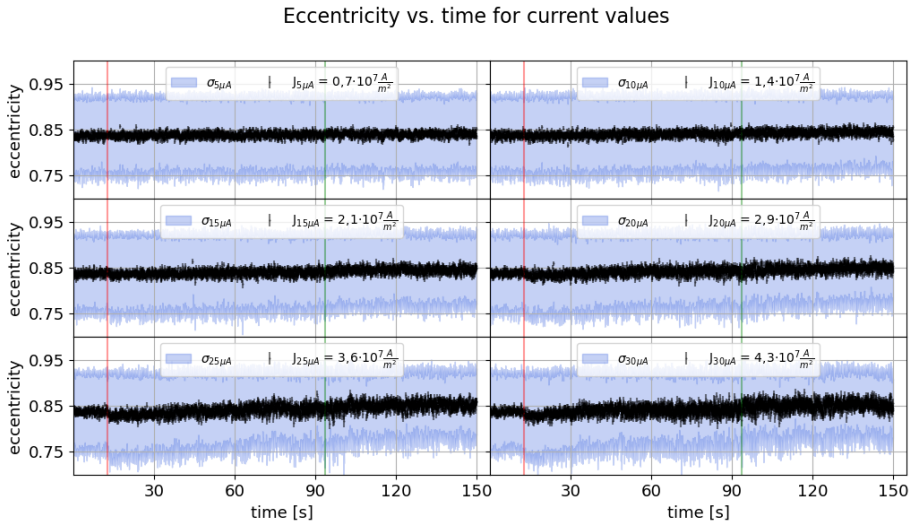

FIGURE C.18: Comparative plot to 5, Section 5.3 for the structural comb barrier. With less skyrmion compression as mentioned in the previous plots, the skyrmion eccentricity develops comparatively similar to the irradiation barrier in the narrow channel. Higher fluctuations at higher current densities, but no clear trend observable.

ferromagnetic layers, such modifications may inadvertently alter the magnetic environment, potentially affecting skyrmion dynamics or stability. Moreover, this approach would require additional sputtering and lithography processes, thereby increasing fabrication complexity and reducing economic viability. Each implementation would also require individual evaluation, in contrast to the relatively straightforward and localized nature of ion irradiation. These considerations underscore the high potential of ion irradiation as a versatile and effective technique for skyrmion confinement and manipulation.

C.5 Contribution

Ga^+ irradiation was performed on the samples with G. Beneke. Theory based on extended Thiele equation, macroscopic description and simulation for qualitative comparison with experimental results was developed by K. Leutner with helpful discussion with Dr. R. Frömter.

Appendix D

Appendix: Brownian Reservoir Computing

D.1 Linear regression weights

D.1.1 Linear regression weights for skyrmion center readout

TABLE D.1: Weights of the linear regression training process for Boolean logic operations using 4 sets of 1000 images each for point-like skyrmion (center readout)

Operator	$\mathbf{W}_{\text{left}}$	$\mathbf{W}_{\text{right}}$	$\mathbf{W}_{\text{top}}$	$\mathbf{W}_{\text{middle}}$	$\mathbf{W}_{\text{intercept}}$
AND	1.124	7.497	0.623	1.022	-0.797
NAND	-1.124	-7.497	-0.623	-1.022	1.797
OR	0.272	1.09	-1.403	-2.908	0.942
NOR	-0.272	-1.09	1.403	2.908	0.058
XOR	-0.852	-6.407	-2.027	-3.93	1.739
XNOR	0.852	6.407	2.027	3.93	-0.739

D.1.2 Linear regression weights for overlap-based read-out

TABLE D.2: Weights of the linear regression training process for Boolean logic operations using 4 sets of 1000 images each for expansive skyrmion (overlap readout)

Operator	$\mathbf{W}_{\text{left}}$	$\mathbf{W}_{\text{right}}$	$\mathbf{W}_{\text{top}}$	$\mathbf{W}_{\text{middle}}$	$\mathbf{W}_{\text{intercept}}$
AND	2.48	9.735	1.595	2.29	-1.287
NAND	-2.48	-9.735	-1.595	-2.29	2.287
OR	0.807	1.915	-1.75	-2.4	0.806
NOR	-0.807	-1.915	1.75	2.4	0.194
XOR	-1.673	-7.82	-3.345	-4.69	2.093
XNOR	1.673	7.82	3.345	4.69	-1.093

D.2 Three-input composite logic operations

(A $\overline{\wedge}$ B) $\wedge$ C & (A $\vee$ C) $\wedge\neg$ B

A	**B**	**C**	$A \wedge B$	$A \overline{\wedge} B$	$(A \overline{\wedge} B) \wedge C$	$A \vee C$	$\neg B$	$(A \vee C) \wedge \neg B$
0	0	0	0	1	0	0	1	0
0	0	1	0	1	1	1	1	1
0	1	0	0	1	0	0	0	0
0	1	1	0	1	1	1	0	0
1	0	0	0	1	0	1	1	1
1	0	1	0	1	1	1	1	1
1	1	0	1	0	0	1	0	0
1	1	1	1	0	0	1	0	0

(A $\wedge$ B) $\vee\neg$ C & ($\neg$ A $\wedge\neg$ C) $\vee$ B

A	**B**	**C**	$A \wedge B$	$\neg C$	$(A \wedge B) \vee \neg C$	$\neg A$	$\neg C$	$\neg A \wedge \neg C$	$(\neg A \wedge \neg C) \vee B$
0	0	0	0	1	1	1	1	1	1
0	0	1	0	0	0	1	0	0	0
0	1	0	0	1	1	1	1	1	1
0	1	1	0	0	0	1	0	0	1
1	0	0	0	1	1	0	1	0	0
1	0	1	0	0	0	0	0	0	0
1	1	0	1	1	1	0	1	0	1
1	1	1	1	0	1	0	0	0	1

D.3 Probabilities

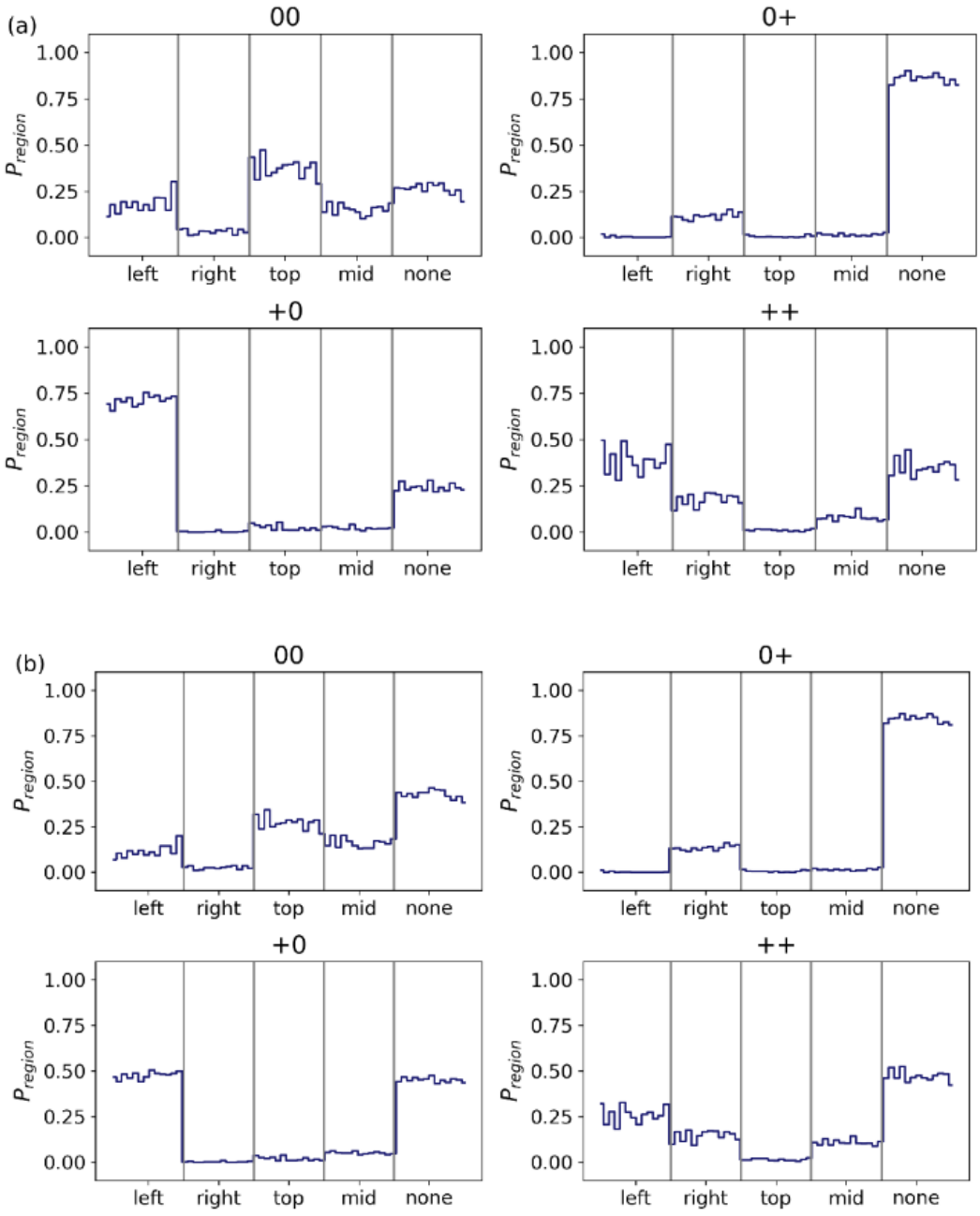

FIGURE D.1: Skyrmion occurrence probabilities were analyzed for the four designated readout locations, as well as for regions outside these areas (denoted as "none"), based on the two-contact input configurations across 13 sets of 1000 frames each. a) for skyrmion center readout and b) areal overlap readout. Taken from [99], supplementary material.

D.4 Energy estimation

D.4.1 Farthest displacement calculation

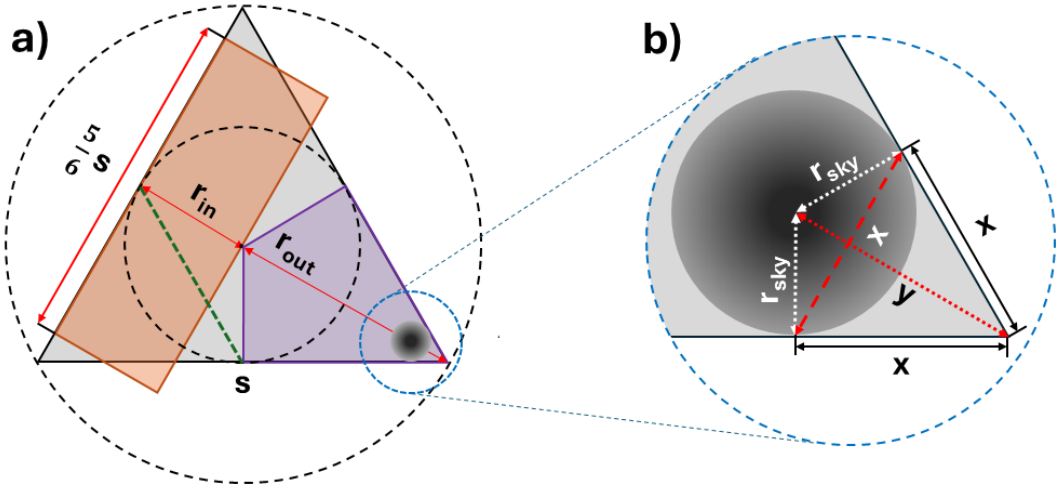

FIGURE D.2: a) Schematic representation of the device. The black dashed inner and outer circles indicate the inner and outer radii. The orange box represents a simplified approximation of the channel used for estimating current flow between two contacts, while the third contact remains floating. The green dashed line marks the half-height width of the triangular geometry, which is used for current density calculations in previous sections. A dark gray sphere illustrates an in-scale skyrmion positioned at its maximum displacement. The violet region highlights the area that a skyrmion must traverse back to the center region (used in energy consumption estimation) b) Close-up of the device corner with the maximum possible skyrmion displacement (considering no skyrmion size change or deformation), indicated by the blue dashed line. Trigonometric calculations reveal that the skyrmion remains at a distance of $y = 2 \cdot r_{\text{sky}}$ from the triangular tip, while the corresponding chord touching the device edges is given by $x = \sqrt{3} \cdot r_{\text{sky}}$ (not considering extrusions with finite width for electric leads).

Referring to the schematic in Figure D.2, the following equations are employed to determine the minimum distance, y , at maximum displacement of the skyrmion toward the tip of the corner without undergoing deformation or a change in size. The chord length, x, represents the distance between the points at which the skyrmion would make contact at its maximum displacement.

$$\begin{aligned} x &= 2 \cdot r_{\text{sky}} \cos(60^\circ) \\ &= \sqrt{3} \cdot r_{\text{sky}} \end{aligned} \tag{D.1}$$

$$\begin{aligned} y &= \sqrt{r_{\text{sky}}^2 + x^2} \\ &= 2 \cdot r_{\text{sky}} \end{aligned} \tag{D.2}$$

D.4.2 Energy - scaling proportionality

The device scaling is applied exclusively to the two in-plane dimensions (length and width), while the thickness remains unchanged to preserve functional integrity. A simplified derivation of the energy dependence on the scaling factor is presented, omitting considerations of the necessary functional overhead associated with MTJ

readout and CMOS connectivity. By combining Ohm's law ($U = R \cdot I$), the electric DC power law ($P = U \cdot I$), the material-specific resistance formula ($R = \rho \cdot {}^{l}/_{A}$), and the definition of energy ($E = P \cdot t$), it can be shown that the device resistance remains independent of the scaling factor x, while the energy E is proportional to x. It is important to acknowledge that the operation time also indirectly depends on the scaling factor and that only a single material parameter, ρ, has been considered in the derivation. However, due to the complexity of estimating the time dependence, it has been excluded from the strictly geometry-based proportionality derivation.

$$\begin{aligned} R &= \rho \cdot \frac{l}{A} = \rho \cdot \frac{(l \cdot \not{x})}{h\,(w \cdot \not{x})} \\ &= \rho \cdot \frac{l}{h \cdot w} \\ &\text{with} \\ A &= h \cdot w \end{aligned} \tag{D.3}$$

$$\begin{aligned} E &= P \cdot t = U \cdot I \cdot t = R \cdot I^2 \cdot t = \rho \cdot \frac{l}{A} (J \cdot A)^2 \cdot t = \rho \cdot l \cdot A \cdot J^2 \cdot t \\ &= \rho \cdot l \cdot A \cdot J^2 \cdot t = \rho \cdot (lhw) J^2 \cdot t = \rho \cdot [(l \cdot x) \cdot h \cdot (w \cdot x)]\, J^2 \cdot t \\ &= \rho \cdot (lhw) \cdot x^2 \cdot J^2 \cdot t \\ E &\propto x^2 \end{aligned} \tag{D.4}$$

using

$$\begin{aligned} U &= R \cdot I & J &= I/A \\ P &= U \cdot I & R &= \rho \cdot \frac{l}{A} \\ A &= h \cdot w \end{aligned} \tag{D.5}$$

with R, the resistance, ρ the material specific resistance, l, the length and A, the cross section of the materials' geometry. Cross section A consists of the stack height h and width w. Scaling factor x for scaling down the device cancels out during calculation. Height h is not affected by scaling.

D.5 Heating energy

To estimate the energy required to heat the presented prototype device and a potential scaled-down version, the material stack is approximated as a single tantalum layer with a thickness of 13 nm, while retaining the previously defined lateral dimensions. Only the volume of the device is considered in this calculation, excluding contributions from contacting leads, the substrate, or additional layers. Consequently, the computed energy represents a lower bound, and in a practical scenario involving active heating, the actual energy consumption would be higher. Using the density of tantalum (ρ_{Ta} = 16 678 ${}^{kg}/_{m^3}$) and its specific heat capacity ($c_{T,Ta}$ = 140 ${}^{J}/_{kg \cdot K}$) [384], along with a temperature increase of 10 K, the required energy can be calculated as follows:

$$
\begin{aligned}
V &= A \cdot h = \frac{\sqrt{3}}{4} s^2 \\
\rho &= \frac{m}{V} \\
c &= \frac{E}{m \cdot dT} \\
E &= c \cdot m \cdot dT = c \cdot \left(\rho \cdot \frac{\sqrt{3}}{4} s^2 \cdot h \right) \cdot dT
\end{aligned}
\tag{D.6}
$$

With V, A , s and h the volume, surface, side length and height of the device, respectively, and ρ, c, m the density, the specific heat capacity and the mass of tantalum. E the energy and dT, the amount of temperature change. The lower energy limit for the 40 μm device is 210 pJ, while for the scaled down version with 400 nm the energy limit would be 21 fJ.

D.6 Contributions

PMOKE measurements were performed with help of G. Beneke, who also helped with the setup. M. Brems used the tracked and analyzed skyrmion data to train the perceptron for the presented Boolean logic operations and created the according plots and graphs. Contribution to [152], the time-multiplexed adaptation of the triangular RC concept discussed in Section 6.8, was only in discussion and sample production. Original Latex template from J. Böttcher under LPPL v1.3c license[1].

D.7 Utilization of AI

In this thesis, AI in the form of a large language model (LLM) developed by OpenAI - specifically ChatGPT (versions GPT-3.5, GPT-4-mini, and GPT-4) - was employed for spell checking and linguistic refinement of draft texts. The tool was used throughout the writing process to enhance readability, improve clarity, and reduce typographical and grammatical errors. Additionally, it helped creating Latex code for tables and formatting.

[1] (http://www.latex-project.org/lppl)

Bibliography

[1] *Energy and AI*. Conference. London: International Energy Agency, Apr. 2025.

[2] IEA. "Data centre electricity consumption by region, Base Case, 2020-2030". In: Paris, 2025.

[3] Louis De Broglie. "Recherches sur la théorie des Quanta". In: *Ann. Phys.* 10.3 (1925), pp. 22–128. ISSN: 0003-4169, 1286-4838. DOI: 10.1051/anphys/192510030022.

[4] M. Born and P. Jordan. "Zur Quantenmechanik". In: *Z. Physik* 34.1 (Dec. 1925), pp. 858–888. ISSN: 1434-6001, 1434-601X. DOI: 10.1007/BF01328531.

[5] Dirac, Paul. "The quantum theory of the emission and absorption of radiation". In: *Proc. R. Soc. Lond. A* 114.767 (Mar. 1927), pp. 243–265. ISSN: 0950-1207, 2053-9150. DOI: 10.1098/rspa.1927.0039.

[6] E. Fermi. "Versuch einer Theorie der Beta-Strahlen." In: *Z. Physik* 88.3 (Mar. 1934), pp. 161–177. ISSN: 1434-6001, 1434-601X. DOI: 10.1007/BF01351864.

[7] Albert Einstein. "Über das Relativitätsprinzip und die aus demselben gezogenen Folgerungen." In: *Jahrbuch der Radioaktivität und Elektronik*. Vol. IV. 1908, pp. 411–462.

[8] James Clerk Maxwell. "VIII. A dynamical theory of the electromagnetic field". In: *Phil. Trans. R. Soc.* 155 (Dec. 31, 1865), pp. 459–512. ISSN: 0261-0523, 2053-9223. DOI: 10.1098/rstl.1865.0008.

[9] Wolfgang Nolting and Anupuru Ramakanth. *Quantum Theory of Magnetism*. Berlin, Heidelberg: Springer Berlin Heidelberg, 2009. ISBN: 978-3-540-85415-9. DOI: 10.1007/978-3-540-85416-6.

[10] Stephen Blundell. *Magnetism in condensed matter*. Reprint. Oxford master series in condensed matter physics 4. Oxford: Oxford Univ. Press, 2014. 238 pp. ISBN: 978-0-19-850591-4.

[11] Julian Schwinger. "On Quantum-Electrodynamics and the Magnetic Moment of the Electron". In: *Phys. Rev.* 73.4 (Feb. 15, 1948), pp. 416–417. ISSN: 0031-899X. DOI: 10.1103/PhysRev.73.416.

[12] X. Fan, T. G. Myers, B. A. D. Sukra, and G. Gabrielse. "Measurement of the Electron Magnetic Moment". In: *Phys. Rev. Lett.* 130.7 (Feb. 13, 2023), p. 071801. ISSN: 0031-9007, 1079-7114. DOI: 10.1103/PhysRevLett.130.071801.

[13] Hermann Haken and Hans Christoph Wolf. *Atom- und Quantenphysik: Einführung in die experimentellen und theoretischen Grundlagen*. Achte, aktualisierte und erweiterte Auflage. Springer-Lehrbuch. Berlin Heidelberg: Springer, 2004. 531 pp. ISBN: 978-3-540-02621-1.

[14] Pranab Kumar Das, Jagoda Sławińska, Ivana Vobornik, Jun Fujii, Anna Regoutz, Juhan M. Kahk, David O. Scanlon, Benjamin J. Morgan, Cormac McGuinness, Evgeny Plekhanov, Domenico Di Sante, Ying-Sheng Huang, Ruei-San Chen, Giorgio Rossi, Silvia Picozzi, William R. Branford, Giancarlo Panaccione, and David J. Payne. "Role of spin-orbit coupling in the electronic structure of Ir O 2". In: *Phys. Rev. Materials* 2.6 (June 4, 2018), p. 065001. ISSN: 2475-9953. DOI: 10.1103/PhysRevMaterials.2.065001.

[15] W. Heisenberg. "Zur Theorie des Ferromagnetismus". In: *Z. Physik* 49.9 (1928), pp. 619–636. ISSN: 1434-6001, 1434-601X. DOI: 10.1007/BF01328601.

[16] E. C. Stoner and E. P. Wohlfarth. "A mechanism of magnetic hysteresis in heterogeneous alloys". In: *Phil. Trans. R. Soc. Lond. A* 240.826 (May 4, 1948), pp. 599–642. ISSN: 0080-4614, 2054-0272. DOI: 10.1098/rsta.1948.0007.

[17] Sir James Alfred Ewing. "VII. On the production of transient electric currents in iron and steel conductors by twisting them when magnetised or by magnetising them when twisted". In: *Proc. R. Soc. Lond.* 33.216 (Dec. 31, 1882), pp. 21–23. ISSN: 0370-1662, 2053-9126. DOI: 10.1098/rspl.1881.0067.

[18] Landau, L. and Lifshitz, E. "On the theory of magnetic permeability dispersion in ferromagnetic solids." In: 8 (1935), pp. 153–166.

[19] Dan Wei. *Micromagnetics and recording materials*. SpringerBriefs in applied sciences and technology. Heidelberg New York: Springer, 2012. ISBN: 978-3-642-28577-6.

[20] Kläui, M. *Festkörperphysik - Magnetismus*. Mainz, Germany, 2016.

[21] Eduardo Mendive Tapia. "Minimisation of the Gibbs Free Energy: Magnetic Phase Diagrams and Caloric Effects". In: *Ab initio Theory of Magnetic Ordering*. Series Title: Springer Theses. Cham: Springer International Publishing, 2020, pp. 55–68. ISBN: 978-3-030-37237-8. DOI: 10.1007/978-3-030-37238-5_4.

[22] Rudolf Gross and Achim Marx. *Festkörperphysik:* OLDENBOURG WISSENSCHAFTSVERLAG, Aug. 19, 2014. ISBN: 978-3-11-035869-8. DOI: 10.1524/9783110358704.

[23] Krüger, B. "Current-Driven Magnetization Dynamics: Analytical Modeling and Numerical Simulation." Doctoral Thesis. Hamburg, Germany: University of Hamburg, 2011.

[24] Litzius, Kai. "Spin-Orbit-Induced Dynamics of Chiral Magnetic Structures". Doctoral Thesis. Mainz, Germany: JGU Mainz, 2018.

[25] Alex Hubert and Rudolf Schäfer. *Magnetic domains: the analysis of magnetic microstructures*. Berlin ; New York: Springer, 1998. 696 pp. ISBN: 978-3-540-64108-7.

[26] C. Zener. "Classical Theory of the Temperature Dependence of Magnetic Anisotropy Energy". In: *Phys. Rev.* 96.5 (Dec. 1, 1954), pp. 1335–1337. ISSN: 0031-899X. DOI: 10.1103/PhysRev.96.1335.

[27] I. E. Dzyaloshinskii. "A thermodynamic theory of weak ferromagnetism of antiferromagnet". In: (1958).

[28] Tôru Moriya. "Anisotropic Superexchange Interaction and Weak Ferromagnetism". In: *Phys. Rev.* 120.1 (Oct. 1, 1960), pp. 91–98. ISSN: 0031-899X. DOI: 10.1103/PhysRev.120.91.

[29] Albert Fert, Vincent Cros, and João Sampaio. "Skyrmions on the track". In: *Nat. Nanotechnol.* 8.3 (Mar. 2013), pp. 152–156. ISSN: 1748-3387, 1748-3395. DOI: 10.1038/nnano.2013.29.

[30] Heng Niu, Hee Young Kwon, Tianping Ma, Zhiyuan Cheng, Colin Ophus, Bingfeng Miao, Liang Sun, Yizheng Wu, Kai Liu, Stuart S. P. Parkin, Changyeon Won, Andreas K. Schmid, Haifeng Ding, and Gong Chen. "Reducing crystal symmetry to generate out-of-plane Dzyaloshinskii–Moriya interaction". In: *Nat Commun* 15.1 (Nov. 25, 2024), p. 10199. ISSN: 2041-1723. DOI: 10.1038/s41467-024-54521-6.

[31] Ivan Lemesh, Felix Büttner, and Geoffrey S. D. Beach. "Accurate model of the stripe domain phase of perpendicularly magnetized multilayers". In: *Phys. Rev. B* 95.17 (May 17, 2017), p. 174423. ISSN: 2469-9950, 2469-9969. DOI: 10.1103/PhysRevB.95.174423.

[32] Maciej Urbaniak. "Magnetic domain walls". Posen, Poland, 2019.

[33] M. Heide, G. Bihlmayer, and S. Blügel. "Dzyaloshinskii-Moriya interaction accounting for the orientation of magnetic domains in ultrathin films: Fe/W(110)". In: *Phys. Rev. B* 78.14 (Oct. 15, 2008), p. 140403. ISSN: 1098-0121, 1550-235X. DOI: 10.1103/PhysRevB.78.140403.

[34] R. Moreno, R. F. L. Evans, S. Khmelevskyi, M. C. Muñoz, R. W. Chantrell, and O. Chubykalo-Fesenko. "Temperature-dependent exchange stiffness and domain wall width in Co". In: *Phys. Rev. B* 94.10 (Sept. 28, 2016), p. 104433. ISSN: 2469-9950, 2469-9969. DOI: 10.1103/PhysRevB.94.104433.

[35] D.G. Rancourt. "Phenomenology of domain wall pinning in ferromagnets and application to Fe-Ni Invar". In: *Journal of Magnetism and Magnetic Materials* 78.2 (Feb. 1989), pp. 153–163. ISSN: 03048853. DOI: 10.1016/0304-8853(89)90261-8.

[36] V. Jeudy, R. Díaz Pardo, W. Savero Torres, S. Bustingorry, and A. B. Kolton. "Pinning of domain walls in thin ferromagnetic films". In: *Phys. Rev. B* 98.5 (Aug. 7, 2018), p. 054406. ISSN: 2469-9950, 2469-9969. DOI: 10.1103/PhysRevB.98.054406.

[37] P. Géhanne, S. Rohart, A. Thiaville, and V. Jeudy. "Strength and length scale of the interaction between domain walls and pinning disorder in thin ferromagnetic films". In: *Phys. Rev. Research* 2.4 (Oct. 26, 2020), p. 043134. ISSN: 2643-1564. DOI: 10.1103/PhysRevResearch.2.043134.

[38] Valentina Zhukova, Paula Corte-Leon, Lorena González-Legarreta, Ahmed Talaat, Juan Maria Blanco, Mihail Ipatov, Jesus Olivera, and Arcady Zhukov. "Review of Domain Wall Dynamics Engineering in Magnetic Microwires". In: *Nanomaterials* 10.12 (Dec. 1, 2020), p. 2407. ISSN: 2079-4991. DOI: 10.3390/nano10122407.

[39] William Fuller Brown. "Thermal Fluctuations of a Single-Domain Particle". In: *Phys. Rev.* 130.5 (June 1, 1963), pp. 1677–1686. ISSN: 0031-899X. DOI: 10.1103/PhysRev.130.1677.

[40] A. Yamaguchi, S. Nasu, H. Tanigawa, T. Ono, K. Miyake, K. Mibu, and T. Shinjo. "Effect of Joule heating in current-driven domain wall motion". In: *Applied Physics Letters* 86.1 (Jan. 3, 2005), p. 012511. ISSN: 0003-6951, 1077-3118. DOI: 10.1063/1.1847714.

[41] M. Laufenberg, W. Bührer, D. Bedau, P.-E. Melchy, M. Kläui, L. Vila, G. Faini, C. A. F. Vaz, J. A. C. Bland, and U. Rüdiger. "Temperature Dependence of the Spin Torque Effect in Current-Induced Domain Wall Motion". In: *Phys. Rev. Lett.* 97.4 (July 25, 2006), p. 046602. ISSN: 0031-9007, 1079-7114. DOI: 10.1103/PhysRevLett.97.046602.

[42] Jacques Miltat, Stanislas Rohart, and André Thiaville. "Brownian motion of magnetic domain walls and skyrmions, and their diffusion constants". In: *Phys. Rev. B* 97.21 (June 22, 2018), p. 214426. ISSN: 2469-9950, 2469-9969. DOI: 10.1103/PhysRevB.97.214426.

[43] Matthias Sitte, Karin Everschor-Sitte, Thierry Valet, Davi R. Rodrigues, Jairo Sinova, and Ar. Abanov. "Current-driven periodic domain wall creation in ferromagnetic nanowires". In: *Phys. Rev. B* 94.6 (Aug. 19, 2016), p. 064422. ISSN: 2469-9950, 2469-9969. DOI: 10.1103/PhysRevB.94.064422.

[44] Simon Mendisch, Fabrizio Riente, Valentin Ahrens, Luca Gnoli, Michael Haider, Matthias Opel, Martina Kiechle, Massimo Ruo Roch, and Markus Becherer. "Controlling Domain-Wall Nucleation in Ta / Co - Fe - B / Mg O Nanomagnets via Local Ga + Ion Irradiation". In: *Phys. Rev. Applied* 16.1 (July 15, 2021), p. 014039. ISSN: 2331-7019. DOI: 10.1103/PhysRevApplied.16.014039.

[45] See-Hun Yang, Kwang-Su Ryu, and Stuart Parkin. "Domain-wall velocities of up to 750 m s-1 driven by exchange-coupling torque in synthetic antiferromagnets". In: *Nature Nanotech* 10.3 (Mar. 2015), pp. 221–226. ISSN: 1748-3387, 1748-3395. DOI: 10.1038/nnano.2014.324.

[46] Charles-Elie Fillion, Johanna Fischer, Raj Kumar, Aymen Fassatoui, Stefania Pizzini, Laurent Ranno, Djoudi Ourdani, Mohamed Belmeguenai, Yves Roussigné, Salim-Mourad Chérif, Stéphane Auffret, Isabelle Joumard, Olivier Boulle, Gilles Gaudin, Liliana Buda-Prejbeanu, Claire Baraduc, and Hélène Béa. "Gate-controlled skyrmion and domain wall chirality". In: *Nat Commun* 13.1 (Sept. 7, 2022), p. 5257. ISSN: 2041-1723. DOI: 10.1038/s41467-022-32959-w.

[47] Stuart S. P. Parkin, Masamitsu Hayashi, and Luc Thomas. "Magnetic Domain-Wall Racetrack Memory". In: *Science* 320.5873 (Apr. 11, 2008), pp. 190–194. ISSN: 0036-8075, 1095-9203. DOI: 10.1126/science.1145799.

[48] Stuart Parkin and See-Hun Yang. "Memory on the racetrack". In: *Nature Nanotech* 10.3 (Mar. 2015), pp. 195–198. ISSN: 1748-3387, 1748-3395. DOI: 10.1038/nnano.2015.41.

[49] Julie Grollier, Damien Querlioz, and Mark D. Stiles. "Spintronic Nanodevices for Bioinspired Computing". In: *Proc. IEEE* 104.10 (Oct. 2016), pp. 2024–2039. ISSN: 0018-9219, 1558-2256. DOI: 10.1109/JPROC.2016.2597152.

[50] Sabpreet Bhatti, Rachid Sbiaa, Atsufumi Hirohata, Hideo Ohno, Shunsuke Fukami, and S.N. Piramanayagam. "Spintronics based random access memory: a review". In: *Materials Today* 20.9 (Nov. 2017), pp. 530–548. ISSN: 13697021. DOI: 10.1016/j.mattod.2017.07.007.

[51] Jacob Torrejon, Mathieu Riou, Flavio Abreu Araujo, Sumito Tsunegi, Guru Khalsa, Damien Querlioz, Paolo Bortolotti, Vincent Cros, Kay Yakushiji, Akio Fukushima, Hitoshi Kubota, Shinji Yuasa, Mark D. Stiles, and Julie Grollier. "Neuromorphic computing with nanoscale spintronic oscillators". In: *Nature*

547.7664 (July 2017), pp. 428–431. ISSN: 0028-0836, 1476-4687. DOI: 10.1038/nature23011.

[52] Atsufumi Hirohata, Keisuke Yamada, Yoshinobu Nakatani, Ioan-Lucian Prejbeanu, Bernard Diény, Philipp Pirro, and Burkard Hillebrands. "Review on spintronics: Principles and device applications". In: *Journal of Magnetism and Magnetic Materials* 509 (Sept. 2020), p. 166711. ISSN: 03048853. DOI: 10.1016/j.jmmm.2020.166711.

[53] B. Dieny, I. L. Prejbeanu, K. Garello, P. Gambardella, P. Freitas, R. Lehndorff, W. Raberg, U. Ebels, S. O. Demokritov, J. Akerman, A. Deac, P. Pirro, C. Adelmann, A. Anane, A. V. Chumak, A. Hirohata, S. Mangin, Sergio O. Valenzuela, M. Cengiz Onbaşlı, M. d'Aquino, G. Prenat, G. Finocchio, L. Lopez-Diaz, R. Chantrell, O. Chubykalo-Fesenko, and P. Bortolotti. "Opportunities and challenges for spintronics in the microelectronics industry". In: *Nat Electron* 3.8 (Aug. 18, 2020), pp. 446–459. ISSN: 2520-1131. DOI: 10.1038/s41928-020-0461-5.

[54] Kyujoon Lee, Dong-Soo Han, and Mathias Kläui. "Chiral Magnetic Domain Wall and Skyrmion Memory Devices". In: *Emerging Non-volatile Memory Technologies*. Ed. by Wen Siang Lee, Gerard Joseph Lim, and Putu Andhita Dananjaya. Singapore: Springer Singapore, 2021, pp. 175–201. ISBN: 9789811569104. DOI: 10.1007/978-981-15-6912-8_5.

[55] E. Raymenants, O. Bultynck, D. Wan, T. Devolder, K. Garello, L. Souriau, A. Thiam, D. Tsvetanova, Y. Canvel, D. E. Nikonov, I. A. Young, M. Heyns, B. Soree, I. Asselberghs, I. Radu, S. Couet, and V. D. Nguyen. "Nanoscale domain wall devices with magnetic tunnel junction read and write". In: *Nat. Electron.* 4.6 (June 2021), pp. 392–398. ISSN: 2520-1131. DOI: 10.1038/s41928-021-00593-x.

[56] Tomohiro Taniguchi, Amon Ogihara, Yasuhiro Utsumi, and Sumito Tsunegi. "Spintronic reservoir computing without driving current or magnetic field". In: *Sci Rep* 12.1 (June 23, 2022), p. 10627. ISSN: 2045-2322. DOI: 10.1038/s41598-022-14738-1.

[57] Walid Al Misba, Harindra S. Mavikumbure, Md Mahadi Rajib, Daniel L. Marino, Victor Cobilean, Milos Manic, and Jayasimha Atulasimha. "Spintronic Physical Reservoir for Autonomous Prediction and Long-Term Household Energy Load Forecasting". In: *IEEE Access* 11 (2023), pp. 124725–124737. ISSN: 2169-3536. DOI: 10.1109/ACCESS.2023.3326414.

[58] Christopher H. Marrows, Joseph Barker, Thomas A. Moore, and Timothy Moorsom. "Neuromorphic computing with spintronics". In: *npj Spintronics* 2.1 (Apr. 29, 2024), p. 12. ISSN: 2948-2119. DOI: 10.1038/s44306-024-00019-2.

[59] Shahriar Mostufa, Shuang Liang, Vinit Kumar Chugh, Jian-Ping Wang, and Kai Wu. "Spintronic devices for biomedical applications". In: *npj Spintronics* 2.1 (July 2, 2024), p. 26. ISSN: 2948-2119. DOI: 10.1038/s44306-024-00031-6.

[60] Diana C. Leitao, Floris J. F. Van Riel, Mahmoud Rasly, Pedro D. R. Araujo, Maria Salvador, Elvira Paz, and Bert Koopmans. "Enhanced performance and functionality in spintronic sensors". In: *npj Spintronics* 2.1 (Nov. 6, 2024), p. 54. ISSN: 2948-2119. DOI: 10.1038/s44306-024-00058-9.

[61] Yufang Xie, Su-Yun Zhang, Yin Yin, Naihang Zheng, Anwar Ali, Muhammad Younis, Shuangchen Ruan, and Yu-Jia Zeng. "Emerging ferromagnetic materials for electrical spin injection: towards semiconductor spintronics". In: *npj Spintronics* 3.1 (Mar. 28, 2025), p. 10. ISSN: 2948-2119. DOI: 10.1038/s44306-024-00070-z.

[62] Flovik, V. "Magnetization dynamics in nanostructures." PhD thesis. Trondheim, Norway: University of Science and Technology, 2016.

[63] T. L. Gilbert. "A Lagrangian Formulation of the Gyromagnetic Equation of the Magnetization Field." In: (1955).

[64] Funkmich008. *Lösung der Landau-Lifshitz Gleichung bei konstantem effektivem Feld - Creative Commons license*. 2021.

[65] Ashcroft, N. W. and Mernin, N. D. "Solid State Physics." In: *Physik in unserer Zeit* 9.1 (1978), pp. 33–33. ISSN: 0031-9252, 1521-3943. DOI: 10.1002/piuz.19780090109.

[66] Herbert B. Callen and Theodore A. Welton. "Irreversibility and Generalized Noise". In: *Phys. Rev.* 83.1 (July 1, 1951), pp. 34–40. ISSN: 0031-899X. DOI: 10.1103/PhysRev.83.34.

[67] Levente Rózsa, Unai Atxitia, and Ulrich Nowak. "Temperature scaling of the Dzyaloshinsky-Moriya interaction in the spin wave spectrum". In: *Phys. Rev. B* 96.9 (Sept. 28, 2017), p. 094436. ISSN: 2469-9950, 2469-9969. DOI: 10.1103/PhysRevB.96.094436.

[68] R. F. L. Evans, D. Hinzke, U. Atxitia, U. Nowak, R. W. Chantrell, and O. Chubykalo-Fesenko. "Stochastic form of the Landau-Lifshitz-Bloch equation". In: *Phys. Rev. B* 85.1 (Jan. 26, 2012), p. 014433. ISSN: 1098-0121, 1550-235X. DOI: 10.1103/PhysRevB.85.014433.

[69] D. A. Garanin. "Fokker-Planck and Landau-Lifshitz-Bloch equations for classical ferromagnets". In: *Phys. Rev. B* 55.5 (Feb. 1, 1997), pp. 3050–3057. ISSN: 0163-1829, 1095-3795. DOI: 10.1103/PhysRevB.55.3050.

[70] U Atxitia, D Hinzke, and U Nowak. "Fundamentals and applications of the Landau–Lifshitz–Bloch equation". In: *J. Phys. D: Appl. Phys.* 50.3 (Jan. 25, 2017), p. 033003. ISSN: 0022-3727, 1361-6463. DOI: 10.1088/1361-6463/50/3/033003.

[71] A. A. Thiele. "Steady-State Motion of Magnetic Domains". In: *Phys. Rev. Lett.* 30.6 (Feb. 5, 1973), pp. 230–233. ISSN: 0031-9007. DOI: 10.1103/PhysRevLett.30.230.

[72] Roberto E. Troncoso and Álvaro S. Núñez. "Brownian motion of massive skyrmions in magnetic thin films". In: *Annals of Physics* 351 (Dec. 2014), pp. 850–856. ISSN: 00034916. DOI: 10.1016/j.aop.2014.10.007.

[73] Christoph Schütte, Junichi Iwasaki, Achim Rosch, and Naoto Nagaosa. "Inertia, diffusion, and dynamics of a driven skyrmion". In: *Phys. Rev. B* 90.17 (Nov. 25, 2014), p. 174434. ISSN: 1098-0121, 1550-235X. DOI: 10.1103/PhysRevB.90.174434.

[74] Felix Büttner, C. Moutafis, M. Schneider, B. Krüger, C. M. Günther, J. Geilhufe, C. v. Korff Schmising, J. Mohanty, B. Pfau, S. Schaffert, A. Bisig, M. Foerster, T. Schulz, C. A. F. Vaz, J. H. Franken, H. J. M. Swagten, M. Kläui, and S. Eisebitt. "Dynamics and inertia of skyrmionic spin structures". In: *Nature Phys* 11.3 (Mar. 2015), pp. 225–228. ISSN: 1745-2473, 1745-2481. DOI: 10.1038/nphys3234.

[75] Yoshishige Suzuki, Soma Miki, Hikaru Nomura, and Eiiti Tamura. *Mass and generalized Thiele equation of the magnetic skyrmion*. Version Number: 2. 2022. DOI: 10.48550/ARXIV.2208.01835.

[76] Xiaofan Wu and Oleg Tchernyshyov. "How a skyrmion can appear both massive and massless". In: *SciPost Phys.* 12.5 (May 12, 2022), p. 159. ISSN: 2542-4653. DOI: 10.21468/SciPostPhys.12.5.159.

[77] Supriyo Bandyopadhyay. "Perspective: There is plenty of room for magnetic straintronics in the analog domain". In: *npj Spintronics* 2.1 (June 3, 2024), p. 15. ISSN: 2948-2119. DOI: 10.1038/s44306-024-00018-3.

[78] V. D. Nguyen, S. Rao, K. Wostyn, and S. Couet. "Recent progress in spin-orbit torque magnetic random-access memory". In: *npj Spintronics* 2.1 (Oct. 1, 2024), p. 48. ISSN: 2948-2119. DOI: 10.1038/s44306-024-00044-1.

[79] F. Jonietz, S. Mühlbauer, C. Pfleiderer, A. Neubauer, W. Münzer, A. Bauer, T. Adams, R. Georgii, P. Böni, R. A. Duine, K. Everschor, M. Garst, and A. Rosch. "Spin Transfer Torques in MnSi at Ultralow Current Densities". In: *Science* 330.6011 (Dec. 17, 2010), pp. 1648–1651. ISSN: 0036-8075, 1095-9203. DOI: 10.1126/science.1195709.

[80] J. E. Hirsch. "Spin Hall Effect". In: *Phys. Rev. Lett.* 83.9 (Aug. 30, 1999), pp. 1834–1837. ISSN: 0031-9007, 1079-7114. DOI: 10.1103/PhysRevLett.83.1834.

[81] Axel Hoffmann. "Spin Hall Effects in Metals". In: *IEEE Trans. Magn.* 49.10 (Oct. 2013), pp. 5172–5193. ISSN: 0018-9464, 1941-0069. DOI: 10.1109/TMAG.2013.2262947.

[82] Jairo Sinova, Sergio O. Valenzuela, J. Wunderlich, C. H. Back, and T. Jungwirth. "Spin Hall effects". In: *Rev. Mod. Phys.* 87.4 (Oct. 27, 2015), pp. 1213–1260. ISSN: 0034-6861, 1539-0756. DOI: 10.1103/RevModPhys.87.1213.

[83] Seonghoon Woo, Kyung Mee Song, Hee-Sung Han, Min-Seung Jung, Mi-Young Im, Ki-Suk Lee, Kun Soo Song, Peter Fischer, Jung-Il Hong, Jun Woo Choi, Byoung-Chul Min, Hyun Cheol Koo, and Joonyeon Chang. "Spin-orbit torque-driven skyrmion dynamics revealed by time-resolved X-ray microscopy". In: *Nat Commun* 8.1 (May 24, 2017), p. 15573. ISSN: 2041-1723. DOI: 10.1038/ncomms15573.

[84] Shilei Ding, Andrew Ross, Dongwook Go, Lorenzo Baldrati, Zengyao Ren, Frank Freimuth, Sven Becker, Fabian Kammerbauer, Jinbo Yang, Gerhard Jakob, Yuriy Mokrousov, and Mathias Kläui. "Harnessing Orbital-to-Spin Conversion of Interfacial Orbital Currents for Efficient Spin-Orbit Torques". In: *Phys. Rev. Lett.* 125.17 (Oct. 22, 2020), p. 177201. ISSN: 0031-9007, 1079-7114. DOI: 10.1103/PhysRevLett.125.177201.

[85] Qiming Shao, Peng Li, Luqiao Liu, Hyunsoo Yang, Shunsuke Fukami, Armin Razavi, Hao Wu, Kang Wang, Frank Freimuth, Yuriy Mokrousov, Mark D. Stiles, Satoru Emori, Axel Hoffmann, Johan Akerman, Kaushik Roy, Jian-Ping Wang, See-Hun Yang, Kevin Garello, and Wei Zhang. "Roadmap of Spin–Orbit Torques". In: *IEEE Trans. Magn.* 57.7 (July 2021), pp. 1–39. ISSN: 0018-9464, 1941-0069. DOI: 10.1109/TMAG.2021.3078583.

[86] Sachin Krishnia, Yanis Sassi, Fernando Ajejas, Nicolas Sebe, Nicolas Reyren, Sophie Collin, Thibaud Denneulin, András Kovács, Rafal E. Dunin-Borkowski, Albert Fert, Jean-Marie George, Vincent Cros, and Henri Jaffrès. "Large Interfacial Rashba Interaction Generating Strong Spin–Orbit Torques in Atomically Thin Metallic Heterostructures". In: *Nano Lett.* 23.15 (Aug. 9, 2023), pp. 6785–6791. ISSN: 1530-6984, 1530-6992. DOI: 10.1021/acs.nanolett.2c05091.

[87] Everspin Technologies. *Everspin 256Mb ST-MRAM with Perpendicular MTJ Sampling*. 2016. URL: https://www.everspin.com/news/everspin-256mb-st-mram-perpendicular-mtj-sampling (visited on 04/20/2025).

[88] X.Z. Yu, N. Kanazawa, W.Z. Zhang, T. Nagai, T. Hara, K. Kimoto, Y. Matsui, Y. Onose, and Y. Tokura. "Skyrmion flow near room temperature in an ultralow current density". In: *Nat Commun* 3.1 (Aug. 7, 2012), p. 988. ISSN: 2041-1723. DOI: 10.1038/ncomms1990.

[89] Junichi Iwasaki, Wataru Koshibae, and Naoto Nagaosa. "Colossal Spin Transfer Torque Effect on Skyrmion along the Edge". In: *Nano Lett.* 14.8 (Aug. 13, 2014), pp. 4432–4437. ISSN: 1530-6984, 1530-6992. DOI: 10.1021/nl501379k.

[90] Yasuhiro Niimi and YoshiChika Otani. "Reciprocal spin Hall effects in conductors with strong spin–orbit coupling: a review". In: *Rep. Prog. Phys.* 78.12 (Dec. 1, 2015), p. 124501. ISSN: 0034-4885, 1361-6633. DOI: 10.1088/0034-4885/78/12/124501.

[91] M. D'yakonov and V. I. Perel. "Possibility of Orienting Electron Spins with Current." In: 13 (1971).

[92] Unknown. *Current Projects - SOT*. https://www.klaeui-lab.physik.uni-mainz.de. 2020. URL: https://www.klaeui-lab.physik.uni-mainz.de/spin-orbit-torques-in-various-multilayers/ (visited on 04/20/2025).

[93] Jungbum Yoon, Seo-Won Lee, Jae Hyun Kwon, Jong Min Lee, Jaesung Son, Xuepeng Qiu, Kyung-Jin Lee, and Hyunsoo Yang. "Anomalous spin-orbit torque switching due to field-like torque–assisted domain wall reflection". In: *Sci. Adv.* 3.4 (Apr. 7, 2017), e1603099. ISSN: 2375-2548. DOI: 10.1126/sciadv.1603099.

[94] Wanjun Jiang, Pramey Upadhyaya, Wei Zhang, Guoqiang Yu, M. Benjamin Jungfleisch, Frank Y. Fradin, John E. Pearson, Yaroslav Tserkovnyak, Kang L. Wang, Olle Heinonen, Suzanne G. E. te Velthuis, and Axel Hoffmann. "Blowing magnetic skyrmion bubbles". In: *Science* 349.6245 (July 17, 2015), pp. 283–286. ISSN: 0036-8075, 1095-9203. DOI: 10.1126/science.aaa1442.

[95] Seonghoon Woo, Kai Litzius, Benjamin Krüger, Mi-Young Im, Lucas Caretta, Kornel Richter, Maxwell Mann, Andrea Krone, Robert M. Reeve, Markus

Weigand, Parnika Agrawal, Ivan Lemesh, Mohamad-Assaad Mawass, Peter Fischer, Mathias Kläui, and Geoffrey S. D. Beach. "Observation of room-temperature magnetic skyrmions and their current-driven dynamics in ultrathin metallic ferromagnets". In: *Nat. Mater.* 15.5 (May 2016), pp. 501–506. ISSN: 1476-1122, 1476-4660. DOI: 10.1038/nmat4593.

[96] A. Hrabec, J. Sampaio, M. Belmeguenai, I. Gross, R. Weil, S. M. Chérif, A. Stashkevich, V. Jacques, A. Thiaville, and S. Rohart. "Current-induced skyrmion generation and dynamics in symmetric bilayers". In: *Nat Commun* 8.1 (June 8, 2017), p. 15765. ISSN: 2041-1723. DOI: 10.1038/ncomms15765.

[97] Kai Litzius, Ivan Lemesh, Benjamin Krüger, Pedram Bassirian, Lucas Caretta, Kornel Richter, Felix Büttner, Koji Sato, Oleg A. Tretiakov, Johannes Förster, Robert M. Reeve, Markus Weigand, Iuliia Bykova, Hermann Stoll, Gisela Schütz, Geoffrey S. D. Beach, and Mathias Kläui. "Skyrmion Hall effect revealed by direct time-resolved X-ray microscopy". In: *Nat. Phys.* 13.2 (Feb. 2017), pp. 170–175. ISSN: 1745-2473, 1745-2481. DOI: 10.1038/nphys4000.

[98] Kai Litzius, Jonathan Leliaert, Pedram Bassirian, Davi Rodrigues, Sascha Kromin, Ivan Lemesh, Jakub Zazvorka, Kyu-Joon Lee, Jeroen Mulkers, Nico Kerber, Daniel Heinze, Niklas Keil, Robert M. Reeve, Markus Weigand, Bartel Van Waeyenberge, Gisela Schütz, Karin Everschor-Sitte, Geoffrey S. D. Beach, and Mathias Kläui. "The role of temperature and drive current in skyrmion dynamics". In: *Nat. Electron.* 3.1 (Jan. 2020), pp. 30–36. ISSN: 2520-1131. DOI: 10.1038/s41928-019-0359-2.

[99] Klaus Raab, Maarten A. Brems, Grischa Beneke, Takaaki Dohi, Jan Rothörl, Fabian Kammerbauer, Johan H. Mentink, and Mathias Kläui. "Brownian reservoir computing realized using geometrically confined skyrmion dynamics". In: *Nat Commun* 13.1 (Nov. 15, 2022), p. 6982. ISSN: 2041-1723. DOI: 10.1038/s41467-022-34309-2.

[100] Leandro Salemi and Peter M. Oppeneer. "First-principles theory of intrinsic spin and orbital Hall and Nernst effects in metallic monoatomic crystals". In: *Phys. Rev. Materials* 6.9 (Sept. 6, 2022), p. 095001. ISSN: 2475-9953. DOI: 10.1103/PhysRevMaterials.6.095001.

[101] Shilei Ding, Zhongyu Liang, Dongwook Go, Chao Yun, Mingzhu Xue, Zhou Liu, Sven Becker, Wenyun Yang, Honglin Du, Changsheng Wang, Yingchang Yang, Gerhard Jakob, Mathias Kläui, Yuriy Mokrousov, and Jinbo Yang. "Observation of the Orbital Rashba-Edelstein Magnetoresistance". In: *Phys. Rev. Lett.* 128.6 (Feb. 10, 2022), p. 067201. ISSN: 0031-9007, 1079-7114. DOI: 10.1103/PhysRevLett.128.067201.

[102] Arnab Bose, Fabian Kammerbauer, Rahul Gupta, Dongwook Go, Yuriy Mokrousov, Gerhard Jakob, and Mathias Kläui. "Detection of long-range orbital-Hall torques". In: *Phys. Rev. B* 107.13 (Apr. 19, 2023), p. 134423. ISSN: 2469-9950, 2469-9969. DOI: 10.1103/PhysRevB.107.134423.

[103] T.H.R. Skyrme. "A unified field theory of mesons and baryons". In: *Nuclear Physics* 31 (Mar. 1962), pp. 556–569. ISSN: 00295582. DOI: 10.1016/0029-5582(62)90775-7.

[104] S. Mühlbauer, B. Binz, F. Jonietz, C. Pfleiderer, A. Rosch, A. Neubauer, R. Georgii, and P. Böni. "Skyrmion Lattice in a Chiral Magnet". In: *Science* 323.5916 (Feb. 13, 2009), pp. 915–919. ISSN: 0036-8075, 1095-9203. DOI: 10.1126/science.1166767.

[105] Stefan Heinze, Kirsten Von Bergmann, Matthias Menzel, Jens Brede, André Kubetzka, Roland Wiesendanger, Gustav Bihlmayer, and Stefan Blügel. "Spontaneous atomic-scale magnetic skyrmion lattice in two dimensions". In: *Nature Phys* 7.9 (Sept. 2011), pp. 713–718. ISSN: 1745-2473, 1745-2481. DOI: 10.1038/nphys2045.

[106] A. Bogdanov and A. Hubert. "Thermodynamically stable magnetic vortex states in magnetic crystals". In: *Journal of Magnetism and Magnetic Materials* 138.3 (Dec. 1994), pp. 255–269. ISSN: 03048853. DOI: 10.1016/0304-8853(94)90046-9.

[107] Wanjun Jiang, Gong Chen, Kai Liu, Jiadong Zang, Suzanne G.E. te Velthuis, and Axel Hoffmann. "Skyrmions in magnetic multilayers". In: *Phys. Rep.* 704 (Aug. 2017), pp. 1–49. ISSN: 03701573. DOI: 10.1016/j.physrep.2017.08.001.

[108] K. Everschor-Sitte, J. Masell, R. M. Reeve, and M. Kläui. "Perspective: Magnetic skyrmions—Overview of recent progress in an active research field". In: *J. Appl. Phys* 124.24 (Dec. 28, 2018), p. 240901. ISSN: 0021-8979, 1089-7550. DOI: 10.1063/1.5048972.

[109] Soong-Geun Je, Hee-Sung Han, Se Kwon Kim, Sergio A. Montoya, Weilun Chao, Ik-Sun Hong, Eric E. Fullerton, Ki-Suk Lee, Kyung-Jin Lee, Mi-Young Im, and Jung-Il Hong. "Direct Demonstration of Topological Stability of Magnetic Skyrmions via Topology Manipulation". In: *ACS Nano* 14.3 (Mar. 24, 2020). Publisher: American Chemical Society, pp. 3251–3258. ISSN: 1936-0851. DOI: 10.1021/acsnano.9b08699.

[110] Jakub Zázvorka, Florian Jakobs, Daniel Heinze, Niklas Keil, Sascha Kromin, Samridh Jaiswal, Kai Litzius, Gerhard Jakob, Peter Virnau, Daniele Pinna, Karin Everschor-Sitte, Levente Rózsa, Andreas Donges, Ulrich Nowak, and Mathias Kläui. "Thermal skyrmion diffusion used in a reshuffler device". In: *Nat. Nanotechnol.* 14.7 (July 2019). Bandiera_abtest: a Cg_type: Nature Research Journals Number: 7 Primary_atype: Research Publisher: Nature Publishing Group Subject_term: Magnetic properties and materials;Spintronics Subject_term_id: magnetic-properties-and-materials;spintronics, pp. 658–661. ISSN: 1748-3395. DOI: 10.1038/s41565-019-0436-8.

[111] Kyung Mee Song, Jae-Seung Jeong, Biao Pan, Xichao Zhang, Jing Xia, Sunkyung Cha, Tae-Eon Park, Kwangsu Kim, Simone Finizio, Jörg Raabe, Joonyeon Chang, Yan Zhou, Weisheng Zhao, Wang Kang, Hyunsu Ju, and Seonghoon Woo. "Skyrmion-based artificial synapses for neuromorphic computing". In: *Nat. Electron.* 3.3 (Mar. 2020), pp. 148–155. ISSN: 2520-1131. DOI: 10.1038/s41928-020-0385-0.

[112] Tristan da Câmara Santa Clara Gomes, Yanis Sassi, Dédalo Sanz-Hernández, Sachin Krishnia, Sophie Collin, Marie-Blandine Martin, Pierre Seneor, Vincent Cros, Julie Grollier, and Nicolas Reyren. "Neuromorphic weighted sum with magnetic skyrmions". In: (2023). Publisher: arXiv Version Number: 1. DOI: 10.48550/ARXIV.2310.16909.

[113] Oscar Lee, Robin Msiska, Maarten A. Brems, Mathias Kläui, Hidekazu Kurebayashi, and Karin Everschor-Sitte. "Perspective on unconventional computing using magnetic skyrmions". In: *Applied Physics Letters* 122.26 (June 26, 2023), p. 260501. ISSN: 0003-6951, 1077-3118. DOI: 10.1063/5.0148469.

[114] Steffen Krusch. "Homotopy of rational maps and the quantization of Skyrmions". In: *Annals of Physics* 304.2 (Apr. 2003), pp. 103–127. ISSN: 00034916. DOI: 10.1016/S0003-4916(03)00014-9.

[115] Birhanu Abera Kolech. "Magnetic Skyrmions and Quasi Particles: A Review on Principles and Applications". In: *Vortex Simulation and Identification*. IntechOpen, Mar. 6, 2023. DOI: 10.5772/intechopen.110448.

[116] Motohiko Ezawa. "Giant Skyrmions Stabilized by Dipole-Dipole Interactions in Thin Ferromagnetic Films". In: *Phys. Rev. Lett.* 105.19 (Nov. 2, 2010), p. 197202. ISSN: 0031-9007, 1079-7114. DOI: 10.1103/PhysRevLett.105.197202.

[117] Mariam Hassan, Sabri Koraltan, Aladin Ullrich, Florian Bruckner, Rostyslav O. Serha, Khrystyna V. Levchenko, Gaspare Varvaro, Nikolai S. Kiselev, Michael Heigl, Claas Abert, Dieter Suess, and Manfred Albrecht. "Dipolar skyrmions and antiskyrmions of arbitrary topological charge at room temperature". In: *Nat. Phys.* 20.4 (Apr. 2024), pp. 615–622. ISSN: 1745-2473, 1745-2481. DOI: 10.1038/s41567-023-02358-z.

[118] Naoto Nagaosa and Yoshinori Tokura. "Topological properties and dynamics of magnetic skyrmions". In: *Nat. Nanotechnol.* 8.12 (Dec. 2013), pp. 899–911. ISSN: 1748-3387, 1748-3395. DOI: 10.1038/nnano.2013.243.

[119] Sheng Li, Xuewen Wang, and Theo Rasing. "Magnetic skyrmions: Basic properties and potential applications". In: *Interdisciplinary Materials* 2.2 (Mar. 2023), pp. 260–289. ISSN: 2767-4401, 2767-441X. DOI: 10.1002/idm2.12072.

[120] Filipp N. Rybakov, Olle Eriksson, and Nikolai S. Kiselev. "Topological invariants of vortices, merons, skyrmions, and their combinations in continuous and discrete systems". In: *Phys. Rev. B* 111.13 (Apr. 11, 2025), p. 134417. ISSN: 2469-9950, 2469-9969. DOI: 10.1103/PhysRevB.111.134417.

[121] Masahito Mochizuki. "Microwave-Driven Dynamics of Magnetic Skyrmions Under a Tilted Magnetic Field: Magnetic Resonances, Translational Motions, and Spin-Motive Forces". In: *Chirality, Magnetism and Magnetoelectricity*. Ed. by Eugene Kamenetskii. Vol. 138. Series Title: Topics in Applied Physics. Cham: Springer International Publishing, 2021, pp. 183–206. ISBN: 978-3-030-62843-7. DOI: 10.1007/978-3-030-62844-4_8.

[122] Yoshinori Tokura and Naoya Kanazawa. "Magnetic Skyrmion Materials". In: *Chem. Rev.* 121.5 (Mar. 10, 2021), pp. 2857–2897. ISSN: 0009-2665, 1520-6890. DOI: 10.1021/acs.chemrev.0c00297.

[123] Roland Wiesendanger. "Nanoscale magnetic skyrmions in metallic films and multilayers: a new twist for spintronics". In: *Nat. Rev. Mater.* 1.7 (July 2016), p. 16044. ISSN: 2058-8437. DOI: 10.1038/natrevmats.2016.44.

[124] Giovanni Finocchio, Felix Büttner, Riccardo Tomasello, Mario Carpentieri, and Mathias Kläui. "Magnetic skyrmions: from fundamental to applications". In: *J. Phys. D: Appl. Phys.* 49.42 (Oct. 26, 2016), p. 423001. ISSN: 0022-3727, 1361-6463. DOI: 10.1088/0022-3727/49/42/423001.

[125] Takaaki Dohi, Robert M. Reeve, and Mathias Kläui. "Thin Film Skyrmionics". In: *Annu. Rev. Condens. Matter Phys.* 13.1 (Mar. 10, 2022), pp. 73–95. ISSN: 1947-5454, 1947-5462. DOI: https://doi.org/10.1146/annurev-conmatphys-031620-110344.

[126] S. Rohart and A. Thiaville. "Skyrmion confinement in ultrathin film nanostructures in the presence of Dzyaloshinskii-Moriya interaction". In: *Phys. Rev. B* 88.18 (Nov. 20, 2013), p. 184422. ISSN: 1098-0121, 1550-235X. DOI: 10.1103/PhysRevB.88.184422.

[127] X. S. Wang, H. Y. Yuan, and X. R. Wang. "A theory on skyrmion size". In: *Commun Phys* 1.1 (July 4, 2018), p. 31. ISSN: 2399-3650. DOI: 10.1038/s42005-018-0029-0.

[128] Niklas Romming, André Kubetzka, Christian Hanneken, Kirsten Von Bergmann, and Roland Wiesendanger. "Field-Dependent Size and Shape of Single Magnetic Skyrmions". In: *Phys. Rev. Lett.* 114.17 (May 1, 2015), p. 177203. ISSN: 0031-9007, 1079-7114. DOI: 10.1103/PhysRevLett.114.177203.

[129] Raphael Gruber, Maarten A. Brems, Jan Rothörl, Tobias Sparmann, Maurice Schmitt, Iryna Kononenko, Fabian Kammerbauer, Maria-Andromachi Syskaki, Oded Farago, Peter Virnau, and Mathias Kläui. "300-Times-Increased Diffusive Skyrmion Dynamics and Effective Pinning Reduction by Periodic Field Excitation". In: *Adv. Mater.* 35.17 (Apr. 2023), p. 2208922. ISSN: 0935-9648, 1521-4095. DOI: 10.1002/adma.202208922.

[130] Sebastian Meyer, Marco Perini, Stephan Von Malottki, André Kubetzka, Roland Wiesendanger, Kirsten Von Bergmann, and Stefan Heinze. "Isolated zero field sub-10 nm skyrmions in ultrathin Co films". In: *Nat Commun* 10.1 (Aug. 23, 2019), p. 3823. ISSN: 2041-1723. DOI: 10.1038/s41467-019-11831-4.

[131] Xiuzhen Yu, Fumitaka Kagawa, Shinichiro Seki, Masashi Kubota, Jan Masell, Fehmi S. Yasin, Kiyomi Nakajima, Masao Nakamura, Masashi Kawasaki, Naoto Nagaosa, and Yoshinori Tokura. "Real-space observations of 60-nm skyrmion dynamics in an insulating magnet under low heat flow". In: *Nat Commun* 12.1 (Aug. 23, 2021), p. 5079. ISSN: 2041-1723. DOI: 10.1038/s41467-021-25291-2.

[132] Jiahao Liu, Zidong Wang, Teng Xu, Hengan Zhou, Le Zhao, Soong-Guen Je, Mi-Young Im, Liang Fang, and Wanjun Jiang. "The 20-nm Skyrmion Generated at Room Temperature by Spin-Orbit Torques". In: *Chinese Phys. Lett.* 39.1 (Jan. 1, 2022), p. 017501. ISSN: 0256-307X, 1741-3540. DOI: 10.1088/0256-307X/39/1/017501.

[133] Dongsheng Song, Weiwei Wang, Shuisen Zhang, Yizhou Liu, Ning Wang, Fengshan Zheng, Mingliang Tian, Rafal E. Dunin-Borkowski, Jiadong Zang, and Haifeng Du. "Steady motion of 80-nm-size skyrmions in a 100-nm-wide track". In: *Nat Commun* 15.1 (July 4, 2024), p. 5614. ISSN: 2041-1723. DOI: 10.1038/s41467-024-49976-6.

[134] Andrei B. Bogatyrëv and Konstantin L. Metlov. "What makes magnetic skyrmions different from magnetic bubbles?" In: *Journal of Magnetism and Magnetic Materials* 465 (Nov. 2018), pp. 743–746. ISSN: 03048853. DOI: 10.1016/j.jmmm.2018.06.058.

[135] Ellen Lu, Alexandra R. Stuart, Artek R. Chalifour, Jonathon C. Davidson, Paul S. Keatley, Kristen S. Buchanan, and Karen L. Livesey. "Analytic theory for Néel skyrmion size, accounting for finite film thickness". In: *Journal of Magnetism and Magnetic Materials* 584 (Oct. 2023), p. 171044. ISSN: 03048853. DOI: 10.1016/j.jmmm.2023.171044.

[136] Christian Denker, Sören Nielsen, Enno Lage, Malte Römer-Stumm, Hauke Heyen, Yannik Junk, Jakob Walowski, Konrad Waldorf, Markus Münzenberg, and Jeffrey McCord. "Size and density control of skyrmions with picometer CoFeB thickness variations—observation of zero-field skyrmions and skyrmion merging". In: *J. Phys. D: Appl. Phys.* 56.49 (Dec. 7, 2023), p. 495302. ISSN: 0022-3727, 1361-6463. DOI: 10.1088/1361-6463/acf6cd.

[137] Wang Kang, Yangqi Huang, Chentian Zheng, Weifeng Lv, Na Lei, Youguang Zhang, Xichao Zhang, Yan Zhou, and Weisheng Zhao. "Voltage Controlled Magnetic Skyrmion Motion for Racetrack Memory". In: *Sci Rep* 6.1 (Mar. 15, 2016), p. 23164. ISSN: 2045-2322. DOI: 10.1038/srep23164.

[138] Yi-fu Chen, Zhi-xiong Li, Zhen-wei Zhou, Qing-lin Xia, Yao-zhuang Nie, and Guang-hua Guo. "Nonlinear gyrotropic motion of skyrmion in a magnetic nanodisk". In: *Journal of Magnetism and Magnetic Materials* 458 (July 2018), pp. 123–128. ISSN: 03048853. DOI: 10.1016/j.jmmm.2018.03.016.

[139] R. Tomasello, K. Y. Guslienko, M. Ricci, A. Giordano, J. Barker, M. Carpentieri, O. Chubykalo-Fesenko, and G. Finocchio. "Origin of temperature and field dependence of magnetic skyrmion size in ultrathin nanodots". In: *Phys. Rev. B* 97.6 (Feb. 9, 2018), p. 060402. ISSN: 2469-9950, 2469-9969. DOI: 10.1103/PhysRevB.97.060402.

[140] Xiuzhen Yu, Fumitaka Kagawa, Shinichiro Seki, Masashi Kubota, Jan Masell, Fehmi S. Yasin, Kiyomi Nakajima, Masao Nakamura, Masashi Kawasaki, Naoto Nagaosa, and Yoshinori Tokura. "Real-space observations of 60-nm skyrmion dynamics in an insulating magnet under low heat flow". In: *Nat Commun* 12.1 (Aug. 23, 2021), p. 5079. ISSN: 2041-1723. DOI: 10.1038/s41467-021-25291-2.

[141] Yiming Sun, Tao Lin, Na Lei, Xing Chen, Wang Kang, Zhiyuan Zhao, Dahai Wei, Chao Chen, Simin Pang, Linglong Hu, Liu Yang, Enxuan Dong, Li Zhao, Lei Liu, Zhe Yuan, Aladin Ullrich, Christian H. Back, Jun Zhang, Dong Pan, Jianhua Zhao, Ming Feng, Albert Fert, and Weisheng Zhao. "Experimental demonstration of a skyrmion-enhanced strain-mediated physical reservoir computing system". In: *Nat Commun* 14.1 (June 10, 2023), p. 3434. ISSN: 2041-1723. DOI: 10.1038/s41467-023-39207-9.

[142] Kayla Fallon, Sean Hughes, Katharina Zeissler, William Legrand, Fernando Ajejas, Davide Maccariello, Samuel McFadzean, William Smith, Damien McGrouther, Sophie Collin, Nicolas Reyren, Vincent Cros, Christopher H. Marrows, and Stephen McVitie. "Controlled Individual Skyrmion Nucleation at Artificial Defects Formed by Ion Irradiation". In: 16.13 (Apr. 2020), p. 1907450. ISSN: 1613-6810, 1613-6829. DOI: 10.1002/smll.201907450.

[143] J C Bellizotti Souza, N P Vizarim, C J O Reichhardt, C Reichhardt, and P A Venegas. "Spontaneous skyrmion conformal lattice and transverse motion during dc and ac compression". In: *New J. Phys.* 25.5 (May 1, 2023), p. 053020. ISSN: 1367-2630. DOI: 10.1088/1367-2630/acd46f.

[144] Hamza Belrhazi and Mohamed El Hafidi. "Skyrmion size-tuning in two-dimensional antiferromagnetic monolayers by applying local spin-polarized current-induced spin-transfer torque". In: *Journal of Physics and Chemistry of Solids* 180 (Sept. 2023), p. 111458. ISSN: 00223697. DOI: 10.1016/j.jpcs.2023.111458.

[145] Rhodri Mansell, Joonatan Huhtasalo, Maria Ameziane, and Sebastiaan Van Dijken. "Skyrmion size and density in lattices". In: *Journal of Applied Physics* 134.24 (Dec. 28, 2023), p. 243901. ISSN: 0021-8979, 1089-7550. DOI: 10.1063/5.0181599.

[146] Brown, Robert. "A brief account of microscopical observations made in the months of June, July and August, 1827, on the particles contained in the pollen of plants; and on the general existence of active molecules in organic and inorganic bodies." In: *Philosophical Magazine* 4 (1828), pp. 161–173.

[147] Adolf Fick. "Ueber Diffusion". In: *Annalen der Physik* 170.1 (Jan. 1855), pp. 59–86. ISSN: 0003-3804, 1521-3889. DOI: 10.1002/andp.18551700105.

[148] A. Einstein. "Über die von der molekularkinetischen Theorie der Wärme geforderte Bewegung von in ruhenden Flüssigkeiten suspendierten Teilchen". In: *Ann. Phys.* 322.8 (1905), pp. 549–560. ISSN: 00033804, 15213889. DOI: 10.1002/andp.19053220806.

[149] Jkrieger. *Mean squared displacement of anomalous and normal diffusion*. Wikipedia - The Free Encyclopedia. 2012. URL: https://commons.wikimedia.org/wiki/File:Msd_anomalous_diffusion.svg (visited on 04/20/2025).

[150] Maarten A. Brems, Klaus Raab, Peter Virnau, and Mathias Kläui. "Brownscher Reservoir-Computer mit Skyrmionen". In: *Physik in unserer Zeit* 54.2 (2023). _eprint: https://onlinelibrary.wiley.com/doi/pdf/10.1002/piuz.202370205, pp. 60–61. ISSN: 1521-3943. DOI: 10.1002/piuz.202370205.

[151] Robin Msiska, Jake Love, Jeroen Mulkers, Jonathan Leliaert, and Karin Everschor-Sitte. "Audio Classification with Skyrmion Reservoirs". In: *Advanced Intelligent Systems* 5.6 (June 2023), p. 2200388. ISSN: 2640-4567, 2640-4567. DOI: 10.1002/aisy.202200388.

[152] Grischa Beneke, Thomas Brian Winkler, Klaus Raab, Maarten A. Brems, Fabian Kammerbauer, Pascal Gerhards, Klaus Knobloch, Sachin Krishnia, Johan H. Mentink, and Mathias Kläui. "Gesture recognition with Brownian reservoir computing using geometrically confined skyrmion dynamics". In: *Nat Commun* 15.1 (Sept. 16, 2024), p. 8103. ISSN: 2041-1723. DOI: 10.1038/s41467-024-52345-y.

[153] Takaaki Dohi, Markus Weißenhofer, Nico Kerber, Fabian Kammerbauer, Yuqing Ge, Klaus Raab, Jakub Zázvorka, Maria-Andromachi Syskaki, Aga Shahee, Moritz Ruhwedel, Tobias Böttcher, Philipp Pirro, Gerhard Jakob, Ulrich Nowak, and Mathias Kläui. "Enhanced thermally-activated skyrmion diffusion with tunable effective gyrotropic force". In: *Nat Commun* 14.1 (Sept. 11, 2023), p. 5424. ISSN: 2041-1723. DOI: 10.1038/s41467-023-40720-0.

[154] Nico Kerber, Markus Weißenhofer, Klaus Raab, Kai Litzius, Jakub Zázvorka, Ulrich Nowak, and Mathias Kläui. "Anisotropic Skyrmion Diffusion Controlled by Magnetic-Field-Induced Symmetry Breaking". In: *Phys. Rev. Appl.* 15.4 (Apr. 20, 2021), p. 044029. ISSN: 2331-7019. DOI: 10.1103/PhysRevApplied.15.044029.

[155] S. Miki, K. Hashimoto, J. Cho, J. Jung, C. Y. You, R. Ishikawa, E. Tamura, H. Nomura, M. Goto, and Y. Suzuki. "Spatial control of skyrmion stabilization energy by low-energy Ga+ ion implantation". In: *Applied Physics Letters* 122.20 (May 15, 2023), p. 202401. ISSN: 0003-6951, 1077-3118. DOI: 10.1063/5.0153768.

[156] D. Toscano, S.A. Leonel, P.Z. Coura, and F. Sato. "Building traps for skyrmions by the incorporation of magnetic defects into nanomagnets: Pinning and scattering traps by magnetic properties engineering". In: *Journal of Magnetism and Magnetic Materials* 480 (June 2019), pp. 171–185. ISSN: 03048853. DOI: 10.1016/j.jmmm.2019.02.075.

[157] Raphael Gruber, Jakub Zázvorka, Maarten A. Brems, Davi R. Rodrigues, Takaaki Dohi, Nico Kerber, Boris Seng, Mehran Vafaee, Karin Everschor-Sitte, Peter Virnau, and Mathias Kläui. "Skyrmion pinning energetics in thin film systems". In: *Nat. Commun.* 13.1 (Dec. 2022), p. 3144. ISSN: 2041-1723. DOI: 10.1038/s41467-022-30743-4.

[158] Domenico Giuliano, Luca Gnoli, Valentin Ahrens, Massimo Ruo Roch, Markus Becherer, Giovanna Turvani, Marco Vacca, and Fabrizio Riente. "Ga^+ Ion Irradiation-Induced Tuning of Artificial Pinning Sites to Control Domain Wall Motion". In: *ACS Appl. Electron. Mater.* 5.2 (Feb. 28, 2023), pp. 985–993. ISSN: 2637-6113, 2637-6113. DOI: 10.1021/acsaelm.2c01510.

[159] Hiu Tung Fook, Wei Liang Gan, and Wen Siang Lew. "Gateable Skyrmion Transport via Field-induced Potential Barrier Modulation". In: *Sci Rep* 6.1 (Feb. 17, 2016), p. 21099. ISSN: 2045-2322. DOI: 10.1038/srep21099.

[160] Felix Büttner, C. Moutafis, A. Bisig, P. Wohlhüter, C. M. Günther, J. Mohanty, J. Geilhufe, M. Schneider, C. V. Korff Schmising, S. Schaffert, B. Pfau, M. Hantschmann, M. Riemeier, M. Emmel, S. Finizio, G. Jakob, M. Weigand, J. Rhensius, J. H. Franken, R. Lavrijsen, H. J. M. Swagten, H. Stoll, S. Eisebitt, and M. Kläui. "Magnetic states in low-pinning high-anisotropy material nanostructures suitable for dynamic imaging". In: *Phys. Rev. B* 87.13 (Apr. 26, 2013), p. 134422. ISSN: 1098-0121, 1550-235X. DOI: 10.1103/PhysRevB.87.134422.

[161] Niklas Romming, Christian Hanneken, Matthias Menzel, Jessica E. Bickel, Boris Wolter, Kirsten Von Bergmann, André Kubetzka, and Roland Wiesendanger. "Writing and Deleting Single Magnetic Skyrmions". In: *Science* 341.6146 (Aug. 9, 2013), pp. 636–639. ISSN: 0036-8075, 1095-9203. DOI: 10.1126/science.1240573.

[162] Le Zhao, Chensong Hua, Chengkun Song, Weichao Yu, and Wanjun Jiang. "Realization of skyrmion shift register". In: *Science Bulletin* 69.15 (Aug. 2024), pp. 2370–2378. ISSN: 20959273. DOI: 10.1016/j.scib.2024.05.035.

[163] Xichao Zhang, G. P. Zhao, Hans Fangohr, J. Ping Liu, W. X. Xia, J. Xia, and F. J. Morvan. "Skyrmion-skyrmion and skyrmion-edge repulsions in skyrmion-based racetrack memory". In: *Sci Rep* 5.1 (Jan. 6, 2015), p. 7643. ISSN: 2045-2322. DOI: 10.1038/srep07643.

[164] A. O. Leonov and M. Mostovoy. "Edge states and skyrmion dynamics in nanostripes of frustrated magnets". In: *Nat Commun* 8.1 (Feb. 27, 2017), p. 14394. ISSN: 2041-1723. DOI: 10.1038/ncomms14394.

[165] J C Bellizotti Souza, N P Vizarim, C J O Reichhardt, C Reichhardt, and P A Venegas. "Magnus induced diode effect for skyrmions in channels with periodic potentials". In: *J. Phys.: Condens. Matter* 35.1 (Nov. 7, 2022), p. 015804. ISSN: 0953-8984, 1361-648X. DOI: 10.1088/1361-648X/ac9cc5.

[166] F S Rocha, J C Bellizotti Souza, N P Vizarim, C J O Reichhardt, C Reichhardt, and P A Venegas. "Skyrmion transport and annihilation in funnel geometries". In: *J. Phys.: Condens. Matter* 36.11 (Mar. 20, 2024), p. 115801. ISSN: 0953-8984, 1361-648X. DOI: 10.1088/1361-648X/ad1218.

[167] Y. C. Wu, W. Kim, S. Couet, K. Garello, S. Rao, S. Van Beek, S. Kundu, S. Houshmand Sharifi, D. Crotti, J. Van Houdt, G. Groeseneken, and G. S. Kar. "Study of precessional switching speed control in voltage-controlled perpendicular magnetic tunnel junction". In: *AIP Advances* 10.3 (Mar. 1, 2020), p. 035123. ISSN: 2158-3226. DOI: 10.1063/5.0002253.

[168] Tatsuya Yamamoto, Takayuki Nozaki, Kay Yakushiji, Shingo Tamaru, Hitoshi Kubota, Akio Fukushima, and Shinji Yuasa. "Perpendicular magnetic anisotropy and its voltage control in MgO/CoFeB/MgO junctions with atomically thin Ta adhesion layers". In: *Acta Materialia* 216 (Sept. 2021), p. 117097. ISSN: 13596454. DOI: 10.1016/j.actamat.2021.117097.

[169] Lisa-Marie Kern, Bastian Pfau, Victor Deinhart, Michael Schneider, Christopher Klose, Kathinka Gerlinger, Steffen Wittrock, Dieter Engel, Ingo Will, Christian M. Günther, Rein Liefferink, Johan H. Mentink, Sebastian Wintz, Markus Weigand, Meng-Jie Huang, Riccardo Battistelli, Daniel Metternich, Felix Büttner, Katja Höflich, and Stefan Eisebitt. "Deterministic Generation and Guided Motion of Magnetic Skyrmions by Focused He^+ -Ion Irradiation". In: *Nano Lett.* 22.10 (May 25, 2022), pp. 4028–4035. ISSN: 1530-6984, 1530-6992. DOI: 10.1021/acs.nanolett.2c00670.

[170] Elizabeth M. Jefremovas, Kilian Leutner, Miriam G. Fischer, Jorge Marqués-Marchán, Thomas B. Winkler, Agustina Asenjo, Jairo Sinova, Robert Frömter, and Mathias Kläui. "The role of magnetic dipolar interactions in skyrmion lattices". In: *Newton* 1.2 (Apr. 2025), p. 100036. ISSN: 29506360. DOI: 10.1016/j.newton.2025.100036.

[171] Kai Wu, Sheng Yang, Yuelei Zhao, Xue Liang, Xiangjun Xing, and Yan Zhou. "Tunable skyrmion–edge interaction in magnetic multilayers by interlayer exchange coupling". In: *AIP Advances* 12.5 (May 1, 2022), p. 055210. ISSN: 2158-3226. DOI: 10.1063/5.0084546.

[172] Chengkun Song, Nico Kerber, Jan Rothörl, Yuqing Ge, Klaus Raab, Boris Seng, Maarten A. Brems, Florian Dittrich, Robert M. Reeve, Jianbo Wang, Qingfang Liu, Peter Virnau, and Mathias Kläui. "Commensurability between Element Symmetry and the Number of Skyrmions Governing Skyrmion Diffusion in Confined Geometries". In: *Adv. Funct. Mater.* 31.19 (May 2021), p. 2010739. ISSN: 1616-301X, 1616-3028. DOI: 10.1002/adfm.202010739.

[173] Yuqing Ge, Jan Rothörl, Maarten A. Brems, Nico Kerber, Raphael Gruber, Takaaki Dohi, Mathias Kläui, and Peter Virnau. "Constructing coarse-grained skyrmion potentials from experimental data with Iterative Boltzmann Inversion". In: *Commun Phys* 6.1 (Feb. 3, 2023), p. 30. ISSN: 2399-3650. DOI: 10.1038/s42005-023-01145-9.

[174] Thomas Brian Winkler, Jan Rothörl, Maarten A. Brems, Grischa Beneke, Hans Fangohr, and Mathias Kläui. "Coarse-graining collective skyrmion dynamics in confined geometries". In: *Applied Physics Letters* 124.2 (Jan. 8, 2024), p. 022403. ISSN: 0003-6951, 1077-3118. DOI: 10.1063/5.0187446.

[175] Jakub Zázvorka, Florian Dittrich, Yuqing Ge, Nico Kerber, Klaus Raab, Thomas Winkler, Kai Litzius, Martin Veis, Peter Virnau, and Mathias Kläui. "Skyrmion Lattice Phases in Thin Film Multilayer". In: *Adv. Funct. Mater.* 30.46 (Nov. 2020), p. 2004037. ISSN: 1616-301X, 1616-3028. DOI: 10.1002/adfm.202004037.

[176] Sebastian C. Kapfer and Werner Krauth. "Two-Dimensional Melting: From Liquid-Hexatic Coexistence to Continuous Transitions". In: *Phys. Rev. Lett.* 114.3 (Jan. 22, 2015), p. 035702. ISSN: 0031-9007, 1079-7114. DOI: 10.1103/PhysRevLett.114.035702.

[177] A. Jaster. "The hexatic phase of the two-dimensional hard disk system". In: *Physics Letters A* 330.1 (Sept. 2004), pp. 120–125. ISSN: 03759601. DOI: 10.1016/j.physleta.2004.07.055.

[178] X. Z. Yu, Y. Onose, N. Kanazawa, J. H. Park, J. H. Han, Y. Matsui, N. Nagaosa, and Y. Tokura. "Real-space observation of a two-dimensional skyrmion crystal". In: *Nature* 465.7300 (June 2010), pp. 901–904. ISSN: 0028-0836, 1476-4687. DOI: 10.1038/nature09124.

[179] Ping Huang, Thomas Schönenberger, Marco Cantoni, Lukas Heinen, Arnaud Magrez, Achim Rosch, Fabrizio Carbone, and Henrik M. Rønnow. "Melting of a skyrmion lattice to a skyrmion liquid via a hexatic phase". In: *Nat. Nanotechnol.* 15.9 (Sept. 2020), pp. 761–767. ISSN: 1748-3387, 1748-3395. DOI: 10.1038/s41565-020-0716-3.

[180] Raab, Klaus. "Dynamics of topologically non-trivial spin structures". Master Thesis. Mainz, Germany: JGU Mainz, 2019.

[181] Michael Stone. "Magnus force on skyrmions in ferromagnets and quantum Hall systems". In: *Phys. Rev. B* 53.24 (June 15, 1996), pp. 16573–16578. ISSN: 0163-1829, 1095-3795. DOI: 10.1103/PhysRevB.53.16573.

[182] C Reichhardt and C J Olson Reichhardt. "Noise fluctuations and drive dependence of the skyrmion Hall effect in disordered systems". In: *New J. Phys.* 18.9 (Sept. 29, 2016), p. 095005. ISSN: 1367-2630. DOI: 10.1088/1367-2630/18/9/095005.

[183] Gong Chen. "Skyrmion Hall effect". In: *Nature Phys* 13.2 (Feb. 2017), pp. 112–113. ISSN: 1745-2473, 1745-2481. DOI: 10.1038/nphys4030.

[184] Wanjun Jiang, Xichao Zhang, Guoqiang Yu, Wei Zhang, Xiao Wang, M. Benjamin Jungfleisch, John E. Pearson, Xuemei Cheng, Olle Heinonen, Kang L. Wang, Yan Zhou, Axel Hoffmann, and Suzanne G. E. te Velthuis. "Direct observation of the skyrmion Hall effect". In: *Nature Phys* 13.2 (Feb. 2017), pp. 162–169. ISSN: 1745-2473, 1745-2481. DOI: 10.1038/nphys3883.

[185] C. Reichhardt and C. J. O. Reichhardt. "Plastic flow and the skyrmion Hall effect". In: *Nat Commun* 11.1 (Feb. 6, 2020), p. 738. ISSN: 2041-1723. DOI: 10.1038/s41467-020-14587-4.

[186] Sheng Yang, Yuelei Zhao, Xichao Zhang, Xiangjun Xing, Haifeng Du, Xiaoguang Li, Masahito Mochizuki, Xiaohong Xu, Johan Åkerman, and Yan Zhou. "Fundamentals and applications of the skyrmion Hall effect". In: *Applied Physics Reviews* 11.4 (Dec. 1, 2024), p. 041335. ISSN: 1931-9401. DOI: 10.1063/5.0218280.

[187] Roméo Juge, Soong-Geun Je, Dayane De Souza Chaves, Liliana D. Buda-Prejbeanu, José Peña-Garcia, Jayshankar Nath, Ioan Mihai Miron, Kumari Gaurav Rana, Lucia Aballe, Michael Foerster, Francesca Genuzio, Tevfik Onur Menteş, Andrea Locatelli, Francesco Maccherozzi, Sarnjeet S. Dhesi, Mohamed Belmeguenai, Yves Roussigné, Stéphane Auffret, Stefania Pizzini, Gilles Gaudin, Jan Vogel, and Olivier Boulle. "Current-Driven Skyrmion Dynamics and Drive-Dependent Skyrmion Hall Effect in an Ultrathin Film". In: *Phys. Rev. Applied* 12.4 (Oct. 3, 2019), p. 044007. ISSN: 2331-7019. DOI: 10.1103/PhysRevApplied.12.044007.

[188] C Reichhardt and C J O Reichhardt. "Thermal creep and the skyrmion Hall angle in driven skyrmion crystals". In: *J. Phys.: Condens. Matter* 31.7 (Feb. 20, 2019), 07LT01. ISSN: 0953-8984, 1361-648X. DOI: 10.1088/1361-648X/aaefd7.

[189] Karin Everschor-Sitte and Matthias Sitte. "Real-space Berry phases: Skyrmion soccer (invited)". In: *Journal of Applied Physics* 115.17 (May 7, 2014), p. 172602. ISSN: 0021-8979, 1089-7550. DOI: 10.1063/1.4870695.

[190] Maarten A. Brems, Mathias Kläui, and Peter Virnau. "Circuits and excitations to enable Brownian token-based computing with skyrmions". In: *Appl. Phys. Lett.* 119.13 (Sept. 27, 2021), p. 132405. ISSN: 0003-6951, 1077-3118. DOI: 10.1063/5.0063584.

[191] Xichao Zhang, Yan Zhou, and Motohiko Ezawa. "Antiferromagnetic Skyrmion: Stability, Creation and Manipulation". In: *Sci Rep* 6.1 (Apr. 21, 2016), p. 24795. ISSN: 2045-2322. DOI: 10.1038/srep24795.

[192] Van Tuong Pham, Naveen Sisodia, Ilaria Di Manici, Joseba Urrestarazu-Larrañaga, Kaushik Bairagi, Johan Pelloux-Prayer, Rodrigo Guedas, Liliana D. Buda-Prejbeanu, Stéphane Auffret, Andrea Locatelli, Tevfik Onur Menteş, Stefania Pizzini, Pawan Kumar, Aurore Finco, Vincent Jacques, Gilles Gaudin, and Olivier Boulle. "Fast current-induced skyrmion motion in synthetic antiferromagnets". In: *Science* 384.6693 (Apr. 19, 2024), pp. 307–312. ISSN: 0036-8075, 1095-9203. DOI: 10.1126/science.add5751.

[193] Haitao Wu, Xuchong Hu, Keyu Jing, and X. R. Wang. "Size and profile of skyrmions in skyrmion crystals". In: *Commun Phys* 4.1 (Sept. 20, 2021), p. 210. ISSN: 2399-3650. DOI: 10.1038/s42005-021-00716-y.

[194] H C Wu, K D Chandrasekhar, T Y Wei, K J Hsieh, T Y Chen, H Berger, and H D Yang. "Physical pressure and chemical expansion effects on the skyrmion phase in Cu_2OSeO_3". In: *J. Phys. D: Appl. Phys.* 48.47 (Dec. 2, 2015), p. 475001. ISSN: 0022-3727, 1361-6463. DOI: 10.1088/0022-3727/48/47/475001.

[195] I. Levatić, P. Popčević, V. Šurija, A. Kruchkov, H. Berger, A. Magrez, J. S. White, H. M. Rønnow, and I. Živković. "Dramatic pressure-driven enhancement of bulk skyrmion stability". In: *Sci Rep* 6.1 (Feb. 19, 2016), p. 21347. ISSN: 2045-2322. DOI: 10.1038/srep21347.

[196] Roméo Juge, Kaushik Bairagi, Kumari Gaurav Rana, Jan Vogel, Mamour Sall, Dominique Mailly, Van Tuong Pham, Qiang Zhang, Naveen Sisodia, Michael Foerster, Lucia Aballe, Mohamed Belmeguenai, Yves Roussigné, Stéphane Auffret, Liliana D. Buda-Prejbeanu, Gilles Gaudin, Dafiné Ravelosona, and Olivier Boulle. "Helium Ions Put Magnetic Skyrmions on the Track". In: *Nano Lett.* 21.7 (Apr. 14, 2021), pp. 2989–2996. ISSN: 1530-6984, 1530-6992. DOI: 10.1021/acs.nanolett.1c00136.

[197] C. Chappert, H. Bernas, J. Ferré, V. Kottler, J.-P. Jamet, Y. Chen, E. Cambril, T. Devolder, F. Rousseaux, V. Mathet, and H. Launois. "Planar Patterned Magnetic Media Obtained by Ion Irradiation". In: *Science* 280.5371 (June 19, 1998), pp. 1919–1922. ISSN: 0036-8075, 1095-9203. DOI: 10.1126/science.280.5371.1919.

[198] Valentin Ahrens, Clara Kiesselbach, Luca Gnoli, Domenico Giuliano, Simon Mendisch, Martina Kiechle, Fabrizio Riente, and Markus Becherer. "Skyrmions Under Control—FIB Irradiation as a Versatile Tool for Skyrmion Circuits". In: *Advanced Materials* 35.2 (Jan. 2023), p. 2207321. ISSN: 0935-9648, 1521-4095. DOI: 10.1002/adma.202207321.

[199] Heinz Niedrig, ed. *Optik: Wellen- und Teilchenoptik: Part 1*. 10. Auflage[Ausg. in 8 Bänden]. Lehrbuch der Experimentalphysik / Bergmann; Schaefer 3, Part 1. Berlin: de Gruyter, 2004. 668 pp. ISBN: 978-3-11-017081-8.

[200] Murmann, Frank. *Kerr Winkel und Elliptizität*. Wikipedia - The Free Encyclopedia. 2011. URL: https://de.wikipedia.org/wiki/Magnetooptischer_Kerr-Effekt#/media/Datei:Kerrwinkel.svg.

[201] Peter M. Oppeneer. *Theory of the Magneto-Optical Kerr Effect in Ferromagnetic Compounds*. Technische Universität Dresden, 1999. DOI: 10.13140/2.1.3171.4083.

[202] Wolfgang Nolting, ed. *Grundkurs Theoretische Physik 3: Elektrodynamik*. Springer-Lehrbuch. Berlin, Heidelberg: Springer Berlin Heidelberg, 2004. ISBN: 978-3-540-20509-8. DOI: 10.1007/3-540-35076-4.

[203] Lars Onsager. "Reciprocal Relations in Irreversible Processes. I." In: *Phys. Rev.* 37.4 (Feb. 15, 1931), pp. 405–426. ISSN: 0031-899X. DOI: 10.1103/PhysRev.37.405.

[204] M. Julliere. "Tunneling between ferromagnetic films". In: *Physics Letters A* 54.3 (Sept. 1975), pp. 225–226. ISSN: 03759601. DOI: 10.1016/0375-9601(75)90174-7.

[205] T. Miyazaki and N. Tezuka. "Giant magnetic tunneling effect in Fe/Al2O3/Fe junction". In: *Journal of Magnetism and Magnetic Materials* 139.3 (Jan. 1995), pp. L231–L234. ISSN: 03048853. DOI: 10.1016/0304-8853(95)90001-2.

[206] Jian-Gang (Jimmy) Zhu and Chando Park. "Magnetic tunnel junctions". In: *Materials Today* 9.11 (Nov. 2006), pp. 36–45. ISSN: 13697021. DOI: 10.1016/S1369-7021(06)71693-5.

[207] S. Ikeda, K. Miura, H. Yamamoto, K. Mizunuma, H. D. Gan, M. Endo, S. Kanai, J. Hayakawa, F. Matsukura, and H. Ohno. "A perpendicular-anisotropy CoFeB–MgO magnetic tunnel junction". In: *Nature Mater* 9.9 (Sept. 2010), pp. 721–724. ISSN: 1476-1122, 1476-4660. DOI: 10.1038/nmat2804.

[208] H. Liu, D. Bedau, D. Backes, J. A. Katine, J. Langer, and A. D. Kent. "Ultrafast switching in magnetic tunnel junction based orthogonal spin transfer devices". In: *Applied Physics Letters* 97.24 (Dec. 13, 2010), p. 242510. ISSN: 0003-6951, 1077-3118. DOI: 10.1063/1.3527962.

[209] Weisheng Zhao, Xiaoxuan Zhao, Boyu Zhang, Kaihua Cao, Lezhi Wang, Wang Kang, Qian Shi, Mengxing Wang, Yu Zhang, You Wang, Shouzhong Peng, Jacques-Olivier Klein, Lirida De Barros Naviner, and Dafine Ravelosona. "Failure Analysis in Magnetic Tunnel Junction Nanopillar with Interfacial Perpendicular Magnetic Anisotropy". In: *Materials* 9.1 (Jan. 12, 2016), p. 41. ISSN: 1996-1944. DOI: 10.3390/ma9010041.

[210] A. Dal Din, O. J. Amin, P. Wadley, and K. W. Edmonds. "Antiferromagnetic spintronics and beyond". In: *npj Spintronics* 2.1 (July 2, 2024), p. 25. ISSN: 2948-2119. DOI: 10.1038/s44306-024-00029-0.

[211] Kartik Samanta, Yuan-Yuan Jiang, Tula R. Paudel, Ding-Fu Shao, and Evgeny Y. Tsymbal. "Tunneling magnetoresistance in magnetic tunnel junctions with a single ferromagnetic electrode". In: *Phys. Rev. B* 109.17 (May 3, 2024), p. 174407. ISSN: 2469-9950, 2469-9969. DOI: 10.1103/PhysRevB.109.174407.

[212] Shaohai Chen, James Lourembam, Pin Ho, Alexander K. J. Toh, Jifei Huang, Xiaoye Chen, Hang Khume Tan, Sherry L. K. Yap, Royston J. J. Lim, Hui Ru Tan, T. S. Suraj, May Inn Sim, Yeow Teck Toh, Idayu Lim, Nelson C. B. Lim, Jing Zhou, Hong Jing Chung, Sze Ter Lim, and Anjan Soumyanarayanan. "All-electrical skyrmionic magnetic tunnel junction". In: *Nature* 627.8004 (Mar. 21, 2024), pp. 522–527. ISSN: 0028-0836, 1476-4687. DOI: 10.1038/s41586-024-07131-7.

[213] Alice Mizrahi, Tifenn Hirtzlin, Akio Fukushima, Hitoshi Kubota, Shinji Yuasa, Julie Grollier, and Damien Querlioz. "Neural-like computing with populations of superparamagnetic basis functions". In: *Nat Commun* 9.1 (Apr. 18, 2018), p. 1533. ISSN: 2041-1723. DOI: 10.1038/s41467-018-03963-w.

[214] Brandon R. Zink, Yang Lv, and Jian-Ping Wang. "Review of Magnetic Tunnel Junctions for Stochastic Computing". In: *IEEE J. Explor. Solid-State Comput. Devices Circuits* 8.2 (Dec. 2022), pp. 173–184. ISSN: 2329-9231. DOI: 10.1109/JXCDC.2022.3227062.

[215] Leo Schnitzspan, Mathias Kläui, and Gerhard Jakob. "Nanosecond True-Random-Number Generation with Superparamagnetic Tunnel Junctions: Identification of Joule Heating and Spin-Transfer-Torque Effects". In: *Phys. Rev. Applied* 20.2 (Aug. 1, 2023), p. 024002. ISSN: 2331-7019. DOI: 10.1103/PhysRevApplied.20.024002.

[216] Yao Guang, Like Zhang, Junwei Zhang, Yadong Wang, Yuelei Zhao, Riccardo Tomasello, Senfu Zhang, Bin He, Jiahui Li, Yizhou Liu, Jiafeng Feng, Hongxiang Wei, Mario Carpentieri, Zhipeng Hou, Junming Liu, Yong Peng, Zhongming Zeng, Giovanni Finocchio, Xixiang Zhang, John Michael David Coey, Xiufeng Han, and Guoqiang Yu. "Electrical Detection of Magnetic Skyrmions in a Magnetic Tunnel Junction". In: *Adv Elect Materials* 9.1 (Jan. 2023), p. 2200570. ISSN: 2199-160X, 2199-160X. DOI: 10.1002/aelm.202200570.

[217] Mengqi Zhao, Aitian Chen, Pei-Yuan Huang, Chen Liu, Laichuan Shen, Jiahao Liu, Le Zhao, Bin Fang, Wen-Cheng Yue, Dongxing Zheng, Ledong Wang, Hao Bai, Ka Shen, Yan Zhou, Shasha Wang, Enlong Liu, Shikun He, Yong-Lei Wang, Xixiang Zhang, and Wanjun Jiang. "Electrical detection of mobile skyrmions with 100% tunneling magnetoresistance in a racetrack-like device". In: *npj Quantum Mater.* 9.1 (June 14, 2024), p. 50. ISSN: 2397-4648. DOI: 10.1038/s41535-024-00655-1.

[218] Joseba Urrestarazu Larrañaga, Naveen Sisodia, Rodrigo Guedas, Van Tuong Pham, Ilaria Di Manici, Aurélien Masseboeuf, Kevin Garello, Florian Disdier, Bruno Fernandez, Sebastian Wintz, Markus Weigand, Mohamed Belmeguenai, Stefania Pizzini, Ricardo C. Sousa, Liliana D. Buda-Prejbeanu, Gilles Gaudin, and Olivier Boulle. "Electrical Detection and Nucleation of a Magnetic Skyrmion in a Magnetic Tunnel Junction Observed via *Operando* Magnetic Microscopy". In: *Nano Lett.* 24.12 (Mar. 27, 2024), pp. 3557–3565. ISSN: 1530-6984, 1530-6992. DOI: 10.1021/acs.nanolett.4c00316.

[219] Cristian S. Calude. "Unconventional Computing: A Brief Subjective History". In: *Advances in Unconventional Computing*. Ed. by Andrew Adamatzky. Vol. 22. Series Title: Emergence, Complexity and Computation. Cham: Springer International Publishing, 2017, pp. 855–864. ISBN: 978-3-319-33923-8. DOI: 10.1007/978-3-319-33924-5_31.

[220] Schmidhuber, Jürgen. *Annotated History of Modern AI and Deep Learning*. 2022. URL: https://people.idsia.ch/~juergen/deep-learning-history.html.

[221] Natalia Andrienko and Gennady Andrienko. *Exploratory Analysis of Spatial and Temporal Data: A Systematic Approach*. SpringerLink Bücher. Berlin, Heidelberg: Springer-Verlag Berlin Heidelberg, 2006. 703 pp. ISBN: 978-3-540-25994-7. DOI: 10.1007/3-540-31190-4.

[222] Gouhei Tanaka, Toshiyuki Yamane, Jean Benoit Héroux, Ryosho Nakane, Naoki Kanazawa, Seiji Takeda, Hidetoshi Numata, Daiju Nakano, and Akira Hirose. "Recent advances in physical reservoir computing: A review". In: *Neural Networks* 115 (July 2019), pp. 100–123. ISSN: 08936080. DOI: 10.1016/j.neunet.2019.03.005.

[223] Nielsen, Michael. *Neural Networks - Chapter 5*. 2019. URL: http://neuralnetworksanddeeplearning.com/chap5.html.

[224] David E. Rumelhart, Geoffrey E. Hinton, and Ronald J. Williams. "Learning representations by back-propagating errors". In: *Nature* 323.6088 (Oct. 1986), pp. 533–536. ISSN: 0028-0836, 1476-4687. DOI: 10.1038/323533a0.

[225] Mantas Lukoševičius and Herbert Jaeger. "Reservoir computing approaches to recurrent neural network training". In: *Comput. Sci. Rev.* 3.3 (Aug. 2009), pp. 127–149. ISSN: 15740137. DOI: 10.1016/j.cosrev.2009.03.005.

[226] Min Yan, Can Huang, Peter Bienstman, Peter Tino, Wei Lin, and Jie Sun. "Emerging opportunities and challenges for the future of reservoir computing". In: *Nature Communications* 15.1 (Mar. 6, 2024), p. 2056. ISSN: 2041-1723. DOI: 10.1038/s41467-024-45187-1.

[227] Oscar Lee, Tianyi Wei, Kilian D. Stenning, Jack C. Gartside, Dan Prestwood, Shinichiro Seki, Aisha Aqeel, Kosuke Karube, Naoya Kanazawa, Yasujiro Taguchi, Christian Back, Yoshinori Tokura, Will R. Branford, and Hidekazu Kurebayashi. "Task-adaptive physical reservoir computing". In: *Nat. Mater.*

23.1 (Jan. 2024), pp. 79–87. ISSN: 1476-1122, 1476-4660. DOI: 10.1038/s41563-023-01698-8.

[228] Guy Van Der Sande, Daniel Brunner, and Miguel C. Soriano. "Advances in photonic reservoir computing". In: *Nanophotonics* 6.3 (May 12, 2017), pp. 561–576. ISSN: 2192-8614, 2192-8606. DOI: 10.1515/nanoph-2016-0132.

[229] Diana Prychynenko, Matthias Sitte, Kai Litzius, Benjamin Krüger, George Bourianoff, Mathias Kläui, Jairo Sinova, and Karin Everschor-Sitte. "Magnetic Skyrmion as a Nonlinear Resistive Element: A Potential Building Block for Reservoir Computing". In: *Phys. Rev. Appl.* 9.1 (Jan. 31, 2018), p. 014034. ISSN: 2331-7019. DOI: 10.1103/PhysRevApplied.9.014034.

[230] Mu-Kun Lee and Masahito Mochizuki. "Handwritten digit recognition by spin waves in a Skyrmion reservoir". In: *Sci Rep* 13.1 (Nov. 8, 2023), p. 19423. ISSN: 2045-2322. DOI: 10.1038/s41598-023-46677-w.

[231] Md Mahadi Rajib, Walid Al Misba, Md Fahim F Chowdhury, Muhammad Sabbir Alam, and Jayasimha Atulasimha. "Skyrmion based energy-efficient straintronic physical reservoir computing". In: *Neuromorph. Comput. Eng.* 2.4 (Dec. 1, 2022), p. 044011. ISSN: 2634-4386. DOI: 10.1088/2634-4386/aca178.

[232] D. Pinna, G. Bourianoff, and K. Everschor-Sitte. "Reservoir Computing with Random Skyrmion Textures". In: *Phys. Rev. Appl.* 14.5 (Nov. 10, 2020), p. 054020. ISSN: 2331-7019. DOI: 10.1103/PhysRevApplied.14.054020.

[233] George Bourianoff, Daniele Pinna, Matthias Sitte, and Karin Everschor-Sitte. "Potential implementation of reservoir computing models based on magnetic skyrmions". In: *AIP Advances* 8.5 (May 1, 2018), p. 055602. ISSN: 2158-3226. DOI: 10.1063/1.5006918.

[234] Tomoyuki Yokouchi, Satoshi Sugimoto, Bivas Rana, Shinichiro Seki, Naoki Ogawa, Yuki Shiomi, Shinya Kasai, and Yoshichika Otani. "Pattern recognition with neuromorphic computing using magnetic field–induced dynamics of skyrmions". In: *Sci. Adv.* 8.39 (Sept. 30, 2022), eabq5652. ISSN: 2375-2548. DOI: 10.1126/sciadv.abq5652.

[235] Yuma Jibiki, Minori Goto, Eiiti Tamura, Jaehun Cho, Soma Miki, Ryo Ishikawa, Hikaru Nomura, Titiksha Srivastava, Willy Lim, Stephane Auffret, Claire Baraduc, Helene Bea, and Yoshishige Suzuki. "Skyrmion Brownian circuit implemented in continuous ferromagnetic thin film". In: *Appl. Phys. Lett.* 117.8 (Aug. 24, 2020), p. 082402. ISSN: 0003-6951, 1077-3118. DOI: 10.1063/5.0011105.

[236] Xichao Zhang, Motohiko Ezawa, and Yan Zhou. "Magnetic skyrmion logic gates: conversion, duplication and merging of skyrmions". In: *Sci Rep* 5.1 (Mar. 24, 2015), p. 9400. ISSN: 2045-2322. DOI: 10.1038/srep09400.

[237] E. Fortunato, P. Barquinha, and R. Martins. "Oxide Semiconductor Thin-Film Transistors: A Review of Recent Advances". In: *Advanced Materials* 24.22 (June 12, 2012), pp. 2945–2986. ISSN: 0935-9648, 1521-4095. DOI: 10.1002/adma.201103228.

[238] Casquillas, G.V., Houssin, T., Durieux, L., and Chidiac, C. *Introduction to lab-on-a-chip 2024: review, history and future*. 2023. URL: https://www.elveflow.com/microfluidic-reviews/introduction-to-lab-on-a-chip-review-history-and-future/ (visited on 04/23/2025).

[239] D. M. Mattox. *Handbook of physical vapor deposition (PVD) processing*. 2nd ed. Oxford, UK: William Andrew, 2010. ISBN: 978-0-8155-2037-5.

[240] B. Janarthanan, C. Thirunavukkarasu, S. Maruthamuthu, M. Aslam Manthrammel, Mohd. Shkir, S. AlFaify, M. Selvakumar, Vasudeva Reddy Minnam Reddy, and Chinho Park. "Basic deposition methods of thin films**". In: *Journal of Molecular Structure* 1241 (Oct. 2021), p. 130606. ISSN: 00222860. DOI: 10.1016/j.molstruc.2021.130606.

[241] Renuka Garg, Spandana Gonuguntla, Saddam Sk, Muhammad Saqlain Iqbal, Adewumi Oluwasogo Dada, Ujjwal Pal, and Mohsen Ahmadipour. "Sputtering thin films: Materials, applications, challenges and future directions". In: *Advances in Colloid and Interface Science* 330 (Aug. 2024), p. 103203. ISSN: 00018686. DOI: 10.1016/j.cis.2024.103203.

[242] Yanhui Zhang, Haojie Yu, Li Wang, Xudong Wu, Jiawen He, Wenbing Huang, Chengaung Ouyang, Dingning Chen, and Basem E. Keshta. "Advanced lithography materials: From fundamentals to applications". In: *Advances in Colloid and Interface Science* 329 (July 2024), p. 103197. ISSN: 00018686. DOI: 10.1016/j.cis.2024.103197.

[243] P. Schmid, M. Orfert, and M. Vogt. "Plasma deposition of Si-N and Si-O passivation layers on three-dimensional sensor devices". In: *Surface and Coatings Technology* 98.1 (Jan. 1998), pp. 1510–1517. ISSN: 02578972. DOI: 10.1016/S0257-8972(97)00300-9.

[244] cadence technology. *The Different Types of Semiconductor Wafers*. 2024. URL: https://resources.pcb.cadence.com/blog/2024-the-different-types-of-semiconductor-wafers.

[245] Ayodele, Abiola. *Silicon Wafers: Production, Properties and Application*. 2024. URL: https://www.wevolver.com/article/silicon-wafers.

[246] X. W. Zhou and H. N. G. Wadley. "Mechanisms of inert gas impact induced interlayer mixing in metal multilayers grown by sputter deposition". In: *Journal of Applied Physics* 90.7 (Oct. 1, 2001), pp. 3359–3366. ISSN: 0021-8979, 1089-7550. DOI: 10.1063/1.1398073.

[247] nikalyte. *How does gas control impact uniformity in physical vapor deposition?* URL: https://www.nikalyte.com/how-does-gas-control-impact-uniformity-in-physical-vapor-deposition/.

[248] farotex. *Technology - A brief explanation of how magnetron sputtering works.* URL: https://farotex.com/technology.html.

[249] Casper Pusch, Holger Hoche, Christina Berger, Ralf Riedel, Emanuel Ionescu, and Andreas Klein. "Influence of the PVD sputtering method on structural characteristics of SiCN-coatings — Comparison of RF, DC and HiPIMS sputtering and target configurations". In: *Surface and Coatings Technology* 205 (July 2011), S119–S123. ISSN: 02578972. DOI: 10.1016/j.surfcoat.2011.04.095.

[250] Rochan Sinha, Reinoud Lavrijsen, Marcel A. Verheijen, Erwin Zoethout, Han Genuit, Mauritius C. M. Van De Sanden, and Anja Bieberle-Hütter. "Electrochemistry of Sputtered Hematite Photoanodes: A Comparison of Metallic DC versus Reactive RF Sputtering". In: *ACS Omega* 4.5 (May 31, 2019), pp. 9262–9270. ISSN: 2470-1343, 2470-1343. DOI: 10.1021/acsomega.8b03349.

[251] Richard C. Bradley. "Sputtering of Alkali Atoms by Inert Gas Ions of Low Energy". In: *Phys. Rev.* 93.4 (Feb. 15, 1954), pp. 719–728. ISSN: 0031-899X. DOI: 10.1103/PhysRev.93.719.

[252] K. Vahaplar, S. Tari, H. Tokuc, and S. Okur. "Effect of Ta buffer layer and thickness on the structural and magnetic properties of Co thin films". In: *Journal of Vacuum Science & Technology B: Microelectronics and Nanometer Structures Processing, Measurement, and Phenomena* 27.5 (Sept. 1, 2009), pp. 2112–2116. ISSN: 1071-1023, 1520-8567. DOI: 10.1116/1.3196784.

[253] Xiaoxuan Zhao, Boyu Zhang, Nicolas Vernier, Xueying Zhang, Mamour Sall, Tao Xing, Liza Herrera Diez, Carolyna Hepburn, Lin Wang, Gianfranco Durin, Arianna Casiraghi, Mohamed Belmeguenai, Yves Roussigné, Andrei Stashkevich, Salim Mourad Chérif, Jürgen Langer, Berthold Ocker, Samridh Jaiswal, Gerhard Jakob, Mathias Kläui, Weisheng Zhao, and Dafiné Ravelosona. "Enhancing domain wall velocity through interface intermixing in W-CoFeB-MgO films with perpendicular anisotropy". In: *Applied Physics Letters* 115.12 (Sept. 16, 2019), p. 122404. ISSN: 0003-6951, 1077-3118. DOI: 10.1063/1.5121357.

[254] Wang Yao, Yanru Li, Meiyin Yang, Feiyan Hou, Tao Li, and Tai Min. "Tuning the magnetic properties of ultrathin magnetic films with MgO as the buffer layer". In: *Journal of Magnetism and Magnetic Materials* 611 (Dec. 2024), p. 172599. ISSN: 03048853. DOI: 10.1016/j.jmmm.2024.172599.

[255] Mohammed, Nadheer Jassim. "Lecture one - Surface Energy and Nucleation Modes".

[256] Amilcar Bedoya-Pinto, Kai Chang, Mahesh G. Samant, and Stuart S. P. Parkin. "Material Preparation and Thin Film Growth". In: *Handbook of Magnetism and Magnetic Materials*. Ed. by J. M. D. Coey and Stuart S.P. Parkin. Cham: Springer International Publishing, 2021, pp. 1153–1202. ISBN: 978-3-030-63208-3. DOI: 10.1007/978-3-030-63210-6_23.

[257] Yanduan Yang, Jinliang Tu, Guangxing Zhan, Haipeng Liu, Xiaoyu Fan, Xin Chen, Xiaolin Hu, and Naifeng Zhuang. "Growth Considering Lattice Mismatch and Thermal Expansion and Magneto-Optical Properties of Bismuth-Doped Rare Earth Iron Garnet Crystals". In: *Crystal Growth & Design* 23.3 (Mar. 1, 2023), pp. 1598–1602. ISSN: 1528-7483, 1528-7505. DOI: 10.1021/acs.cgd.2c01231.

[258] Harsh Vardhan, V. Srihari, Kavita Sharma, Surendra Singh, Mukul Gupta, V.R. Reddy, S.C. Das, Anil Gome, Ajay Gupta, and Gagan Sharma. "Ta interfaced CoFeB: Role of CoFeB thickness and thermal annealing in modification of structural and magnetic properties". In: *Surfaces and Interfaces* 41 (Oct. 2023), p. 103156. ISSN: 24680230. DOI: 10.1016/j.surfin.2023.103156.

[259] *Singulus Technologies AG; www.singulus.com*.

[260] Jonathan J. Colin, Grégory Abadias, Anny Michel, and Christiane Jaouen. "On the origin of the metastable Beta-Ta phase stabilization in tantalum sputtered thin films". In: *Acta Materialia* 126 (Mar. 2017), pp. 481–493. ISSN: 13596454. DOI: 10.1016/j.actamat.2016.12.030.

[261] E O Nasakina, M A Sevostyanov, A B Mikhaylova, A S Baikin, K V Sergienko, A V Leonov, and A G Kolmakov. "Formation of alpha and beta tantalum at the variation of magnetron sputtering conditions". In: *IOP Conf. Ser.: Mater. Sci. Eng.* 110 (Feb. 23, 2016), p. 012042. ISSN: 1757-8981, 1757-899X. DOI: 10.1088/1757-899X/110/1/012042.

[262] Anmol Mahendra, Peter P. Murmu, Susant Kumar Acharya, Atif Islam, Holger Fiedler, Prasanth Gupta, Simon Granville, and John Kennedy. "Role of interface intermixing on perpendicular magnetic anisotropy of cobalt-iron-boron alloy". In: *Appl. Phys. A* 129.7 (July 2023), p. 500. ISSN: 0947-8396, 1432-0630. DOI: 10.1007/s00339-023-06759-y.

[263] Sajid Husain, Nanhe Kumar Gupta, Vineet Barwal, and Sujeet Chaudhary. "Magneto-optical properties of CoFeB ultrathin films: Effect of Ta buffer and capping layer". In: 2ND INTERNATIONAL CONFERENCE ON CONDENSED MATTER AND APPLIED PHYSICS (ICC 2017). Bikaner, India, 2018, p. 120048. DOI: 10.1063/1.5033113.

[264] Jacob Torrejon, Junyeon Kim, Jaivardhan Sinha, Seiji Mitani, Masamitsu Hayashi, Michihiko Yamanouchi, and Hideo Ohno. "Interface control of the magnetic chirality in CoFeB/MgO heterostructures with heavy-metal underlayers". In: *Nat Commun* 5.1 (Aug. 18, 2014), p. 4655. ISSN: 2041-1723. DOI: 10.1038/ncomms5655.

[265] Yifang Chen. "Nanofabrication by electron beam lithography and its applications: A review". In: *Microelectronic Engineering* 135 (Mar. 2015), pp. 57–72. ISSN: 01679317. DOI: 10.1016/j.mee.2015.02.042.

[266] John N. Randall, James H. G. Owen, Joseph Lake, and Ehud Fuchs. "Next generation of extreme-resolution electron beam lithography". In: *Journal of Vacuum Science & Technology B, Nanotechnology and Microelectronics: Materials, Processing, Measurement, and Phenomena* 37.6 (Nov. 1, 2019), p. 061605. ISSN: 2166-2746, 2166-2754. DOI: 10.1116/1.5119392.

[267] International Organization for Standardization. *13.040.35 - Cleanrooms and associated controlled environments*. 2015.

[268] R.S-NESS Group. *Cleanroom Design*. Cleanroom Design. 2025. URL: https://rs-ness.com/cleanroom-design/.

[269] Anushka S. Gangnaik, Yordan M. Georgiev, and Justin D. Holmes. "New Generation Electron Beam Resists: A Review". In: *Chem. Mater.* 29.5 (Mar. 14, 2017), pp. 1898–1917. ISSN: 0897-4756, 1520-5002. DOI: 10.1021/acs.chemmater.6b03483.

[270] *Allresist GmbH - https://www.allresist.com/*.

[271] Harry J. Levinson. "High-NA EUV lithography: current status and outlook for the future". In: *Jpn. J. Appl. Phys.* 61 (SD June 1, 2022), SD0803. ISSN: 0021-4922, 1347-4065. DOI: 10.35848/1347-4065/ac49fa.

[272] Xiaolin Wang, Peipei Tao, Qianqian Wang, Rongbo Zhao, Tianqi Liu, Yang Hu, Ziyu Hu, Yimeng Wang, Jianlong Wang, Yaping Tang, Hong Xu, and Xiangming He. "Trends in photoresist materials for extreme ultraviolet lithography: A review". In: *Materials Today* 67 (July 2023), pp. 299–319. ISSN: 13697021. DOI: 10.1016/j.mattod.2023.05.027.

[273] Dimitrios Kazazis, Jara Garcia Santaclara, Jan Van Schoot, Iacopo Mochi, and Yasin Ekinci. "Extreme ultraviolet lithography". In: *Nat Rev Methods Primers* 4.1 (Nov. 28, 2024), p. 84. ISSN: 2662-8449. DOI: 10.1038/s43586-024-00361-z.

[274] Markku Tilli and Atte Haapalinna. "Properties of silicon". In: *Handbook of Silicon Based MEMS Materials and Technologies*. Elsevier, 2020, pp. 3–17. ISBN: 978-0-12-817786-0. DOI: 10.1016/B978-0-12-817786-0.00001-3.

[275] University Wafer. *Annealed Silicon Wafer All Specifications*. URL: https://www.universitywafer.com/annealed-silicon-wafer.html.

[276] Charles Greenlee, J. Luo, K. Leedy, B. Bayraktaroglu, R. A. Norwood, M. Fallahi, A. K.-Y. Jen, and N. Peyghambarian. "Electro-optic polymer spatial light modulator based on a Fabry–Perot interferometer configuration". In: *Opt. Express* 19.13 (June 20, 2011), p. 12750. ISSN: 1094-4087. DOI: 10.1364/OE.19.012750.

[277] A.N. Broers, A.C.F. Hoole, and J.M. Ryan. "Electron beam lithography—Resolution limits". In: *Microelectronic Engineering* 32.1 (Sept. 1996). Publisher: Elsevier BV, pp. 131–142. ISSN: 0167-9317. DOI: 10.1016/0167-9317(95)00368-1.

[278] C. Vieu, F. Carcenac, A. Pépin, Y. Chen, M. Mejias, A. Lebib, L. Manin-Ferlazzo, L. Couraud, and H. Launois. "Electron beam lithography: resolution limits and applications". In: *Applied Surface Science* 164.1 (Sept. 2000), pp. 111–117. ISSN: 01694332. DOI: 10.1016/S0169-4332(00)00352-4.

[279] Vitor R. Manfrinato, Lihua Zhang, Dong Su, Huigao Duan, Richard G. Hobbs, Eric A. Stach, and Karl K. Berggren. "Resolution Limits of Electron-Beam Lithography toward the Atomic Scale". In: *Nano Lett.* 13.4 (Apr. 10, 2013), pp. 1555–1558. ISSN: 1530-6984, 1530-6992. DOI: 10.1021/nl304715p.

[280] Cheol Eui Lee. "Secondary electron generation in electron-beam-irradiated solids:resolution limits to nanolithography". In: *J. Korean Phy. Soc.* 55.4 (Oct. 15, 2009). Publisher: Korean Physical Society, pp. 1720–1723. ISSN: 0374-4884. DOI: 10.3938/jkps.55.1720.

[281] ASML. *EUV lithography systems*. URL: https://www.asml.com/en/products/euv-lithography-systems.

[282] Jones, Scotten. *VLSI Symposium – TSMC and Imec on Advanced Process and Devices Technology Toward 2nm*. 2021. URL: https://semiwiki.com/events/300552-vlsi-technology-forum-short-course-logic-devices/.

[283] Allresist GmbH. *E-Beam Resist AR-N 7520 new series*. URL: https://www.allresist.com/portfolio-item/e-beam-resist-ar-n-7520-new-series/#tab-id-3.

[284] Allresist GmbH. *Polymers (film formers)*. URL: https://www.allresist.com/resist-wiki-polymers-film-formers/.

[285] Liming Ren and Baoqin Chen. "Proximity effect in electron beam lithography". In: *Proceedings. 7th International Conference on Solid-State and Integrated Circuits Technology, 2004.* 2004 7th International Conference on Solid-State and Integrated Circuits Technology Proceedings. Beijing, China: IEEE, 2004, 579–582 vol.1. DOI: 10.1109/icsict.2004.1435073.

[286] University of Washington. *Proximity Correction*. 2014. URL: https://ebeam.wnf.uw.edu/ebeamweb/doc/patternprep/patternprep/proximity_main.html.

[287] Raith. *Multifunctional system family for maximum versatility*. 2025. URL: https://raith.com/products/multifunctional-ebl/.

[288] Fred the Oyster. *Electron Beam scattering*. 2014.

[289] Diener electronics. *RIE - Reactive Ion Etching*. URL: https://www.plasma.com/plasmatechnik-lexikon/reactive-ion-etching-rie/.

[290] Matteo Todeschini, Alice Bastos Da Silva Fanta, Flemming Jensen, Jakob Birkedal Wagner, and Anpan Han. "Influence of Ti and Cr Adhesion Layers on Ultrathin Au Films". In: *ACS Appl. Mater. Interfaces* 9.42 (Oct. 25, 2017). Publisher: American Chemical Society (ACS), pp. 37374–37385. ISSN: 1944-8244, 1944-8252. DOI: 10.1021/acsami.7b10136.

[291] Evico Magnetics GmbH. *Website of Evico Magnetics GmbH*. URL: https://evicomagnetics.com/ (visited on 05/14/2025).

[292] *Schoolphysics*. URL: https://www.schoolphysics.co.uk/ (visited on 04/19/2025).

[293] J. Sampaio, V. Cros, S. Rohart, A. Thiaville, and A. Fert. "Nucleation, stability and current-induced motion of isolated magnetic skyrmions in nanostructures". In: *Nature Nanotech* 8.11 (Nov. 2013), pp. 839–844. ISSN: 1748-3387, 1748-3395. DOI: 10.1038/nnano.2013.210.

[294] Zhenzhen Chen, Xinyan He, Xinyi Cai, Yang Qiu, Mingmin Zhu, Guoliang Yu, and Haomiao Zhou. "Magnetic skyrmion nucleation via current injection in confined nanotrack with modified perpendicular anisotropy region". In: *Applied Physics Letters* 122.14 (Apr. 3, 2023), p. 142401. ISSN: 0003-6951, 1077-3118. DOI: 10.1063/5.0138688.

[295] Felix Büttner, Bastian Pfau, Marie Böttcher, Michael Schneider, Giuseppe Mercurio, Christian M. Günther, Piet Hessing, Christopher Klose, Angela Wittmann, Kathinka Gerlinger, Lisa-Marie Kern, Christian Strüber, Clemens Von Korff Schmising, Josefin Fuchs, Dieter Engel, Alexandra Churikova, Siying Huang, Daniel Suzuki, Ivan Lemesh, Mantao Huang, Lucas Caretta, David Weder, John H. Gaida, Marcel Möller, Tyler R. Harvey, Sergey Zayko, Kai Bagschik, Robert Carley, Laurent Mercadier, Justine Schlappa, Alexander Yaroslavtsev, Loïc Le Guyarder, Natalia Gerasimova, Andreas Scherz, Carsten Deiter, Rafael Gort, David Hickin, Jun Zhu, Monica Turcato, David Lomidze, Florian Erdinger, Andrea Castoldi, Stefano Maffessanti, Matteo Porro, Andrey Samartsev, Jairo Sinova, Claus Ropers, Johan H. Mentink, Bertrand Dupé, Geoffrey S. D. Beach, and Stefan Eisebitt. "Observation of fluctuation-mediated picosecond nucleation of a topological phase". In: *Nat. Mater.* 20.1 (Jan. 2021), pp. 30–37. ISSN: 1476-1122, 1476-4660. DOI: 10.1038/s41563-020-00807-1.

[296] William Legrand, Davide Maccariello, Nicolas Reyren, Karin Garcia, Christoforos Moutafis, Constance Moreau-Luchaire, Sophie Collin, Karim Bouzehouane, Vincent Cros, and Albert Fert. "Room-Temperature Current-Induced Generation and Motion of sub-100 nm Skyrmions". In: *Nano Lett.* 17.4 (Apr. 12, 2017), pp. 2703–2712. ISSN: 1530-6984, 1530-6992. DOI: 10.1021/acs.nanolett.7b00649.

[297] Seungmo Yang, Kyoung-Woong Moon, Tae-Seong Ju, Changsoo Kim, Hyun-Joong Kim, Juran Kim, Bao Xuan Tran, Jung-Il Hong, and Chanyong Hwang. "Electrical Generation and Deletion of Magnetic Skyrmion-Bubbles via Vertical Current Injection". In: *Adv. Mater.* 33.45 (Nov. 2021), p. 2104406. ISSN: 0935-9648, 1521-4095. DOI: 10.1002/adma.202104406.

[298] Felix Büttner, Ivan Lemesh, Michael Schneider, Bastian Pfau, Christian M. Günther, Piet Hessing, Jan Geilhufe, Lucas Caretta, Dieter Engel, Benjamin Krüger, Jens Viefhaus, Stefan Eisebitt, and Geoffrey S. D. Beach. "Field-free deterministic ultrafast creation of magnetic skyrmions by spin–orbit

torques". In: *Nat. Nanotechnol.* 12.11 (Nov. 2017), pp. 1040–1044. ISSN: 1748-3387, 1748-3395. DOI: 10.1038/nnano.2017.178.

[299] I. V. Soldatov, W. Jiang, S. G. E. Te Velthuis, A. Hoffmann, and R. Schäfer. "Size analysis of sub-resolution objects by Kerr microscopy". In: *Applied Physics Letters* 112.26 (June 25, 2018), p. 262404. ISSN: 0003-6951, 1077-3118. DOI: 10.1063/1.5027539.

[300] August Köhler. "Ein neues Beleuchtungsverfahren für mikrophotographische Zwecke". In: *Zeitschrift für wissenschaftliche Mikroskopie und für Mikroskopische Technik* 10 (1893), pp. 433–440.

[301] Scientifica. *A 6 step guide to Koehler Illumination*. URL: https://www.scientifica.uk.com/learning-zone/a-6-step-guide-to-koehler-illumination.

[302] IPC Plating Processes Subcommittee. *Performance Specification for Electroless Nickel/Immersion Gold (ENIG) Plating for Printed Boards - Standard IPC-4552A*. 2017.

[303] Johannes Schindelin, Ignacio Arganda-Carreras, Erwin Frise, Verena Kaynig, Mark Longair, Tobias Pietzsch, Stephan Preibisch, Curtis Rueden, Stephan Saalfeld, Benjamin Schmid, Jean-Yves Tinevez, Daniel James White, Volker Hartenstein, Kevin Eliceiri, Pavel Tomancak, and Albert Cardona. "Fiji: an open-source platform for biological-image analysis". In: *Nat Methods* 9.7 (July 2012), pp. 676–682. ISSN: 1548-7091, 1548-7105. DOI: 10.1038/nmeth.2019.

[304] Dmitry Ershov, Minh-Son Phan, Joanna W. Pylvänäinen, Stéphane U. Rigaud, Laure Le Blanc, Arthur Charles-Orszag, James R. W. Conway, Romain F. Laine, Nathan H. Roy, Daria Bonazzi, Guillaume Duménil, Guillaume Jacquemet, and Jean-Yves Tinevez. "TrackMate 7: integrating state-of-the-art segmentation algorithms into tracking pipelines". In: *Nat Methods* 19.7 (July 2022). Publisher: Springer Science and Business Media LLC, pp. 829–832. ISSN: 1548-7091, 1548-7105. DOI: 10.1038/s41592-022-01507-1.

[305] Jean-Yves Tinevez, Nick Perry, Johannes Schindelin, Genevieve M. Hoopes, Gregory D. Reynolds, Emmanuel Laplantine, Sebastian Y. Bednarek, Spencer L. Shorte, and Kevin W. Eliceiri. "TrackMate: An open and extensible platform for single-particle tracking". In: *Methods* 115 (Feb. 2017). Publisher: Elsevier BV, pp. 80–90. ISSN: 1046-2023. DOI: 10.1016/j.ymeth.2016.09.016.

[306] Khuloud Jaqaman, Dinah Loerke, Marcel Mettlen, Hirotaka Kuwata, Sergio Grinstein, Sandra L Schmid, and Gaudenz Danuser. "Robust single-particle tracking in live-cell time-lapse sequences". In: *Nat Methods* 5.8 (Aug. 2008), pp. 695–702. ISSN: 1548-7091, 1548-7105. DOI: 10.1038/nmeth.1237.

[307] Daniel B. Allan, Thomas Caswell, Nathan C. Keim, Casper M. van der Wel, and Ruben W. Verweij. *soft-matter/trackpy: v0.6.4*. Version v0.6.4. July 10, 2024. DOI: 10.5281/ZENODO.1213240.

[308] John C. Crocker and David G. Grier. "Methods of Digital Video Microscopy for Colloidal Studies". In: *J. Colloid Interface Sci.* 179.1 (Apr. 1996), pp. 298–310. ISSN: 00219797. DOI: 10.1006/jcis.1996.0217.

[309] Isaac Labrie-Boulay, Thomas Brian Winkler, Daniel Franzen, Alena Romanova, Hans Fangohr, and Mathias Kläui. "Machine-learning-based detection of spin structures". In: *Phys. Rev. Applied* 21.1 (Jan. 10, 2024), p. 014014. ISSN: 2331-7019. DOI: 10.1103/PhysRevApplied.21.014014.

[310] Thomas Brian Winkler, Isaac Labrie-Boulay, Alena Romanova, Hans Fangohr, Mathias Kläui, Raphael Gruber, Fabian Kammerbauer, Klaus Raab, Jaukub Zazvorka, and Kilian Leutner. *MOKE-microscopy-Skyrmion-dataset*. Version 1.0. Apr. 20, 2024. DOI: 10.5281/ZENODO.7636109.

[311] Thibaud Denneulin, Jan Caron, Knut Müller-Caspary, Olivier Boulle, András Kovács, and Rafal E Dunin-Borkowski. "Visibility and Apparent Size of Néel-Type Magnetic Skyrmions in Fresnel Defocus Images of Multilayer Films". In: *Microscopy and Microanalysis* 27.6 (Dec. 1, 2021), pp. 1356–1365. ISSN: 1435-8115, 1431-9276. DOI: 10.1017/S1431927621012927.

[312] T. Devolder. "Light ion irradiation of Co/Pt systems: Structural origin of the decrease in magnetic anisotropy". In: *Phys. Rev. B* 62.9 (Sept. 1, 2000), pp. 5794–5802. ISSN: 0163-1829, 1095-3795. DOI: 10.1103/PhysRevB.62.5794.

[313] A. Maziewski, P. Mazalski, Z. Kurant, M. O. Liedke, J. McCord, J. Fassbender, J. Ferré, A. Mougin, A. Wawro, L. T. Baczewski, A. Rogalev, F. Wilhelm, and T. Gemming. "Tailoring of magnetism in Pt/Co/Pt ultrathin films by ion irradiation". In: *Phys. Rev. B* 85.5 (Feb. 24, 2012), p. 054427. ISSN: 1098-0121, 1550-235X. DOI: 10.1103/PhysRevB.85.054427.

[314] T. Devolder, I. Barisic, S. Eimer, K. Garcia, J.-P. Adam, B. Ockert, and D. Ravelosona. "Irradiation-induced tailoring of the magnetism of CoFeB/MgO ultrathin films". In: *Journal of Applied Physics* 113.20 (May 28, 2013), p. 203912. ISSN: 0021-8979, 1089-7550. DOI: 10.1063/1.4808102.

[315] A. Sud, S. Tacchi, D. Sagkovits, C. Barton, M. Sall, L. H. Diez, E. Stylianidis, N. Smith, L. Wright, S. Zhang, X. Zhang, D. Ravelosona, G. Carlotti, H. Kurebayashi, O. Kazakova, and M. Cubukcu. "Tailoring interfacial effect in multilayers with Dzyaloshinskii–Moriya interaction by helium ion irradiation". In: *Sci Rep* 11.1 (Dec. 8, 2021), p. 23626. ISSN: 2045-2322. DOI: 10.1038/s41598-021-02902-y.

[316] Yue Hu, Senfu Zhang, Yingmei Zhu, Chengkun Song, Junfeng Huang, Chen Liu, Xuan Meng, Xia Deng, Liu Zhu, Chaoshuai Guan, Hongxin Yang, Mingsu Si, Junwei Zhang, and Yong Peng. "Precise Tuning of Skyrmion Density in a Controllable Manner by Ion Irradiation". In: *ACS Appl. Mater. Interfaces* 14.29 (July 27, 2022), pp. 34011–34019. ISSN: 1944-8244, 1944-8252. DOI: 10.1021/acsami.2c07268.

[317] Valentin Ahrens, Luca Gnoli, Domenico Giuliano, Simon Mendisch, Martina Kiechle, Fabrizio Riente, and Markus Becherer. "Skyrmion velocities in FIB irradiated W/CoFeB/MgO thin films". In: *AIP Advances* 12.3 (Mar. 1, 2022), p. 035325. ISSN: 2158-3226. DOI: 10.1063/9.0000287.

[318] Annalena Wolff. "Focused ion beams: An overview of the technology and its capabilities". In: *Wiley Analytical Science* Analytical Science Article DO Series (2020).

[319] *Gallium*. Wikipedia - The Free Encyclopedia. Mar. 15, 2025. URL: https://en.wikipedia.org/wiki/Gallium.

[320] *Spin-ion Technologies*. 10 Boulevard Thomas Gobert, 91120 Palaiseau, France.

[321] R. C. Jaklevic, John Lambe, A. H. Silver, and J. E. Mercereau. "Quantum Interference Effects in Josephson Tunneling". In: *Phys. Rev. Lett.* 12.7 (Feb. 17, 1964), pp. 159–160. ISSN: 0031-9007. DOI: 10.1103/PhysRevLett.12.159.

[322] G. Binnig, C. F. Quate, and Ch. Gerber. "Atomic Force Microscope". In: *Phys. Rev. Lett.* 56.9 (Mar. 3, 1986), pp. 930–933. ISSN: 0031-9007. DOI: 10.1103/PhysRevLett.56.930.

[323] Y. Martin and H. K. Wickramasinghe. "Magnetic imaging by "force microscopy" with 1000 Å resolution". In: *Applied Physics Letters* 50.20 (May 18, 1987), pp. 1455–1457. ISSN: 0003-6951, 1077-3118. DOI: 10.1063/1.97800.

[324] J. J. Sáenz, N. García, P. Grütter, E. Meyer, H. Heinzelmann, R. Wiesendanger, L. Rosenthaler, H. R. Hidber, and H.-J. Güntherodt. "Observation of magnetic forces by the atomic force microscope". In: *Journal of Applied Physics* 62.10 (Nov. 15, 1987), pp. 4293–4295. ISSN: 0021-8979, 1089-7550. DOI: 10.1063/1.339105.

[325] Sai Li, Wang Kang, Xichao Zhang, Tianxiao Nie, Yan Zhou, Kang L. Wang, and Weisheng Zhao. "Magnetic skyrmions for unconventional computing". In: *Mater. Horiz.* 8.3 (2021), pp. 854–868. ISSN: 2051-6347, 2051-6355. DOI: 10.1039/D0MH01603A.

[326] M Weißenhofer and U Nowak. "Diffusion of skyrmions: the role of topology and anisotropy". In: *New J. Phys.* 22.10 (Oct. 29, 2020), p. 103059. ISSN: 1367-2630. DOI: 10.1088/1367-2630/abc1c9.

[327] Shi-Zeng Lin, Charles Reichhardt, Cristian D. Batista, and Avadh Saxena. "Particle model for skyrmions in metallic chiral magnets: Dynamics, pinning, and creep". In: *Phys. Rev. B* 87.21 (June 17, 2013), p. 214419. ISSN: 1098-0121, 1550-235X. DOI: 10.1103/PhysRevB.87.214419.

[328] Maarten A. Brems, Tobias Sparmann, Simon M. Fröhlich, Leonie-C. Dany, Jan Rothörl, Fabian Kammerbauer, Elizabeth M. Jefremovas, Oded Farago, Mathias Kläui, and Peter Virnau. "Realizing Quantitative Quasiparticle Modeling of Skyrmion Dynamics in Arbitrary Potentials". In: *Phys. Rev. Lett.* 134.4 (Jan. 28, 2025), p. 046701. ISSN: 0031-9007, 1079-7114. DOI: 10.1103/PhysRevLett.134.046701.

[329] Ivan Lemesh, Kai Litzius, Marie Böttcher, Pedram Bassirian, Nico Kerber, Daniel Heinze, Jakub Zázvorka, Felix Büttner, Lucas Caretta, Maxwell Mann, Markus Weigand, Simone Finizio, Jörg Raabe, Mi-Young Im, Hermann Stoll, Gisela Schütz, Bertrand Dupé, Mathias Kläui, and Geoffrey S. D. Beach. "Current-Induced Skyrmion Generation through Morphological Thermal Transitions in Chiral Ferromagnetic Heterostructures". In: *Adv. Mater.* 30.49 (Dec. 2018), p. 1805461. ISSN: 0935-9648, 1521-4095. DOI: 10.1002/adma.201805461.

[330] Kilian Leutner, Thomas Brian Winkler, Raphael Gruber, Robert Frömter, Johannes Güttinger, Hans Fangohr, and Mathias Kläui. "Skyrmion automotion and readout in confined counter-sensor device geometries". In: *Phys. Rev. Applied* 20.6 (Dec. 12, 2023), p. 064021. ISSN: 2331-7019. DOI: 10.1103/PhysRevApplied.20.064021.

[331] Chaofan Gong, Yan Zhou, and Guoping Zhao. "Dynamics of magnetic skyrmions under temperature gradients". In: *Applied Physics Letters* 120.5 (Jan. 31, 2022), p. 052402. ISSN: 0003-6951, 1077-3118. DOI: 10.1063/5.0080778.

[332] Raphael Gruber, Jan Rothörl, Simon M. Fröhlich, Maarten A. Brems, Fabian Kammerbauer, Maria-Andromachi Syskaki, Elizabeth M. Jefremovas, Sachin Krishnia, Asle Sudbø, Peter Virnau, and Mathias Kläui. *Imaging Topological Defect Dynamics Mediating 2D Skyrmion Lattice Melting*. Version Number: 1. 2025. DOI: 10.48550/ARXIV.2501.13151.

[333] Kosterlitz, J. M. "Topological Defects and Phase Transitions". 2016.

[334] Xichao Zhang, Jing Xia, Oleg A. Tretiakov, Motohiko Ezawa, Guoping Zhao, Yan Zhou, Xiaoxi Liu, and Masahito Mochizuki. "Laminar and transiently disordered dynamics of magnetic-skyrmion pipe flow". In: *Phys. Rev. B* 108.14 (Oct. 24, 2023), p. 144428. ISSN: 2469-9950, 2469-9969. DOI: 10.1103/PhysRevB.108.144428.

[335] Yongkang Luo, Shi-Zeng Lin, Maxime Leroux, Nicholas Wakeham, David M. Fobes, Eric D. Bauer, Jonathan B. Betts, Joe D. Thompson, Albert Migliori, Marc Janoschek, and Boris Maiorov. "Skyrmion lattice creep at ultra-low current densities". In: *Commun Mater* 1.1 (Nov. 11, 2020), p. 83. ISSN: 2662-4443. DOI: 10.1038/s43246-020-00083-1.

[336] Brian J. Kirby. *Micro- and nanoscale fluid mechanics: transport in microfluidic devices*. OCLC: ocn499130062. New York: Cambridge University Press, 2010. 512 pp. ISBN: 978-0-521-11903-0.

[337] Mark S. Ramsey. "Rheology, Viscosity, and Fluid Types". In: *Practical Wellbore Hydraulics and Hole Cleaning*. Elsevier, 2019, pp. 217–237. ISBN: 978-0-12-817088-5. DOI: 10.1016/B978-0-12-817088-5.00006-X.

[338] Landau, L. D. and Lifshitz, E. M. *Course of Theoretical Physics*. p. 47–53. 1966.

[339] S P Sutera and R Skalak. "The History of Poiseuille's Law". In: *Annu. Rev. Fluid Mech.* 25.1 (Jan. 1993), pp. 1–20. ISSN: 0066-4189, 1545-4479. DOI: 10.1146/annurev.fl.25.010193.000245.

[340] Miguel Alfonso Mendez and Jean-Marie Buchlin. "Notes on 2D Pulsatile Poiseuille Flows: An Introduction to Eigenfunction Expansion and Complex Variables using Matlab". In: (2016). Publisher: von Karman Institute Technical Note. DOI: 10.13140/RG.2.2.32209.02404.

[341] H. Başağaoğlu, P. Meakin, S. Succi, G. R. Redden, and T. R. Ginn. "Two-dimensional lattice Boltzmann simulation of colloid migration in rough-walled narrow flow channels". In: *Phys. Rev. E* 77.3 (Mar. 20, 2008), p. 031405. ISSN: 1539-3755, 1550-2376. DOI: 10.1103/PhysRevE.77.031405.

[342] Klaus Raab, Maurice Schmitt, Maarten A. Brems, Jan Rothörl, Fabian Kammerbauer, Sachin Krishnia, Mathias Kläui, and Peter Virnau. "Skyrmion flow in periodically modulated channels". In: *Phys. Rev. E* 110.4 (Oct. 25, 2024), p. L042601. ISSN: 2470-0045, 2470-0053. DOI: 10.1103/PhysRevE.110.L042601.

[343] Jim C. Chen and Albert S. Kim. "Brownian Dynamics, Molecular Dynamics, and Monte Carlo modeling of colloidal systems". In: *Advances in Colloid and Interface Science* 112.1 (Dec. 2004), pp. 159–173. ISSN: 00018686. DOI: 10.1016/j.cis.2004.10.001.

[344] J Vermant and M J Solomon. "Flow-induced structure in colloidal suspensions". In: *J. Phys.: Condens. Matter* 17.4 (Feb. 2, 2005), R187–R216. ISSN: 0953-8984, 1361-648X. DOI: 10.1088/0953-8984/17/4/R02.

[345] Lucio Isa, Rut Besseling, and Wilson C K Poon. "Shear Zones and Wall Slip in the Capillary Flow of Concentrated Colloidal Suspensions". In: *Phys. Rev. Lett.* 98.19 (May 10, 2007), p. 198305. ISSN: 0031-9007, 1079-7114. DOI: 10.1103/PhysRevLett.98.198305.

[346] Akira Matsui, Takuya Nomoto, and Ryotaro Arita. "Skyrmion-size dependence of the topological Hall effect: A real-space calculation". In: *Phys. Rev. B* 104.17 (Nov. 23, 2021), p. 174432. ISSN: 2469-9950, 2469-9969. DOI: 10.1103/PhysRevB.104.174432.

[347] M. N. Potkina, I. S. Lobanov, H. Jónsson, and V. M. Uzdin. "Stability of magnetic skyrmions: Systematic calculations of the effect of size from nanometer scale to microns". In: *Phys. Rev. B* 107.18 (May 8, 2023), p. 184414. ISSN: 2469-9950, 2469-9969. DOI: 10.1103/PhysRevB.107.184414.

[348] R. Takagi, Y. Yamasaki, T. Yokouchi, V. Ukleev, Y. Yokoyama, H. Nakao, T. Arima, Y. Tokura, and S. Seki. "Particle-size dependent structural transformation of skyrmion lattice". In: *Nat Commun* 11.1 (Nov. 11, 2020), p. 5685. ISSN: 2041-1723. DOI: 10.1038/s41467-020-19480-8.

[349] Hee Young Kwon, Kyung Mee Song, Juyoung Jeong, Ah-Yeon Lee, Seung-Young Park, Jeehoon Kim, Changyeon Won, Byoung-Chul Min, Hye Jung Chang, and Jun Woo Choi. "High-density Néel-type magnetic skyrmion phase stabilized at high temperature". In: *NPG Asia Mater* 12.1 (Dec. 2020), p. 86. ISSN: 1884-4049, 1884-4057. DOI: 10.1038/s41427-020-00270-z.

[350] Xichao Zhang, Jing Xia, and Xiaoxi Liu. "Structural transition of skyrmion quasiparticles under compression". In: *Phys. Rev. B* 105.18 (May 2, 2022), p. 184402. ISSN: 2469-9950, 2469-9969. DOI: 10.1103/PhysRevB.105.184402.

[351] Daniel J. Jacob. *Introduction to atmospheric chemistry*. Online-Ausg. Princeton, N.J: Princeton University Press, 1999. 266 pp. ISBN: 978-0-691-00185-2.

[352] Frank M. White. *Fluid mechanics*. 6. ed., international ed. McGraw-Hill series in mechanical engineering. pp. 63, 66. Boston: McGraw-Hill, 2008. 864 pp. ISBN: 978-0-07-128645-9.

[353] Clapeyron, E. *Mémoire sur la puissance motrice de la chaleur*. Vol. XIV. pp. 90-153. Facsimile at the Bibliothèque nationale de France: Journal de l'École Polytechnique, 1835.

[354] A. Krönig. "Grundzüge einer Theorie der Gase". In: *Annalen der Physik* 175.10 (Jan. 1856), pp. 315–322. ISSN: 0003-3804, 1521-3889. DOI: 10.1002/andp.18561751008.

[355] R. Clausius. "Ueber die Art der Bewegung, welche wir Wärme nennen". In: *Annalen der Physik* 176.3 (Jan. 1857), pp. 353–380. ISSN: 0003-3804, 1521-3889. DOI: 10.1002/andp.18571760302.

[356] Junichi Iwasaki, Masahito Mochizuki, and Naoto Nagaosa. "Current-induced skyrmion dynamics in constricted geometries". In: *Nature Nanotech* 8.10 (Oct. 2013), pp. 742–747. ISSN: 1748-3387, 1748-3395. DOI: 10.1038/nnano.2013.176.

[357] Karin Everschor-Sitte, Matthias Sitte, Thierry Valet, Artem Abanov, and Jairo Sinova. "Skyrmion production on demand by homogeneous DC currents". In: *New J. Phys.* 19.9 (Sept. 1, 2017), p. 092001. ISSN: 1367-2630. DOI: 10.1088/1367-2630/aa8569.

[358] Giovanni Finocchio, Massimiliano Di Ventra, Kerem Y. Camsari, Karin Everschor-Sitte, Pedram Khalili Amiri, and Zhongming Zeng. "The promise of spintronics for unconventional computing". In: *Journal of Magnetism and Magnetic Materials* 521 (Mar. 2021), p. 167506. ISSN: 03048853. DOI: 10.1016/j.jmmm.2020.167506.

[359] Wei D. Lu, Christof Teuscher, Stephen A. Sarles, Yuchao Yang, Aida Todri-Sanial, and Xiao-Bo Zhu. "A perfect storm and a new dawn for unconventional computing technologies". In: *npj Unconv. Comput.* 1.1 (Sept. 12, 2024), 9, s44335–024–00011–3. ISSN: 3004-8672. DOI: 10.1038/s44335-024-00011-3.

[360] Albert Fert, Nicolas Reyren, and Vincent Cros. "Magnetic skyrmions: advances in physics and potential applications". In: *Nat. Rev. Mater.* 2.7 (June 13, 2017), p. 17031. ISSN: 2058-8437. DOI: 10.1038/natrevmats.2017.31.

[361] Alexei N. Bogdanov and Christos Panagopoulos. "Physical foundations and basic properties of magnetic skyrmions". In: *Nat. Rev. Phys.* 2.9 (Sept. 2020), pp. 492–498. ISSN: 2522-5820. DOI: 10.1038/s42254-020-0203-7.

[362] Takaaki Dohi, Samik DuttaGupta, Shunsuke Fukami, and Hideo Ohno. "Formation and current-induced motion of synthetic antiferromagnetic skyrmion bubbles". In: *Nat. Commun.* 10.1 (Dec. 2019), p. 5153. ISSN: 2041-1723. DOI: 10.1038/s41467-019-13182-6.

[363] D. Pinna, F. Abreu Araujo, J.-V. Kim, V. Cros, D. Querlioz, P. Bessiere, J. Droulez, and J. Grollier. "Skyrmion Gas Manipulation for Probabilistic Computing". In: *Phys. Rev. Appl.* 9.6 (June 13, 2018), p. 064018. ISSN: 2331-7019. DOI: 10.1103/PhysRevApplied.9.064018.

[364] Friedemann Pulvermüller, Rosario Tomasello, Malte R. Henningsen-Schomers, and Thomas Wennekers. "Biological constraints on neural network models of cognitive function". In: *Nat Rev Neurosci* 22.8 (Aug. 2021), pp. 488–502. ISSN: 1471-003X, 1471-0048. DOI: 10.1038/s41583-021-00473-5.

[365] Ana Halužan Vasle and Miha Moškon. "Synthetic biological neural networks: From current implementations to future perspectives". In: *BioSystems* 237 (Mar. 2024), p. 105164. ISSN: 03032647. DOI: 10.1016/j.biosystems.2024.105164.

[366] Samuel Schmidgall, Rojin Ziaei, Jascha Achterberg, Louis Kirsch, S. Pardis Hajiseyedrazi, and Jason Eshraghian. "Brain-inspired learning in artificial neural networks: A review". In: *APL Machine Learning* 2.2 (June 1, 2024), p. 021501. ISSN: 2770-9019. DOI: 10.1063/5.0186054.

[367] Ryan Alexander Pepper, Marijan Beg, David Cortés-Ortuño, Thomas Kluyver, Marc-Antonio Bisotti, Rebecca Carey, Mark Vousden, Maximilian Albert, Weiwei Wang, Ondrej Hovorka, and Hans Fangohr. "Skyrmion states in thin confined polygonal nanostructures". In: *Journal of Applied Physics* 123.9 (Mar. 7, 2018), p. 093903. ISSN: 0021-8979, 1089-7550. DOI: 10.1063/1.5022567.

[368] Matthew J. Marinella and Sapan Agarwal. "Efficient reservoir computing with memristors". In: *Nat. Electron.* 2.10 (Oct. 2019), pp. 437–438. ISSN: 2520-1131. DOI: 10.1038/s41928-019-0318-y.

[369] Riccardo Tomasello, Marco Ricci, Pietro Burrascano, Vito Puliafito, Mario Carpentieri, and Giovanni Finocchio. "Electrical detection of single magnetic skyrmion at room temperature". In: *AIP Adv.* 7.5 (May 2017), p. 056022. ISSN: 2158-3226. DOI: 10.1063/1.4975998.

[370] *COMSOL Multiphysics. v. 6.0 www.comsol.com. COMSOL AB, Stockholm, Sweden*. 2021.

[371] Pedregosa, F., Varoquaux, G., Gramfort, A, Michel, V., Thirion, B., Grisel, O., Blondel, M., Prettenhofer, P., Weiss, R., Dubourg, V., Vanderplas, J., Passos, A., Cournapeau, D., Brucher, M., Perrot, M., and Duchesnay, E. "Scikit-learn: Machine Learning in Python". In: *Journal of Machine Learning Research* 12 (2011), pp. 2825–2830.

[372] Markus Weißenhofer, Levente Rózsa, and Ulrich Nowak. "Skyrmion Dynamics at Finite Temperatures: Beyond Thiele's Equation". In: *Phys. Rev. Lett.* 127.4 (July 22, 2021), p. 047203. ISSN: 0031-9007, 1079-7114. DOI: 10.1103/PhysRevLett.127.047203.

[373] K. Karube, J. S. White, N. Reynolds, J. L. Gavilano, H. Oike, A. Kikkawa, F. Kagawa, Y. Tokunaga, H. M. Rønnow, Y. Tokura, and Y. Taguchi. "Robust metastable skyrmions and their triangular–square lattice structural transition in a high-temperature chiral magnet". In: *Nature Mater* 15.12 (Dec. 2016), pp. 1237–1242. ISSN: 1476-1122, 1476-4660. DOI: 10.1038/nmat4752.

[374] K. Watanabe, B. Jinnai, S. Fukami, H. Sato, and H. Ohno. "Shape anisotropy revisited in single-digit nanometer magnetic tunnel junctions". In: *Nat Commun* 9.1 (Feb. 14, 2018), p. 663. ISSN: 2041-1723. DOI: 10.1038/s41467-018-03003-7.

[375] B. Jinnai, J. Igarashi, T. Shinoda, K. Watanabe, S. Fukami, and H. Ohno. "Fast Switching Down to 3.5 ns in Sub-5-nm Magnetic Tunnel Junctions Achieved by Engineering Relaxation Time". In: *2021 IEEE International Electron Devices Meeting (IEDM)*. 2021 IEEE International Electron Devices Meeting (IEDM). San Francisco, CA, USA: IEEE, Dec. 11, 2021, pp. 1–4. ISBN: 978-1-66542-572-8. DOI: 10.1109/IEDM19574.2021.9720509.

[376] R. Landauer. "Irreversibility and Heat Generation in the Computing Process". In: *IBM J. Res. & Dev.* 5.3 (July 1961), pp. 183–191. ISSN: 0018-8646, 0018-8646. DOI: 10.1147/rd.53.0183.

[377] Miguel Romera, Philippe Talatchian, Sumito Tsunegi, Flavio Abreu Araujo, Vincent Cros, Paolo Bortolotti, Juan Trastoy, Kay Yakushiji, Akio Fukushima, Hitoshi Kubota, Shinji Yuasa, Maxence Ernoult, Damir Vodenicarevic, Tifenn Hirtzlin, Nicolas Locatelli, Damien Querlioz, and Julie Grollier. "Vowel recognition with four coupled spin-torque nano-oscillators". In: *Nature* 563.7730 (Nov. 2018), pp. 230–234. ISSN: 0028-0836, 1476-4687. DOI: 10.1038/s41586-018-0632-y.

[378] Mohammad Zahedinejad, Himanshu Fulara, Roman Khymyn, Afshin Houshang, Mykola Dvornik, Shunsuke Fukami, Shun Kanai, Hideo Ohno, and Johan Åkerman. "Memristive control of mutual spin Hall nano-oscillator synchronization for neuromorphic computing". In: *Nat. Mater.* 21.1 (Jan. 2022), pp. 81–87. ISSN: 1476-1122, 1476-4660. DOI: 10.1038/s41563-021-01153-6.

[379] A. Houshang, E. Iacocca, P. Dürrenfeld, S. R. Sani, J. Åkerman, and R. K. Dumas. "Spin-wave-beam driven synchronization of nanocontact spin-torque oscillators". In: *Nat. Nanotechnol.* 11.3 (Mar. 2016), pp. 280–286. ISSN: 1748-3387, 1748-3395. DOI: 10.1038/nnano.2015.280.

[380] Tsz Chung Cheng, Lin Zhang, Yuichiro Kurokawa, Ryuta Satone, Kazuhiko Tokunaga, and Hiromi Yuasa. "Computational study of skyrmion stability and transport on W/CoFeB". In: *Sci Rep* 15.1 (Mar. 5, 2025), p. 7708. ISSN: 2045-2322. DOI: 10.1038/s41598-025-91415-z.

[381] Runze Chen and Yu Li. "Voltage-Controlled Skyrmionic Interconnect with Multiple Magnetic Information Carriers". In: *ACS Appl. Mater. Interfaces* 14.26 (July 6, 2022), pp. 30420–30434. ISSN: 1944-8244, 1944-8252. DOI: 10.1021/acsami.2c07470.

[382] Seungmo Yang, Jong Wan Son, Tae-Seong Ju, Duc Minh Tran, Hee-Sung Han, Sungkyun Park, Bae Ho Park, Kyoung-Woong Moon, and Chanyong Hwang. "Magnetic Skyrmion Transistor Gated with Voltage-Controlled Magnetic Anisotropy". In: *Advanced Materials* 35.9 (Mar. 2023), p. 2208881. ISSN: 0935-9648, 1521-4095. DOI: 10.1002/adma.202208881.

[383] Börge Göbel, Ingrid Mertig, and Oleg A. Tretiakov. "Beyond skyrmions: Review and perspectives of alternative magnetic quasiparticles". In: *Physics Reports* 895 (Feb. 2021), pp. 1–28. ISSN: 03701573. DOI: 10.1016/j.physrep.2020.10.001.

[384] *Tantal*. Wikipedia - The Free Encyclopedia. Mar. 15, 2025. URL: https://de.wikipedia.org/wiki/Tantal.

Necessities and Statements

Synopsis

This dissertation investigates controlled manipulation of skyrmions - topologically protected spin textures with quasi-particle characteristics in magnetic thin films - with a focus on their dynamics, the influence of artificial boundaries, and their application in energy-efficient unconventional computing.
The study examines skyrmion flow in the creep regime, where motion is driven by spin-orbit torque at velocities in the micrometer-per-second range, superimposed with thermally induced diffusive movement. This dynamic is strongly influenced by skyrmion-skyrmion and skyrmion-edge interactions, as well as the non-flat energy landscape. Experiments in both straight and modulated channels revealed boundary-dependent velocity profiles, in qualitative agreement with Thiele-based simulations. Moreover, skyrmions serve as a 2D rheological model system. Simulations revealed novel phenomena when incorporating a non-negligible skyrmion Hall angle: back-propagation, motion against the direction of applied force.
An additional method of manipulation explored is ion irradiation, which locally alters magnetic properties permanently. Ion irradiation enables the creation of artificial barriers, for instance in skyrmion compression, where skyrmions are pushed against a boundary. This process reduces both the inter-skyrmion distance in the lattice - analogous to gas molecules under pressure - but also their individual size. The experimental findings are supported by adapted theoretical models and simulations.
A central component is the development of a novel reservoir computing (RC) device based on skyrmion dynamics, particularly the Brownian diffusion of confined skyrmions. Even in simple confining geometries such as an equilateral triangle, the system demonstrates the ability to perform Boolean logic operations, including nonlinear logic, at ultra-low current densities. Its scalability and potential for enhanced complexity position skyrmion-based RC as a promising system for low-power, unconventional computing. The detailed analysis of skyrmion dynamics and the presented RC demonstrator underscore the vast potential of spintronics - and skyrmions in particular - for next-generation information technologies.

Kurzzusammenfassung

Diese Dissertation untersucht das magnetische Verhalten und die gezielte Manipulation von Skyrmionen - topologisch geschützten Spintexturen mit Quasi-Teilchencharakter in metallischen Dünnschichten - mit Fokus auf deren Dynamik, Einfluss der Strukturenwände und Anwendung in energieeffizientem unconventional computing. Untersucht wurde der Skyrmionenfluss im Creep-Regime, also der durch Spin-Bahn-Drehmoment (Spin-Orbit Torque) induzierte Antrieb mit Geschwindigkeiten im Mikrometer-pro-Sekunde-Bereich in Überlagerung mit thermisch diffusionsgetriebener Bewegung. Dieser wird stark beeinflusst durch

Skyrmion-Skyrmion- und Skyrmion-Rand-Wechselwirkungen sowie durch die nicht-flache Energielandschaft. In geraden und modulierten Kanälen zeigten sich geschwindigkeitsprofile mit Randabhängigkeit, welche qualitativ mit Thiele-basierten Simulationen übereinstimmen. Skyrmionen dienen darüber hinaus als zweidimensionales rheologisches Modellsystem. In Simulationen traten neue Phänomene auf, insbesondere unter Berücksichtigung eines Skyrmion-Hall-Winkels von 15°: sogenannte Rückwärtspropagation – eine Bewegung der Skyrmionen entgegen der Richtung der angelegten Kraft, hervorgerufen durch Wechselwirkungen mit Rändern und benachbarten Skyrmionen. Eine weitere Möglichkeit der gezielten Manipulation stellt die Ionenbestrahlung dar, bei der die magnetischen Eigenschaften lokal und dauerhaft verändert werden. Durch kontrollierte He^+- und Ga^+-Bestrahlung lassen sich künstliche Barrieren erzeugen, etwa zur Skyrmion-Kompression. Dabei werden Skyrmionen gegen eine Barriere gedrückt, wodurch nicht nur der Abstand zwischen den Skyrmionen im Gitter – analog zu Gasmolekülen unter Druck – verringert wird, sondern auch deren Größe. Die experimentellen Ergebnisse hierzu werden durch angepasste theoretische Modelle und Simulationen gestützt. Ein zentrales Element dieser Arbeit ist die Entwicklung eines neuartigen Reservoir-Computing-(RC)-Konzepts, das auf der Dynamik von Skyrmionen, insbesondere deren Brown'scher Diffusion unter Konfinierung, basiert. Selbst in einfachen Geometrien wie einem gleichseitigen Dreieck zeigt das System die Fähigkeit zur Ausführung boolescher Logikoperationen, einschließlich nichtlinearer Logik, bei extrem niedrigen Stromdichten. Ein wesentlicher Aspekt der Energieeffizienz ist der automatische Reset-Mechanismus des Reservoirs. Seine Skalierbarkeit und das Potenzial zur Erhöhung der Systemkomplexität machen skyrmionenbasiertes RC zu einer vielversprechenden Plattform für energieeffizientes, unkonventionelles Rechnen. Die detaillierte Analyse der komplexen Dynamik sowie der Demonstrator zur unkonventionellen Informationsverarbeitung verdeutlichen das enorme Potenzial der Spintronik – insbesondere von Skyrmionen.

Versicherung

a) Ich, Klaus RAAB, versichere, dass diese Arbeit (SKYRMIONS AS QUASI-PARTICLES - FROM DYNAMICS IN UNCONVENTIONAL COMPUTING) selbständig verfasst ist, ausschließlich die angegebenen Quellen und Hilfsmittel verwendet wurden und von der Ordnung zur Sicherung guter wissenschaftlicher Praxis in Forschung und Lehre und zum Verfahren zum Umgang mit wissenschaftlichem Fehlverhalten Kenntnis genommen.
b) Ich versichere, dass die Dissertation nicht als Prüfungsarbeit für eine andere Prüfung eingereicht wurde.
c) Ich versichere, dass die gleiche Abhandlung oder Teile davon noch nicht als Dissertation bei einer anderen Fakultät oder einem anderen Fachbereich eingereicht wurde.

Ort, Datum und
Unterschrift:

Eigenständigkeitserklärung

Hiermit erkläre ich, Klaus RAAB, dass die vorliegende Arbeit selbstständig verfasst und keine anderen als die angegebenen Quellen und Hilfsmittel (dazu zählen auch KI-basierte Anwendungen oder Werkzeuge) benutzt habe. Sämtliche wörtlichen oder sinngemäßen Übernahmen und Zitate sind kenntlich gemacht und nachgewiesen. Im Anhang D.7 „Utilization of AI“ habe ich die verwendeten KI-Tools dokumentiert. Mit Abgabe der vorliegenden Leistung übernehme ich die Verantwortung für das eingereichte Gesamtprodukt. Ich verantworte damit auch jegliche KI-generierten Inhalte, die ich in meine Arbeit übernommen habe. Die Richtigkeit übernommener (KI-generierter) Aussagen und Inhalte habe ich nach bestem Wissen und Gewissen geprüft.
Mir ist bekannt, dass ein Verstoß gegen die genannten Punkte prüfungsrechtliche Konsequenzen hat.

Ort, Datum und
Unterschrift:

Curriculum Vitae

The curriculum Vitae is displayed on the next pages.

Filler

page

instead

of

CV